

Electronic Thesis and Dissertation Repository

6-21-2012 12:00 AM

Performance of Hollow Bar Micropiles Under Axial and Lateral Loads in Cohesive Soils

Ahmed Yehia Abd El-aziz
The University of Western Ontario

Supervisor
M. Hesham El Naggari
The University of Western Ontario

Graduate Program in Civil and Environmental Engineering
A thesis submitted in partial fulfillment of the requirements for the degree in Doctor of Philosophy
© Ahmed Yehia Abd El-aziz 2012

Follow this and additional works at: <https://ir.lib.uwo.ca/etd>



Part of the [Geotechnical Engineering Commons](#)

Recommended Citation

Abd El-aziz, Ahmed Yehia, "Performance of Hollow Bar Micropiles Under Axial and Lateral Loads in Cohesive Soils" (2012). *Electronic Thesis and Dissertation Repository*. 595.
<https://ir.lib.uwo.ca/etd/595>

This Dissertation/Thesis is brought to you for free and open access by Scholarship@Western. It has been accepted for inclusion in Electronic Thesis and Dissertation Repository by an authorized administrator of Scholarship@Western. For more information, please contact wlsadmin@uwo.ca.

**PERFORMANCE OF HOLLOW BAR MICROPILES UNDER AXIAL AND
LATERAL LOADS IN COHESIVE SOILS**

(Spine title: Performance of hollow bar micropiles under different loads)

(Thesis format: Monograph)

by

Ahmed Yehia Abd Elaziz

Graduate Program in
Engineering Science
Department of Civil and Environmental Engineering

A thesis submitted in partial fulfillment
of the requirements for the degree of
Doctor of Philosophy

The School of Graduate and Postdoctoral Studies
The University of Western Ontario
London, Ontario, Canada

© Ahmed Yehia Abd Elaziz 2012

THE UNIVERSITY OF WESTERN ONTARIO
School of Graduate and Postdoctoral Studies

CERTIFICATE OF EXAMINATION

Supervisor

Examiners

Dr. M. Hesham El Naggar

Dr. Tim Newson

Supervisory Committee

Dr. Abouzar Sadrekarimi

Dr. Maged Youssef

Dr. Pawel Kurowski

Dr.

Dr. Dennis Becker

The thesis by

Ahmed Yehia Abd Elaziz

Entitled:

Performance of hollow bar micropiles under axial and lateral loads in cohesive soils

is accepted in partial fulfillment of the requirements for the degree of
Doctor of Philosophy

Date

Chair of the Thesis Examination Board

ABSTRACT

The use of hollow core bars in micropiles has greatly increased over the past ten years. Hollow core construction, also known as “self drilled”, is becoming a popular option because it allows a faster installation processes and ground improvement at the same time. Despite the growing demand for hollow bar micropiles, little work has been devoted to evaluating the nominal bond strength between the micropile grout and the surrounding soil, especially in clayey soils. Moreover, the performance of such micropiles under different kinds of loading is still largely unknown and needs to be investigated.

In this study, a research methodology encompassing two primary elements is adopted. The first element is a series of full scale field studies on hollow bar micropiles installed in cohesive soils, while the second is numerical investigations on hollow bar micropiles. To accomplish the study, four hollow core micropiles were installed using an air flushing technique employing large drilling carbide bits. Twenty-two load tests were conducted on the four hollow bar micropiles. The hollow bar micropiles were loaded in four consecutive phases, which included; five axial monotonic, five axial cyclic load tests on single micropiles, four axial monotonic tests on pairs of hollow bar micropiles, two monotonic and six cyclic lateral tests on single micropiles. The results of each set of tests were utilized to validate a numerical model. Parametric studies were conducted on the calibrated model to provide design guide lines for hollow bar micropiles under different loads.

An equation is proposed to estimate the axial capacity of hollow bar micropiles in cohesive soils depending on the installation method adopted. In addition, an equation for the stiffness degradation under axial cyclic loading is proposed. It reveals that the group efficiency factor for hollow bar micropiles should be taken equal to 1, despite the spacing to diameter ratio employed. Moreover, a family of interaction factor diagrams is established to estimate the settlement of hollow bar micropiles group. Finally, the study demonstrated that hollow bar micropiles can carry moderate lateral loads with proper reinforcement configurations and pile head fixity condition.

Keywords

Micropiles, hollow bar micropiles, monotonic and cyclic field test, cohesive soils, finite element analysis, micropile group, lateral behavior, bond strength.

CO-AUTHORSHIP STATEMENT

This thesis is prepared in accordance with the regulation for a monograph format thesis stipulated by the school of graduate and post graduate studies at Western University. Dr. M. Hesham El Naggari, the author supervisor, is co-author of all the work presented in this thesis. The results of the field tests presented in chapter five are published in three different conference and one journal papers.

ACKNOWLEDGMENTS

The author wishes to express his deep gratitude to Dr. M. Hesham El Naggar for his supervision, encouragement, and never ending contribution and guidance during the process of this work. I am thankful to him for giving me this opportunity to work in his research team which expanded my geotechnical knowledge. Dr. El Naggar facilitated for me so many resources for finishing this project.

I would also like to express my appreciation to Williams Form Hard Ware for funding support through the course of the field tests. Special thanks to Mr. Martin Hodgson from Williams for his technical support throughout the research project. Sincere appreciations for EBS Engineering and Construction Company for installing the micropiles and for help setting the reaction frame at no cost. In addition, I want to thank BASF the chemical company for providing the 1341 Master flow grout at no cost.

The genuine assistance from the staff of the Geotechnical Research Centre, (GRC) and the University Machine Services (UMS) is acknowledged. Furthermore, I want to thank Wilbert Logan, Western Engineering labs supervisor, for his suggestions and assisting during piles instrumentation and Melody Richards, geotechnical lab supervisor, for helping during the laboratory tests of the soil samples.

I want to express very deep thanks to all graduate students who assisted me during my PhD studies, provided me with insight suggestions and their friendship that kept me going, even at times when the hurdles of developing the work seemed insurmountable.

No words can describe my thanks, gratitude and appreciation to my wife, Radwa; the candle that was burning herself to shed light on my path during both stressful and pleasant moments. Her patience, encouragement and love were peerless. I like to thank my son Kareem for being the source of great joy that kept my life in balance. Finally, the author wishes to express his sincere thanks to his father and mother for their endless love and support, which without their prayers I couldn't have accomplished this work.

Table of Contents

	Page
CERTIFICATE OF EXAMINATION	ii
ABSTRACT	iii
CO-AUTHORSHIP STATEMENT	v
ACKNOWLEDGMENTS	vi
Table of Contents	viii
List of Tables	xiv
List of Figures	xviii
List of Symbols	xxix
List of Appendices	xxxvii
CHAPTER 1: INTRODUCTION	1
1.1 Overview	1
1.2 Historical Background	2
1.3 Research Objectives	5
1.4 Research Methodology	6
1.5 Organization of the Dissertation	7
CHAPTER 2: LITERATURE REVIEW	9
2.1 Introduction	9

2.2	Micropiles Classification	10
2.2.1	Design classification of micropiles	11
2.2.2	Construction classification of micropiles	11
2.2.3	Classification of hollow-bar micropiles	15
2.3	Design Considerations for Micropiles	16
2.3.1	Structural design of micropiles	17
2.3.2	Geotechnical design capacity of micropiles	19
2.3.3	Design consideration of hollow bar micropiles	20
2.4	Review of Previous Studies	21
2.4.1	Investigations of different types of micropiles	23
2.4.2	Previous work on hollow bar micropiles	32
CHAPTER 3: SOIL INVESTIGATION AND GROUT EVALUATION		36
3.1	Soil Investigation	36
3.1.1	Site location and description	36
3.1.2	Site investigation program	36
3.1.3	Standard penetration test equipment and procedure	37
3.2	Subsurface Conditions	40
3.2.1	Soil stratigraphy	40
3.2.2	Soil classification and properties	45

3.2.3	Soil shear strength parameters	50
3.2.4	Soil stress history	60
3.2.5	Soil stiffness parameter	64
3.3	Grout Testing and Evolution	67
CHAPTER 4: HOLLOW CORE MICROPILE MATERIAL AND INSTALLATION		69
4.1	Hollow Core Steel Bar and Accessories	69
4.2	Hollow Bar Micropile Installation	77
4.2.1	Preparing the drilling rig	80
4.2.2	Installation and grouting	83
4.3	Embedded Strain Gauges Instrumentation	88
CHAPTER 5: AXIAL MONOTONIC AND CYCLIC PERFORMANCE OF HOLLOW BAR MICROPILES		91
5.1	Introduction	91
5.2	Axial Monotonic Load Tests	92
5.2.1	Testing equipment	92
5.2.2	Pile head instrumentation	95
5.2.3	Monotonic load test procedure	97
5.2.4	Monotonic test results and analysis	99
5.3	Axial Cyclic Load Tests	105

5.3.1	Test equipment and instrumentation	106
5.3.2	Cyclic load test procedure	106
5.3.3	Cyclic load test results and analysis	107
5.4	Numerical Analysis	118
5.5	Axial Loading Numerical Models	119
5.5.1	Monotonic axial loading models	120
5.5.2	Calibration of the monotonic field test results	135
5.5.3	Failure criteria	147
5.5.4	Load transfer mechanism	152
5.5.5	Parametric study	158
5.5.6	Closed form solution for hollow bar micropiles embedded in clayey soils under monotonic loading	177
5.5.7	Cyclic axial model	178
5.5.8	Calibration of the cyclic field test	181
CHAPTER 6: HOLLOW BAR MICROPILES GROUP BEHAVIOR		188
6.1	Introduction	188
6.2	Field Pile Group Load Tests	188
6.2.1	Testing equipment	188
6.2.2	Pile head instrumentation	191
6.2.3	Pile group load test procedure	194

6.2.4	Pile group test results and analysis	197
6.3	Numerical Analysis	202
6.3.1	Geometric modeling	203
6.3.2	Material modeling	208
6.4	Calibration of Pile Group Field Tests	209
6.4.1	Micropile group capacity	211
6.5	Parametric Study	215
6.5.1	Parametric study for group capacity	215
6.5.2	Parametric study for group performance	220
CHAPTER 7: LATERAL MONOTONIC AND CYCLIC PERFORMANCE OF HOLLOW BAR MICROPILES		234
7.1	Introduction	234
7.2	Monotonic Lateral Load tests	234
7.2.1	Lateral load testing equipment and pile head instrumentation	235
7.2.2	Lateral monotonic load test procedure and results	238
7.2.3	Failure mechanism and ultimate capacity for micropiles under lateral loads	240
7.2.4	Numerical simulation of monotonic lateral load tests	244
7.2.5	Calibration of the monotonic lateral field test	248
7.2.6	Parametric study	256

7.3 Lateral Cyclic Load Tests	266
7.3.1 Lateral cyclic load test procedure	267
7.3.2 Cyclic load test results and analysis	268
CHAPTER 8: SUMMARY, CONCLUSIONS, AND RECOMMENDATIONS	281
8.1 Summary	281
8.2 Results and Conclusions	283
8.2.1 Axial capacity of hollow bar micropile	283
8.2.2 Lateral performance of hollow bar micropiles	284
8.2.3 Hollow bar micropile group behavior	286
8.3 Recommendations for future work	287
REFERENCES	289
APPENDIX A: COPYRIGHT PERMISSIONS	298
CURRICULUM VITAE	304

List of Tables

Description	Page
Table 2.1. Typical α bond (Grout-to-Ground Bond) Values for Micropile Design (after FHWA NHI 2005)	22
Table 3.1. Index properties of the silty clay layer	46
Table 3.2. Soil properties for samples extracted from BH-2	47
Table 3.3. Summary of (UU) triaxial tests on samples from BH2	52
Table 3.4. Undrained shear strength values for the cohesive deposit	55
Table 3.5. Computed angle of friction from SPT values for BH-1	58
Table 3.6. Computed angle of friction from SPT values for BH-2	58
Table 3.7. Relative density and friction angle for BH-1	58
Table 3.8. Relative density and friction angle for BH-2	59
Table 3.9. Average values of k_o	62
Table 3.10. Summary of grout strength	68
Table 4.1. B7X Geo-drill bars (Ground Anchor System 2011)	71
Table 4.2. Types of lost bits and the applicable type of soil for each one (Ground Anchor System 2011)	74
Table 4.3. Types and the available drill bit diameters	75
Table 4.4. Strain gauge properties	90
Table 5.1. Micropiles creep at maximum applied load	103

Table 5.2. Summary of the monotonic testes phase results	105
Table 5.3. Design, amplitude and maximum applied load for cyclic load tests...	107
Table 5.4. Percentage increase in pile head displacement at the end of cyclic loading	115
Table 5.5. Initial and final stiffness of all the micropiles after the cyclic load test	115
Table 5.6. Geotechnical parameters assigned to the Mohr-Coulomb model	127
Table 5.7. Summary of the mesh sensitivity analysis parameter used	145
Table 5.8. Most common failure criteria for micropiles	149
Table 5.9. Failure loads for Micropiles in compression	150
Table 5.10. Compression capacity of hollow bar micropile, $L = 5.75\text{m}$, $L/d = 30$, $d_E = 1.25d$	162
Table 5.11. Compression capacity of hollow bar micropile, $L = 5.75\text{m}$, $L/d = 30$, $d_E = 1.5d$	162
Table 5.12. Compression capacity of hollow bar micropile, $L = 5.75\text{m}$, $L/d = 30$, $d_E = 1.75d$	163
Table 5.13. Compression capacity of hollow bar micropile, $L = 5.75\text{m}$, $L/d = 30$, $d_E = 1.75d$	163
Table 5.14. Compression capacity of hollow bar micropile, $L = 5.75\text{m}$, $L/d = 30$, $d_E = 2d$	164
Table 5.15. Compression capacity of hollow bar micropile, $L = 8.8\text{m}$, $L/d = 50$, $d_E = 1.25d$	164
Table 5.16. Compression capacity of hollow bar micropile, $L = 8.8\text{m}$, $L/d = 50$, $d_E = 1.5d$	165

Table 5.17. Compression capacity of hollow bar micropile, $L = 8.8\text{m}$, $L/d = 50$, $d_E = 1.75d$	165
Table 5.18. Compression capacity of hollow bar micropile, $L = 8.8\text{m}$, $L/d = 50$, $d_E = 1.75d$	166
Table 5.19. Compression capacity of hollow bar micropile, $L = 8.8\text{m}$, $L/d = 50$, $d_E = 2d$	166
Table 5.20. Uplift capacity of hollow bar micropile, $L = 5.75\text{m}$, $L/d = 30$, $d_E =$ $1.25d$	167
Table 5.21. Uplift capacity of hollow bar micropile, $L = 5.75\text{m}$, $L/d = 30$, $d_E =$ $1.5d$	167
Table 5.22. Uplift capacities of hollow bar micropile, $L = 5.75\text{m}$, $L/d = 30$, $d_E =$ $1.75d$	168
Table 5.23. Uplift capacity of hollow bar micropile, $L = 5.75\text{m}$, $L/d = 30$, $d_E =$ $1.75d$	168
Table 5.24. Uplift capacity of hollow bar micropile, $L = 5.75\text{m}$, $L/d = 30$, $d_E =$ $2d$	169
Table 5.25. Uplift capacity of hollow bar micropile, $L = 8.8\text{m}$, $L/d = 50$, $d_E =$ $1.25d$	169
Table 5.26. Uplift capacity of hollow bar micropile, $L = 8.8\text{m}$, $L/d = 50$, $d_E =$ $1.5d$	170
Table 5.27. Uplift capacity of hollow bar micropile, $L = 8.8\text{m}$, $L/d = 50$, $d_E =$ $1.75d$	170
Table 5.28. Uplift capacity of hollow bar micropile, $L = 8.8\text{m}$, $L/d = 50$, $d_E =$ $1.75d$	171
Table 5.29. Uplift capacity of hollow bar micropile, $L = 8.8\text{m}$, $L/d = 50$, $d_E =$ $2d$	171
Table 6.1. Micropiles group creep test at maximum applied load	201

Table 6.2. Pile group stiffness	202
Table 6.3. Number of elements for each model	205
Table 6.4. Group efficiency factor abased on pile spacing	212
Table7.1. Lateral interpretation criteria for piles	243
Table7.2. Interpreted failure load for MP1 and MP2	243
Table7.3. Grout and steel properties adopted in material modeling	250
Table7.4. Values of ϵ_{50} for stiff clay model in LPile (after Isenhower and Wang 2011)	251

List of Figures

Description	Page
Figure 1.1. Hollow bar micropiles system components (after micropiles brochures- Con-Tec system Ltd. 2011)	4
Figure 2.1. Micropile classification system based on philosophy of behavior (after FHWA 2000) (a) Case 1 (b) Case 2	12
Figure 2.2. Micropile classification system based on method of grouting (after FHWA 2000)	14
Figure 2.3. Final hollow core micropile (after Con-Tec system Ltd. 2011)	16
Figure 3.1. Location of test site (Google Map)	37
Figure 3.2. Plan view for the layout of Site 1 and Site 2	38
Figure 3.3. The Mounted (Morocka) rig and the solid stem used	39
Figure 3.4. Steps during field exploration	39
Figure 3.5. Borehole log for Site 2 (Livneh 2006)	41
Figure 3.6. The borehole log and the SPT (N_{field}) values versus depth for BH-1	42
Figure 3.7. The borehole log and the SPT (N_{field}) values versus depth for BH-2	43
Figure 3.8. Soil stratigraphy	44
Figure 3.9. Piece of the soil at the top 1 m from the test site	44
Figure 3.10. Index properties with respect to Plasticity chart	47
Figure 3.11. Hydrometer Grain size distribution of sample from BH-1 at depth 1.5m	48
Figure 3.12. Hydrometer Grain size distribution of sample from BH-1 at depth 4m	48

Figure 3.13. Grain Size distribution of sample from BH-2 at depth 5.8m	49
Figure 3.14. Grain Size distribution of sample from BH-1 at depth 7	49
Figure 3.15. Triaxial test result for sample at depth 3.0 m, BH-2	51
Figure 3.16. Triaxial test result for sample at depth 3.7 m, BH-2	51
Figure 3.17. Triaxial test result for sample at depth 4.3 m, BH-2	52
Figure 3.18. s_u profile versus depth; (a) BH-1; and (b) BH-2	56
Figure 3.19. Relative density- N_{field} relation based on Holtz and Gibbs (1979)	59
Figure 3.20. OCR profile for (a) BH-1; and (b) BH-2.....	63
Figure 3.21. Soil modulus versus depth; (a) BH-1, and (b) BH-2	66
Figure 4.1. Hollow core bar micropile parts (after Ground Anchor System 2011)...	70
Figure 4.2. B7X2-76 coupler	73
Figure 4.3. Three new large bits; (a) Tungsten carbide cross bit (d= 176mm); (b) Double cross bit (d = 176 mm), and (c) Carbide button cross drill bit (d= 225 mm)	76
Figure 4.4. Hot dip galvanized centralizer (after Ground Anchor System 2011)	76
Figure 4.5. Installation process of hollow core micropile (after Ground Anchor System 2011)	78
Figure 4.6. B7X1-76 Geo-drilled hollow core bars	80
Figure 4.7. TE 550 hydraulic drifter mounted on an excavator	81
Figure 4.8. All possible connections between the drafter hammer and the hollow bar (after Ground Anchor System 2011)	82
Figure 4.9. Final connections at the top of the drifter	83

Figure 4.10. Water delivered out of the drilling bit	85
Figure 4.11. The broken double cross bit	85
Figure 4.12. Type XAS 375 JD6 portable air compressor	87
Figure 4.13. Colloidal mixer grout plant	87
Figure 4.14. A group of four micropiles	88
Figure 4.15. EM-5 strain gauge parts and dimensions	90
Figure 5.1. Cross-section and dimensions of main loading beam (dimension are in mm)	93
Figure 5.2. Reaction frame used during monotonic and cyclic loading	94
Figure 5.3. Location of tested and position of reaction piles	95
Figure 5.4. Micropile head instrumentation during compression tests	97
Figure 5.5. Micropile head instrumentation during tension tests	98
Figure 5.6. Load-displacement curves for three monotonic compression tests	102
Figure 5.7. Load-displacement curves for two monotonic tension tests	102
Figure 5.8. Load and displacement versus time of the cyclic compression tests on MP1	109
Figure 5.9. Load and displacement versus time of the cyclic compression tests on MP2	109
Figure 5.10. Load and displacement versus time of the cyclic compression tests on MP3	110
Figure 5.11. Load and displacement versus time of the cyclic compression tests on MP4	110

Figure 5.12. Load and displacement versus time of the tension cyclic load test on MP4	111
Figure 5.13. Load – displacement curves for the compression cyclic test on MP1...	111
Figure 5.14. Load -displacement curves for the tension cyclic test on MP4	112
Figure 5.15. Accumulation of displacement for 15 cycles of loading and unloading	114
Figure 5.16. Pile head stiffness versus number of cycles for compression cyclic tests on MP1	116
Figure 5.17. Pile head stiffness versus number of cycles for compression cyclic tests on MP2	116
Figure 5.18. Pile head stiffness versus number of cycles for compression cyclic tests on MP3	117
Figure 5.19. Pile head stiffness versus number of cycles for compression cyclic tests on MP4	117
Figure 5.20. Pile head stiffness versus number of cycles for tension cyclic tests on MP4	118
Figure 5.21. Axisymmetric geometry model	122
Figure 5.22. CAX4 bilinear element with four integration points	122
Figure 5.23. The geometry of the axisymmetric model and the boundary conditions	123
Figure 5.24. Meshing techniques on two models: (a) coarse mesh; (b) fine mesh...	124
Figure 5.25. Tri-linear stress-strain relation used to model the grout material	125
Figure 5.26. Default pressure – overclosure relationship	128
Figure 5.27. Slip regions for the friction model with a limit on the critical shear stress	129

Figure 5.28. Elastic slip versus shear traction relationship for sticking and slipping friction	132
Figure 5.29. Step and total time for a simulation	134
Figure 5.30. The proposed micropile geometry	136
Figure 5.31. Flow chart of the methodology used to evaluate d_E and L_E	138
Figure 5.32. Calibration of MP1 in compression	139
Figure 5.33. Calibration of MP3 in compression	140
Figure 5.34. Calibration of MP2 in compression	140
Figure 5.35. Field test results and hyperbolic function of MP1 in compression	142
Figure 5.36. Extended field results and FE model for MP1 in compression	142
Figure 5.37. Calibration of MP2 in tension	143
Figure 5.38. Calibration of MP4 in tension	143
Figure 5.39. Effect of horizontal boundary in Mesh_1	145
Figure 5.40. Effect of number of elements on the micropile capacity, 10m model, $\alpha = 0.9$	146
Figure 5.41. Effect of number of elements on the micropile capacity, 12m model, $\alpha = 0.9$	147
Figure 5.42. Failure load MP1 compression	151
Figure 5.43. Failure Loads MP2 in compression	151
Figure 5.44. Failure load MP3 Compression	152
Figure 5.45. Load transfer for MP1 Compression	154

Figure 5.46. Load transfer for MP2 Compression	154
Figure 5.47. Load transfer for MP3 in compression	155
Figure 5.48. Shear stress along the micropile at failure loads	157
Figure 5.49. Example of failure load obtained at $s_u = 150\text{kPa}$, $\alpha = 1.0$, $L/d = 30$	161
Figure 5.50. Load distribution obtained from at $Q_F = 614\text{ kN}$, $s_u = 150\text{kPa}$, $\alpha = 1.0$, $L/d = 30$	161
Figure 5.51. The relation between percentage of the increase in the hole volume and the normalized shaft resistance under compression, $L/d=30$	174
Figure 5.52. The relation between percentage of the increase in the hole volume and the normalized shaft resistance under compression, $L/d=50$	174
Figure 5.53. The relation between percentage of the increase in the hole volume and the normalized shaft resistance under compression	175
Figure 5.54. The relation between percentage of the increase in the hole volume and the normalized shaft resistance under tension, $L/d=30$	175
Figure 5.55. The relation between percentage of the increase in the hole volume and the normalized shaft resistance under tension, $L/d=50$	176
Figure 5.56. The relation between percentage of the increase in the hole volume and the normalized shaft resistance under tension	176
Figure 5.57. Applying the temperature field and the degradation in soil shear modulus during calibration of cyclic field test	181
Figure 5.58. Load-displacement calibration of cyclic test on MP1	183
Figure 5.59. Load-displacement calibration of cyclic test on MP2	183
Figure 5.60. Load-displacement calibration of cyclic test on MP3	184
Figure 5.61. Load-displacement calibration of cyclic test on MP4	184

Figure 5.62. Variation of stiffness due to cyclic loading for MP1	185
Figure 5.63. Variation of stiffness due to cyclic loading for MP2	186
Figure 5.64. Variation of stiffness due to cyclic loading for MP3	186
Figure 5.65. Variation of stiffness due to cyclic loading for MP4	187
Figure 6.1. Plane view of loading plate, all dimensions are in mm	190
Figure 6.2. Details of the hollow bar micropile's head connection	190
Figure 6.3. Pile group assembly	192
Figure 6.4. Positioned the lower beam above the load instrumentations	192
Figure 6.5. Centering and leveling the upper beam over the lower one	193
Figure 6. 6. Final pile group setup	193
Figure 6.7. Arrangements of the instruments at the top of the steel pile raft	195
Figure 6.8. Center to center spacing of the tested micropiles	196
Figure 6.9. Load-displacement curves for PG1 and MP1	198
Figure 6.10. Load-displacement curves for PG2, MP2 and MP3	199
Figure 6.11. Load-displacement curves for PG3, MP1 and MP2	199
Figure 6.12. Load-displacement curves for PG4 and MP3	200
Figure 6.13. Load-displacement curve for all field pile group tests	200
Figure 6.14. Axes of symmetry in micropile group assembly	205
Figure 6.15. C3D8R element geometry	205

Figure 6.16. The 3D quarter shape model of the soil	206
Figure 6.17. The 3D circular shape of the soil	206
Figure 6.18. The geometric model of the micropile in the group analysis	207
Figure 6.19. Effect of model shape and vertical boundary on model behavior	207
Figure 6.20. Load – displacement of field test and its FE calibration: (a) PG1; (b) PG2; (c) PG3; and (d) PG4	210
Figure 6.21. Capacity of pile group at group efficiency equal to 1.0: (a) PG1; (b) PG2; (c) PG3; and (d) PG4	214
Figure 6.22. Load – group displacement for $s_u= 90$ kPa and $L/d =30$	218
Figure 6.23. Load – group displacement for $s_u= 175$ kPa and $L/d = 30$	218
Figure 6.24. Load – group displacement for $s_u= 100$ kPa and $L/d = 50$	219
Figure 6.25. Load – group displacement for $s_u= 175$ kPa and $L/d = 50$	219
Figure 6.26. Load – group displacement for $s_u= 50$ kPa and $L/d =30$	220
Figure 6.27. Geometric model adopted for interaction calculations	224
Figure 6.28. Interaction factors at the design load for $L/d=30$	225
Figure 6.29. Interaction factors at the design load for $L/d =50$	226
Figure 6.30. Interaction factors at the design load for $L/d=75$	226
Figure 6.31. Influence of L/d on the interaction factor between hollow bar micropiles, $E_p/E_s =1000$	227
Figure 6.32. Influence of L/d on the interaction factor between hollow bar micropiles, $E_p/E_s =1000$	227
Figure 6.33. Geometric model for three adjacent hollow bar micropiles	229

Figure 6.34. Effect of intermediate hollow bar micropile on the interaction factor, $S/d_{\text{hole}} = 7.5, L/d = 30$	229
Figure 6.35. Effect of intermediate hollow bar micropile on the interaction factor, $S/d_{\text{hole}} = 10, L/d = 30$	231
Figure 6.36. Effect of intermediate hollow bar micropile on the interaction factor, $S/d_{\text{hole}} = 15, L/d = 30$	231
Figure 6.37. Effect of intermediate hollow bar micropile on the interaction factor, $S/d_{\text{hole}} = 7.5, L/d = 50$	232
Figure 6.38. Effect of intermediate hollow bar micropile on the interaction factor, $S/d_{\text{hole}} = 10, L/d = 50$	232
Figure 6.39. Effect of intermediate hollow bar micropile on the interaction factor, $S/d_{\text{hole}} = 15, L/d = 50$	233
Figure 7.1. Lateral load test setup	236
Figure 7.2. Work shop drawing for the three main plates	237
Figure 7.3. Position of the applied load during the monotonic lateral tests	239
Figure 7.4. Position of the LDTs with respect to the point of applied load	239
Figure 7.5. Load-deflection for monotonic lateral tests	241
Figure 7.6. Head rotation versus the applied load	241
Figure 7.7. Model for pile under lateral loading with p - y curves	246
Figure 7.8. Distribution of normal stress against a pile (after Isenhower and Wang 2011) (a) Before lateral loading, (b) After lateral deflection	246
Figure 7.9. Round concrete shaft with permanent casing and core utilizing hollow bar micropile cross section	249
Figure 7.10. Bending stiffness versus bending moment for the adopted cross section	249
Figure 7.11. Characteristic shape of p - y curve for static loading in stiff clay without free water (after Isenhower and Wang 2011)	251

Figure 7.12. Numerical calibration of lateral field test with LPile	253
Figure 7.13. Deflection of the micropile versus depth, LPile analysis	254
Figure 7.14. Bending moment along the micropile shaft, LPile analysis	254
Figure 7.15. Distribution of shear force developed along the micropile shaft, LPile analysis	255
Figure 7.16. p - y curves generated by LPile analysis	255
Figure 7.17. Bending stiffness versus bending moment of the micropile cross-section	256
Figure 7.18. The geometry of the hollow bar micropiles used in the parametric study	258
Figure 7.19. The effect of casing length on ultimate resistance of free head pile....	259
Figure 7.20. The effect of casing length on maximum moment of free head pile....	260
Figure 7.21. The effect of casing length on ultimate resistance of fixed head pile...	260
Figure 7.22. The effect of casing length on maximum moment of fixed head pile...	261
Figure 7.23. Load-deflection for three degree of fixity, $L_c/d_c = 5$, $d_c = 200\text{mm}$, $s_u = 100\text{ kPa}$	262
Figure 7.24. Load-maximum moment for three degree of fixity, $L_c/d_c = 5$, $d_c = 200\text{mm}$, $s_u = 100\text{ kPa}$	262
Figure 7.25. Load-deflection for three degree of fixity, $L_c/d_c = 7.5$, $d_c = 200\text{mm}$, $s_u = 175$	263
Figure 7.26. Load-maximum moment for three degree of fixity, $L_c/d_c = 7.5$, $d_c = 200\text{mm}$, $s_u = 175\text{ kPa}$	263
Figure 7.27. Load-deflection for three degree of fixity, $L_c/d_c = 5$, $d_c = 225\text{mm}$, $s_u = 175\text{ kPa}$	264
Figure 7.28. Load-maximum moment for three degree of fixity, $L_c/d_c = 5$, $d_c = 225\text{mm}$, $s_u = 175\text{ kPa}$	264

Figure 7.29. Load-deflection for three degree of fixity, $L_c/d_c = 7.5$, $d_c = 225\text{mm}$, $s_u = 100\text{ kPa}$	265
Figure 7.30. Load-maximum moment for three degree of fixity, $L_c/d_c = 7.5$, $d_c = 225\text{mm}$, $s_u = 100\text{ kPa}$	265
Figure 7.31. The sequence and position of the field lateral cyclic tests	267
Figure 7.32. Load-deflection curve for MP3 during cyclic test on MP3 and MP4...	268
Figure 7.33. Load-deflection curve for MP4 during cyclic test on MP3 and MP4...	269
Figure 7.34. Load-deflection curve for MP2 during cyclic test on MP2 and MP3...	269
Figure 7.35. Load-deflection curve for MP3 during cyclic test on MP2 and MP3...	270
Figure 7.36. Load-deflection curve for MP1 during cyclic test on MP1 and MP4...	270
Figure 7.37. Load-deflection curve for MP4 during cyclic test on MP1 and MP4...	271
Figure 7.38. Load – deflection for all the tested micropiles at 3kN; (a) 1st cycle of loading, (b) 5th cycle of loading	273
Figure 7.39. Load – deflection for all the tested micropiles at 9kN; (a) 1st cycle of loading, (b) 5th cycle of loading	274
Figure 7.40. Load – deflection for all the tested micropiles at 15kN; (a) 1st cycle of loading, (b) 5th cycle of loading	275
Figure 7.41. Load – deflection for all the tested micropiles at 18kN; (a) 1st cycle of loading, (b) 5th cycle of loading	276
Figure 7.42. Normalized head stiffness versus number of cycles at all load magnitudes tested, (a) at load = 3kN; (b) at load = 6kN; (c) at load = 9kN, (d) at load = 12kN; (e) at load = 15kN; (f) = at load = 18kN; (g) at load = 21 kN	279
Figure 7.43. Degradation parameter at different stress levels	280

List of Symbols

a	curve fitting parameter
A_i	cross section of the pile at elevation i
A_g	area of the grout in micropile section
A_s	steel area in the micropile section (bar + casing)
A_{hole}	area of the hole
A_{inc}	increasing in the hole area
b	curve fitting parameters
\bar{b}	the width of the block containing piles and soil
BBC	back bone curve
BH	borehole
c	cohesion of the material
C_B	borehole diameter correction factor
C_E	energy correction factor
C_N	overburden correction factor
C_R	rod length correction factor
C_S	sampler type correction factor
d	micropile diameter utilizing the bit diameter
d_c	casing diameter
d_E	enlarged diameter of micropile
d_{bit}	diameter of the drilling bit
d_{hole}	average diameter of the micropiles hole

D_b	diameter of the drill hole
D_r	relative density of the soil
DL	anticipated design load
e	void ratio
E	Young's modulus of the material
E_c	elastic modulus of concrete (or grout)
E_p	modulus of elasticity of the micropile material
E_u	undrained modulus of elasticity of the soil
E_s	modulus of elasticity of the soil
E_{di}	tangential drained modulus
E_{ui}	undrained tangent modulus
E_{us}	undrained secant modulus
EA	combined elastic axial stiffness of the micropile section in compression
EI	bending stiffness of the micropile cross-section
ER	the elastic ratio
f_l	Enlargement factor
f'_c	compressive strength of the grout (typically after 28-days)
f'_t	tensile strength of the grout
f_y	yield stress of steel
F_f	slip tolerance
FE	finite element
FOS	factor of safety
G	the shear modulus of the soil

G_s	specific gravity
G_{s1}	secant shear modulus at cycle 1
G_{sN}	secant shear modulus at cycle N
I_c	concrete moment of inertia
I_L	liquidity index
I_p	plasticity index
k_o	coefficient of earth pressure at rest
k_p	passive coefficient of lateral earth pressure of the soil, or, the limiting in-situ coefficient of earth pressure.
k_s	coefficient of earth pressure at pile periphery
K	pile head stiffness
K_1	stiffness of single the hollow bar micropile at the 1 st cycle
K_g	vertical stiffness of the hollow bar micropiles group
K_L	lateral pile head stiffness
K_N	stiffness of single the hollow bar micropile at the N th cycle;
K_r	flexibility factor
K_{sp}	vertical stiffness of single pile
l_i	characteristic contact surface length
L	embedded length of the pile
L_b	bond length
L_c	cased length
L_e	elastic length of the pile
L_E	length of enlarged segment of the micropile
L/d	slenderness ratio

$(M_u)_c$	maximum bending moment for the cased micropile
$(M_u)_{unc}$	maximum bending moment for the uncased micropile
$M_{allowable}$	allowable bending moment in the micropile
M_{max}	maximum bending moment in the micropile
n	the number of pile within the group
N	number of cycles
$N_{(60)}$	corrected Standard Penetration Field number for equipments
$(N_1)_{60}$	corrected Standard Penetration Field number for equipments and effective
N_c	bearing capacity factor
N_{field}	Standard Penetration Field number
p	contact pressure at the interface
Δp	change in the contact pressure due to the applied load
p	load per unit length of the pile
p_u	ultimate resistance of the soil at a depth x
$(p_u)_c$	the ultimate resistance of micropile with case length
$(p_u)_{unc}$	the ultimate resistance of micropile without casing length
p_{max}	maximum applied lateral loads during each load cycle
p_{min}	minimum applied lateral loads during each load cycle
P	applied load at the pile head
ΔP	magnitude of the unloading load
P_c	maximum axial compression load
P_G	geotechnical capacity of the single pile
P_{max}	maximum applied loads during each load cycle

P_{\min}	minimum applied loads during each load cycle
P_{ij}	load transfer at elevation i due to load applied j ;
$P_{c\text{-allowable}}$	allowable compression structural capacity of the micropile
$P_{t\text{-allowable}}$	allowable uplift structural capacity of the micropile
Q_F	failure load according to Butler and Hoy 1977
Q_g	group capacity
Q_s	shaft resistance employing the drilling bit diameter
Q_{bearing}	load transfer through end bearing
Q_{shaft}	shaft resistance obtained from the enlargement geometry employed
OCR	overconsolidation ratio
u_r	degree of freedom in the radial direction
u_x	degree of freedom in the X-direction
u_y	degree of freedom in the Y-direction
u_z	degree of freedom in the Z-direction
r	cylindrical polar coordinate
s	maximum shear stress = $\frac{1}{2} (\sigma_1 - \sigma_3)$
s_u	undrained shear strength parameter of soil
s_{ub}	undrained shear strength parameter of soil presents at the pile tip
S	spacing between the micropiles
S_a	degree of saturation
S_g	estimated settlement of the group;
S_{sp}	settlement of a single pile
S/d	spacing to diameter ratio

t	degradation parameter.
T	temperature field
V_{bit}	volume of the hole utilizing the bit diameter
V_{inc}	percentage of increase in the hole volume
V_{hole}	volume of the grout required to fill the hole after installation
w_c	natural moisture content
W_{PL}	plasticity limit
W_{LL}	liquid limit
X	global Cartesian directions
y	lateral deflection of the micropile
y_{50}	deflection corresponding to ε_{50}
y_{max}	pile head deflections corresponding to p_{max} during each load cycle
y_{min}	pile head deflections corresponding to p_{min} during each load cycle
Y	global Cartesian directions
Z	global Cartesian directions
z	cylindrical polar coordinate
α	adhesion factor
α_{ri}	the interaction factor between the reference pile, r , and the i^{th} pile in the group
α_{bond}	grout to ground ultimate bond strength
δ	friction angle between the soil and micropile surfaces
δ_e	elastic rebound measured or estimated during unloading cycle
δ_g	corresponding group displacement
δ_N	amount of degradation at the N^{th} cycle

δ_r	residual displacement
δ_t	total displacement
δ_{\max}	maximum pile head displacement during each load cycle
δ_{\min}	minimum pile head displacement during each load cycle
Δ	head displacement
η	the group efficiency factor.
ε_{50}	axial strain corresponding to a shear stress equal to one-half of the shear strength of the material
ψ	dilation angle
γ_i	elastic slip
γ'_{avg}	average unit weight of the soil surrounding the micropile
γ_{dry}	dry unit weight of the soil
γ_{sat}	saturated unit weight
γ_w	unit weight of water
κ	the stiffness of the interface
\bar{K}	the ratio between the micropile modulus and the surrounding soil modulus
ν	Poisson's ratio
μ	coefficient of friction
ϕ	friction angle of the material
ϕ'	effective friction angle
σ	normal stress
σ_1	maximum principal stress and
σ_3	minimum principal stress.
σ'_h	in-situ horizontal stress

σ_m	average of the maximum and minimum principal stresses
σ_p'	preconsolidation pressure
σ_v'	in-situ effective vertical pressure
$(\sigma_z)_{ij}$	axial stress at elevation i due to load amplitude j
τ_{in}	developed shear stress due to micropile-soil interaction
τ_{max}	maximum shear stress at the interface
θ	cylindrical polar coordinate

List of Appendices

APPENDIX A : COPYRIGHT PERMISSIONS

CHAPTER 1

INTRODUCTION

1.1 Overview

A micropile is a small-diameter (typically less than 300 mm) specially drilled and grouted pile. Micropiles are constructed by drilling a borehole, placing a steel reinforcing element into the borehole and grouting the borehole. They are typically reinforced by solid central bar that occupies about one-third of the hole volume. The grout is placed by gravity, under pressure methods or by a combination of both (post grouting). Thus, micropiles can be considered as small drilled-shafts.

Micropiles are advantageous because they can be installed in most soil types and rocks. In addition, they can be installed in karstic limestone, glacial till with boulders, urban fills and soils with high water level causing minimum disturbance to adjacent structures, soil, and the environment. Due to the small size of installation equipment, micropiles can be installed in very limited head room with access-restrictive environments. These advantages combined make the micropiles, in some situations, not only the optimum deep foundation solution, but the only feasible one.

Structurally, most of the applied load on conventional cast-in-place piles is resisted by the reinforced concrete; enhanced structural capacity is achieved by increased cross-sectional and surface area. However, micropiles rely on high capacity steel elements to resist most or the entire applied load with the surrounding grout serving mainly to transfer, through friction and/or adhesion, the applied loads from the steel to the surrounding soils.

The special drilling and grouting methods used in micropile installation allow for high grout/ground bond values along the grout-ground interface. The grout transfers the load through friction from the reinforcement to the ground in the micropile bond zone in a manner similar to that of ground anchors. The grout-ground bond strength achieved is influenced primarily by the ground type and grouting method used. Due to the small pile diameter, any end-bearing contribution in micropiles is generally neglected (FHWA NHI, 2005). Micropiles can therefore resist significant axial loads, as well as moderate lateral loads, either as individual elements or serving as one component in a composite reinforced soil/pile mass, depending on the design concept selected.

1.2 Historical Background

Historically, micropiles have been introduced as an innovative foundation system mainly to be used for retrofits and underpinning of structures that had sustained damage during World War II. The first generation of micropiles were conceived in Italy by Dr. Fernando Lizzi in the 1950's in response to the requirement for the underpinning of historic buildings where access for conventional piling equipment was not possible. This generation of micropiles was called the "*palo radice*" or "root pile". The *palo radice* is a small-diameter, drilled, cast-in-place, lightly reinforced, grouted pile that can carry load less than 100 kN.

The second generation of micropiles was developed in the 1970's, which were installed by using either an open or cased hole drilling method. This generation was known with various names including: mini piles, pin piles, needle piles and in North America by "GEWI-Pile". These micropiles were typically a pressure grouted pile of small diameter

with a central mono all thread bar, which is encapsulated in a cement grout body. This generation of micropiles is capable of carrying load in excess of 1500 kN, if embedded in soils, and 3000 kN if embedded in rocks. In 1993, the Federal Highway Administration (FHWA) and the International Society of Micropiles (ISM) internationally standardized the name of the new piles to “micropiles”.

A new generation of micropiles was devised by Ernst Ischebeck in 1983; and named The Titan Injection Bore (IBO) micropile. A continuously all threaded hollow steel bar is used as the drill steel, allowing drilling and grouting to proceed simultaneously without the need for a casing. A sacrificial bit that contains openings that allow for pressure grouting of the surrounding soil is threaded onto the end of the hollow bar, and is left in place following drilling. The drilling fluid (air, water, or grout) is introduced through the hollow bar and allows the spoils to flush from the borehole. This also improves the density and support capability of the surrounding soil. Figure 1.1 depicts the hollow bar micropile system components.

The system had historically been known as “self-drilling anchoring” because the hollow fully-threaded bar serves as both the drill string and the grouted anchor, thus installation is performed in a single operation (William Form–Ground Anchor system 2010). In addition to IBO and self-drilled anchoring, several names were used to describe the new micropile such as injection bars and hollow core bar micropiles. In this study, a generic name is employed to identify this kind of micropile: hollow bar micropiles.

The use of hollow bars for micropile construction has greatly increased over the past 10 years. Hollow bar construction became a technique preferred by many contractors in the

piling industry because it allows drilling, installation and grouting of the pile simultaneously. It eliminates the need to remove the drill string after completion and the casing for collapsible ground conditions. As a result, it increases production rates typically by 2 to 3 times, which decreases the overall cost of the project. The dynamic installation employed in hollow bar micropiles produces a rough borehole with an increased geotechnical connection to the soil and thus enhances the geotechnical grout/ground bond developed along the micropile shaft.

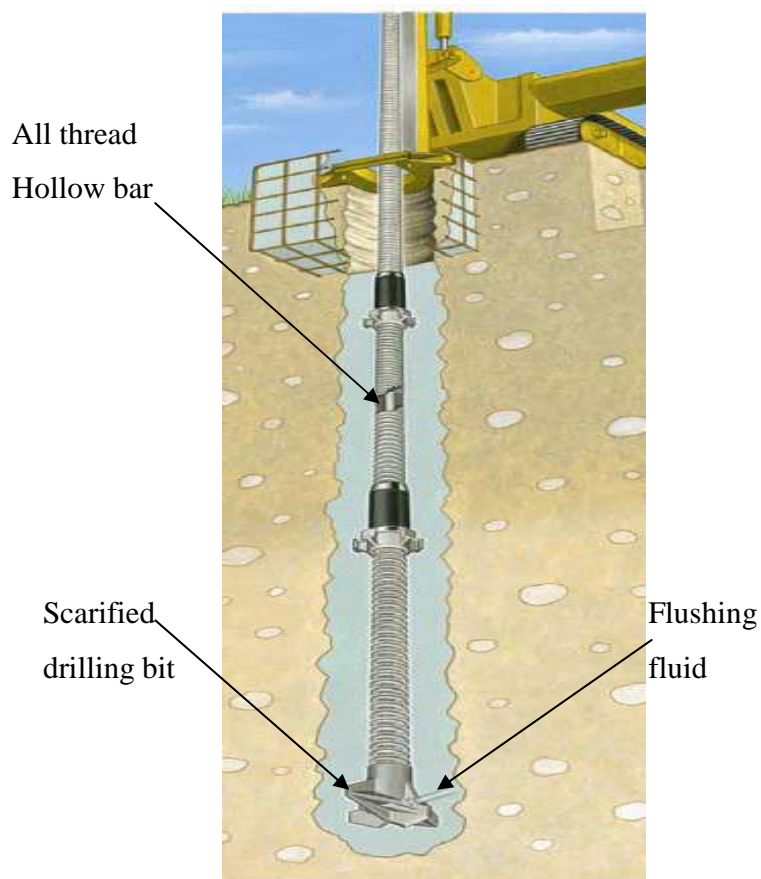


Figure 1. 1. Hollow bar micropiles system components (after micropiles brochures- Con-Tec system Ltd. 2011)

1.3 Research Objectives

This research is focused on investigating the behaviour of hollow bar micropiles in cohesive soils. The main objectives of this thesis are:

1. To investigate the monotonic and cyclic axial performance of hollow bar micropiles through full-scale field load tests.
2. To develop finite element models to simulate the performance of micropiles under different loading conditions. The numerical models are calibrated with the field tests results, then employed in order to establish guidelines for hollow bar micropiles considering their installation technique.
3. To assess the degradation of hollow bar micropile stiffness due to axial cyclic loading through field test results and the calibrated finite element model.
4. To evaluate the group action of pairs of hollow bar micropiles under axial loading, and to recommend an efficiency group factor that can be used to calculate the hollow bar micropile group capacity.
5. To develop a set of interaction factor graphs that can be employed to estimate the settlement of a group of hollow bar micropiles.
6. To examine the behavior of hollow bar micropiles under monotonic and cyclic lateral loading, and propose guidelines for their lateral response analysis employing appropriate numerical model.

1.4 Research Methodology

The goals of this research will be fulfilled through two primary elements: performing a series of physical field load tests on hollow core micropiles; and developing two-dimensional, 2D, and three-dimensional, 3D, finite element models. The field load tests involve the construction of full-scale hollow core micropiles and load testing them under different loading conditions. The load testing program encompasses four different and consecutive phases. The first phase includes axial monotonic load tests on single micropiles. The second phase involves a series of axial cyclic tests on single micropiles. The third phase employs axial monotonic tests on pairs of hollow bar micropile, while the last phase encompasses lateral monotonic and cyclic load tests on single micropiles.

The results from the field tests will be used to calibrate and verify non-linear finite element models for the soil-micropiles system properties and geometry. Upon calibrating the numerical models, they will be employed to carry out a parametric study. In the parametric study, the performance of the micropile-soil system will be evaluated considering different conditions that have not been investigated within the scope of the physical load testing program. The results obtained from the field tests and the finite element analyses will be analyzed in order to establish design guidelines for the hollow bar micropiles under different loadings and configurations.

1.5 Organization of the Dissertation

This thesis is comprised of eight chapters. The first chapter (Chapter 1) provides an historical background to the micropiles under investigation and introduces the research objectives and methodology of this work.

Chapter two presents a review of the-state-of-practice, including the classification system and design consideration for different types of micropile, followed by brief description of previous studies that were conducted to investigate the design methods and analysis considerations of micropiles.

Chapter three describes the soil investigation program for the test site. The soil field and laboratory tests conducted to determine the required soil profile and properties are also presented in this chapter. In addition, the material properties of the grout used for micropiles construction are provided.

Chapter four presents the different hollow bar system parts, materials, and installation techniques, with an emphasis on the installation technique and accessories employed.

Chapter five: documents the axial monotonic and cyclic loading tests procedures and results of the first and second phases of load testing program. In addition, a detailed description of the 2D finite element model established utilizing the ABAQUS finite element analysis software to simulate the field tests. Furthermore, a summary of the parametric study is provided including some guidelines that can be used to calculate the capacity of hollow bar micropile under axial loading. Finally, a method is proposed to evaluate the degradation of the axial pile stiffness under cyclic loading.

Chapter six: presents the details of the axial monotonic loading setup, procedures and results conducted on pairs of micropiles. A full description of the 3D geometric finite element model developed to simulate the field tests is also provided. In addition, the results of the numerical investigation of micropile group capacity are summarized and a group efficiency factor is proposed to account for group effects. Moreover, a set of interaction factors graphs is elaborated to estimate the settlement of hollow bar micropile when used in groups.

Chapter seven: reports on the lateral monotonic and cyclic loading tests procedures and results conducted on the hollow bar micropiles. The components of the load test setup designed to apply lateral load to a pair of micropiles simultaneously are explained. The numerical analysis adopted to simulate the monotonic lateral tests utilizing the p - y curves approach employing the LPile software is also presented. A parametric study on the monotonic behavior of hollow bar micropiles under lateral loading is given. In addition, some recommendations for lateral performance of micropiles are provided.

Chapter eight: includes the summary and conclusions together with recommendations for future research.

CHAPTER 2

LITERATURE REVIEW

2.1 Introduction

Micropiles are gaining popularity as an efficient deep foundation system. Over the last 30 years, a considerable number of field and laboratory load tests were performed by either contractors or researchers on different types of micropiles in attempts to provide a more rigorous way to estimate the capacity of micropiles. Not surprisingly, the current design practice for micropiles is based either on the methods developed for large diameter drilled shafts and ground anchors (e.g. codes and specifications available in North America), or simplistic interpretation of micropile load tests. Design methods developed for large diameter piles may not be suitable for micropiles due to the unique load transfer mechanism in micropiles, which relies on the high grout/ground bond between the pile and the surrounding soil arising from the installation method adopted.

The following sections in this chapter provide a brief description of the worldwide micropile classification system and the design consideration for micropiles. This will be followed by a review of the published research addressing the previous and current practices in micropiles industry. The purpose of such a review is to evaluate the adequacy of previous work and to establish the scope of the current research. Special attention is particularly focused on hollow bar micropiles.

2.2 Micropiles Classification

Micropiles have been adopted worldwide for a variety of applications. Most recent applications involve using micropiles for underpinning of existing foundations that support structures subjected to additional axial and/or lateral loads. In addition, micropiles have been used in seismic retrofitting applications, especially in west North America. Nowadays, micropiles are increasingly used as foundation for new construction in urban areas, abutments and piers foundations, wind turbines, and transmission and communication towers. In parallel, micropiles are used worldwide for slope stabilization and heave prevention applications. The variety of applications necessitates using different types of micropiles, some of them may be similar in shape and reinforcement, but differ significantly in terms of performance.

Not until 1997, the FHWA published a 4-volume report summarizing the state-of-the-practice for micropiles including a comprehensive micropiles classification system. This system is based on two criteria: (1) Philosophy of behaviour (design); and (2) Method of grouting (construction). As defined by the FHWA (1997, 2000, and 2005), the philosophy of behaviour indicates the method employed in designing the micropile, whilst the method of grouting defines the grout/ground bond strength, and thus, the micropile capacity. The classification system introduced by the FHWA consists of a two-part designation: a number, which denotes the micropile behaviour (design), and a letter, which designates the method of grouting (construction).

2.2.1 Design classification of micropiles

In accordance with the FHWA NHI (2005), micropiles are classified based on the philosophy of behaviour into two different case types:

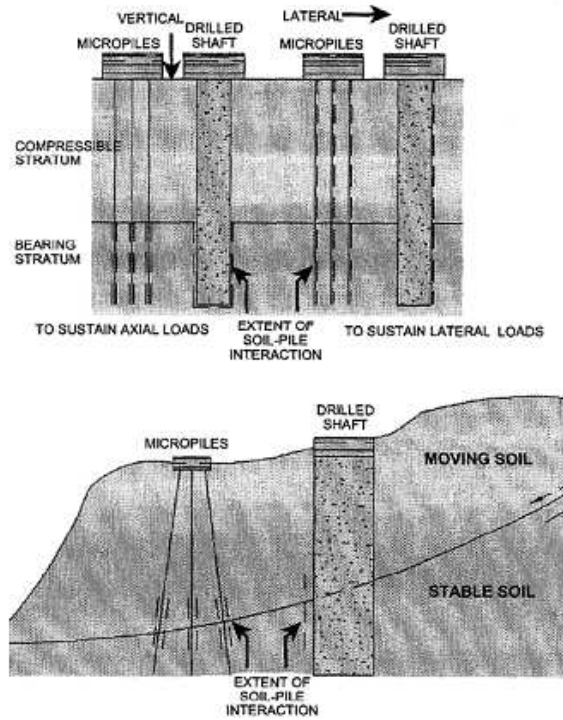
Case 1 micropiles: These are directly loaded micropiles. Structurally, the load is resisted by the steel reinforcement and geotechnically by the grout/ground bond strength of the individual piles. Case 1 micropiles can be used as singles or in groups.

Case 2 micropiles: is used in a reticulated arrangement such that they serve as reinforcing elements to the soil to create a composite reinforced soil mass system.

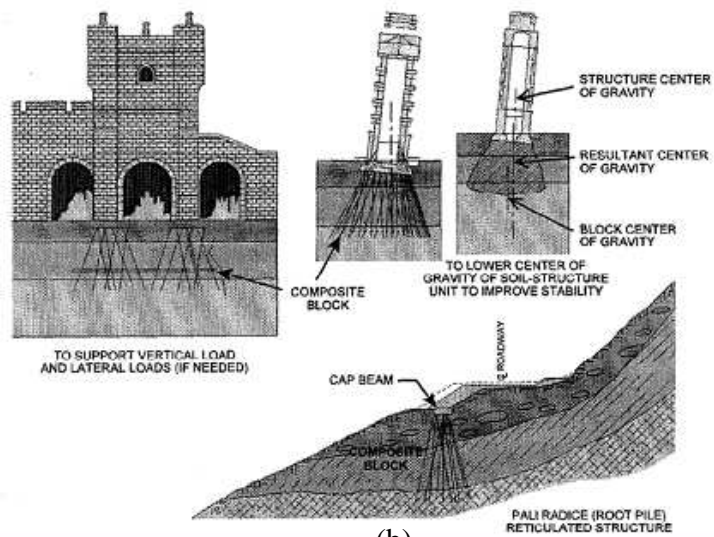
These two design concepts are illustrated in Fig.2.1. Micropiles used for structural support are usually loaded directly and, therefore, categorized as Case 1 design philosophy.

2.2.2 Construction classification of micropiles

Micropiles are an installation dependent piles; the method used during construction and grouting of the micropiles will affect its performance dramatically upon loading. Hence, the second part of the micropile classification developed by the FHWA consists of a letter (A through D) based primarily on the method of grouting utilized during construction. This is because the grout-to-ground bond capacity varies according to the grouting method employed. There are four principal methods of grouting employed in micropile construction as depicted in Fig. 2.2. According to the classification set forth by FHWA NHI (2005), each grouting type can be further defined as:



(a)



(b)

Figure 2. 1. Micropile classification system based on philosophy of behaviour (after FHWA 2000) (a) Case 1 (b) Case 2

- Type A (gravity grouted micropiles): The grout is placed in the pile under gravity only.
- Type B (low pressure grouted micropiles): Grouting pressures are typically in the range of 0.5 to 1 MPa, with neat cement grout injected into the drill hole under pressure as the temporary steel casing is withdrawn.
- Type C (high pressure grouted micropiles): The neat cement grout is first placed in the hole under gravity head as for Type A, but before hardening of the primary grout, similar grout is injected once with a preplaced sleeved grout pipe at a pressure of at least 1 MPa.
- Type D (post-grouted micropiles): This involves a two-step process similar to Type C. The neat cement grout is first placed under gravity in the hole as for Type A or C. When this primary grout has hardened, similar grout is injected via a preplaced sleeved port grout pipe. The use of a packer inside allows that specific horizons can be treated several times if necessary at pressures between 2 and 8 MPa.

Additional sub classification numbers (e.g., A1, A2, and A3) sometimes are used to indicate the type of drill casing and reinforcement used. These sub-classifications also represent the type of reinforcement required by design (e.g. reinforcing bar, casing, none). Hence, according to the FHWA, the final combined classification system of micropile is based on design application (i.e., Case 1 or Case 2), micropile type (i.e., Type A, B, C, or D) and reinforcement used (i.e., 1, 2, or 3).

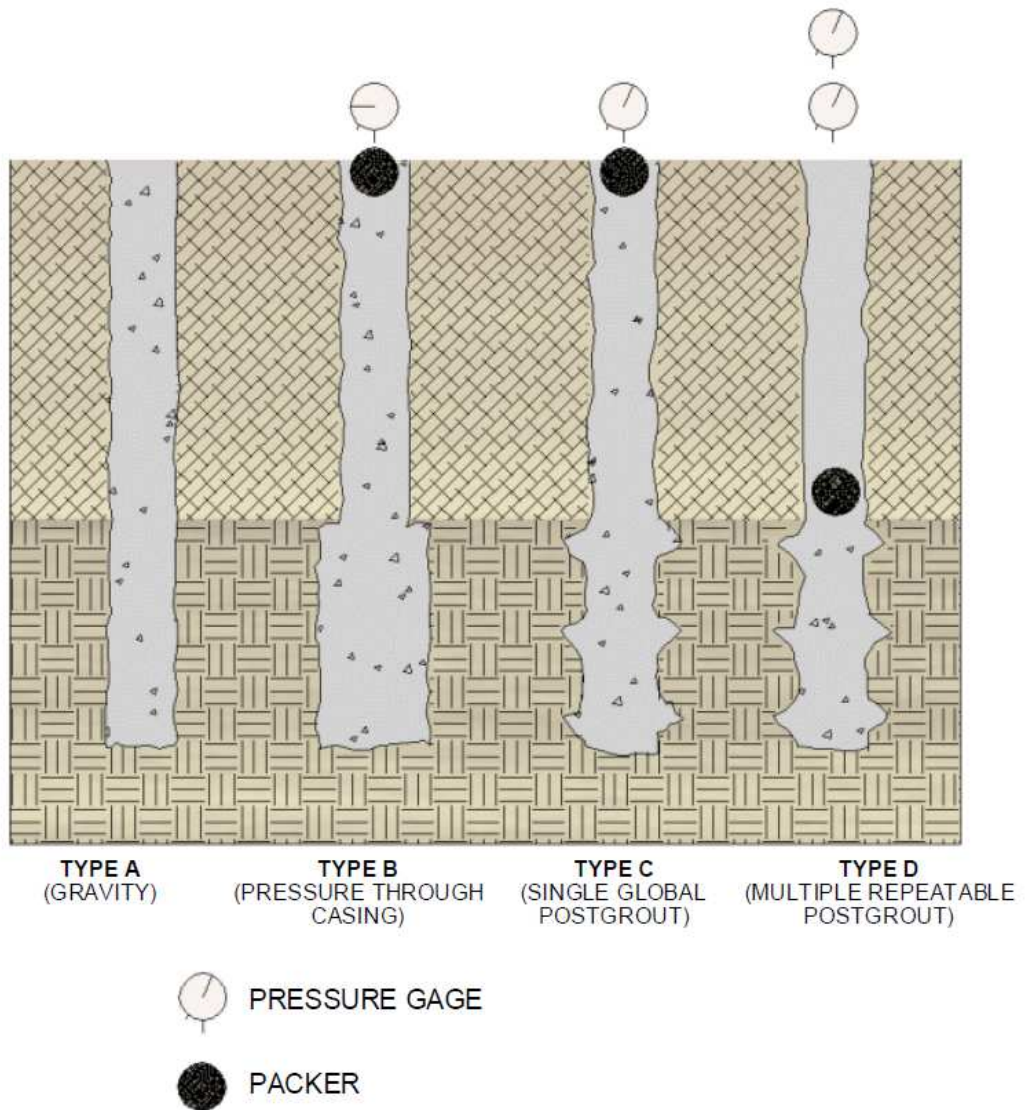


Figure 2. 2. Micropile classification system based on method of grouting (after FHWA 2000)

2.2.3 Classification of hollow-bar micropiles

In this type of micropile, the solid central mono bar, usually used as reinforcement, is replaced by a hollow core one. By threading onto the bar a sacrificial bit that contains openings, the hollow steel bar is employed as the drilling rod during installation, then as a conduit for delivering the flushing fluid (air, water, or grout) under pressure through the lost bit holes allowing the spoils to flush from the borehole. Upon reaching the desired depth, the grout is pressurized through the hollow bar to fill the annulus between the bar and the hole. Typically, a pressure between 0.5 and 2 MPa is used during flushing, and between 2 to 6 MPa during grouting. Figure 2.3 illustrates a final produced hollow bar micropile in the ground.

Hollow bar micropiles represent a unique grouting type due to the dynamic process of simultaneously installing and grouting the pile used during construction. However, most of the data published in the literature categorized the hollow bar micropiles as Type B, only because it is pressure grouted. The difference between Type B micropiles and hollow bar micropiles, however, lies in the definition of the FHWA for Type B micropiles as: “pressure grouted micropile as the temporary steel casing is withdrawn”. A hollow bar micropile does not need a temporary steel casing to be installed and is grouted much higher pressure (not less than 2 MPa) compared to Type B micropiles. The aforementioned differences between hollow bar and Type B micropiles call for categorizing the hollow bar micropile as a new type of micropiles construction, the author proposes Type E. However, as will be elaborated later, this classification is still missing a comprehensive set of data characterizing their performance in different types of ground and under different types of load.

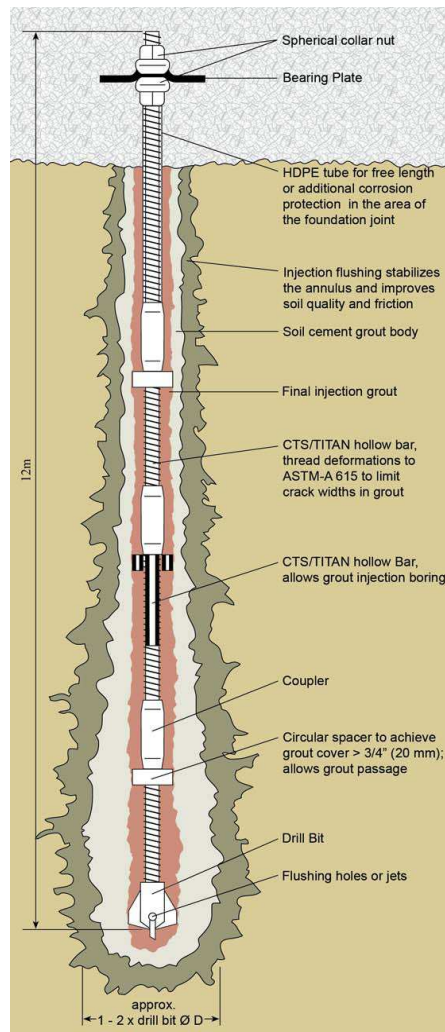


Figure 2. 3. Final hollow core micropile (after Con-Tec system Ltd. 2011)

2.3 Design Consideration of Micropiles

Conventional drilled shafts are characterized by large cross-sectional area resulting in huge structural capacity and stiffness. Thus, the design of those piles is governed by the geotechnical capacity contributions from its shaft and base resistances. Unlike conventional drilled shafts, micropiles have a small cross-sectional area, and hence low base resistance. On the other hand, micropiles exhibit high grout/ground bond strength

that will typically result in high geotechnical load capacity through shaft resistance. However, micropiles must be designed to support the anticipated loading conditions at tolerable stress levels with resulting movements being within allowable limits. Hence, micropiles should be designed for both structural and geotechnical load capacities.

2.3.1 Structural design of micropiles

No doubt, the structural capacity will govern the load capacity of micropiles founded in rock. Micropiles structural design can be performed considering either the load and resistance factor design (LRFD) or the service load design (SLD) approaches. In either approach, the factors utilized are governed by the local building codes. For example, in accordance with the FHWA NHI (2005), the allowable structural capacity of the micropiles is calculated from:

$$P_{c\text{-allowable}} = 0.4 f'_c A_g + 0.47 f_y A_s \quad (2.1)$$

Under compression, and:

$$P_{t\text{-allowable}} = 0.55 f_y A_s \quad (2.2)$$

Under tension loads

Where: $P_{c\text{-allowable}}$ is the allowable compression capacity of the micropile, $P_{t\text{-allowable}}$ is the allowable uplift capacity of the micropile, f'_c is the compressive strength of the grout (typically after 28-days), f_y is the yield stress of steel, A_g is the area of the grout in micropile section, and A_s is the steel area in the micropile section (bar + casing).

The load factor of the steel and the grout in the aforementioned equations are also suggested by the AASHTO (2002) if the SLD method is utilized in design. However, NYSDOT standard specifications (2008) recommend using a factor of 0.5 for steel and 0.33 for grout in calculating the allowable compression capacity.

Strain compatibility under compression loads should be considered for the steel components and grout by limiting allowable compressive stresses to the minimum allowable for any individual component (i.e., steel casing, steel reinforcement, or grout). Therefore, the maximum yield stress of steel to be used in Eq. 2.1 is the minimum of: (1) yield stress of steel reinforcing elements, and (2) maximum stress based on considerations of grout failure. Since, the maximum usable strain at the extreme concrete compression fiber is equal to 0.003; therefore, if the grout is limited to a compression strain of 0.003, the steel components must also be limited to this value. The stress in the steel at this strain level is equal to the Young's modulus of steel, E_{steel} , multiplied by strain (i.e., 0.003). For a typical Young's modulus for steel of 200,000 MPa, the allowable steel yield stress is then $200,000 \text{ MPa} \times 0.003 = 600 \text{ MPa}$. Therefore, the maximum stress based on considerations of grout failure is 600 MPa. This value must be compared by the yield stress suggested by the manufacturer of the micropile steel elements in use.

Other considerations must be evaluated to complete the structural design, including: the effect of coupled sections on compression capacity of micropiles; the possibility of buckling of the cased length of micropile, if present. In addition, allowance for corrosion is an essential aspect in the design of micropiles structurally, but only in aggressive grounds. The corrosion protection for reinforcing steel can be provided by numerous

methods such as grout protection, epoxy coating, or galvanized coating. Corrosion protection for outer steel casing subject to compressive loads in aggressive environments is considered by including a sacrificial steel thickness in the design. However, casing should not be used to carry tension loads in aggressive ground environments (FHWA NHI 2005)

For micropiles subjected to significant lateral load or overturning moment, it is important to account for the combined axial compression and bending of the upper portion in their design. Richards and Rothbauer (2004) proposed a combined stress check that can account for the contribution of the grout inside the casing to the compression capacity. This method assumes that buckling potential is negligible. The Richards and Rothbauer combined stress check is given by:

$$\frac{P_c}{P_{c - \text{allowable}}} + \frac{M_{\text{max}}}{M_{\text{allowable}}} \leq 1.0 \quad (2.3)$$

Where: $P_{c\text{-allowable}}$ is determined from Eq. 2.1, P_c is the maximum axial compression load, M_{max} is the maximum bending moment in the micropile, and $M_{\text{allowable}} = 0.55 f_y \times 2I_{\text{casing}}/\text{OD}$.

2.3.2 Geotechnical design capacity of micropiles

For micropiles with cased segments, the geotechnical capacity of the micropile is evaluated based on the uncased length only. This length is referred to as the bond zone or bond length. The ultimate geotechnical capacity, P_G , is calculated from:

$$P_G = \alpha_{\text{bond}} \pi D_b L_b \quad (2.4)$$

Where: α_{bond} is the grout to ground ultimate bond strength; D_b is the diameter of the drill hole; and L_b is the bond length. The allowable geotechnical capacity, $P_{G-allowable}$ is obtained by dividing the ultimate geotechnical capacity by a prescribed factor of safety, FOS. If the objective for the geotechnical design is to evaluate the length of this bond zone required to resist the applied tension and compression loads with a prescribed factor of safety, FOS, Eq. 2.4 takes the following form:

$$L_b = \frac{P_c - \text{allowable} \text{ FOS}}{\alpha_{\text{bond}} \pi D_b} \quad (2.5)$$

Table 2.1 provides the grout to ground ultimate bond strength suggested by the FHWA NHI (2005). The table includes ranges for the four methods of grouting (Types A, B, C, and D) installed in different ground conditions. However, these values vary with ground conditions and installation techniques and higher bond values may be used but only upon proper evaluation, documentation and load test data. Due to its small diameter, any contribution of the micropiles end bearing resistance to the geotechnical capacity is neglected unless the micropiles is installed in sound rock (FHWA NHI 2005).

2.3.3 Design consideration of hollow bar micropiles

The structural design of hollow bar micropiles is no different than other types of micropiles. From a geotechnical prospective, FHWA NHI (2005) considers the hollow core micropiles as Type B pressure grouted micropiles. The general practice for estimating their geotechnical capacity is to use bond strength values that are given in Table 2.1 for type B micropiles, depending on the experience of the design engineer. In

addition, the value of the diameter, D_b , in Eq. 2.4 is taken as the drilling bit diameter multiplied by an enlargement factor. MacLean (2010) showed that this enlargement factor was between 1.2 and 1.4 for hollow bar micropiles embedded in cohesive soils and between 1.3 and 1.5 for hollow bar micropiles embedded in cohesionless soils.

As an alternative of the bond strength provided by the FHWA, MacLean (2010) recommended using the minimum or the average bond strength values given by the Post-Tension Institution, PTI (2004) for permanent pressured grout anchored in either soil or rock. As will be shown in the following section, the former bond strength values are more accepted worldwide than the latter values for hollow bar micropiles. The bond strength values should be confirmed by at least one verification test, and proof tests on 5% of the produced hollow bar micropiles. However, until now, there is no comprehensive set of data specified for hollow bar micropiles bond strength.

2.4 Review of Previous Studies

A relatively wide range of field and laboratory investigations had been performed attempting to evaluate the actual performance of micropiles. These experimental investigations had been concerned with the load-deflection behaviour of micropiles both singly and in groups, loaded statically and/or cyclically, in the axial and lateral direction. Additionally, numerical investigations were carried out to cover a variety of micropile types and soil conditions. A review of the available literature on micropiles is presented herein. The presentation will be divided into two main sections. The first section will cover selected documented published data on different types of micropiles, while the

second section will focus on all the available field load tests of hollow bar micropiles subjected to different loading conditions

Table 2. 1. Typical α_{bond} (Grout-to-Ground Bond) Values for Micropile Design (after FHWA NHI 2005)

Soil/Rock	Grout-to-ground bond ultimate strengths, α_{bond} , kPa			
	Type A	Type B	Type C	Type D
Silt and clay (soft to medium plasticity)	35-70	35-95	50-120	50-145
Silt and clay (stiff, dense to very dense)	50-120	70-190	95-190	95-190
Sand (some silt) (fine, loose-medium dense)	70-145	70-190	95-190	95- 240
Sand (some silt, gravel) (fine-coarse, med.-very dense)	95-215	120-360	145-360	145-385
Gravel (some sand) (medium-very dense)	95-265	120-360	145-360	145-385
Glacial Till (silt, sand, gravel) (medium-very dense, cemented)	95-190	95-310	120-310	120-335
Soft Shales (fresh-moderate fracturing, little to no weathering)	205-550	N/A	N/A	N/A
Slates and Hard Shales (fresh moderate fracturing, little to no weathering)	515-1,380	N/A	N/A	N/A
Limestone (fresh-moderate fracturing, little to no weathering)	1,035-2,070	N/A	N/A	N/A
Sandstone (fresh-moderate fracturing, little to no weathering)	520-1,725	N/A	N/A	N/A
Granite and Basalt (fresh moderate fracturing, little to no weathering)	1,380-4,200	N/A	N/A	N/A

2.4.1 Investigations of different types of micropiles

This section recounts selected case studies of single micropile field load tests. These tests have been conducted on a variety of micropile types embedded in a gamut of soil conditions, and loaded both monotonically and cyclically either in the axial or lateral directions. In parallel with the field tests cases, some of the numerical investigations conducted considering different types of micropiles are reviewed. The available analytical and theoretical solutions for micropiles are summarized here as well.

2.4.1.1 Axial field load testing

Bruce et al. (1993) performed laboratory and field tests on different micropile types and configurations. The laboratory testing program encompassed three phases considering three different configurations: single grouted filled steel casing, simulating the upper section of cased micropile; grouted filled steel casing with connecting section employing threaded ends; and internally reinforced grout column to simulate the lower bonded length. The field tests were conducted on Type A micropiles embedded in rock and Type B embedded in soils. Each set of field tests was conducted on two different configurations; with and without internal reinforcement steel cages, but both were reinforced by outer casing. The data gained from these tests was used to develop the Elastic Ratio concept, which is proving to be useful in analyzing and predicting micropile performance and the phenomenon of progressive debonding with increasing load.

Gronek et al. (1993) reported a case history of micropiles used for retrofitting the foundation of a major grain-export facility, three 60 year old silos, in Vancouver. The

project involved 840 x 176 mm diameter micropiles. Three load tests were conducted to a maximum load of 200% of the working load (300 ton). The pile deflection measured at working load was 9.5 mm. The silos experienced an earthquake after construction was completed, and the maximum settlement observed was less than 9.5 mm.

Russo (2004) presented two full-scale load tests on instrumented micropiles constructed as single post grouted Type C following different procedures. He used an innovative technique to install embedded vibrating wire strain gauges. The load test results demonstrated that the installation procedures had a significant influence on the micropiles performance.

Han and Ye (2006 a and b) investigated the behavior of micropiles in soft clay. Four Type A, gravity grouted, micropiles were installed in Shanghai clay, China. The micropiles were instrumented by vibrating wire strain gauges to evaluate their load transfer mechanism. Two sets of tests were conducted in their field study: monotonic load tests on single micropiles including two compression and two tension tests (Han and Ye, 2006a); and one pile group test on the four micropiles to mimic the behavior of a foundation underpinned by micropiles (Han and Ye, 2006b). The results of the single pile load tests revealed that the mobilized ultimate skin friction for micropiles was between 0.9 and 1.2 of the undrained shear strength parameter of surrounding soil. They also found that the load transfer at the pile toe during single pile load tests was between 8.7 and 12.5 % from the applied load. From the four-micropile group, the authors confirmed that micropiles represent an excellent solution to underpinning foundations through strain gauges reading. The micropile carried about 80% of the additional load applied during the pile group test, and the rest were carried by the raft (supported on the ground).

Thomson et al. (2007) presented the results of axial compression, axial tension and lateral load tests on pre-production micropiles prior to use micropiles in upgrading the existing pier foundations of the Nipigon River Bridge in Ontario, Canada. The micropiles cross-sections were reinforced with outer steel casing (273 mm outside diameter, 13 mm wall thickness), additional inner steel casing, and a steel thread bar that was extended to the full length of the micropile. Among the six pre-production micropiles, three micropiles were gravity grouted and three were pressure-post grouted. Thomson and his co-workers noted that the ultimate bond resistance under compression at the grout-ground interface was between 140 kPa and 250 kPa. They concluded that the ultimate bond resistances for pressure grouted micropiles provided in FHWA (2000) appear to be reasonable. They observed that uplift failure of the micropile did not occur. However, the uplift tests were terminated based on structural strength of the central steel bar. The calculated average mobilized grout-ground bond stresses under uplift loads along the micropiles were between 150 kPa and 190 kPa. As they noted, the as-built grout volumes were significantly higher than the theoretical borehole volumes. These additional grout volumes indicated that the diameters of the uncased micropile portions were generally greater than the diameters assumed in design.

2.4.1.2 Cyclic field load tests

Cavey et al. (2000) documented the results of a series of cyclic load-reversal tests on pressure grouted Type B micropiles embedded in loose to medium sand and silt. The results showed that the reversed cyclic loading induced significant reduction in the micropile capacity. Their observations indicated that micropiles installed in cohesionless

soils have a critical level of repeated loading that is well below the ultimate micropile capacity under static conditions.

Gomez et al. (2003) performed an instrumented load test on a micropile founded in rock subjected to cyclic load increments. The analysis of the test results provided a useful insight into the mechanism of load transfer. From the bond strength values calculated based on the test results, they concluded that physical debonding of the grout-ground interface did not occur. However, post-peak reduction of bond strength was observed, which induced a progressive increase in the elastic length and elastic ratio of the micropile under increasing loads. They confirmed that determination of the elastic length of the micropile is useful for assessing micropile response. Gomez and his co-workers highlighted the limitation of the elastic length approach in cases where significant residual elastic compression exists upon unloading due to locked-in bond stresses along the micropile. This may provide un-conservative estimation of bond strength.

Yacyshyn (2007) reviewed two full scale verification load tests employing quasi-static alternating compression and tensile loads, with no dynamic component. The tested micropiles were 14.3 m embedded in sandy soils and diameter of 133 mm. The micropiles were primary grouted under 517 kPa pressure, followed by one stage of post-grouting to 5,170 kPa (i.e. Type C). The cyclic test starting from a 250 kN tension alignment load to 600 kN compression load by increasing compression loading 75 kN each successive cycle. The author stated that the permanent movement of the micropiles under cyclic loading recorded at maximum compression ranged from 2.6 to 4.5 mm. while, the permanent movements of the micropiles under tension load ranged from 4.5 to

8.2 mm. He noted that cyclic performance of micropiles, especially number of load cycles, in different soils should be documented to help designers for future projects.

2.4.1.3 Lateral experimental load tests

Richards and Rothbauer, (2004) compared the results of lateral load tests, performed as part of eight different projects, with the response predictions using LPILE (Ensoft, Reese et al. 2000), NAVFAC (1986), and characteristic load method (Duncan et al. 1994). The observed deflections of the lateral load tests were generally less than the predicted values. They attributed this to the typical conservatism in assigned soil parameters or neglecting elastic “passive surcharge” due to the top of the pile being below ground surface. The observed responses had shown that the lateral load performance was very sensitive to the soil type and shear strength in the upper 2 to 5 m of the pile.

Long et al. (2004) presented the results of 10 lateral load tests conducted on micropiles 15.2 m long installed in clay overlying sand. The micropiles were reinforced with a central high-strength threaded bar along the entire length. The bending stiffness and capacity in the upper 9 m of the micropile were increased by including a 244 mm-OD casing with a 13.8 mm thick wall. They compared the results of the tests with behaviour predicted using the conventional p-y curves approach employing the program LPILE. The calculated and measured displacements were in good overall agreement within ± 10 percent.

Juran et al. (2007) conducted a series of centrifugal tests on micropile groups and network systems to investigate the system response to earthquake loading as well as the superstructure-soil-micropile interaction. The tests were performed on models of vertical

and batter micropiles embedded in loose to medium-dry sand under different levels of shaking. One of the study findings was the positive group effect increasing with the number of piles and the batter angle. Additionally, it was found that pile inclinations of 10° and 30° resulted in substantial improvements in the superstructure response with acceleration reduction up to 40 percent of that obtained in the case of vertical piles. Juran et al. (2007) performed numerical analyses using programs LPILE and GROUP (Ensoft, Reese et al. 2002) in a pseudostatic analysis approach to simulate the centrifugal model tests. The comparisons between the numerical and experimental results confirmed the ability of the numerical models to predict the seismic behaviour of micropile groups and network systems.

2.4.1.4 Case histories on micropiles

Traylor et al. (2002) explored using micropiles in karst ground to provide structural support as a foundation system. They reported three case histories of Type A micropiles on karstic bedrock. The working load ranged between 600 to 1000 kN in compression. They calculated the average ultimate bond values of Type A piles in massive hard rock to be in excess of 17.5 MPa. They argued that for anchors in rock, bond lengths greater than about 3m rarely produce much increase in capacity, except for the case highly variable elevation of the founding rock.

Cadden et al. (2004) summarized 14 case studies reported in the literature involving different types of micropiles, mostly constructed in rock. They evaluated the allowable capacity of a typical 178 mm OD, 12.5 mm wall micropile installed into a 203 mm drill hole using different codes guidelines. They found that the allowable structural capacities

ranged from about 800 to 2100 kN. However, the load testing of this pile confirmed that it sustained more than 4000 kN without displaying any sign of failure. These findings demonstrated that most codes underestimate the capacity of micropiles and underscored the need for more complete database on achieved bond stresses, or on measured bond strength in micropiles installed in different geological environments in order to improve the codes recommendations for their design.

Jeon (2004) examined the load-displacement behaviour of twenty one axial compression tests from ten different sites. Eight tests were performed on Type B, C and D micropiles constructed in cohesive soils and the rest was constructed in sand. The capacity of the micropiles established from the field tests were compared with the design values using alpha and beta methods for drilled shafts. The results showed that micropiles can have much higher unit skin friction compared to larger-diameter drilled shafts, especially at shallower depths with $D/B \leq 100$. He reported that the unit skin resistance of micropiles was 1.5 to 2.5 the values for drilled shafts. He attributed this increase to the different grouting methods employed during installation of micropiles.

Holman and Tuozzolo (2006) analyzed three instrumented micropile load tests from two case histories. A total of 34 vibrating wire spot-weldable and embedment strain gauges were employed in the three load tests. Two of three piles were tested to plunging failure and one to impending failure. They found that the pile secant modulus degraded with increased strain level, primarily as a function of the nonlinear behaviour of the cement grout, however, linearized degradation relationships were synthesized for the load test data sets and found to be reasonable when compared to the field data. Moreover, the load distribution in the bond zone of the tested piles was generally non-uniform, indicating

that the mobilized unit bond stress was not constant. The authors noted that the plunging failure demonstrated that significant tip resistance was mobilized in a nonlinear fashion, even at loads less than that causing plunging failure. The former finding conflicted with the assumed behaviour in state of practice in micropile design. However, it could potentially be used to produce more efficient pile designs for suitable situations (i.e. where the soils at the micropile tip are equally or more competent than those of the bond zone).

2.4.1.5 Analytical and theoretical analyses

Misra et al. (2004) proposed analytical relationships to describe pullout load-displacement behavior accounting for micropile–soil interaction. They considered a partially bonded micropile, consisting of a top debonded zone and a bottom bond zone such that it transmitted its load to the surrounding soil. Furthermore, they assumed that the micropile–soil interface behaved as elastic-perfectly plastic and homogeneous material such that the effects of soil layering and grout inhomogeneity were averaged. The model was shown to replicate the field measured load-displacement curves from different case studies. The analyzed case studies were employed to develop preliminary data for the dependence of micropile–soil interface shear strength and shear modulus upon grout or post-grout pressure utilized.

Cadden and Gomez (2002) considered the effect of buckling on the capacity of micropiles and produced a graphical chart based on the Euler buckling equation. It can be used as a tool for checking whether buckling of a given micropile section should be explored further for a given site. However, this procedure neglected the grout

contribution in the buckling evaluation. The authors also noted that the evaluation of lateral and buckling capacities of micropiles should include a consideration of the location of threaded connections relative to the shear and moment distribution in the pile. However, the graph was reproduced by the FHWA NHI (2005).

2.4.1.6 Numerical analysis

Ousta and Shahrour (2001) investigated the seismic behaviour of micropiles used for the reinforcement of saturated soils numerically. The analysis was carried out using approximation for the fluid-soil coupling and a cyclic elasto-plastic constitutive relation for the description of the soil behaviour implemented in a three-dimensional finite element program. The authors showed that the presence of micropiles slightly affected the earthquake-induced pore-pressure. As they noted, when micropiles were used in loose to medium sand, the seismic loading induced an increase in the pore-pressure, which lead to a large degradation in soil stiffness and resistance, and consequently caused a large increase in the bending moment. However, the group effect resulted in a significant reduction in the bending moment.

Sadek and Shahrour (2004) utilized a three-dimensional finite element modeling to analyze the influence of micropiles inclination on their response to seismic loading. The study considered two cases: micropiles embedded in a homogeneous soil layer with a constant stiffness; and a soil layer with a depth based-increasing stiffness. Their results showed that the micropile inclination improved its seismic performance compared to vertical piles. The inclination allowed a better mobilization of the axial stiffness of

micropiles and consequently leads to a decrease in both shearing forces and bending moment induced by seismic loading.

Sadek and Shahrour (2006) investigated numerically the influence of the head and tip connection on the seismic performance of vertical and inclined micropiles installed in linear elastic soil. They indicated that a pinned connection between the micropiles and the cap reduced the axial force and bending moment in micropiles, especially for inclined micropiles. For example, a group of four micropiles with a pinned connection inclined 20° to the vertical axis, the maximum bending moment decreased by about 80%. They also found that embedment of the micropiles tip in a stiff layer resulted in a dramatic increase in the seismic-induced internal forces, in particular at the interface between the two layers. Additionally, the maximum axial force induced for a group of four micropiles inclined 20° to the vertical axis in layered soil was about 27 times of that obtained in micropiles with a free tip. However, they recommended that additional research is still needed to evaluate the seismic behavior of micropiles considering the nonlinearity for both the soil and micropiles.

2.4.2 Previous work on hollow bar micropiles

Despite the growing demand on hollow core bar micropiles, little work has been devoted to evaluating its performance under different types of loadings, especially in cohesive soils. In particular, there is a scarce data available regarding the grout-ground nominal bond strength, α_{bond} , from field load test under compression and/or tension.

Bishop et al. (2006) compiled observations on hollow bar micropiles over eleven years in five different projects involving both Class I and Class II Titan hollow bar micropiles

founded in highly varying soils of Salt Lake City. Some projects included load tests on pre-bid and production micropiles in order to verify load transfer assumptions. They postulated that the load capacity of a single hollow bar micropile was substantially greater than its crushing strength, when loaded in compression. In addition, a hollow bar micropile was capable of creating competent skin friction bond which can carry moderate to moderately high loads where the stiffness of the soil/hollow bar system can exhibit relatively low deflections under design load. Moreover, the capacity of a pile group with piles placed at 0.5m was at least equal to the sum of the individual micropiles, and may be greater, depending largely upon the amount of soil improvement that is affected by the grouting process.

Gomez et al. (2007) analyzed the results of 260 hollow bar micropiles installed to retrofit two bridges in New Jersey, including 180 in submerged sand and 80 installed in stiff silty clay. All production micropiles were proof-tested up to 150 percent of the design load. In addition, four verification tests were performed on sacrificial micropiles to at least two and a half times the design load or to failure. In addition to their benefits in significantly reducing the cost and construction time, they demonstrated that the ultimate bond strengths of hollow core bar micropiles installed in both granular and fine soils were significantly greater than that typically expected in pressure-grouted (Type B) micropiles in granular soils.

Telford et al. (2009) reported the results of verification compression and tension micropile loading tests conducted on a Titan 73/45 IBO micropile in variable sand and gravel deposits. The micropile was 9.8 m in length and was drilled utilizing 115mm cross drilling bit. The results verification testing confirmed that the micropile was capable of supporting high compression (1350 kN) and tensile loads (980 kN) with small pile head

movements (15mm). The calculated grout to soil bond strengths from their test program matched well with the FHWA (2000) preliminary bond strength values when considering an enlarged pile diameter to 1.5 times the drilling bit diameter. However, the ultimate capacity of the micropiles was not achieved during the pile load tests. Based upon the small pile head movements, they concluded that the ultimate grout to soil bond strength was expected to be considerably higher.

Bruce and Gursaud (2009) replaced 223x324mm-diameter driven steel tube piles by 357 hollow bar micropiles to overcome an aquifer under artesian head at shallow depth, in Toronto. The micropiles could be installed to elevations deeper than the 4 m assigned to driven piles because their grout flush installation process practically eliminated the risk of creating a pathway for artesian piping. The Ischebek Titan 52/26 system was constructed employing 115mm cross cut bit. Five different load tests were performed: two loaded to failure and three proof tests. The magnitude of applied test loading was 200% of compression design load. The load tests proved that the micropiles performed well, both in terms of stiffness and capacity, in these soil conditions.

Bennett and Hothem (2010) conducted a series of load tests on hollow bar micropiles constructed in soft coastal plain soils to support heavily loaded equipment pads at an aircraft manufacturing facility. Four pairs of sacrificial test piles were constructed to lengths 7 m, 8.5 m, 10 m and 11.5 m. Each pair of micropiles was installed utilizing one 150mm clay bit and one 115mm cross bit for comparison in terms of installation efficiency and load carrying capacity. Each test pile was tested to ultimate geotechnical failure. The results showed that the 7 m micropiles attained applied axial loads of approximately 480 kN and 460 kN for the 150mm clay bit and 115mm cross bits,

respectively, at the target settlement value of 6mm. The increased axial stiffness due to hollow bar micropiles construction provided substantial reductions in settlement even in very soft soils. Additionally, finite element modeling was utilized to quantify the amount of improvement achieved by the micropiles. The predicted settlements from the finite element analysis was in reasonable agreement with the observed experimental results.

As presented in this section, the majority of the investigations conducted on hollow bar micropiles focused on the load carrying capacity under monotonic loading. The back calculated bond value obtained from most of the field tests exceed that suggested by the FHWA (2005) by a factor between 1.2 and 1.5. also, hollow bar micropile is used in foundation upgrade application, very limited research was dedicated to the group action of hollow bar micropiles. In addition, the research on the performance of hollow bar micropiles response to other loading modes such as axial cyclic loading, lateral monotonic and cyclic loadings is largely absent. Hence, there is a need for a comprehensive investigation into the performance of hollow bar micropiles under different type of loadings and configurations, especially in cohesive soils.

CHAPTER 3

SOIL INVESTIGATION AND GROUT EVALUATION

This chapter documents the site investigation program adopted in this research and the properties of the grout material used. It is important to properly characterize the soil deposits and correctly evaluate soil strength, stiffness, and engineering properties. These properties will be used in interpreting the load test data and in simulating the behavior of the hollow bar micropiles through finite element analysis. Hence, the soil investigation program incorporated both field exploration and laboratory tests. The grout material used during installing the hollow bar was laboratory tested and its strength and stiffness parameters were reported.

3.1 Soil Investigation

3.1.1 Site location and description

The piles were installed and tested at Western University Environmental Site, located at 22312 Wonderland RD. N adjacent to Middlesex County Rd. # 56. The site is located approximately 8 km north of the City of London, Ontario, on a ten hectare parcel of land. Figure 3.1 shows the location of the site. The ground surface is flat and is roughly 200 meters above sea level.

3.1.2 Site investigation program

A site exploration program was carried out at the test site prior to micropile installation and field testing. The field exploration program encompassed two mechanical boreholes

(denoted BH-1 and BH-2). During each borehole, three consecutive stages were followed: solid stem auguring, standard penetration test (SPT) with split spoon sampler, and finally Shelby tube sampling, if possible. Previously, a mechanical borehole (denoted BH) was conducted as a part of previous pile test studies (Livenh 2006). The borehole was located about 80 m north east of the current tested site. The locations of the three available boreholes with respect to the tested micropiles are given in Fig. 3.2. The site exploration was followed by laboratory testing on disturbed and undisturbed samples extracted from the site. The laboratory testing conducted included determination of natural moisture content, Atterberg limits, grain size distribution, as well as triaxial tests.

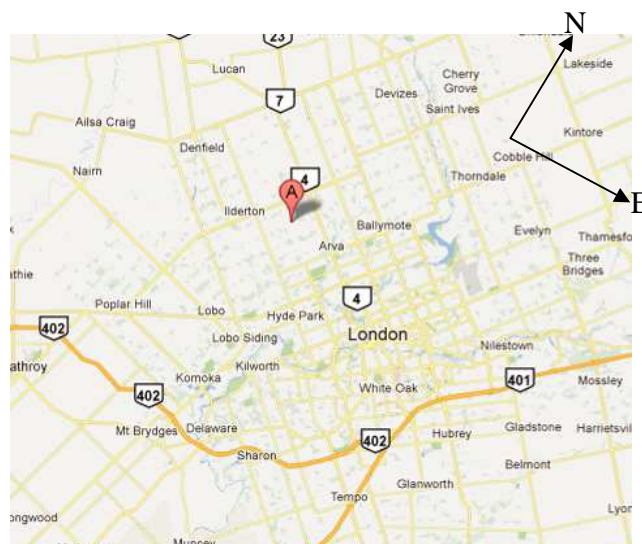


Figure 3. 1. Location of test site (Google Map)

3.1.3 Standard penetration test equipment and procedure

The two boreholes BH-1 and BH-2 were conducted in October 2009 as part of the current study, within the area where the micropiles were installed and load tested (Site 1). The two boreholes at Site 1 are located 16.6 meters apart. The two mechanical boreholes were

carried out and operated using mounted Morocka Rig. Figure 3.3 depicts the used rig and its components.

Each mechanical borehole involved three stages. The first stage was using the solid stem auger, shown in Fig. 3.3, in cutting the soil and advancing the borehole until the desired depth. Upon reaching the desired depth, a sampler with split spoon was inserted and standard penetration test was performed, Fig. 3.4a. During the standard penetration test, a 50.8 mm external diameter thick-walled sample tube was driven into the ground at the bottom of the borehole by means of a 635 N automated hammer falling freely through 760 mm stroke. The tube was first driven an initial 150 mm to allow for the presence of distributed material at the bottom of the borehole. The number of the blows (N) required driving the sampler a further 300 mm was recorded, Fig. 3.4b. The sampler with the disturbed sample was extracted and the samples were collected from the sampler, Fig 3.4c. The standard penetration test was conducted at interval equal to 0.75m. A Shelby tube was then used to extract undisturbed samples, when possible.

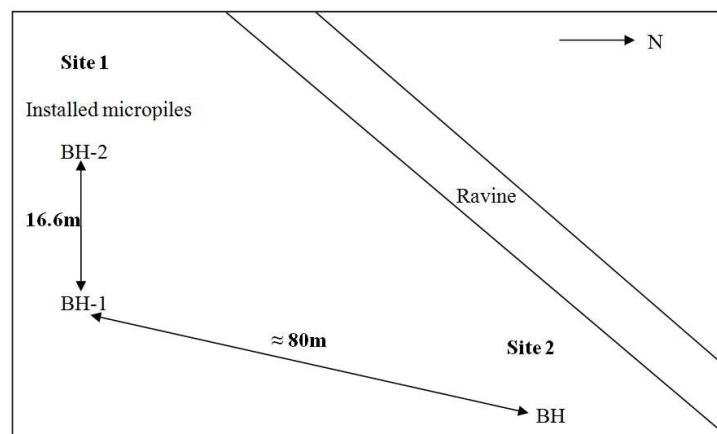


Figure 3. 2. Plan view for the layout of Site 1 and Site 2

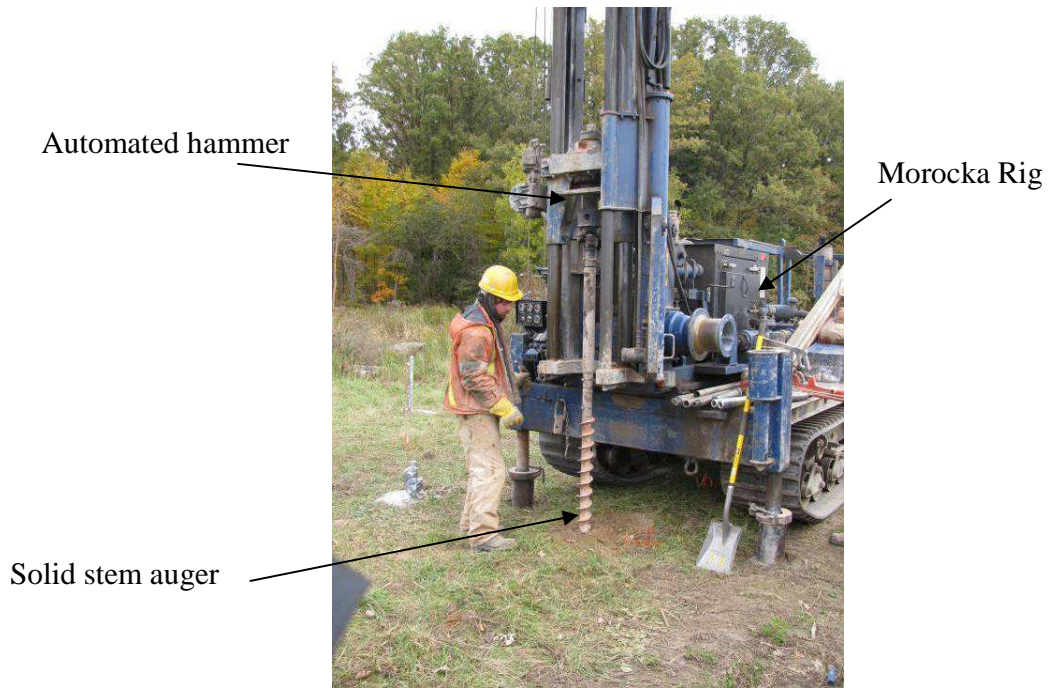


Figure 3. 3. The Mounted (Morocka) rig and the solid stem used

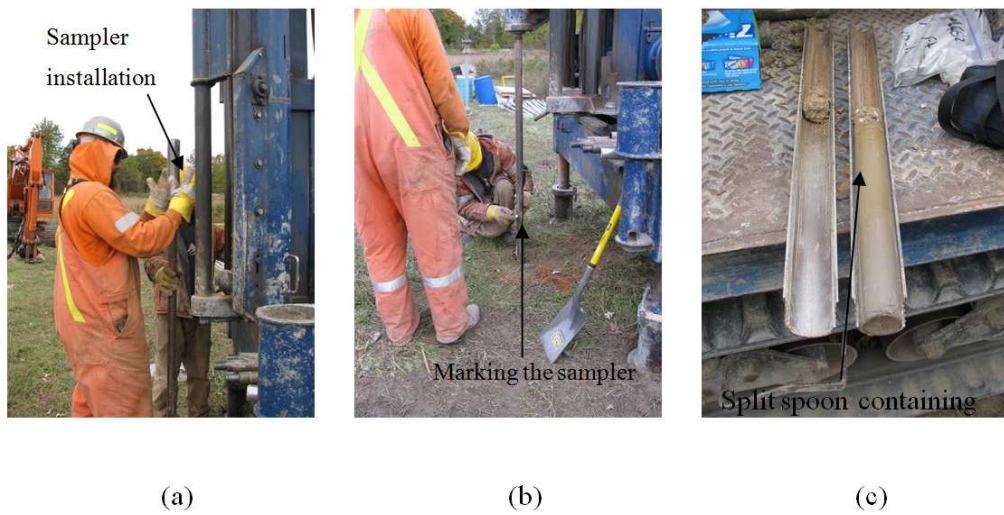


Figure 3. 4. Steps during field exploration

3.2 Subsurface Conditions

3.2.1 Soil stratigraphy

Figures 3.5, 3.6, and 3.7 illustrate the borehole logs and the Standard Penetration Test (SPT) number, N_{field} , versus depth for the three available boreholes, BH, BH-1, BH-2, respectively. In addition, the soil stratigraphy interpreted from the three boreholes and the location of test micropiles are given in Fig. 3.8. The borehole logs show that the soil deposit is composed of layers of silty clay to clayey silt, overlying layer of compact to dense sand with occasionally seams of silt.

The first layer at BH-1 is 1 m thick, weathered brown clayey silt with seams of compacted silty sand and gravel (a soil sample is shown in Fig. 3.9). This layer is underlain by a 4.7 to 5.7 m thick layer of stiff to very stiff silty clay to clayey silt soil. Significant seams of gravel with different sizes and traces of small cobbles have been observed at various depths within the layer. This layer is underlain by compact to dense sand with traces of silt, 2.5 to 3.5 m thick. A layer of compact gray silt of variable thickness appeared at location of BH-1 and gradually vanished with distance in all directions. The groundwater table was found at a depth varying from 3.7 m to 4.0 m below the ground surface at the time of drilling the boreholes. The GWT was found at depth 2.6 m at Site 2 because it is close to a ravine. It should be mentioned that during installation of the reaction piles, the groundwater table was observed at a depth of 1 m from the ground surface.

REF. NO.: 1-3405 LOG OF BOREHOLE NO. 3 Encl. No. 2
 CLIENT: CES Engineering/INC DRILLING DATA:
 PROJECT: Test Pile Facility METHOD: Auger
 LOCATION: Manderland Road South, London DIAMETER: 6-inch
 DATUM ELEVATION: DATE: 6 July 9, 2004

Elev.	Reten	Depth meters	SUBSURFACE PROFILE		SAMPLES			Penetration Resistance (Blows/ft)				PLASTIC LIMIT %	NATURAL WATER %	LIQUID LIMIT %	
			DESCRIPTION	SYMBOL	CLASSIF. NO.	NUMBER	TYPE	W	20	40	60				80
0.0			Ground Surface												
			300mm topsoil.												
			Stiff to very stiff brown sandy clayey silt, subbedded gravel.				1	SS	8						
2.6			Very stiff grey clayey silt.				3	SS	29						
4.7			Very stiff grey clayey silt, subbedded gravel.				4	SS	20						
5.2			Compact to dense grey fine sand, traces of silt. (saturated)				5	SS	35						
8.1			End of borehole				6	SS	38						

Figure 3. 5. Borehole log for Site 2 (Livneh 2006)



Atkinson Davies Inc.

12 - 60 Meg Drive, London, ON, N6E 3T6

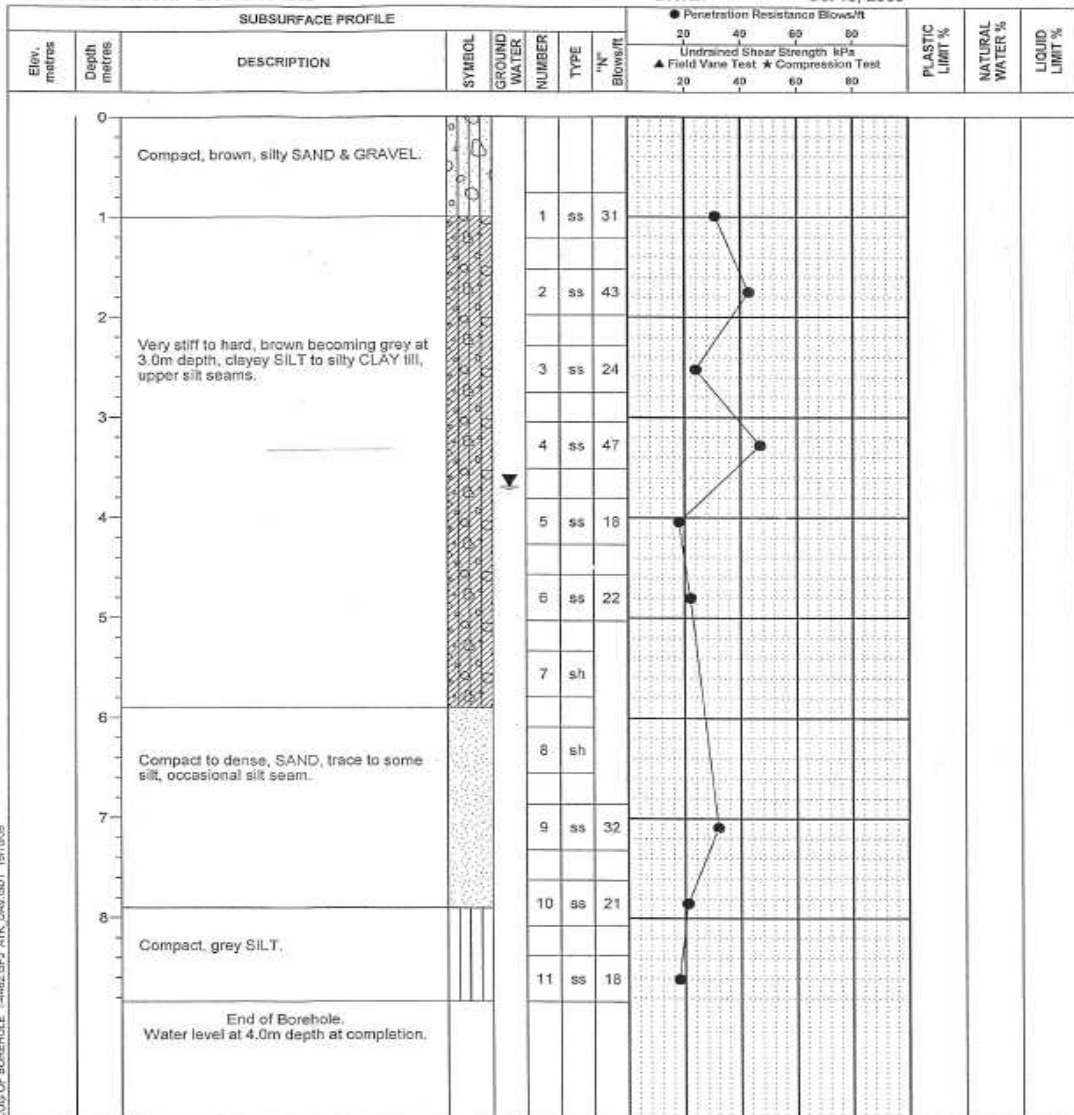
CONSULTING SOILS AND MATERIALS ENGINEERS

Phone: 519-685-6400 Fax: 519-685-0943

REF. NO.: 1-4462
 CLIENT: University of Western Ontario
 PROJECT: Borehole Sampling Project
 LOCATION: 22312 Wonderland Rd N, London
 DATUM ELEVATION: Ground Surface

LOG OF BOREHOLE NO. **1**

Encl. No. 1 (Sheet 1 of 1)
 DRILLING DATA: Morocca Rig
 METHOD: Solid Stem Augers
 DIAMETER: 150mm
 DATE: Oct 15, 2009



LOG OF BOREHOLE 1-4462.BPJ, ATK, DAV, GDT, 15/10/09

Figure 3. 6. The borehole log and the SPT (N_{field}) values versus depth for BH-1



Atkinson Davies Inc.

CONSULTING SOILS AND MATERIALS ENGINEER

12 - 60 Meg Drive, London, ON, N6E 3T6

Phone: 519-685-6400 Fax: 519-685-09

REF. NO.: 1-4462
 CLIENT: University of Western Ontario
 PROJECT: Borehole Sampling Project
 LOCATION: 22312 Wonderland Rd N, London
 DATUM ELEVATION: Ground Surface

LOG OF BOREHOLE NO. **2**

Encl. No. 2 (Sheet 1 of 1)
 DRILLING DATA: Morooka Rig
 METHOD: Solid Stem Augers
 DIAMETER: 150mm
 DATE: Oct 15, 2009

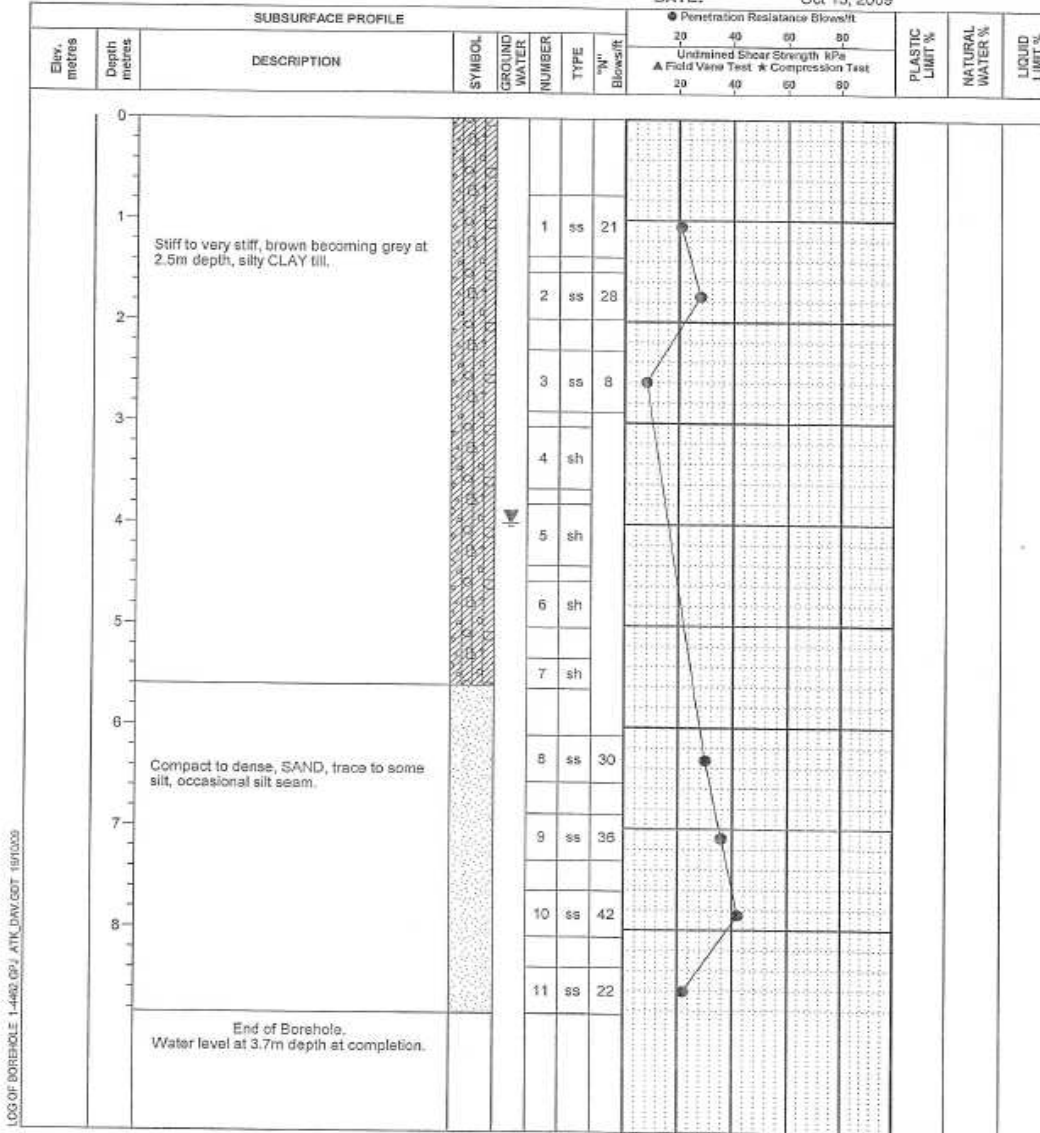


Figure 3. 7. The borehole log and the SPT (N_{field}) values versus depth for BH-2

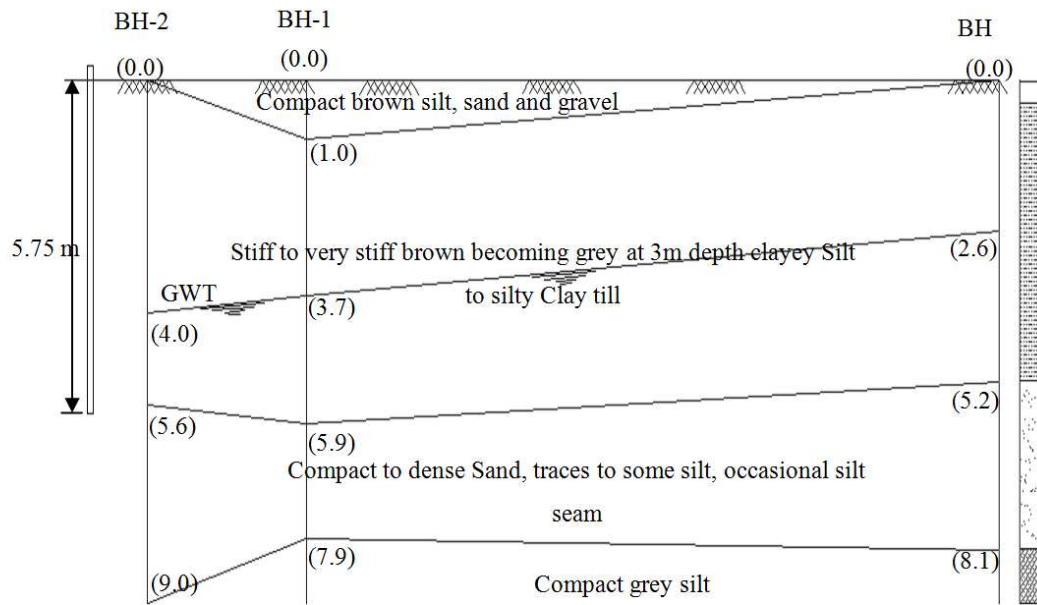


Figure 3. 8. Soil stratigraphy



Figure 3. 9. Piece of the soil at the top 1 m from the test site

3.2.2 Soil classification and properties

Disturbed samples were extracted using the split spoon at various depths during the soil exploration from both boreholes, BH-1 and BH-2. These samples were subjected to several laboratory tests to determine the engineering properties of soils at different depths. The laboratory tests include determination of natural moisture content, w_c , Atterberg limits, specific gravity, G_s , and dry unit weight, γ_{dry} . Some other properties, such as; void ratio, e , and saturated unit weight, γ_{sat} , were calculated using standard phase relations.

Table 3.1 shows the index properties of the silty clay to clayey silty layer. As inferred from Table 3.1, the moisture content of this layer is between 10 to 15%. It is observed that the moisture content is generally close to the plasticity limit, W_{PL} . The layer has plasticity index, I_p , between 16 and 20%, which indicates low to medium plasticity. The liquidity index, I_L , of the layer is less than one, which indicates that the soil is non-plastic and non-liquefiable. Employing the measured plasticity indices and liquid limits, the positions of the samples relative to the A-Line of the Casagrande's Plasticity chart are illustrated in Fig. 3.10. All samples are falling above the A-Line, which indicates that this layer comprised mainly of silty clay to clay material.

The specific gravity, G_s , dry unit weight, γ_d , and moisture content were determined for samples collected from BH-2. The measured properties at different depths were used to calculate other engineering properties, such as; void ratio, e , and saturated unit weight, γ_{sat} .

The engineering properties of the samples extracted from BH-2 are summarized in Table 3.2. It is observed from Table 3.2 that the void ratio decreases with depth to reach a low value of 0.37 at the bottom of the silty clay layer. This can explain the small difference in moisture content above and below the ground water table within the same layer.

Sieve and hydrometer analyses for disturbed samples extracted from BH-1 at depths 1.6 and 4m were performed and the results are presented Figures 3.11 and 3.12. The hydrometer analysis indicated that the percent of clay content increases with depth while the silt content decreases, and generally, the layer best described as clayey silt to silty clay deposit.

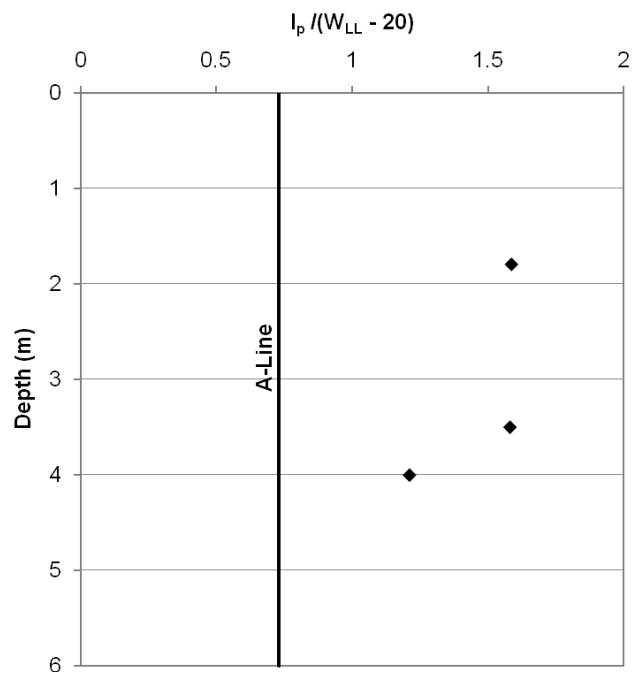
Figure 3.13 shows that the soil at depth 5.8m contains 75% sand and 8% gravel and the rest is fine grains, while the soil at depth 7 m contains 85% sand, 2% gravel and 13 % fine grains (Fig. 3.14). It can be concluded from the sieve analysis that the cohesionless soil underlying the silty clay layer is sandy soil with traces to some silt.

Table 3. 1. Index properties of the top cohesive layer

Borehole (depth in m)	Moisture content, w_c	Plastic limit, W_{PL}	Liquid limit, W_{LL}	Plasticity index, I_P	Liquidity index, I_L
	%	%	%	%	
BH-1 (1.8)	10.3	12.9	32.1	19.2	-0.135
BH-1 (4.0)	13.8	16.6	36	19.4	-0.144
BH-2 (3.5)	12.1	14.3	29.8	15.5	-0.135

Table 3. 2. Soil properties for samples extracted from BH-2

Depth m	Specific gravity, G_s	Dry unit weight, γ_{dry} kN/m^3	Voids ratio e	Bulk unit weight γ_{bulk} , kN/m^3	Saturated unit weight γ_{sat} , kN/m^3	Moisture content, w_c %
0.7 to 1.3	2.695	15.0 – 16.0	0.74	16.6	19.5	9.0
1.5 to 2.1	2.706	16.0 – 17.0	0.59	18.8	20.33	10.7
2.2 to 2.8	2.706	17.0 – 18.0	0.52	19.8	20.82	11.5
4.5 to 4.9	2.732	19.0 - 20.0	0.37	22.5	22.5	13.0

**Figure 3. 10. Index properties with respect to Plasticity chart**

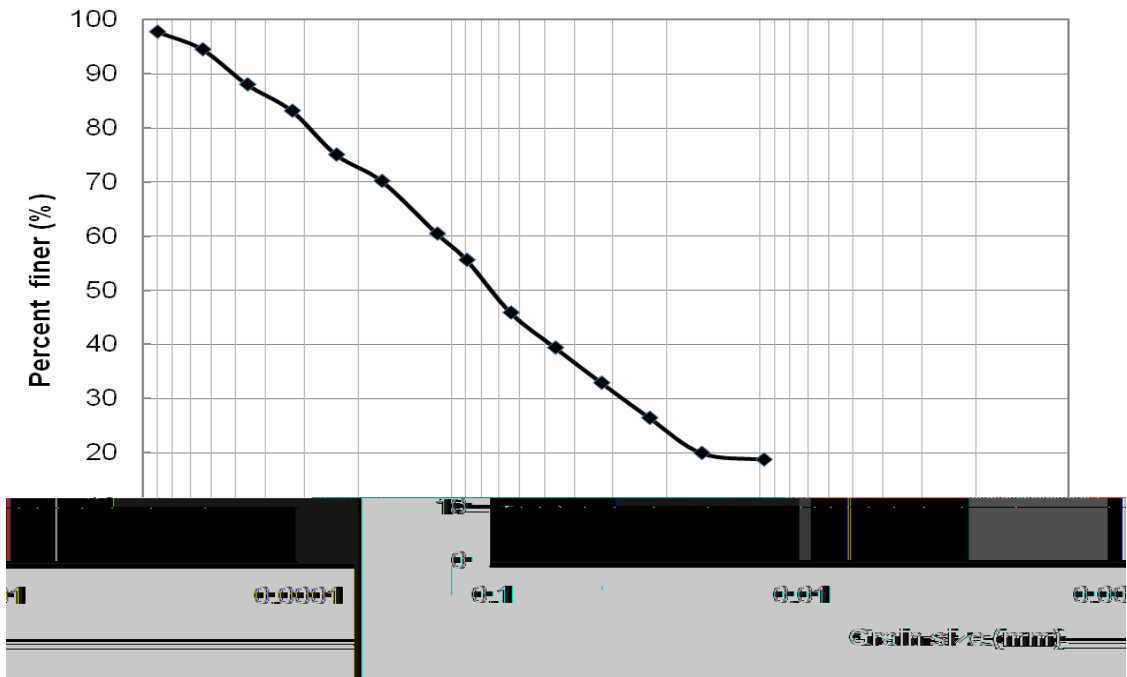


Figure 3. 11. Hydrometer Grain size distribution of sample from BH-1 at depth 1.5m

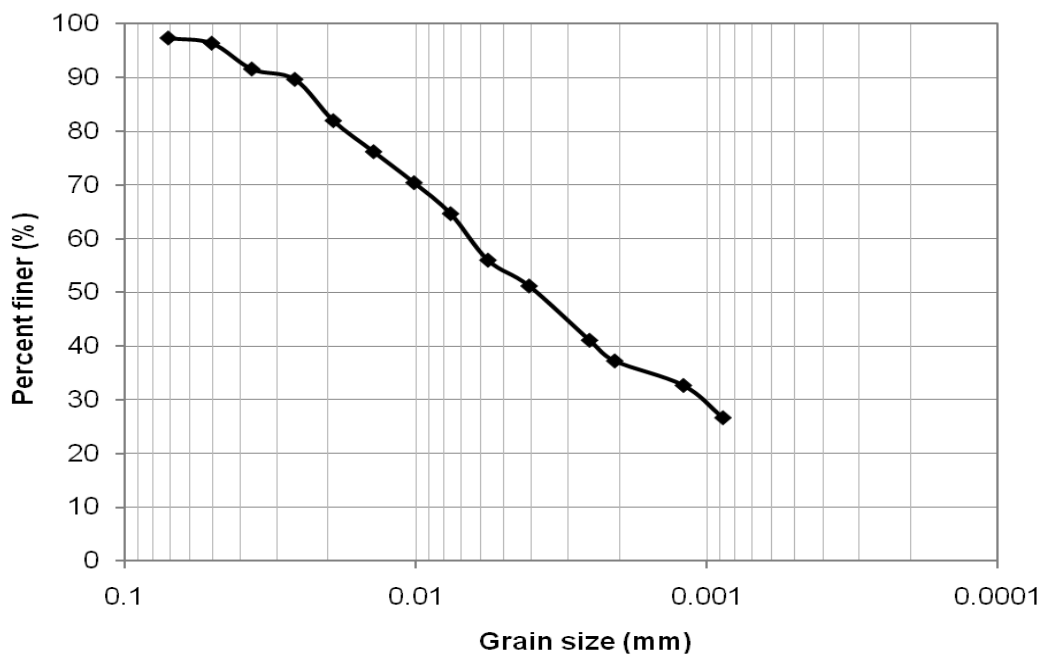


Figure 3. 12. Hydrometer Grain size distribution of sample from BH-1 at depth 4m

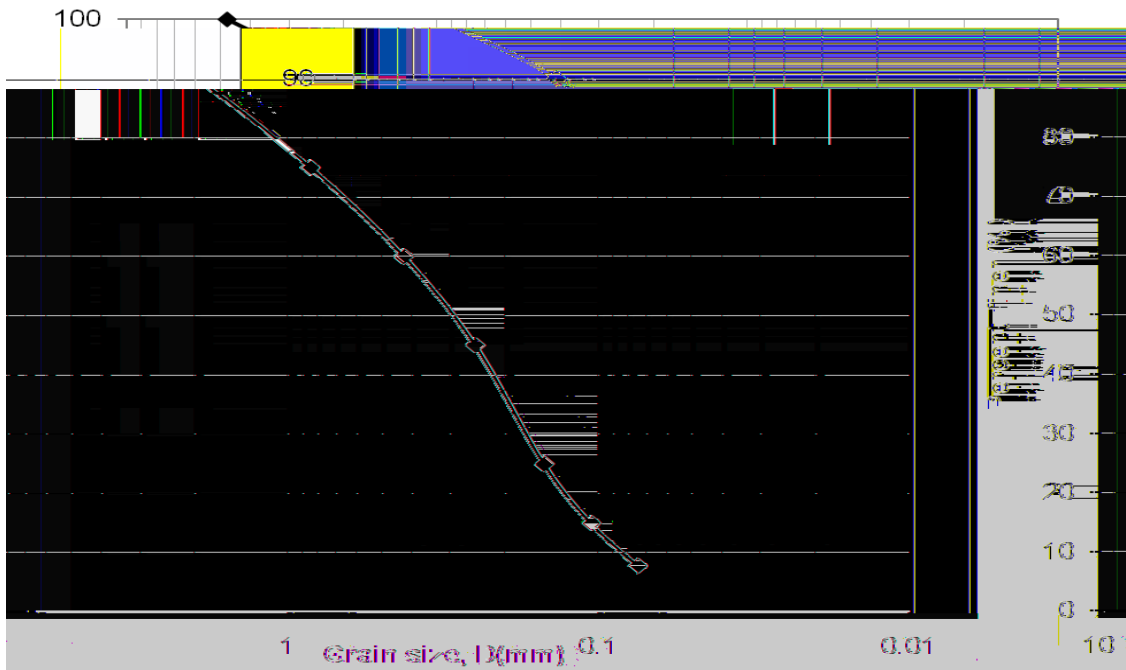


Figure 3. 13. Grain Size distribution of sample from BH-2 at depth 5.8m

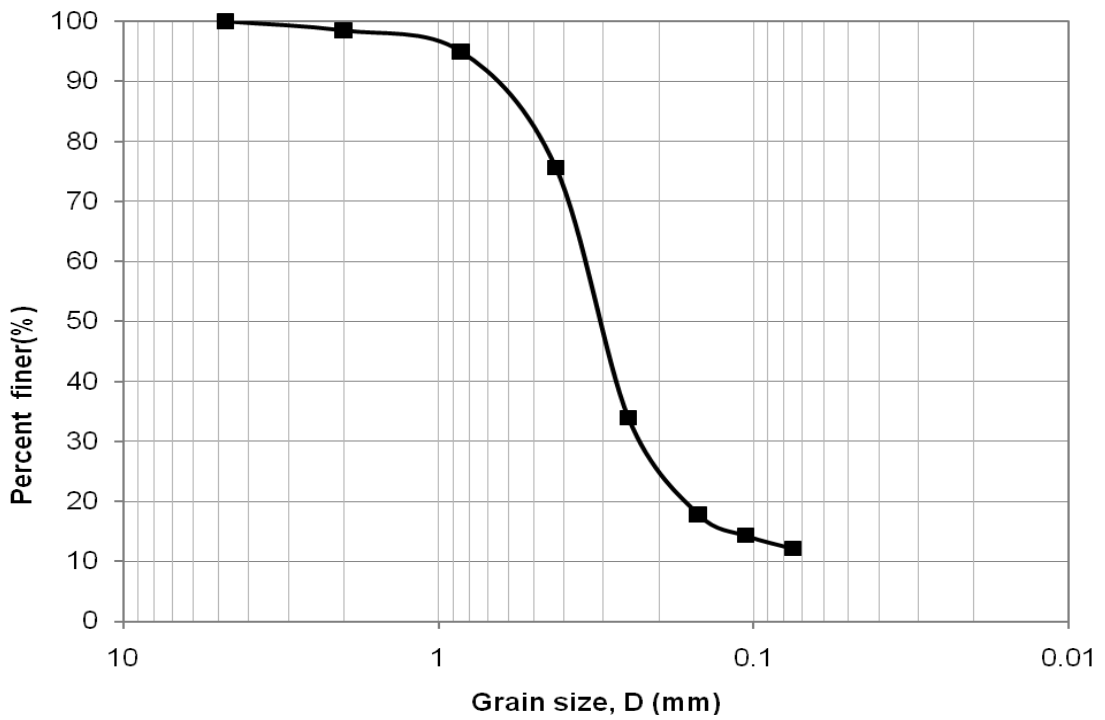


Figure 3. 14. Grain Size distribution of sample from BH-1 at depth 7m

3.2.3 Soil shear strength parameters

The soil profile at the test site can be divided into two main layers; one with cohesive nature, which starts from the ground surface down to depth of 5.7m, and layer of sand with traces of silt, from depth 5.7 until the end of the borehole depth. Because the micropiles were loaded in a rapid fashion, and due to the cohesive nature of the upper soil, the shear strength of that layer will be represented by its undrained shear strength parameter, s_u . However, the shear strength of the sand soil underlying it will be evaluated utilizing angle of internal friction, ϕ' , of the sand

Several attempts were made to extract undisturbed samples from the boreholes using a Shelby tube at depths up to 5.7m. All attempts failed due to the fissured over-consolidated nature of the silty clay soil in BH-1. The seams of gravel contributed to this failure due to its low recovery ratio. In BH-2, samples were successfully extracted from depths between 3 to 5.0m. The samples extracted using the Shelby tubes were tested in a triaxial cell under Unconsolidated Undrained condition (UU).

For s_u to be representative of the micropile loading test conditions, it was important to use a loading rate during the UU triaxial tests similar to that utilized during the field test on the micropiles. Thus, all triaxial tests were conducted at a strain rate equal to 0.051mm/min. The procedure of ASTM (D 2850-95 Re-approved 1999) was followed on three samples tested using a 10 Ton Wykeham Farrance compression machine. Figures 3.15 to 3.17 elaborate the deviatoric stress, q , versus axial strain for the three triaxial tests conducted. The results of the performed UU tests are summarized in Table 3.3.

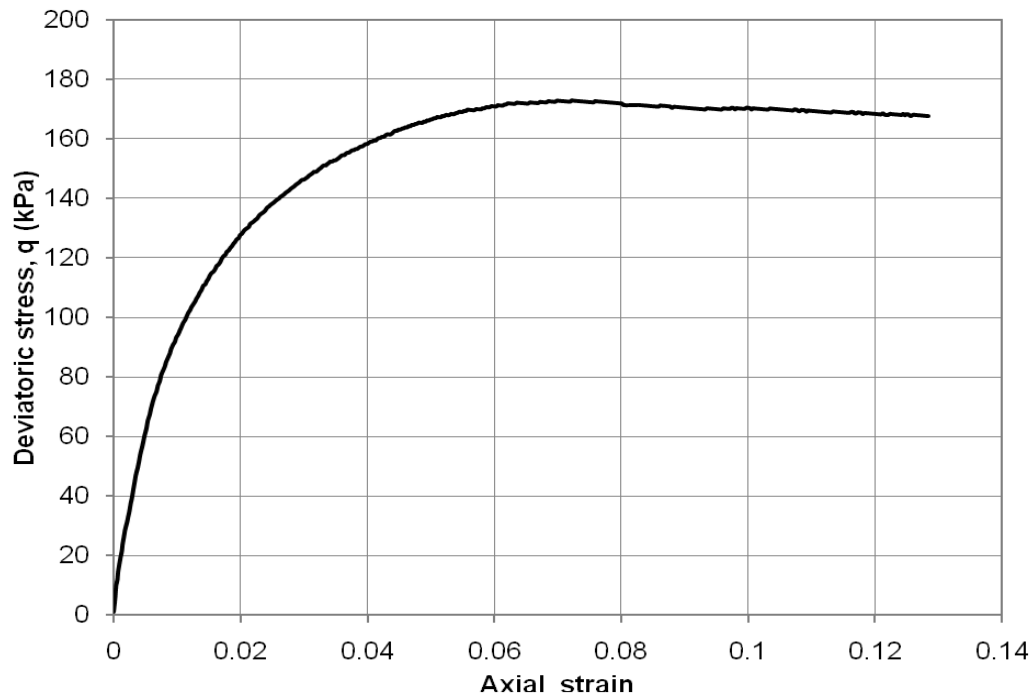


Figure 3. 15. Triaxial test result for sample at depth 3.0 m, BH-2

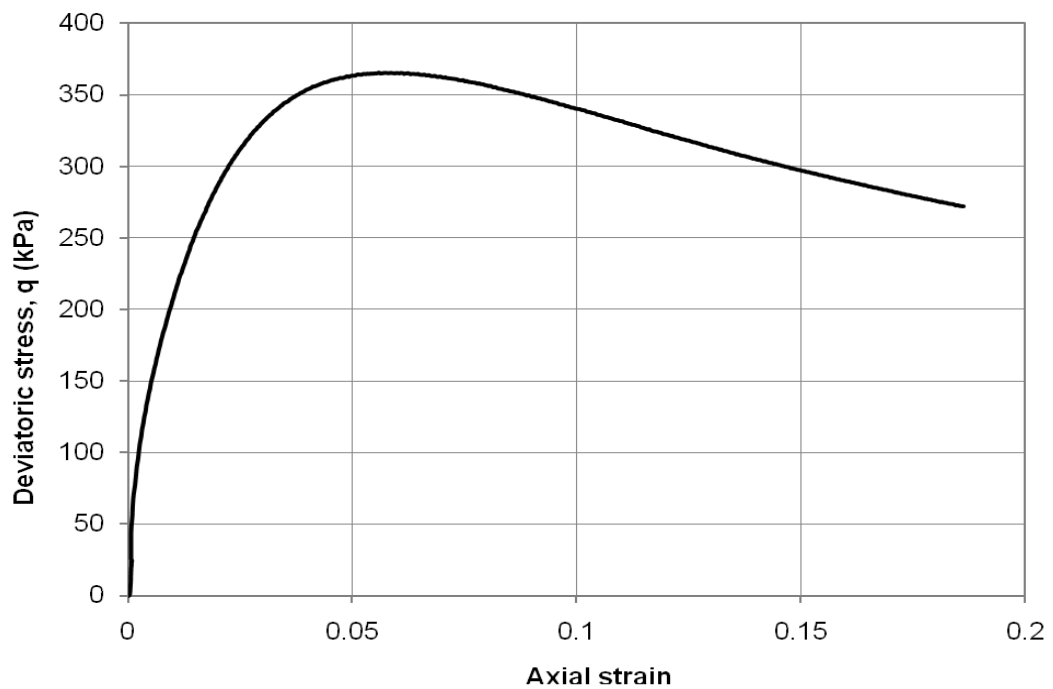


Figure 3. 16. Triaxial test result for sample at depth 3.7 m, BH-2

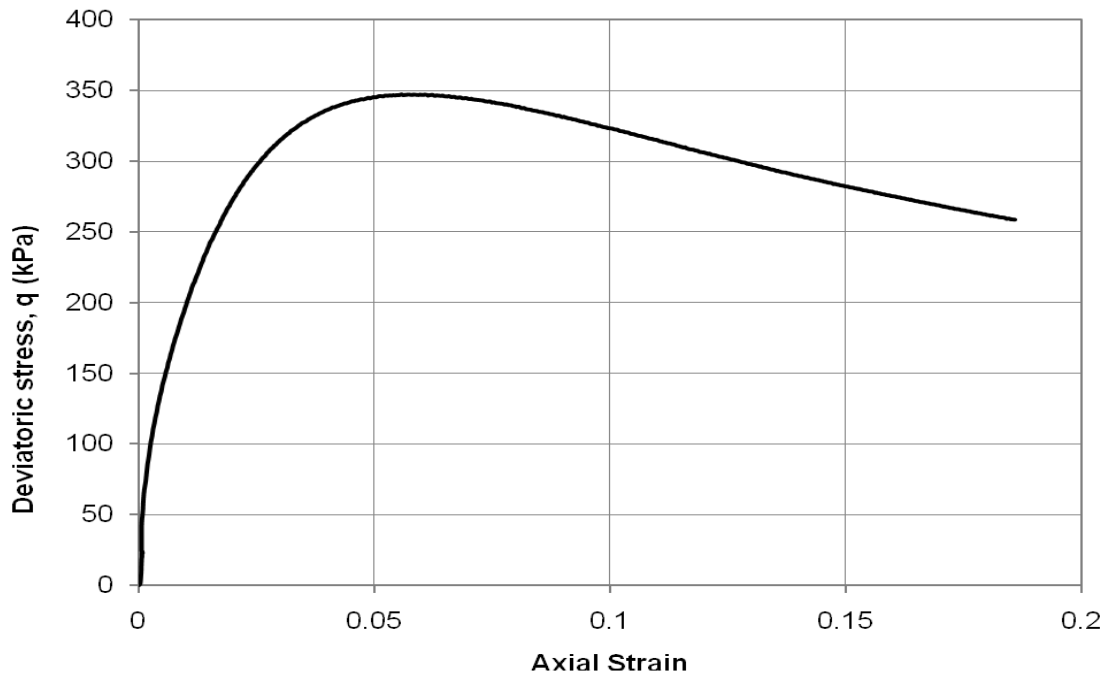


Figure 3. 17. Triaxial test result for sample at depth 4.3 m, BH-2

Table 3. 3. Summary of (UU) triaxial tests on samples from BH2

Depth (m)	Undrained shear strength, s_u kPa	Undrained tangent modulus, E_{ui} MPa	Undrained secant modulus, E_{us} MPa	Water content, w_c , %
3.0	86	30	10	9.5
3.70	183	58	24	10.7
4.30	174	70	23	12.2

The value of s_u was further evaluated from the SPT field value, N_{field} . Several correlations between the SPT N value and the s_u were developed by many researches. The correlations available in the literature either relate s_u to the SPT N_{field} value, or to the corrected value of $N_{(60)}$. Two correlations were adopted here for the estimation of s_u and will be utilized to provide the profile of s_u versus depth to cover the gap in the results obtained from the UU triaxial tests. The first one is the formula proposed by Terzaghi et al. (1996), which is given by:

$$s_u = 6.25 N_{(60)} \quad (3.1)$$

The corrected value, $N_{(60)}$, is related to SPT field values (N) through the equation (Sivrikaya and Toğrol, 2006):

$$N_{(60)} = (C_B C_E C_R C_S) N_{\text{field}} \quad (3.2)$$

Where: N_{field} is the field SPT value; C_B is the borehole diameter correction factor =1.05 (for borehole diameter of 150mm); C_E is the energy correction factor, $(ER/60) = 0.92$ for automatic hammer; C_R is the rod length correction factor = 0.85 for rod length 4 to 6m, and 0.7 for depth less than 4.0m; and C_S is the sampler type correction factor, standard sampler without liner =1.2.

No correction for the effective overburden pressure is needed, as fine grained soils during penetration are undrained as recommended by Sivrikaya and Toğrol, (2006). Introducing these values into Eq. 3.2 then substituting into Eq. 3.1 yields:

$$s_u = a_c N_{\text{field}} \quad (3.3)$$

Where: $a_c = 5$ (for depth less than 4m) and, $= 6.13$ (for depth greater than 4m).

The second correlation considered here is that proposed by Kulhawy and Mayne (1990).

This formula is base on correlating the N_{field} value to the s_u , such that:

$$s_u = 6 N_{\text{field}} \quad (3.4)$$

Figure 3.18 illustrates the s_u profile determined from Eqs. 3.3 and 3.4 as well as the results of the three samples tested in the triaxial cell. The two methods give similar value for depths bigger than 4m. At shallow depths, the effect of the correction factor employed in Eq. 3.1 is obvious, as Eq. 3.3 always gives lower s_u values. Hence, the values obtained from Eq. 3.4 will be excluded from further discussion and implementation. It should be mentioned that the s_u of the soil deeper than 5.7m was not calculated, as the soils at that depth is mainly sand and its shear strength parameter will be evaluated by angle of internal friction.

Based on the values of the s_u illustrated in Fig. 3.18, the silty clay layer can be divided into four sub layers, each of which has its average s_u . Table 3.4 provides the best estimated s_u computed for each suggested sub layer.

The soil below 5.7m is mainly sand with occasionally traces of silt. The shear strength of such soil is represented by its angle of internal friction, ϕ' . Many theories and correlations have been developed to relate the SPT N_{field} values with both ϕ' and the relative density of the sand D_r . Peck et al. (1974) and Terzaghi et al. (1996) give an empirical correlation in graphic format between the corrected SPT N value, $(N_1)_{60}$, and the effective friction angle for both, fine and coarse grained sands.

Table 3. 4. Undrained shear strength values for the cohesive deposit

Depth m	Type	s_u (average over the depth) kPa		Consistency ¹
		BH-1	BH-2	
0 to 1	Silty clay to clayey silt	-*	105	Stiff
1 to 2	Silty clay to clayey silt	180	120	Stiff to very stiff
2 to 3	Clay silt to silty clay	120	63**	Stiff to very stiff
3 to 5.7	Silty clay to clayey silt	155	180***	very stiff

¹ Based on classification of Terzaghi et al. (1996),

* The layer at that depth in this location is brown silt with sand and gravel

** Average values include triaxial test values,

*** Average values depend on triaxial values only

Wolf (1989) represented the same correlation, i.e:

$$\phi = 27.1 + 0.3 (N_1)_{60} - 0.0054 (N_1)_{60}^2 \quad (3.5)$$

Where: $(N_1)_{60}$ is the SPT N value corrected for the energy-equipment factors and the overburden pressure. The $(N_1)_{60}$ is related to the $(N)_{60}$ through:

$$(N_1)_{60} = (N)_{60} C_N \quad (3.6)$$

Where: C_N is overburden correction factor, calculated as: (CFM 2006)

$$C_N = 0.77 \log_{10} \frac{1920}{\sigma'_v} \quad (3.7)$$

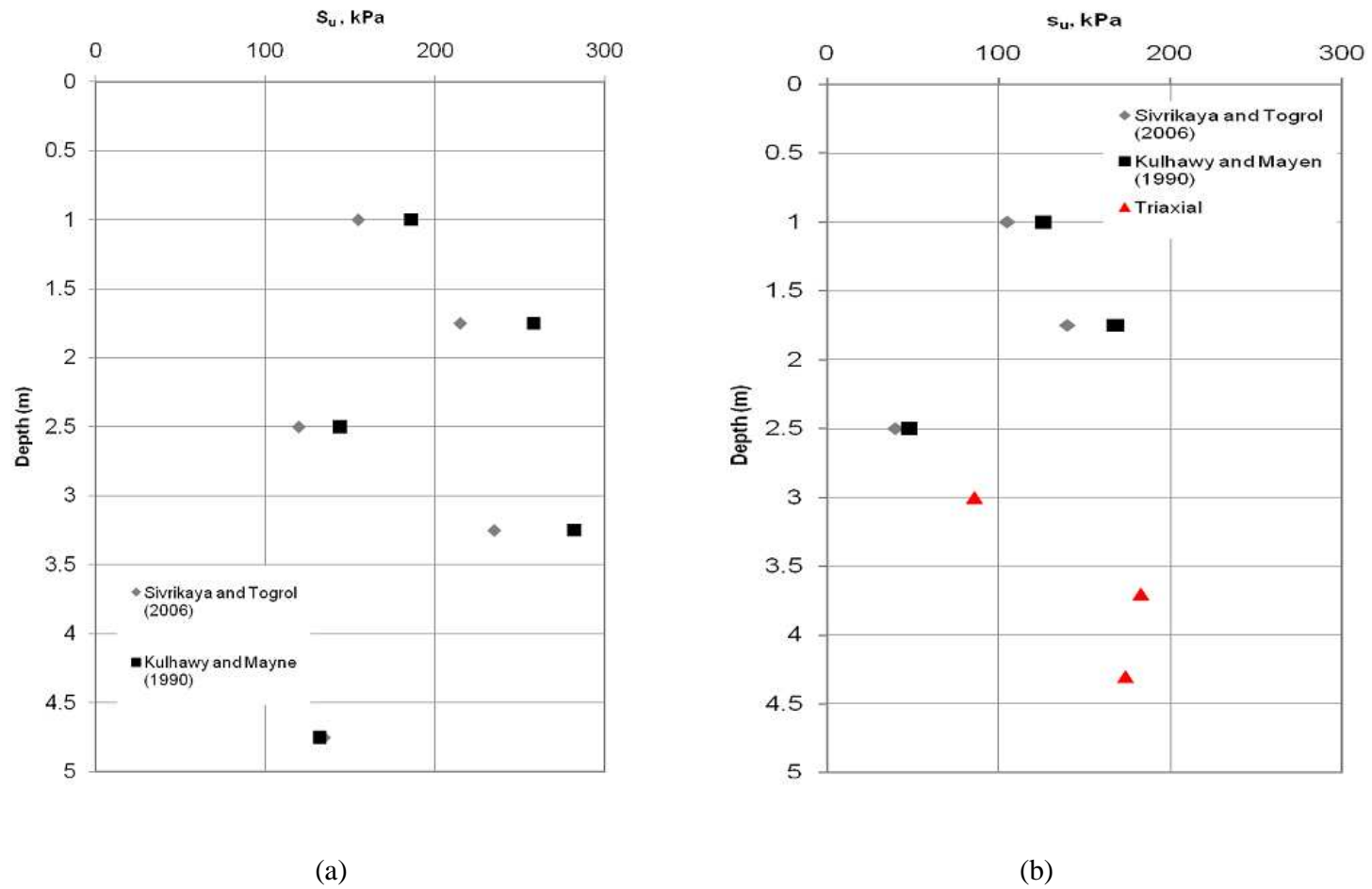


Figure 3. 18. s_u profile versus depth; (a) BH-1; and (b) BH-2

Where: σ'_v is the effective overburden pressure at the level of N_{field} -value in kPa

The length factor, C_R for depth greater than 5.7 m should be 0.95 (CFM 2006). Anderson et al. (2003) approximated the graph given by Terzaghi et al. (1996) into a logarithmic equation to estimate ϕ' :

$$\phi' = 53.881 - 27.6034e^{-0.0147(N_1)_{60}} \quad (3.8)$$

The values of ϕ' estimated from the two aforementioned methods are presented and compared in Tables 3.5 and 3.6, for the two boreholes, BH-1 and BH-2, respectively. The two methods provided almost the same values. The results show that the angle of internal friction increases with depth for the sand layer until depth of 7.9m., but decreases between depth of 7.9m and 9 m. This may be attributed to the existence of a layer of grey compact silt at 7.9m, especially at BH-1.

The consistency of the sand soil is defined by its relative density, D_r . Mayne et al. (2002) correlated D_r directly with the $(N_{60})_1$ from the analyses of more than 100 different points of NC and OC sand, to be:

$$D_r = 100 \left(\frac{(N_1)_{60}}{60} \right)^{0.5} \quad (3.9)$$

The outcome of Eq. 3.9 is presented in Tables 3.7 and 3.8 for BH-1 and BH-2 respectively. The computed D_r of the sand layer is between 76% and 86 % which implies dense to very dense sand, while that of the compact grey silt layer is between 56% and 61%. The silt layer can be considered as soil with medium to dense consistency.

Table 3. 5. Computed angle of friction from SPT values for BH-1

Depth, m	N_{field}	$(N)_{60}$	$(N_1)_{60}$	$\phi' ^\circ$ (Wolf 1990)	$\phi' ^\circ$ (Anderson et al. 2003)
7.1	32	35	35	37	37
7.9	21	23	22	33	34
8.6	18	20	19	32	33

Table 3. 6. Computed angle of friction from SPT values for BH-2

Depth, m	N_{field}	$(N)_{60}$	$(N_1)_{60}$	$\phi' ^\circ$ (Wolf 1990)	$\phi' ^\circ$ (Anderson et al. 2003)
6.3	30	33	34	36	37
7.1	36	40	39	38	38
7.9	42	46	45	39	40
8.6	22	24	23	34	34

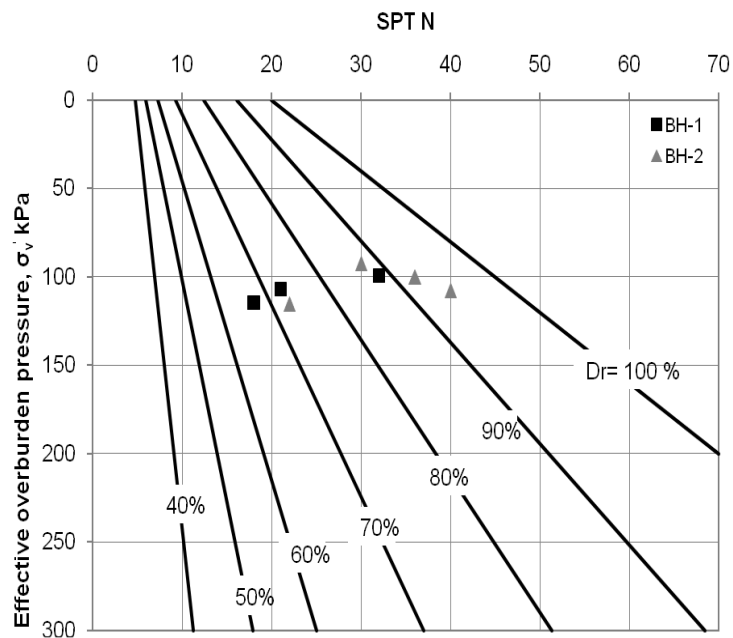
Table 3. 7. Relative density and friction angle for BH-1

Depth, m	$(N_1)_{60}$	D_r	Consistency
7.1	35	76	Dense
7.9	23	61	Medium to dense
8.6	20	56	Medium

Table 3. 8. Relative density and friction angle for BH-2

Depth, m	$(N_1)_{60}$	D_r	Consistency
6.3	33	75	Dense
7.1	40	80	Dense
7.9	46	86	Very Dense
8.6	24	61	Medium to dense

The relative density of sand was further evaluated using the graph given by Holtz and Gibbs (1979). They relate the SPT N value to the relative density considering the effective overburden pressure, σ_v' . According to Holtz and Gibbs (1979), Fig. 3.19 shows that D_r is around 90% while that of the grey compact silt is around 70%. Hence, the sand layer is considered very dense and the compact silt layer is dense.

**Figure 3. 19. Relative density- N_{field} relation based on Holtz and Gibbs (1979)**

3.2.4 Soil stress history

To better understand the soil characteristics, a stress history profile of the soil is required. The stress history of soils is best represented by the overconsolidation ratio (OCR) defined as the ratio between the preconsolidation pressure, σ_p' , and the in-situ-effective vertical stress, σ_v' . The OCR can be evaluated from oedometer tests conducted on undisturbed samples at different normal stress, and computing the σ_p' from the e - $\log\sigma_v'$ chart.

In the absence of the oedometer tests, a first order estimate of the OCR of clayey soil can be obtained from the ratio between the in-situ strength ratio, s_u/σ_{vo}' , and the corresponding ratio for a normally consolidated state, $(s_u/\sigma_{vo}')_{NC}$. Mayne and Kemper (1988) correlated the in-situ s_u/σ_{vo}' to $(s_u/\sigma_{vo}')_{NC}$ on the bases of the concepts of critical state soil mechanics and given that the OCR can be computed from:

$$\text{OCR} = \left(\frac{(s_u/\sigma_{vo}')}{(s_u/\sigma_{vo}')_{NC}} \right)^{(1/\Lambda)} \quad (3.10)$$

Typical values of $(s_u/\sigma_{vo}')_{NC}$ is between 0.2 and 0.3 (Mayne and Kemper 1988) and $\Lambda \approx 0.8$ for low sensitivity clay. Another correlation was suggested by Kulhawy and Mayne (1990) based on the modified Cam Clay model results and the in-situ s_u/σ_{vo}' :

$$\text{OCR} = 2 \left(\frac{(s_u/\sigma_{vo}')}{0.5M} \right)^{(1/\Lambda)} \quad (3.11a)$$

Where:

$$M = \frac{6 \sin \phi'}{3 - \sin \phi'} \quad (3.11b)$$

Employing the value of $(s_u/\sigma_{vo})_{Nc}$ given by Mayne and Kemper (1988), OCR from Eq. 3.10 was calculated. In addition, the angle of internal friction ϕ' of the clay soil was estimated from the chart given by Terzaghi et al. (1996) for fine soils. Figure 3.20 depicts the OCR versus depth computed from the two aforementioned methods. It is observed from the figure that the two methods are in favorable agreement. The soil crust (the top 2 m) has OCR in the range of 35. This indicates that the top soil was exposed to huge desiccation and weathering factors, which resulted in heavy overconsolidation. At depth of 1.75m, the OCR decreases to about 25, while at depth more than 2 m the OCR is between 12 and 7.

Even though, the OCR computed from Eqs. 3.10 and 3.11a is only a first order approximation, it provides a general description of the soil stress history. Meanwhile, the values of OCR shown in Fig. 3.20 can be used to estimate the coefficient of lateral earth pressure at rest, k_o , which is employed to determine the horizontal stress, σ_h' . Mayne and Kulhawy (1982) correlated k_o to OCR via the soil angle of internal friction, ϕ' , such that:

$$k_o = (1 - \sin \phi') \text{OCR}^{\sin \phi'} < k_p \quad (3.12)$$

Where: k_p is the passive coefficient of lateral earth pressure of the soil, or, the limiting in-situ coefficient of earth pressure, evaluated from:

$$k_p = \frac{1 + \sin \phi'}{1 - \sin \phi'} \quad (3.13)$$

The lateral stress for sand can also be calculated using Eq. 3.12. However, the OCR for cohesionless soil is controversial. Hence, the coefficient of lateral earth pressure at rest for the sandy soil will be computed employing Eq. 3.12 and substituting for OCR by 1. The k_o values represent the average of values obtained from BH-1 and BH-2 are given in Table 3.9.

Table 3.9. Average values of k_o

Depth, m	Type	k_o
0 to 1	Silty clay to clayey silt	3.1
1 to 2	Silty clay to clayey silt	3.0
2 to 3	Clay silt to silty clay	1.32
3 to 5.7	Silty clay to clayey silt	1.6
5.7 to 7.9	Sand	0.8
7.9 to 9.0	Silt	0.5

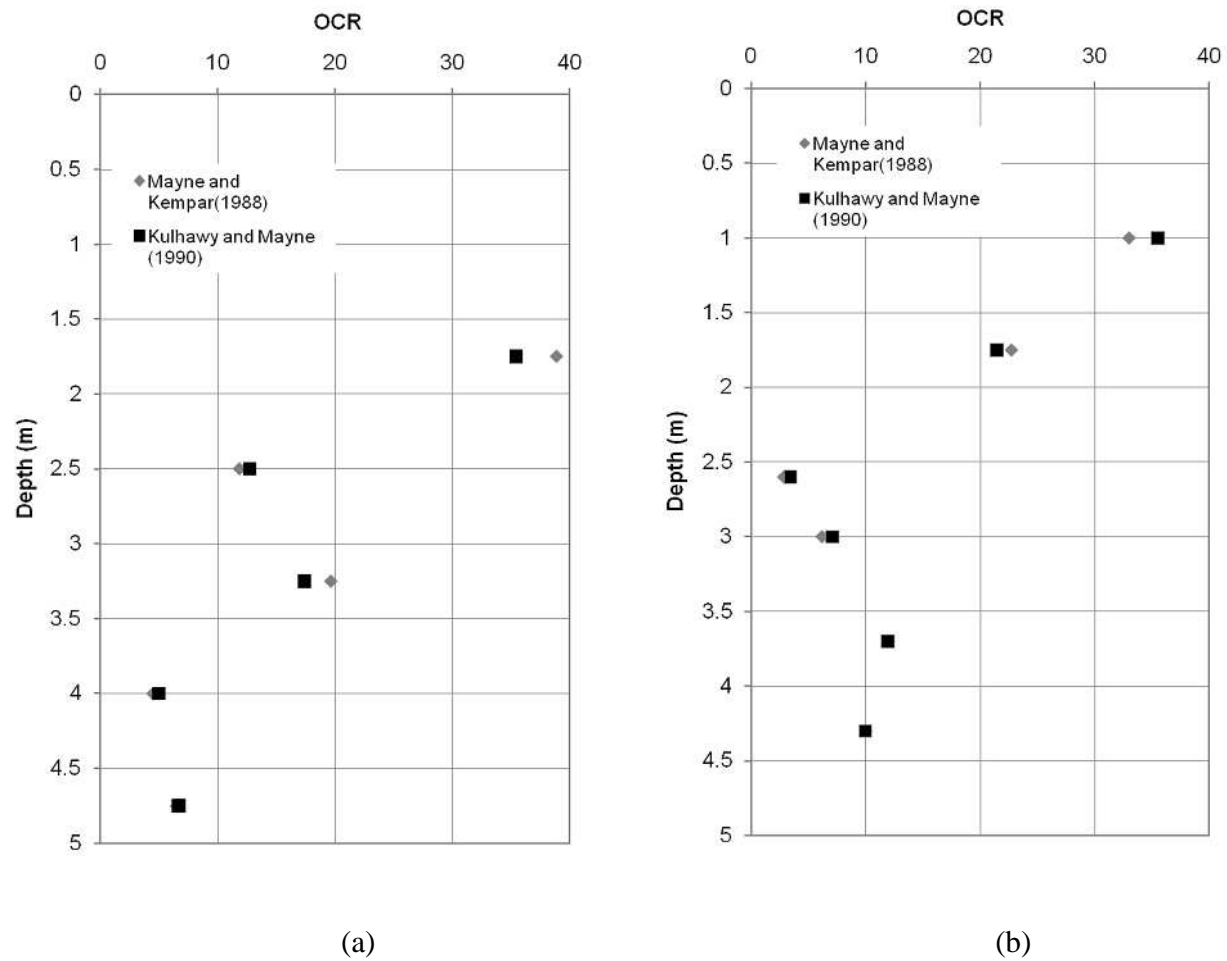


Figure 3. 20. OCR profile for (a) BH-1; and (b) BH

3.2.5 Soil stiffness parameter

The stiffness of cohesive soils under undrained conditions is usually represented by its undrained tangential modulus, E_{ui} , and undrained Poisson's ratio, ν_u . On the other hand, the stiffness of cohesionless soils is represented by its drained tangential modulus, E_{di} , and Poisson's ratio, ν_d . However, the stress-strain behavior of soil is highly nonlinear with very limited initial linear elastic behavior observed at small strains. This non-linearity is represented by a degradation in the tangential modulus with either strain or stress levels. Considering stiffness degradation, the secant modulus, E_s , represents the deformation behavior of soil at specific stress (strain) level.

The triaxial test results presented in Figs. 3.14 to 3.16 demonstrate stiffness degradation as stress level increased. At initial stress level, the ratio between tangential undrained modulus and the undrained shear strength of the soil, E_{ui}/s_u , is in the range of 350 to 400. As the stress level increases to 50% of deviatoric stress, the ratio E_u/s_u decreases to the range of 115 to 130.

For cohesive soils, Bowles (1997) presented ranges for the ratio E_u/S_u based on laboratory and in-situ tests, with a best estimate of:

$$E_u = 500 s_u \quad (3.14)$$

Bowles (1997) stated that values of E_u obtained from the triaxial tests were lower by about a factor of 2 than what it should be. Furthermore, he did not explicitly state whether Eq. 3.14 provides the tangential or secant stiffness values. However, when comparing the

E_{ui}/s_u values computed from the three triaxial tests with Eq. 3.14, it can be inferred that Eq. 3.14 is most likely evaluates the tangential modulus.

For cohesionless soils, several empirical correlations are available to estimate the Young's modulus as a function of SPT values. For example, Bowles (1997) correlates E_s to N_{60} and OCR, in the form of:

$$E_s = 500 (N_{60} + 15) (\text{OCR})^{0.5} \quad (\text{kPa}) \quad (3.15)$$

Also, Kulhawy and Mayne (1990) propose:

$$E_s = 1500N_{60} \quad (\text{kPa}) \quad (3.16)$$

Figure 3.21 depicts the Young's modulus calculated from Eq. 3.14 (for the upper cohesive soil) and Eqs. 3.15 and 3.16 (for the lower sandy soils). Figure 3.21 shows that Eq. 3.15 gives higher modulus than Eq. 3.16.

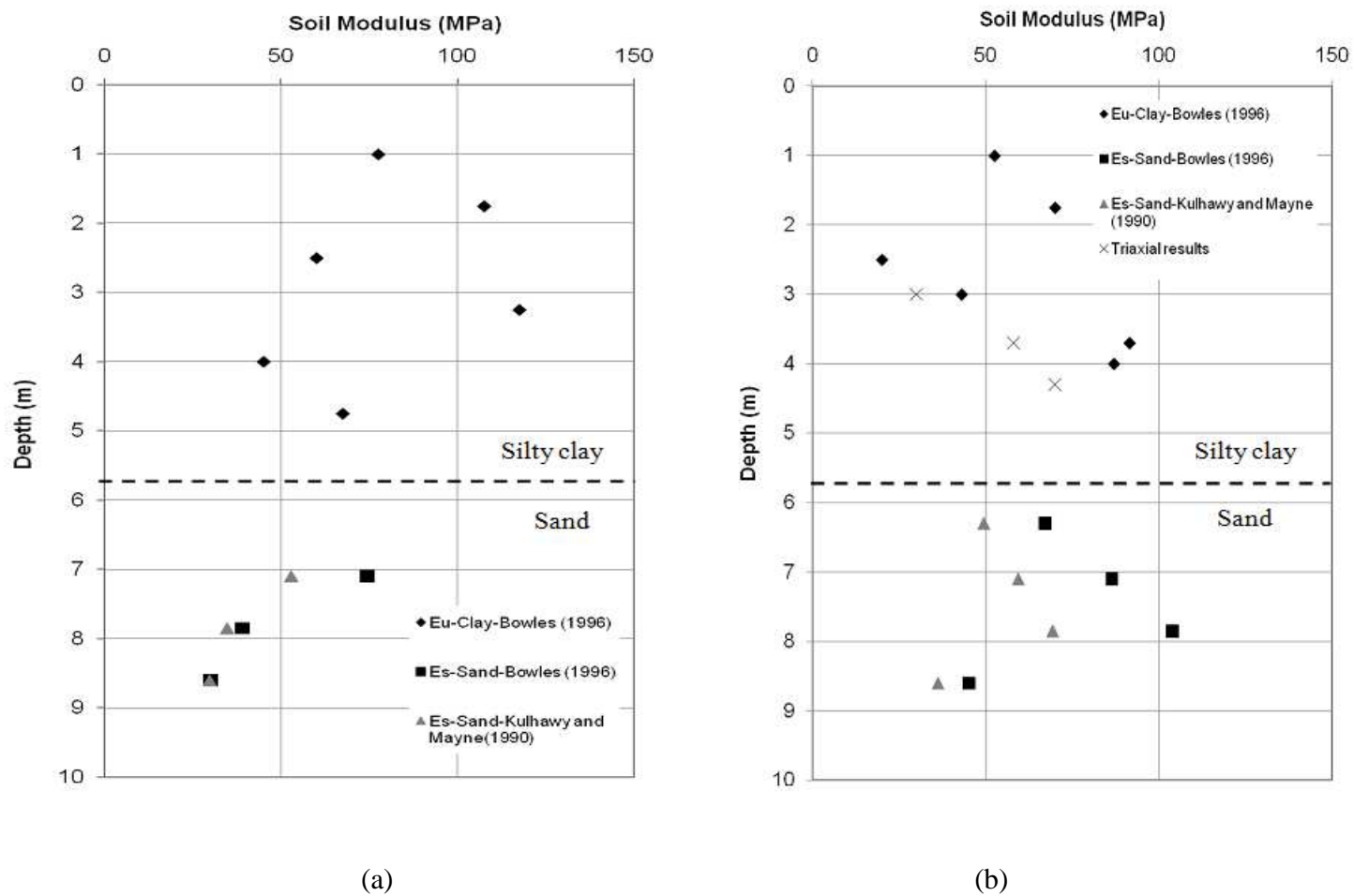


Figure 3.21. Soil modulus versus depth; (a) BH-1, and (b) BH-2

3.3 Grout Testing and Evaluation

The hollow bar micropile consists of a central hollow steel bar encapsulated in a grout body. The steel bar is connected to the superstructure to transfer the load to the surrounding soil through the grout body. Hence, the grout plays a very important role in the load transfer mechanism that governs the behavior of the micropile. In hollow core micropile construction, the grout may also be used as a flushing fluid. The performance of hollow core micropiles is highly influenced by the performance of its grout.

The grout used during installation of micropiles in this study is Masterflow® grout supplied by BASF. Masterflow® 1341 is a cement-based product with specially graded spherical aggregate that produces a pumpable non-bleeding high-strength grout. It has extended working time, especially in vertical duct placements or configurations with a steep vertical rise without settlement shrinkage. Masterflow® 1341 meets all compressive strength and vertical height change requirements at a modified flow and complies with the PTI (2004) specification for grouting of post tensioned structures with vertical rises of 1.8 – 30 m or slightly more.

To evaluate the grout behavior during micropile load tests, compression and splitting tensile strength tests were conducted prior to the micropile field testing. The tests were conducted on cylindrical samples (150x75 mm) at ages 7 and 28 days. All samples were tested using an AVERY 7112 CCG Model compression testing machine.

Twenty four 150 x 75 mm cylinders were prepared using the Masterflow® 1341 grout product data sheet. Twelve samples were prepared in the lab prior to micropile installation, while the other samples were prepared in-site from the grout used during

installation of the micropiles. All samples had water/cement (w/c) ratio of 0.32. The samples were cured in the moisture room. Six samples from each group were tested to obtain their splitting tensile strength (3 samples tested after 7 days and 3 tested after 28 days). The other six samples were capped and tested under compression (3 samples tested after 7 days and 3 tested after 28 days). Table 3.10 summarizes the average results of the compressive and tensile testing strength conducted on all the samples after 7 and 28 days.

Table 3. 10. Summary of grout strength

	Compressive Strength, f_c MPa	Tensile Strength, f_t MPa
7 days	18.6	3.0
28 days	30.0	4.2

CHAPTER 4

HOLLOW CORE MICROPILE MATERIAL AND INSTALLATION

This chapter provides the description of the components of the hollow bar micropile system. It also discusses the preparation and procedure for the micropiles installation, as well as the instrumentation used for collecting the test data.

4.1 Hollow Core Steel Bar and Accessories

The hollow core bar micropile consists of three main parts: threaded hollow core bar, a sacrificial bit, and coupler to connect the hollow bar segments to reach the desired depth in ground. There are three hollow core bar types available on the market: the CTS/TITAN IBO manufactured by Ischback, the DYWI[®] drill hollow bars manufactured by Dywidag-System International, and Geo-Drilled Injection Anchor manufactured by Williams. In this study, the tested hollow bar micropiles employed Geo-drilled injection anchors manufactured and supplied by Williams Form Hardware & Rock bolt Ltd. Figure 4.1 illustrates the hollow core bar parts.

The hollow core bars are available in various diameters. The bar name is defined by its outer diameter or by its outer and inner diameters. Table 4.1 gives the available Williams Geo-Drill bars and the properties of each bar. Williams Geo-Drill injection bar offers an excellent choice for micropiles in difficult ground conditions. The continuously threaded bar profile lends itself perfectly for restricted headroom applications because the bar can be cut and coupled at any length. The FHWA had approved hollow bar anchors for permanent use in micropile applications.

The hollow bar is manufactured from high strength-impact resistant heavy wall steel tubing conforming to ASTM A519. The bar is continuously threaded over its entire length with a heavy duty left hand thread/deformation pattern. The steel tubing provides maximum flow with minimum resistance during high pressure flushing and grouting operations. The threaded form of the Geo-Drill anchor (similar for all diameters) is a unique Williams feature that provides a lower thread pitch angle to provide easier coupling disengagement without locking up.

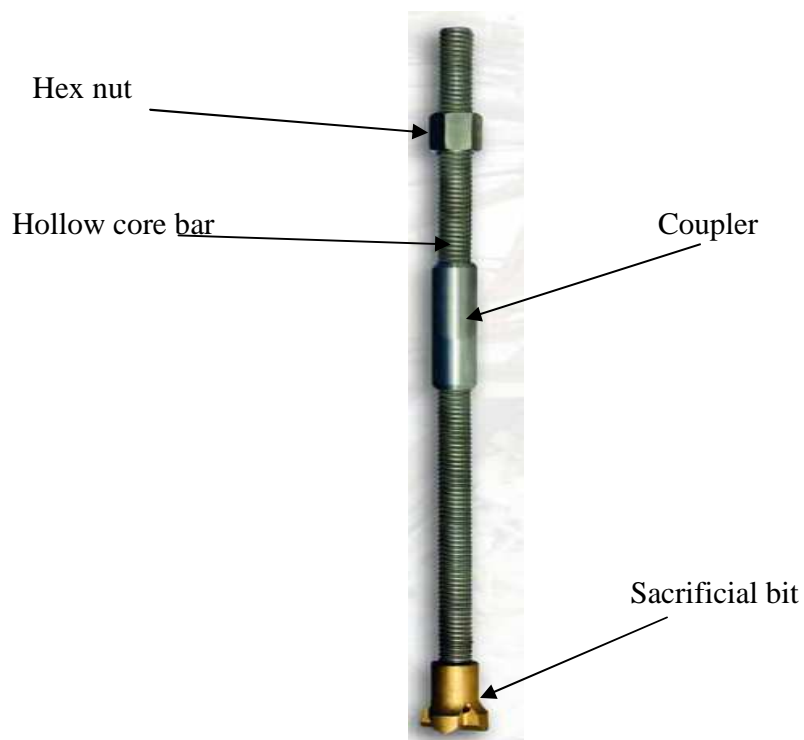


Figure 4. 1. Hollow core bar micropile parts (after Ground Anchor System 2011).

Table 4. 1. B7X Geo-drill bars (Ground Anchor System 2011)

Part number	Bar diameter mm	Minimum net area through the threads mm²	Minimum ultimate strength kN	Minimum yield strength kN	Nominal weight Kg/m	Average inner diameter mm
B7X1-32	32	359	260	210	3.1	20.0
B7X1-32X	32X	501	363	294	4.0	15.9
B7X1-38	38	688	498	404	5.6	21.1
B7X1-51	51	1158	837	677	9.3	30.1
B7X1-76	76	2503	1811	1466	20.5	48.0

This thread form is better than the conventional rope threads commonly used in drilling operations. In addition, this unique thread provides more surface area and thread/deformations per unit length; thus might be linked to superior bond capabilities. Moreover, the lower thread angle allows the installed anchor to be torque-tensioned for fast tie back installations. Installation adapters for the Geo-Drill Injection Anchors are available for all drill rigs. (Williams Form- Ground Anchor System, 2011).

The Geo-drilled bars are supplied in 3m length. Typically, the hollow core micropile is longer than 3 m, therefore, Geo-Drill injection anchor couplings (as shown in Fig 4.2) are usually used to connect the 3m segments to reach the desired depth. The couplings have a unique tapered center stop, which seals the hollow bar connection to prevent grout leakage during simultaneous grouting and drilling operations.

The internal stop design also assures a full positive thread connection in both injection bar ends while providing a matching end bearing between bars that reduce percussion energy loss to the drill bit. The couplings are machined from ASTM A29 grade C1045 high strength steel to provide 100% ultimate tensile or compression strength capacity of the installed anchorage. The coupling OD is tapered on both ends to allow drill cuttings and grout displacement during drilling while the ID has internal chamfers to assist alignment and connection of the bars as given in Fig. 4.2.



Figure 4. 2. B7X2-76 coupler

An important part of the hollow bar system is the sacrificial bit, also called “lost bit”. It offers the hollow core micropile system two unique advantages: the hollow bar micropile can be installed in virtually any type of soil using the appropriate drilling bit; the micropiles can be simultaneously installed and grouted, without the need to stop the grouting process and withdraw the drilling steel. The second advantage increases the production rate of the micropiles and, thus, decreases the overall cost of the project.

Table 4.2 presents some of the available drilling bits in the market nowadays. As given in Table 4.2, each bit type is applicable to specific soil type. However, not all drilling bit types can fit any bar size.

Table 4. 2. Types of lost bits and the applicable type of soil for each one (Ground Anchor System 2011)






	<p style="text-align: center;">HC Drill Bit</p> <p style="text-align: center;">Hardened cross cut drill bit, suitable for the majority of applications including narrow bands of soft rock. Soil Types: Fills, Shales, and Gravels</p>
	<p style="text-align: center;">HB Drill Bit</p> <p style="text-align: center;">Hardened hemispherical button profile drill bit suitable for gravels and medium strength rock. Rock Types: Soft to Medium Rock</p>
	<p style="text-align: center;">CC Drill Bit</p> <p style="text-align: center;">Tungsten carbide cross-cut drill bit. Excellent choice for majority of granular soils with mixed hard formations. Soil Types: Fills, Gravels, and seamy rock formations.</p>
	<p style="text-align: center;">CB Drill Bit</p> <p style="text-align: center;">Tungsten carbide hemispherical button drill bit for moderately strong to strong rock, boulders and rubble. Rock Types: Mudstone, Limestone, and Granite</p>
	<p style="text-align: center;">SC Drill Bit</p> <p style="text-align: center;">Two stage cross cut drill bit, suitable for loose ground and fills. Soil Types: Sand, Clay and Medium Dense Gravels</p>

Table 4.3 summarizes the available bit diameters with its corresponding applicable hollow bar diameter. Practically, the ratio of the drilling bit to the bar diameter is in the range of 1:1 to 2.5:1. Due to the high demand on using larger drilling bits, Williams Form Hardware developed three new large bits as part of this research program. Figure 4.3 depicts the three new developed drilling bits, two of them are 176mm in diameter and the third is 225mm in diameter. They were manufactured to fit B7X1-76 hollow bar.

During installation, the hollow bar can be centred in the drill hole on 3m centers by attaching a steel centralizer in front of the coupling. The centralizer is available in plain or hot dip galvanized steel. Figure 4.4 shows the hot dip galvanized centralizer.

Table 4. 3. Types and the available drill bit diameters

Nominal bar diameter mm	Available drill bit diameters mm				
	HC	CC	HB	CB	SC
32	51 , 65 , 76 , 100	51 , 65 , 76 , 100	51	51	127
38	51 , 65 , 76 , 100	51 , 65 , 76 , 100	76	76	150
51	N/A	76 , 90 , 100	100	100	150
76	N/A	150 , 176	N/A	N/A	175

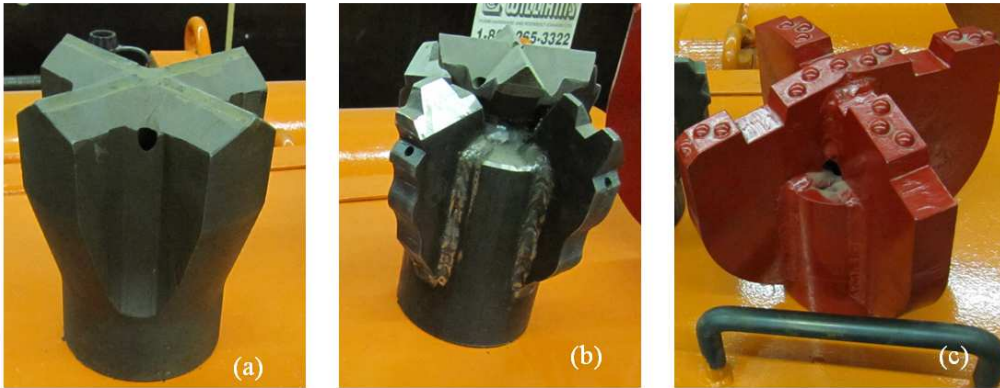


Figure 4. 3. Three new large bits; (a) Tungsten carbide cross bit (d= 176mm); (b) Double cross bit (d = 176 mm), and (c) Carbide button cross drill bit (d= 225 mm)



Figure 4. 4. Hot dip galvanized centralizer (after Ground Anchor System 2011)

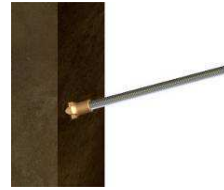
The hollow bar micropile is connected to the pile cap usually by bearing plates to satisfy the fixity conditions suggested by the designer engineer. Depending on the application, the bearing plate holes can be round, for standard embedment applications, or slotted for angled injection bars installed through steel walers or in contact with a rock slope. These plates should be designed properly to transfer the structural load to the micropile. Any

failure in the connection between the bearing plates and the pile cap will cause failure in the whole cap-micropile-soil system.

4.2 Hollow Bar Micropile Installation

The hollow bar system is particularly suitable for soils that do not allow for open-hole drilling (i.e. granular soils that are collapsible in nature). In such cases, drilling with a grout fluid serves the purpose of flushing spoils from the borehole and prevents looser surrounding material from collapsing due to the higher relative density of the grout. The hollow bar injection system is suitable for projects requiring fast production that would otherwise need to involve a casing system in order to maintain borehole stability. It can also be used successfully in self supported soils, employing any flushing fluid. In all cases, the behavior and performance of hollow bar micropiles are influenced by the installation technique and procedure employed. The typical steps of installing hollow bar micropile is demonstrated in Fig. 4.5.

In this study, four hollow core micropiles were installed and load tested. The installation of the hollow core micropiles is performed in one step containing flushing the soil debris during installing the hollow core bar, and grouting the micropiles. The installed hollow bar micropiles consisted of 6m Geo-drilled injection anchor, B7X1-76. The Geo-drilled injection bar used had an outer diameter of 76mm, and an inner diameter of 48mm. The all-thread bar employed had a specified yield stress of approximately 580 MPa and a cross-sectional area of 2503 mm² between the threads of the bar (Table 4.1).



- (1) The hollow bar set into position for installation



- (2) Installation begins with rotary percussive drilling and grout, water or air is used for flushing.



- (3) Once the first 3m section is installed, drilling stops long enough to add the second section.



- (4) Raise the hollow bar high enough to get visible evidence of flush return from the mouth of the borehole and begin drilling again in a normal fashion.



- (1) Add sections in the manner noted in step four until micropile reaches final depth. Completely flush all drilling grout and debris with competent grout

Figure 4. 5. Installation process of hollow core micropile (after Ground Anchor System 2011)

The hollow core bar was supplied in 3m lengths (Fig. 4.6) and coupled together with 251 mm long B7X2-76 geo-drilled anchor coupler, Fig.4.2, to reach the desired length. Generally, the system is installed with rotary percussive drilling as this method offers good directional stability and high rates of production and continuous grouting. Suppliers and contractors recommend mixing the grout in a colloidal (shear type) mixer, so once pumped, the fine grout particles are fully able to disperse into the small voids of the surrounding soil.

This well mixed grout exits the side ports of the drill bit under pressure to flush and remove the softer parts of the soil while penetrating into the firmer material for increased bond capacity. It is recommended to partially withdrawing each fully drilled section up the drill mast prior to attaching new sections, this way the drilling can begin in a plunging type action to even further improve grout penetration. Utilizing proper drilling and grouting techniques is important as the system would generally fail between the soil/grout interface, rather than the grout/bar interface.

Drilling should be slow enough to ensure rotation through the soil as opposed to excessive percussion and feed pressure with limited rotation. Such practice will provide the formation of a true borehole with consistent grout cover. Grouting pressure should be sufficient to maintain circulation at all times with a small amount of grout return visible at the mouth of the borehole. Normal drilling rotation is in the range of 40 and 100 RPM.



Figure 4. 6. B7X1-76 Geo-drilled hollow core bars

4.2.1 Preparing the drilling rig

The hollow core bar micropiles were installed using an excavator mounted TE 550 Hydraulic Drifter, as show in Fig. 4.7. The head of the rig must be prepared prior to installing the hollow bar micropiles utilizing the appropriate parts to allow flushing and grouting simultaneously. Figure 4.8 summarizes the entire parts and connections at the top of the drifter for the installation process. The drifter containing the hammer is connected to a grout swivel system to allow for simultaneous installation and grouting. The grout-swivel consists of a grout body and grout shank. The grout shank fits within the grout body and contains grout inlet ports. One end of the shank attaches to the striker bar while the other end attaches to the hollow bar anchor.

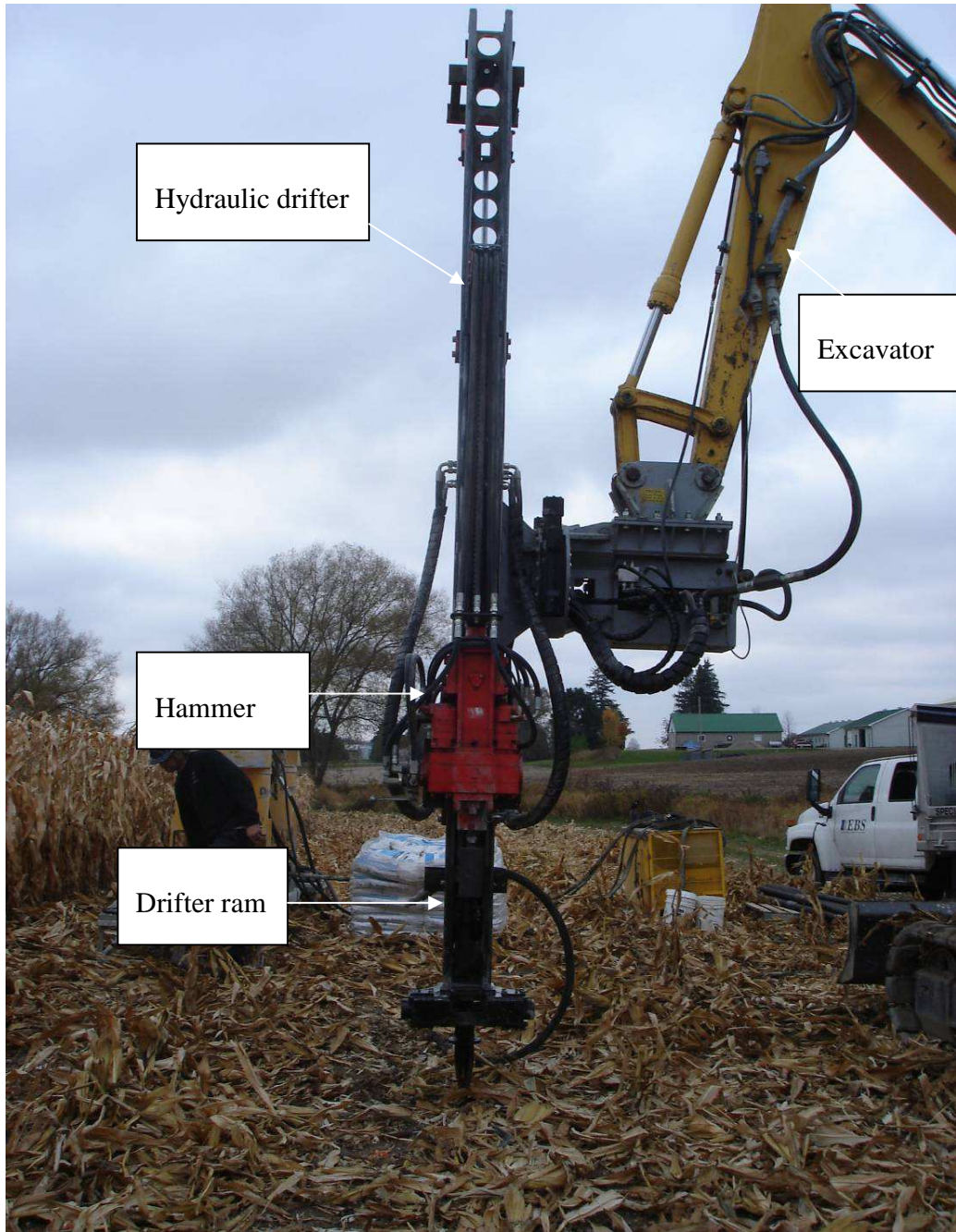


Figure 4. 7. TE 550 hydraulic drifter mounted on an excavator

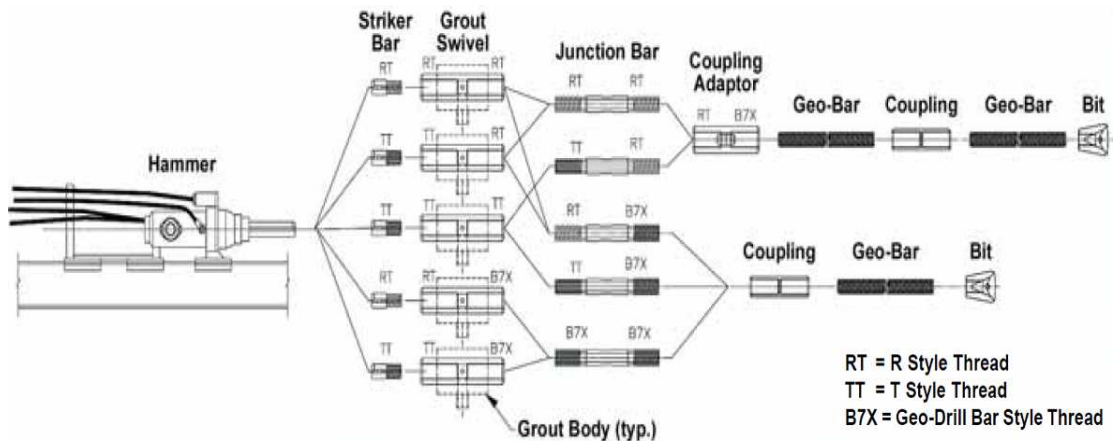


Figure 4. 8. All possible connections between the drafter hammer and the hollow bar (after Ground Anchor System 2011)

The grout body contains an inlet pipe to allow grout to enter into the shank and down the hollow bar. The body remains stationary while the shank spins with the rotary action of the drill. To hold the body into position and prevent spinning with the rotary action of the drill, it is necessary to attach a locator frame from the body to the drifter. Caution should be applied that only water or grout flush be used with the grout-swivel system. In all cases, grease should be applied to the grout-swivel system prior to use.

A junction bar is used between the grout swivel and the adaptor to transition between the grout shank and the hollow bar. Coming out the bar end of the junction bar would either be a Geo-Drill coupling or coupling adaptor. All disengagement during drilling to add sections or move to another anchor location would be done from below the junction bar and not at the grout shank, thus prolonging the life of the grout swivel. Finally, a coupling adaptor, which is usually located just below the drill hammer, is used to connect the striker bar to the hollow bar. The coupling adaptor is a machined and case hardened adapter. Sizes are available in any striker bar thread type to connect to any Geo-Drill Bar

size. Generally a coupling adapter would be used in place of a grout-swivel during an air flush installation.

During drilling, the air-flush technique was used to undercut the soils and flush the drill cutting to the ground. Hence, the grout swivel was used without a grout body and connected directly to the coupling adapter through the junction bar. The final arrangement at the top of the drifter is show in Fig. 4.9.



Figure 4. 9. Final connections at the top of the drifter

4.2.2 Installation and grouting

Air flushing was employed in order to examine its ability to advance the hollow core bar down hole with the same efficiency as grout flushing and without any losses in the grout

material. The cohesive nature of the deposit helps in successful use of this technique because a hole in silty clay soils can stand, at least for a short period, without support.

The installation started by threading the sacrificial bit onto the hollow bar from the bottom. Upon clapping the first segment of the hollow bar to the adaptor at the top of the drifter, water was pressurized before the start of digging into the ground. This step was crucial to ensure that no leaking in the system or in the connections at the top of the drifter was present. Figure 4.10 depicts the running of the water out of the bit holes, before hitting the ground.

During installation of the first micropile, the double cross drilling bit (Fig. 4.3 b), was employed. The drilling was successful for the first 3m segment. After connecting the second segment, a hard knocking was heard. The hollow bar was withdrawn and the bit was found broken, Fig. 4.11. It seems that there was some large cobble that was too hard for this bit type.

The suppliers recommended replacing the double cross bit with carbide cross bit (Fig 4.3 a). The new drilling bit was designed to overcome the large cobbles found in the ground. This drilling was completed successfully using the new bit design. The aforementioned field case highlighted the benefits of the lost bit, and the importance to employ the appropriate type.

During air flushing, the hydraulic drifter connected to the hollow bar was connected to an XAS 375 JD6 portable air compressor, shown in Fig, 4.12, through the swivel at the top of the drilling rig.



Figure 4. 10. Water delivered out of the drilling bit.



Figure 4. 11. The broken double cross bit.

The air was delivered at pressure around 0.9 MPa to advance the hollow core bar downward and flush the debris out from the top of the hole. After reaching the desired depth, the swivel at the top of the drifter was changed and connected to the colloidal mixer grout plant, presented in Fig. 4.13, to start grouting the micropiles.

The micropile installation was completed without the need to withdraw either a temporary casing or a drilling string. Only changing the swivel at the top of the machine is required. The bar was grouted continuously to fill the annulus between the hollow core bar and the surrounding soil. The filled grout body had water cement ratio of about 0.32 supplied by the grout plant under pressure of approximately 2 MPa. When the grout flowed at the mouth of the hole, the pump pressurizing the grout was turned off and the hollow bar was unplugged from the drifter.

Following the previous procedure, four micropiles were installed in the same day. The installed hollow bar micropiles were characterized by bond length equal to 5.75m. They were spaced 776mm apart, or at spacing to diameter ratio around 4.4. The micropiles are labeled MP1, MP2, MP3, and MP4, as illustrated in Fig. 4.14. The installed micropiles were left for curing after installation and before field testing for more than 5 weeks.



Figure 4. 12. Type XAS 375 JD6 portable air compressor



Figure 4. 13. Colloidal mixer grout plant



Figure 4. 14. A group of four micropiles

4.3 Embedded Strain Gauges Instrumentation

During installation, each micropile was instrumented by five embedded vibrating wire strain gauges of type EM-5. The strain gauges spaced at 1.5 m along the pile shaft. The properties of the used strain gauge are given in Table 4.4. The embedded strain gauge is composed of two end pieces joined by a tube that protects a length of steel wire. The wire is sealed in the tube by a set of o-rings on each end piece. Both end pieces have a flat circular flange to allow transfer of concrete deformation to the wire. An electromagnet is fitted at the center of the gauge. Strain developing in the concrete modifies the tension in the wire, therefore changing its resonant frequency, which is read by the electromagnet. Figure 4.15 depicts the components of the EM-5 embedded strain gauges.

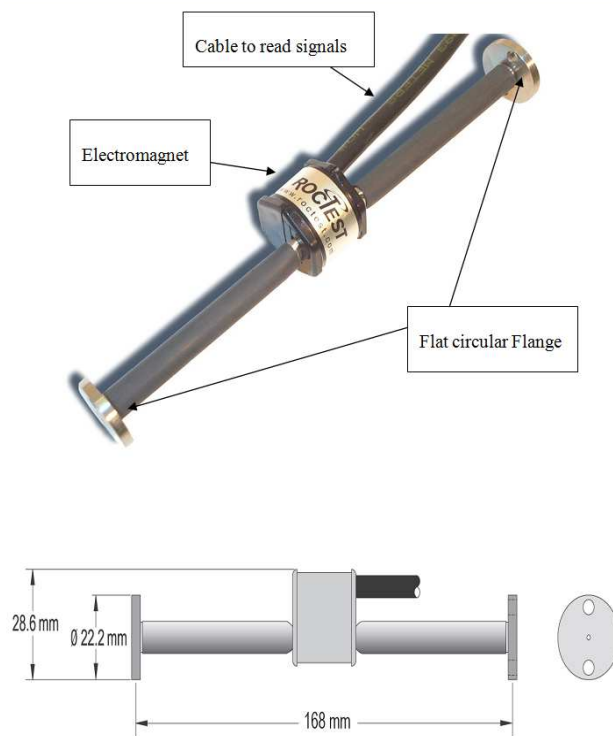
The hollow core steel consists of all-thread bar from outside and smooth steel surface from inside. The best way to embed the strain gauges is inside the hollow bar after

grouting the micropiles. During the planning phase of the experimental program, there was a concern that placing the strain gauges inside the hollow core of the bar may render its ineffective if the grout inside the hollow core separated from the smooth internal wall of the steel bar as the applied loads increase during the load test. Accordingly, the strain gauges were inserted within the grout annulus outside the hollow core bar after grouting was completed. To facilitate inserting the strain gauges in the grout, the strain gauges were attached to 12mm steel bar.

Two readings were recorded for each strain gauge before starting the load test. The first reading was to record the strain in each gauge prior to inserting it in grout. This step was important to assess the effect of installation on the strain gauges and to zero the gauge before the load test started. After installing the micropiles and before starting the load test, the strain gauges were checked using a read out unit. Unfortunately, the lower gauges were damaged during pushing them into the grout and only the top two strain gauges survived. The two gauges that survived were located at the top of the micropile and at depth of 1.5m below the micropile butt.

Table 4. 4. Strain gauge properties

Model	EM-5
Range	3000 $\mu\epsilon$
Resolution	1 $\mu\epsilon$
Operating temperature	-20 to +80
Thermostat	3k Ω
Electrical cable	IRC-41A

**Figure 4. 15. EM-5 strain gauge parts and dimensions**

CHAPTER 5

AXIAL MONOTONIC AND CYCLIC PERFORMANCE OF HOLLOW BAR MICROPILE

5.1 Introduction

Twenty two full scale field load tests were conducted on the four hollow bar micropiles constructed as discussed in Chapter 4. The micropiles were load tested in four consecutive phases. The first phase involved five monotonic axial tests (three compression tests and two uplift tests). In the second phase, five axial cyclic load tests (four compression tests and one uplift test) were conducted. The third and fourth phases involved loading pairs of micropiles: four axial load tests; and six lateral load tests (two monotonic and six cyclic). The results obtained from the load testing program were used to establish, verify and calibrate finite element models for the single and group pile load tests. Upon verification, the models are capable of simulating the behavior of hollow bar micropiles under different load conditions and to establish design guidelines for hollow bar micropiles under different loading conditions.

This chapter documents the monotonic and cyclic load testing results and the analyses conducted on hollow bar micropiles. The load test procedures followed during the monotonic and cyclic field load test are described. The results obtained from the first and second phases are presented and discussed. In addition, the details of the numerical models established are presented and the calibration process is described. A comparison between the field tests and the numerical model results is given and discussed as well.

Finally, a parametric study is carried out in order to investigate and develop a closed form solution for axial loading conditions.

5.2 Axial Monotonic Load Tests

Five monotonic axial load tests were conducted on the four hollow core micropiles. The tests included: three compression load tests and two uplift axial load tests.

5.2.1 Testing equipment

A reaction frame system was used to execute the pile load tests. The reaction frame involved two steel reaction beams, main and secondary, anchored to four helical piles that are used as reaction piers. The main beam was 4.5 m in length and consisted of two channels C380X50 attached back to back with a spacing of 86 mm. The two beams were connected with 300X400X25.4 mm plates at 500 mm intervals and were reinforced by vertical stiffeners made of steel plate 25.4mm thick at the same spacing. Two special plates have been welded at the middle of the beam, one at the top and the other at the bottom, to facilitate supporting the hydraulic jack during uplift tests. Figure 5.1 depicts a workshop drawing for the main loading beam.

The secondary beam was 4.0 m long and consisted of two channels C380X50 attached back to back at a spacing of 51mm. The two channels were held together by means of two channels C310X31 face to face, one at the top and one at the bottom. The webs of the upper and lower channels contain holes to allow connecting the beam to the loading frame. Figure 5.2 illustrates the frame setup in the test location.

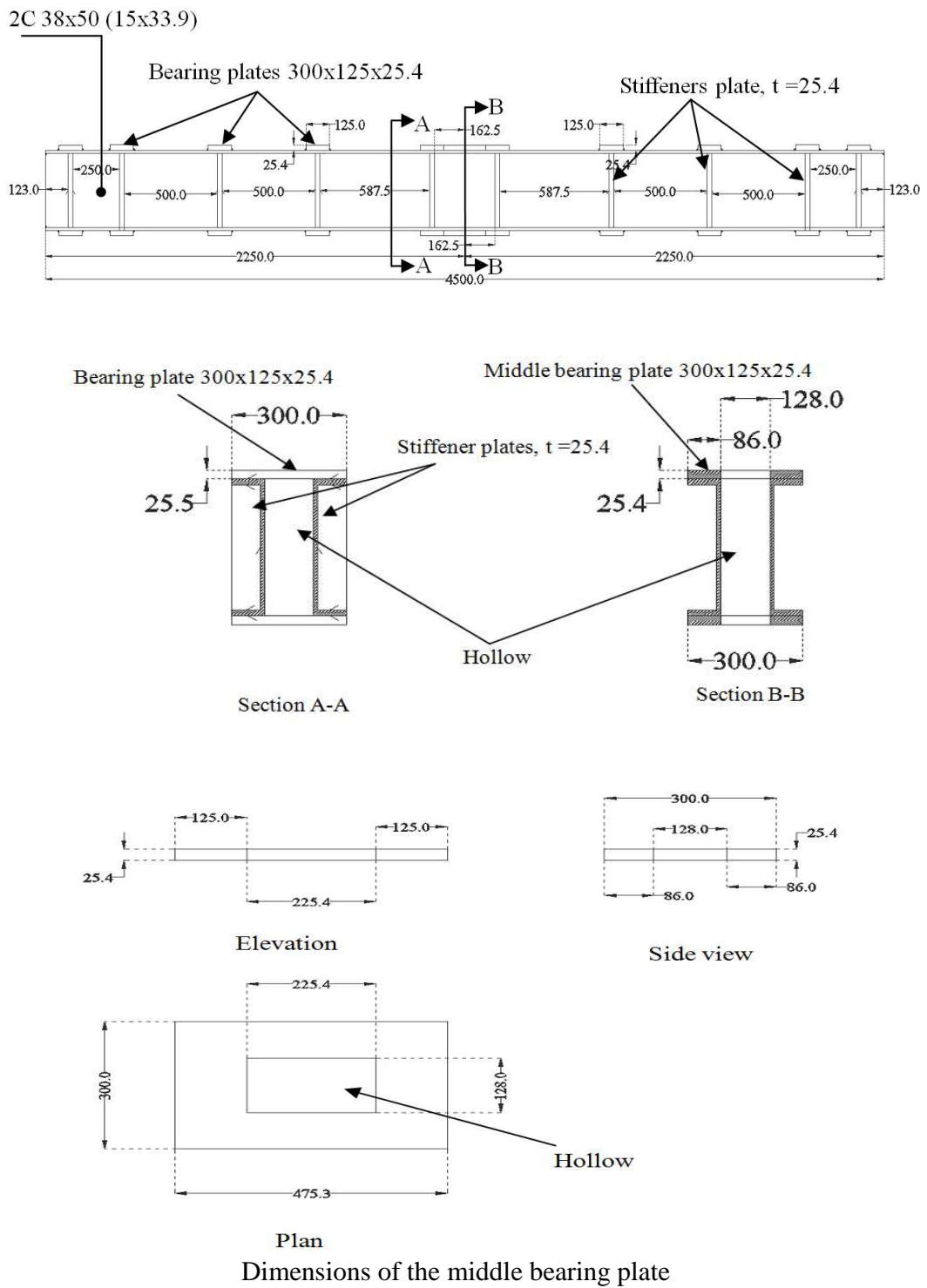


Figure 5. 1. Cross-section and dimensions of main loading beam (dimension are in mm)



Figure 5. 2. Reaction frame used during monotonic and cyclic loading

The helical piles, used as reaction piers, were square shaft Chance SS175 helical foundation system. The pile shaft consisted of one lead section and several extensions. The lead section consisted of a 45 mm round corner square welded to three helical bearing plates, or helices. The helical plates were 9.5 mm thick with plate diameters of 200 mm, 250 mm, and 300 mm. The helical plate diameters increase with distance from the pilot point. Extension segments of 1.5 m and 2.1 m length were added to the lead section during installation to reach the desired bearing soil stratum at 9.0 m below the ground surface (approximately 1.5 times the tested micropiles length).

Figure 5.3 shows the locations of the reaction helical piles with respect to the location of the test micropiles. The anchor piles were located at 2.0m far from the center of the test micropile (i.e. at a distance greater than 10 times the tested micropiles diameter).

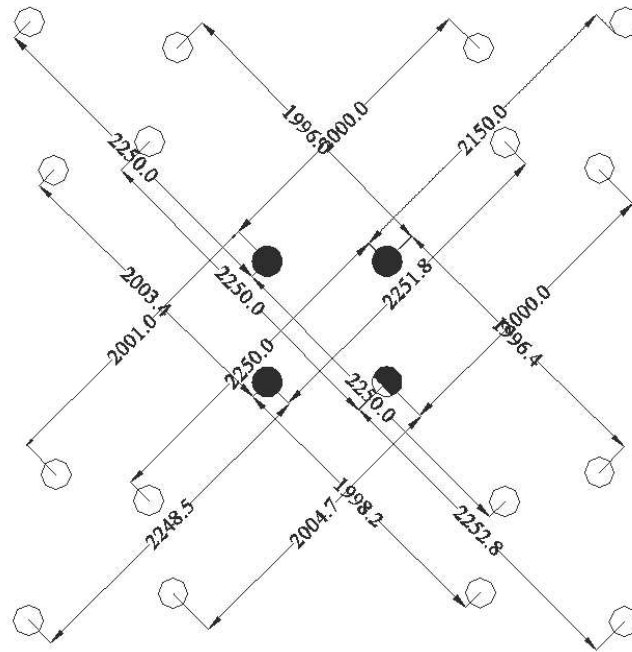


Figure 5. 3. Location of tested and position of reaction piles

5.2.2 Pile head instrumentation

The load was exerted through a hollow cylinder hydraulic jack connected to a hydraulic pump. The jack was located on top of the head and reacting against the reaction frame. The jack has 100 ton advance capacity and 68 ton retract capacity and a maximum stroke of 150 mm. The load was recorded through an interface load cell 1240-AF-200K-B of 890 kN capacity. The load cell was situated on top of a square steel loading plate, with 300 mm sides and 38 mm thickness. The plate has a thread bar socket welded to its top to attach the interface load cell. The loading plate threaded to the head of the hollow core bar from its bottom by mean of circular threaded collar.

The pile head axial displacement was measured through four HLP 190/FS1/100/4K linear displacement transducers (LDTs), mounted on magnetic base. The LDTs magnetic bases were mounted on two reference steel extensions supported independently from the loading system. The LDTs have 100 mm stroke with an accuracy of 0.01 mm. The LDTs were distributed in a square arrangement over the steel loading plate attached to the pile head.

During the axial compressive load tests, other loading plates were provided above the hydraulic jack cylinder to close any gap between the main reaction beam and the hydraulic jack. The loading instruments arrangements during compression tests are shown in Fig.5.4. The same configuration of LDTs and load cell was employed for either compression or uplift test. However, during monotonic uplift load tests, the hydraulic jack was mounted above the loading beam to execute the load against the reaction frame. The jack was connected to the load cell via 89 mm threaded bar. The configuration of the pile head instruments during uplift load testing is given in Fig. 5.5.

The load cell and the LDTs were connected to a data acquisition system to record and store the load and movement at the pile head during the load test. Once the hydraulic jack advanced in each loading increment against the reaction beam, the load was transferred to the pile and measured by the load cell. At the same time, the four LDTs measured the axial displacement of the pile head. The displacement average is considered in the data analysis in an attempt to overcome any inaccuracies in the measurement of any one LDT.

5.2.3 Monotonic load test procedure

The monotonic testing phase started by conducting two compression load tests on micropiles MP1 and MP3 in sequence. This was followed by two uplift tests conducted on MP2 and MP4. A final compression test was conducted on MP2. The quick maintained load test procedure was followed during the monotonic load testing phase. The ASTM D-1143 (2007) standard specifies that during the test, the load should be applied in increments of 5% the anticipated failure load with constant time interval increments. The time interval increment should be between 4 and 15 minutes.



Figure 5. 4. Micropile head instrumentation during compression tests

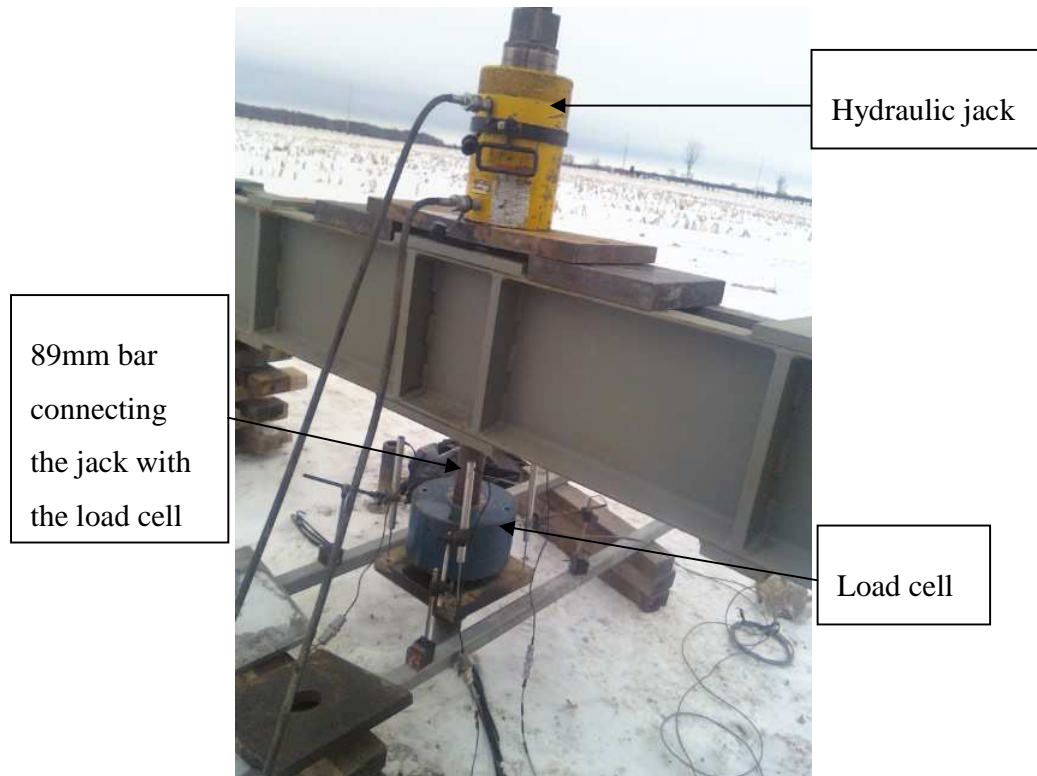


Figure 5. 5. Micropile head instrumentation during tension tests

Smaller increments, longer time intervals, or both can be used. In this study, loads were applied in increments of 5 % of the anticipated failure load and maintained for at least 5 minutes. Generally, the micropiles were tested in compression in accordance with the ASTM D-1143 (2007) quick maintained load test procedure. The uplift load tests were accomplished in accordance to ASTM D-3689 (2007) quick maintained load test procedure.

Due to the relatively close spacing between the piles (spacing to diameter ratio, $S/d = 4.4$), and because of the cohesive nature of the soil deposits, a long testing schedule was adopted. The testing schedule incorporated a waiting period of at least 10 days between any two consequent tests to allow the soil surrounding the piles some time to rest and

regain strength. During the test, the piles were loaded monotonically, where each load increment was applied and maintained for at least 5 minutes until the maximum load of the test was achieved. When the pre-specified maximum load was reached, a 10 min creep test was conducted in accordance with the guidelines of the Post-Tensioning Institute (2004) to examine the geotechnical failure of the micropiles.

5.2.4 Monotonic test results and analysis

One of the main objectives of this study is to examine the performance of the hollow-core bar micropiles geotechnically rather than structurally. For this pile type, the bond at the bar / grout interface is not an issue for all thread bars used nowadays in micropiles. It is always the grout / ground interface that is the limiting factor. Utilizing data from Tables (3.11) and (4.1), and employing equations 2.1 and 2.2, the ultimate structural capacity of the hollow core micropile used here should be:

In compression:

$$P_c = 0.85 f'_c A_g + f_y A_s = 2006 \text{ kN},$$

And, in tension (uplift):

$$P_t = f_y A_s = 1450 \text{ kN}$$

From a geotechnical prospective, FHWA NHI (2005) considers the hollow core micropiles as Type B micropiles, pressure grouted. FHWA NHI (2005) specifies preliminary values for the nominal bond strength for Type B micropiles embedded in stiff silty clay soils between 70 and 190 kPa (Table 2.1). However, these values vary with

ground conditions and installation techniques, higher bond values may be used but only upon proper documentation and load test data.

Given the values of s_u evaluated from the soil investigation, the highest bond value suggested by the FHWA NHI (2005) will be considered, i.e. 190 kPa. Therefore, the theoretical ultimate geotechnical capacity of the micropiles with 176 mm diameter would be 600 kN for either compression or uplift loading. Accordingly, the pile load test was initially carried to a maximum load at the pile head around 600 kN.

Figures 5.6 and 5.7 show the load-displacement curves for three compression and two uplift tests, respectively. MP2 was loaded monotonically in tension first then in compression. Figure 5.6 indicates that the responses of MP1 and MP3 are almost identical, while MP2 shows a more flexible response especially at the beginning of loading. This may be attributed to the fact that the pile was loaded in tension prior to the compression load test. Hence, its compression behavior was affected by a permanent upward displacement, which resulted in a relatively larger displacement at the beginning of the compression load test. As the compressive loading continued, the stiffness increased and became similar to that of MP1 and MP3.

Figure 5.7 reveals that the two tension piles behaved differently. Micropile MP2 displayed a stiffer response compared to MP4. Nonetheless, the two piles, as well as the piles tested under compression were loaded to a maximum load between 575 and 600 kN with no signs of failure in any of them. This demonstrates that the α_{bond} suggested by the FHWA NHI (2005) for Type B micropile underestimates the hollow core micropiles

geotechnical capacity. This is further confirmed by the small values of creep recorded at the pile head presented at Table 5.1.

There was a concern during the initial planning of the testing program whether slippage would occur between the grout inside the bar and the smooth surface of the bar inner wall, and thus it was ruled against inserting the strain gauges inside the bar. Pushing the strain gauges into the outer grout, however, damaged most strain gauges and only two strain gauges at each pile survived the installation. Unfortunately, the data obtained from these strain gauges were inconsistent as the values changed from compression to tension during the monotonic axial compression tests. This might be caused by a tilt in the axis of the strain gauge with the vertical during installation. However, it was observed after the load testing was completed that no slippage took place between the grout inside the hollow core and the enclosing bar. It is therefore recommended for further field load testing on this type of micropiles to insert the strain gauges inside the hollow core bar after grouting, with no concern of slippage occurring unless structural failure of the pile is reached.

Bruce et al. (1993) proposed the concept of “elastic ratio” for evaluating micropiles performance. They showed that the measurement of the elastic deflections can be used to evaluate the length of the pile that is being stressed, i.e. engaged in transferring the load through the grout-ground bonding. This length is useful in evaluating the magnitude and distribution of the load being transferred to the ground the elastic ratio, ER, is defined as the ratio between the elastic deformation of the pile (elastic rebound) and the applied load, that is:

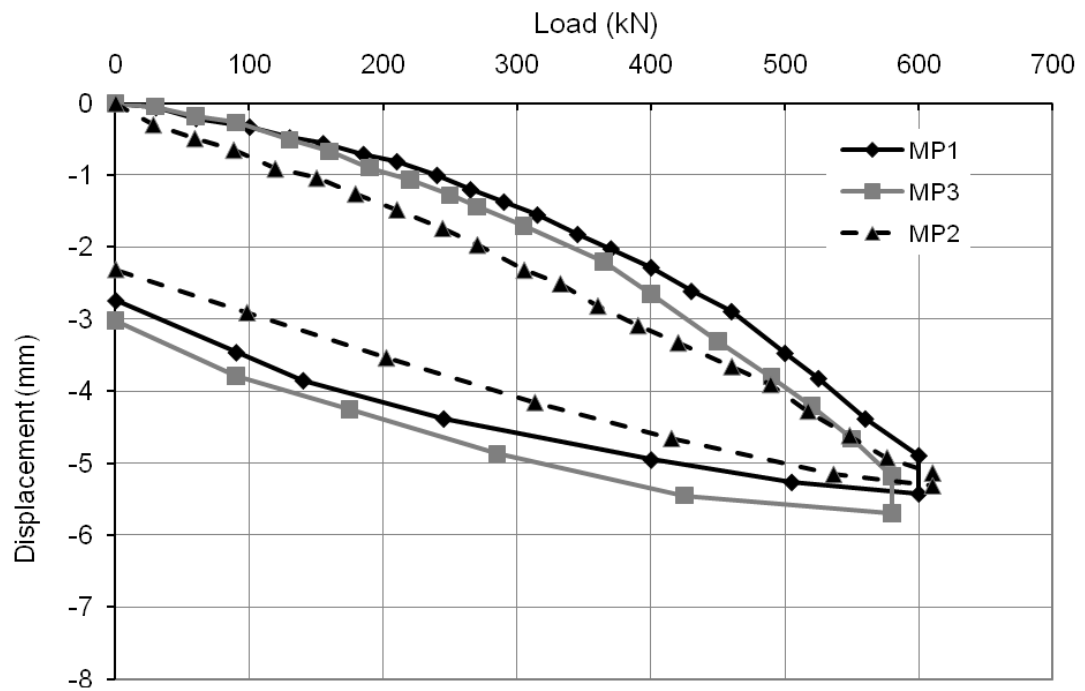


Figure 5. 6. Load-displacement curves for three monotonic compression tests

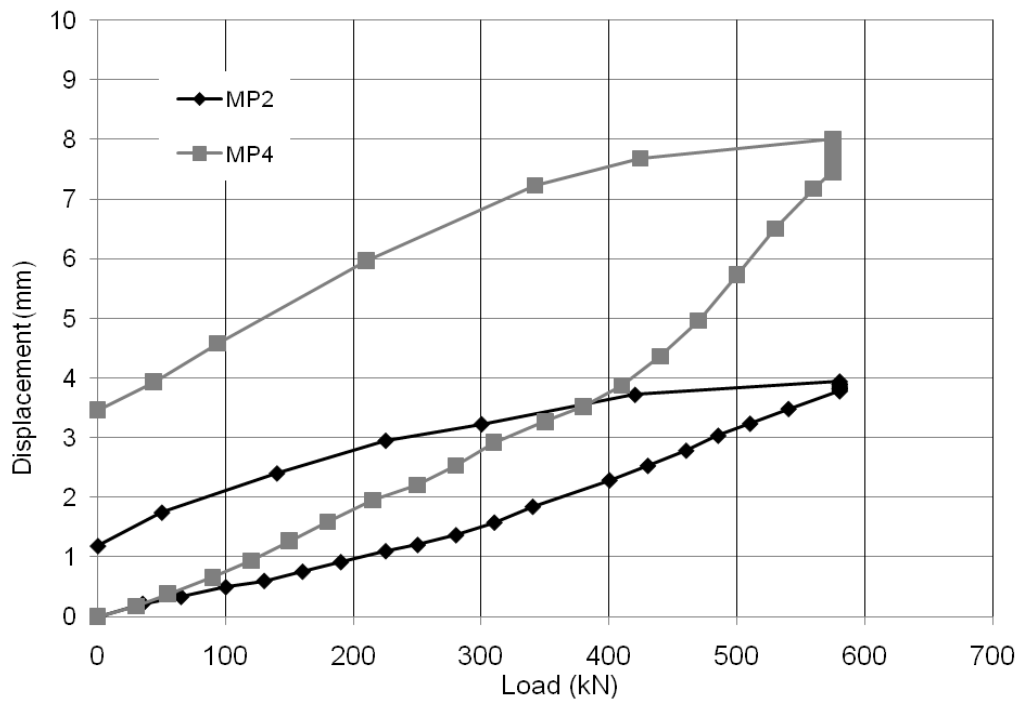


Figure 5. 7. Load-displacement curves for two monotonic tension tests

Table 5. 1. Micropiles creep at maximum applied load

	Test	Applied Load	Creep from 1 to 10 min
		kN	mm
MP1	Compression	600	0.54
MP2	Tension	580	0.17
MP3	Compression	580	0.53
MP4	Tension	575	0.54
MP2	Compression	610	0.18

$$ER = \frac{\delta_e}{\Delta P} \quad (5.1)$$

Where: ER is the elastic ratio; δ_e is the elastic rebound of the micropile measured or estimated during unloading cycle; ΔP is the magnitude of the unloading calculated as the maximum applied load minus the final load after unloading. Another important parameter that is used to assess the performance of the tested micropiles is the apparent elastic length, L_e , given by:

$$L_e = \frac{\delta_e \Sigma EA}{\Delta P} \quad (5.2)$$

Where: L_e is the elastic length of the pile; ΣEA = the combined elastic axial stiffness of the micropile section in compression or the elastic axial stiffness of the steel bar in tension.

It should be noted that L_e and ER are intrinsically related; one of them can be used to evaluate the other. The value of δ_e for a pile is estimated as the total movement minus the residual movement after unloading cycle. Practically, upon unloading, the pile will still have some level of elastic deformation caused by locked-in bond stresses as examined by Gómez et al. (2003). This causes the elastic rebound to be underestimated as well as the load transfer portion of the bond zone, i.e. the apparent elastic length. This behavior is shown clearly during the analysis of the cyclic load test phase presented later on.

For fully bonded micropile, i.e., no casing zone, the value of L_e can be related to the portion of the micropile subjected to substantial axial load. Hence, it can be used to estimate the ultimate average bond strength acting along the micropile where debonding is most probably to occur. Also, it can be used to assess whether an end bearing condition is developed or not. Bruce et al. (1993) explained the development of the end bearing condition as a probability of micropile failure, which they attributed to the small diameter of micropiles. Table 5.2 illustrates the results obtained from the monotonic test phase on the micropiles by computing the total, residual and elastic movement as well as the corresponding elastic length calculated using Eq. 5.2. It is noted from Table 5.2 that the developed L_e is less than the total length for all micropiles. However, for all the cases, except MP2 in uplift, the L_e is about 0.75 of the micropiles bonded length or higher. This also emphasizes that no geotechnical failure has occurred for any of the tested micropiles but the micropiles start to approach the failure point. Nonetheless, the micropiles ultimate load is higher than the maximum load applied during the monotonic load test.

Table 5. 2. Summary of the monotonic test phase results

	Type of Test	P_{\max} kN	Total displacement	Residual displacement	Elastic displacement	Elastic length
			δ_t , mm	δ_r , mm	δ_e , mm	L_e , m
MP1	Compression	600	5.4	2.70	2.7	4.5
MP2	Tension	580	3.95	1.18	2.77	2.4
MP3	Compression	580	5.70	3.02	2.68	4.7
MP4	Tension	575	8.00	3.46	4.54	4.0
MP2	Compression	610	5.31	2.31	3.0	5.0

Due to the over-consolidated nature of the stiff silty clay layer, a strain-softening behavior may take place along grout/ground interface at the apparent elastic length rather than full debonding of this portion of the micropile. This phenomenon could be examined through cyclic load testing. The results of the cyclic load tests will help in assessing whether a full debonding or softening (post-peak behavior) of the micropiles would take place in this type of soils. This may be an important issue for design of micropiles subject to machinery loading, and/or micropiles installed in seismic areas.

5.3 Axial Cyclic Load Tests

The second phase of the field load tests involves five cyclic load tests. Four compression and one tension cyclic load tests were conducted on the four hollow bar micropiles. The

micropiles were tested cyclically in the following sequence: cyclic tension on MP4, cyclic compression on MP1, MP3, MP4, and MP2.

5.3.1 Test equipment and instrumentation

It is anticipated that the load levels applied during the cyclic load tests will be the same or less than that applied in the first phase. Hence, the same loading frame illustrated in Fig. 5.2 was used to execute the cyclic load during the cyclic load tests phase. No additional instrumentations were employed at the pile head during this phase testing.

5.3.2 Cyclic load test procedure

In each cyclic load test, the micropile was subjected to 15 cycles of loading and unloading at a rate of one cycle per minute. The loading rate was governed by the reliability of the hydraulic jack used. In each loading cycle, the examined micropile was tested to a peak load equal to 133% of the anticipated design load (DL) and unloaded to a minimum load equal to 67% of the anticipated DL. The DL considered herein is about one half of the maximum load applied during the monotonic load test, i.e., 280 kN to 310 kN. Table 5.3 shows the amplitude of the cyclic load applied as well as the DL calculated for each micropile.

Each cyclic load test started by loading the micropile monotonically to the DL following the quick maintained load test procedure; each load increment was maintained for 5 minutes. Upon reaching the DL, the micropile was loaded to the maximum load and then unloaded to the minimum load (as given in Table 5.3) at a relatively rapid loading rate.

Table 5. 3. Design, amplitude and maximum applied load for cyclic load tests

	Type of cyclic test	Design load kN	Amplitude of the cyclic load kN	Maximum applied \load/ cycle, kN	Minimum applied load/ cycle, kN
MP1	Compression	310	100	415	215
MP2	Compression	305	95	400	210
MP3	Compression	280	95	375	185
MP4	Compression	300*	100	400	200
MP4	Tension	300	100	400	200

* MP4 was tested monotonically in tension only, and one half of the applied load was consider as the design load in both; compression and tension

This test procedure was chosen to approximate the axial response of a micropile subjected to earthquake conditions that would lead to a cyclic load equal to one third of the pile design capacity, i.e., around 100kN above and below the DL for the test piles. The load test procedure employed has deviated from the ASTM D-1143 (2007) cyclic load test procedure.

5.3.3 Cyclic load test results and analysis

The hollow bar micropile cyclic loading and displacement versus time are plotted in Figs. 5.8 through 5.11 for the four cyclic compression tests and in Fig. 5.12 for the single uplift

cyclic test. The response of piles to cyclic loading is quite complex (El Naggar and Wei, 2000), therefore, the results of the cyclic tests are analyzed considering several aspects.

The response of each pile was examined considering the magnitude of the pile head load-movement at each cycle, as illustrated in Figs 5.13 for all the compression and 5.14 for the tension cyclic load tests. Generally, all tested micropiles, whether in compression or tension, showed an increase in the pile head movement with the increase in the number of load cycles. However, the initial and final displacements of the micropiles at the beginning and at the end of the cyclic portion of the test are not similar.

It seems that the performance of tested micropiles was affected by the sequence and amplitude of monotonic tests conducted on the piles prior to the cyclic tests. MP1 and MP3 were tested under compression only; monotonically then cyclically. However, MP1 was tested to higher load amplitudes in both tests. MP1 displayed higher initial and final displacements than MP3 during the cyclic portion of the test. On the other hand, the effect of sequence of loading can be clearly seen in the response of MP4, which was tested monotonically then cyclically under tension, and eventually cyclically under compression. MP4 exhibited more displacement under cyclic compression that is nearly twice that which occurred during cyclic tension.

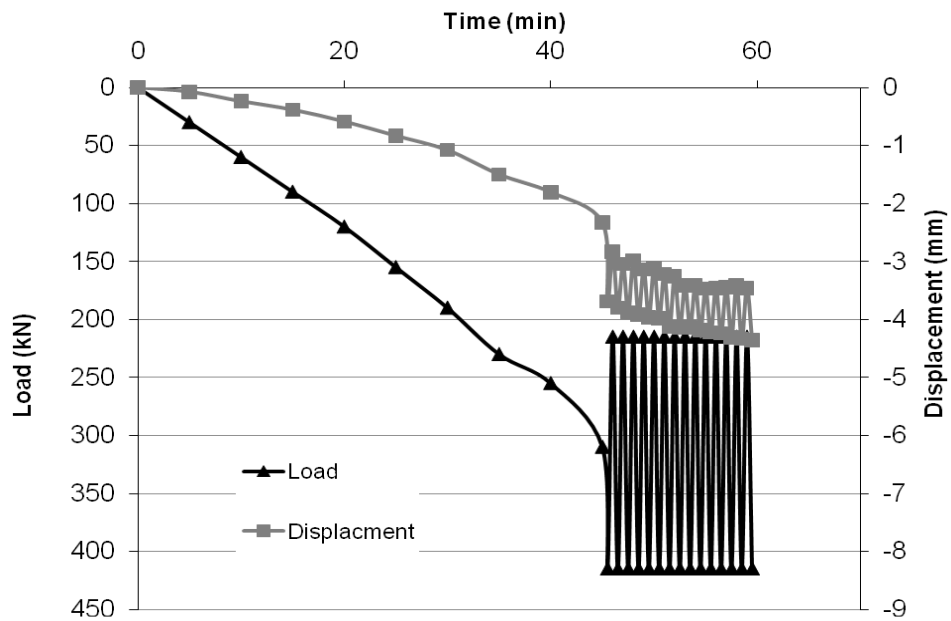


Figure 5. 8. Load and displacement versus time of the cyclic compression tests on MP1

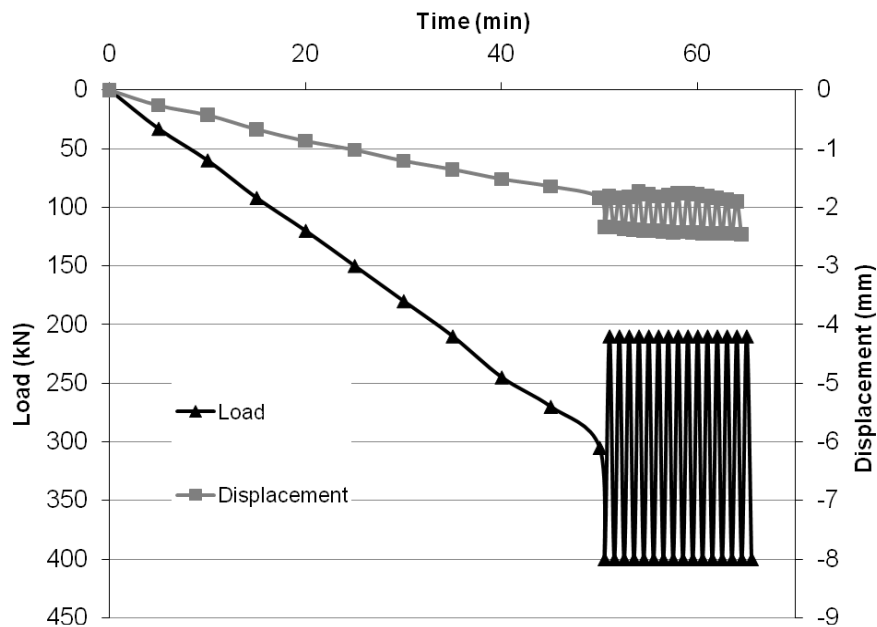


Figure 5. 9. Load and displacement versus time of the cyclic compression tests on MP2

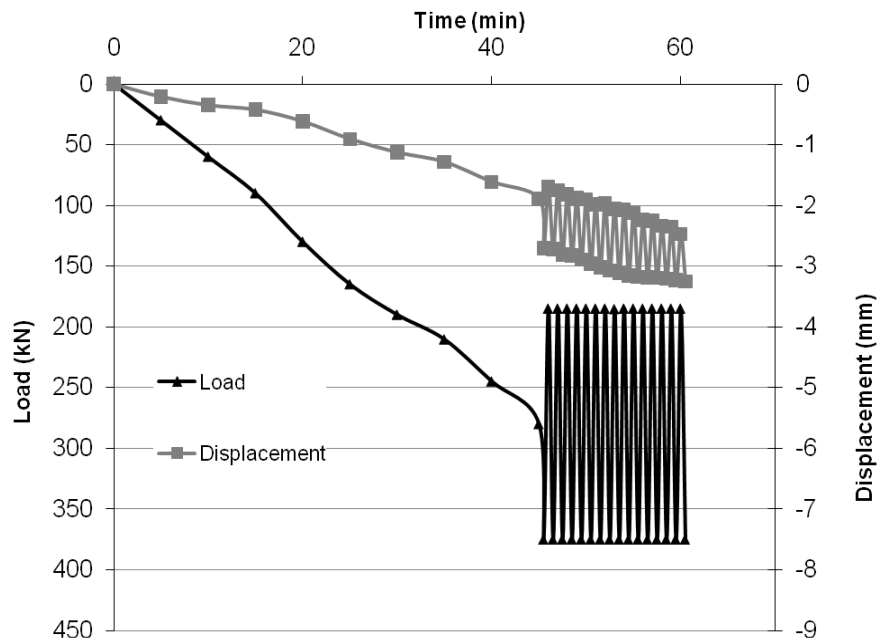


Figure 5. 10. Load and displacement versus time of the cyclic compression tests on MP3

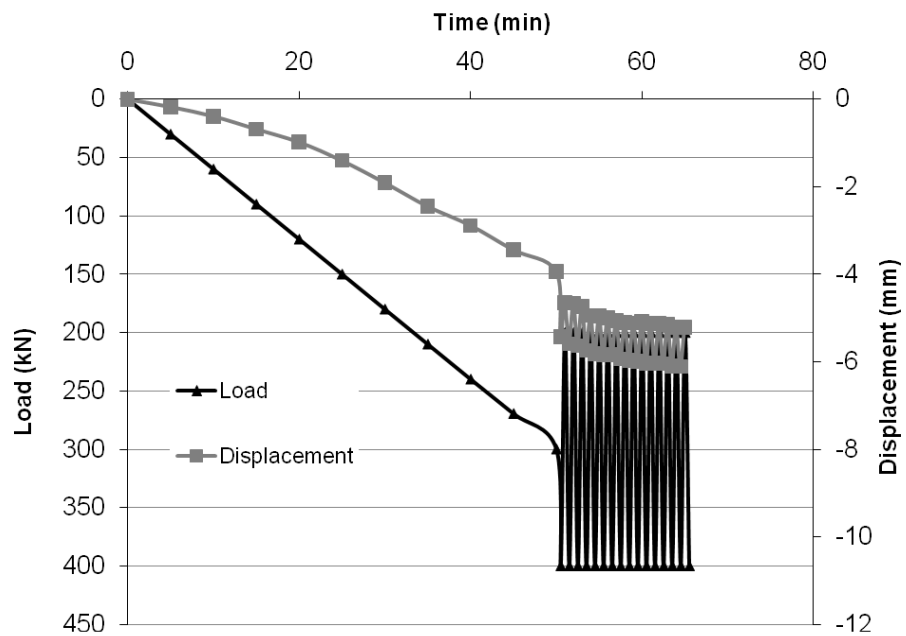


Figure 5. 11. Load and displacement versus time of the cyclic compression tests on MP4

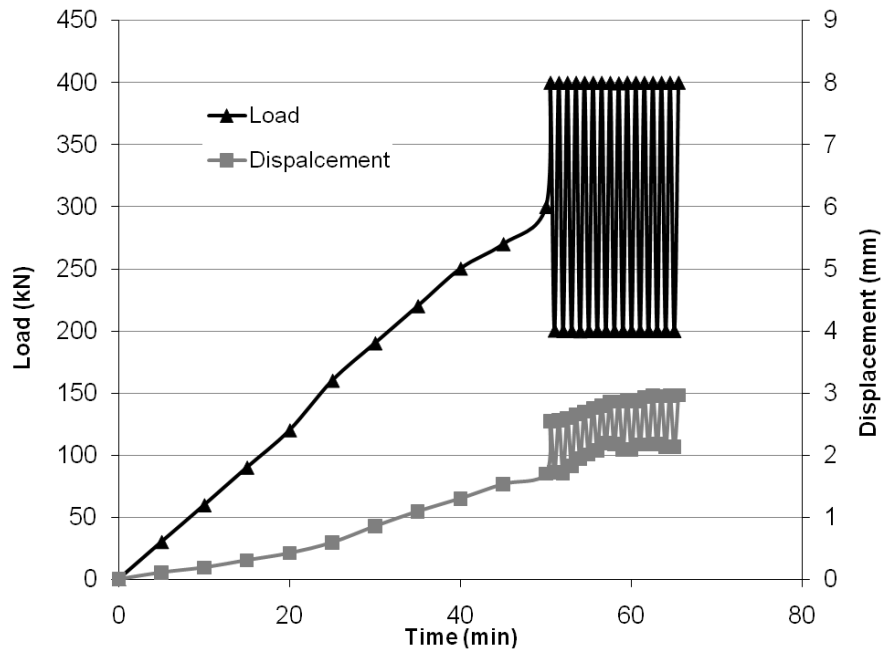


Figure 5. 12. Load and displacement versus time of the tension cyclic load test on MP4

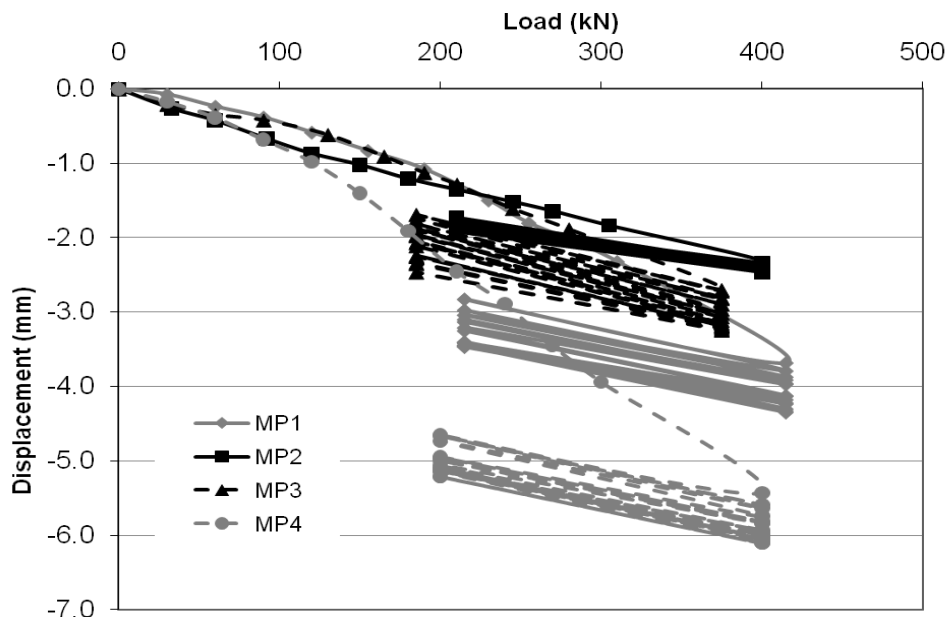


Figure 5. 13. Load – displacement curves for the compression cyclic test on MP1

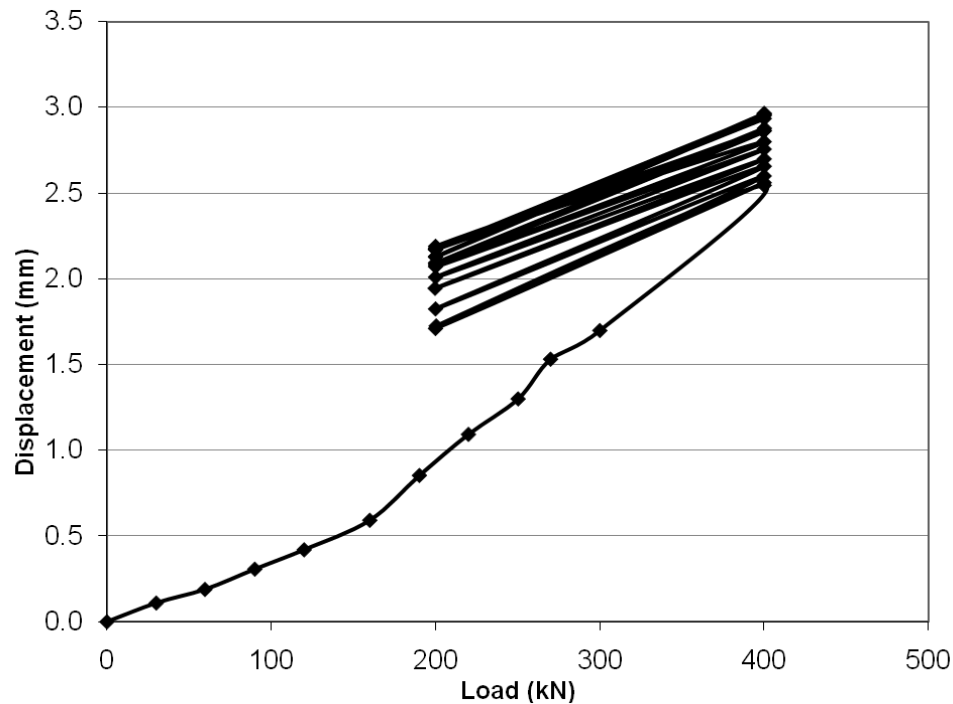


Figure 5. 14. Load -displacement curves for the tension cyclic test on MP4

Micropile MP2 showed a stiffer response to cyclic loading than the other micropiles because it was subjected initially to monotonic tension, then monotonic compression followed by cyclic compression. It can be concluded from the difference between the initial and final displacements (at the beginning and end of cyclic loading) presented in Figs. 5.13 and 5.14 that the clayey soils along the pile-soil interface has experienced some plastic deformation over what they experienced during the monotonic load test. This permanent deformation may occur due to the breaking of interparticle bonds between the clay particles accompanied by local realignment of those particles whenever the skin friction is mobilized at the monotonic load tests phases.

To further examine the effect of cyclic loading on the micropile head movement, the accumulated displacement of the pile head is plotted against the number of cycles in Fig.

5.15. At cycle zero, the displacement corresponds to the initial displacement of the micropiles when the maximum cyclic load was reached the first time.

Figure 5.15 demonstrates that there was a small increase in the pile head movement due to the cyclic loading, but this increase was not accompanied by progressive degradation of the pile performance as the number of load cycles increased. Table 5.4 presents the percentage increase at the pile head displacement at the end of the cyclic loading relative to the observed displacement at the end of the monotonic loading phase (and the beginning of cyclic loading). The stiffness of the micropiles at each load cycle can be approximated by the slope of the load-movement curve during each load cycle, i.e.:

$$K = \frac{P_{\max} - P_{\min}}{\delta_{\max} - \delta_{\min}} \quad (5.3)$$

Where: K is the pile head stiffness; P_{\max} and P_{\min} are the maximum and minimum applied loads during each load cycle; δ_{\max} and δ_{\min} are the corresponding pile head displacement.

The pile head stiffness was calculated using Eq. 5.3 and the results are plotted in Figs. 5.16 through 5.20. It is noted from these figures that the micropile stiffness didn't experience any cumulative change in any given direction during the load cycles, i.e., it increased slightly in some cycles and decreased in others. It is interesting to note that all tested micropiles demonstrated approximately the same initial stiffness values (see Table 5.5), except for MP2, which exhibited a stiffer response than all other piles. Not surprisingly, as MP2 exhibited stiffer response under monotonic compression (Fig. 5.6) and monotonic tension (Fig. 5.7).

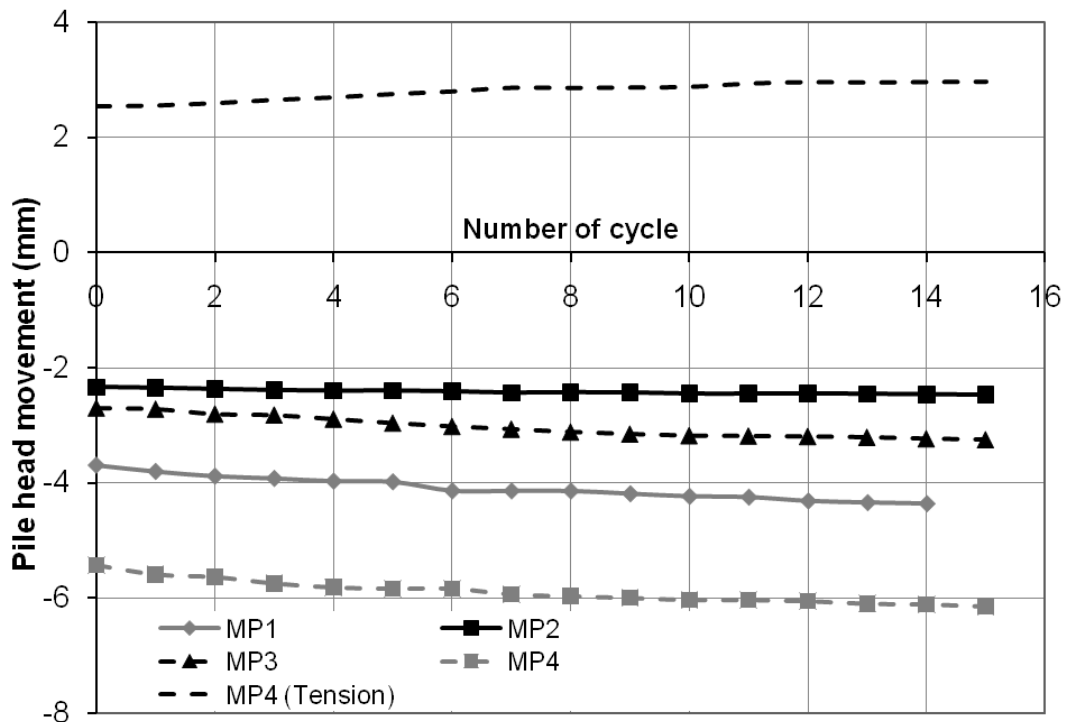


Figure 5. 15. Accumulation of displacement for 15 cycles of loading and unloading

The overall observation is that the stiffness change was marginal with no cumulative degradation; rather a small increase was observed for some of the tested micropiles. It can be concluded from these observations that the micropiles did not exhibit any form of full debonding at the pile-soil interface. In addition, the cyclic loading phase demonstrated that the over-consolidated clay was not sensitive to small changes in magnitude and amplitudes of the cyclic load but it is affected by the sequence of load applied. It should be noted, however, that these observations are only relevant to the range of applied magnitudes of cyclic loading. The behaviour of hollow core micropiles could be different if higher cyclic loads are applied.

Table 5. 4. Percentage increase in pile head displacement at the end of cyclic loading

	Type of test	Percentage increase in displacement from cycle 1 to cycle 15, %
MP1	Compression	18
MP2	Compression	6
MP3	Compression	20
MP4	Compression	13
	Tension	16.5

Table 5. 5. Initial and final stiffness of all the micropiles after the cyclic load test

	Type of Cyclic Test	Initial Stiffness MN/m	Final Stiffness MN/m
MP1	Compression	219.5	225.7
MP2	Compression	350.3	348.3
MP3	Compression	186	245
MP4	Compression	234	219
	Tension	241	240

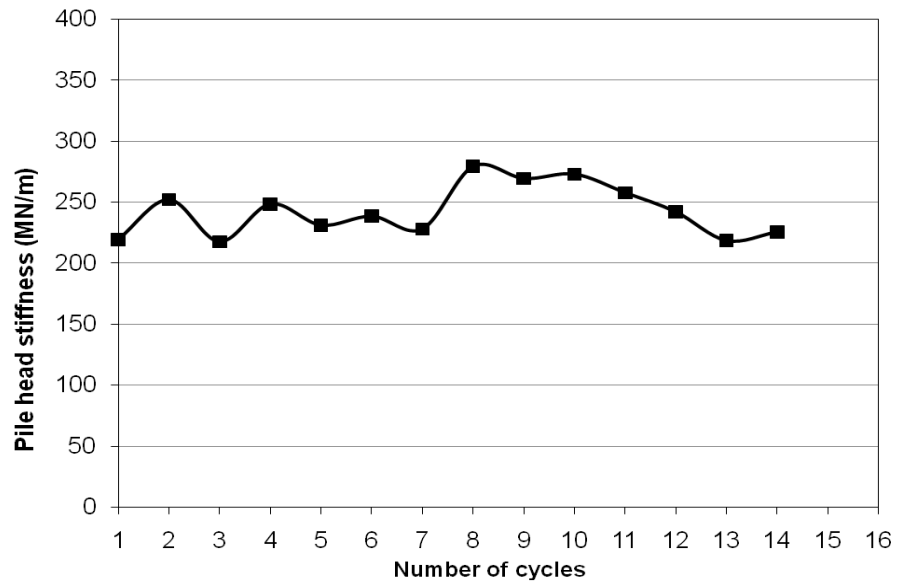


Figure 5. 16. Pile head stiffness versus number of cycles for compression cyclic tests on MP1

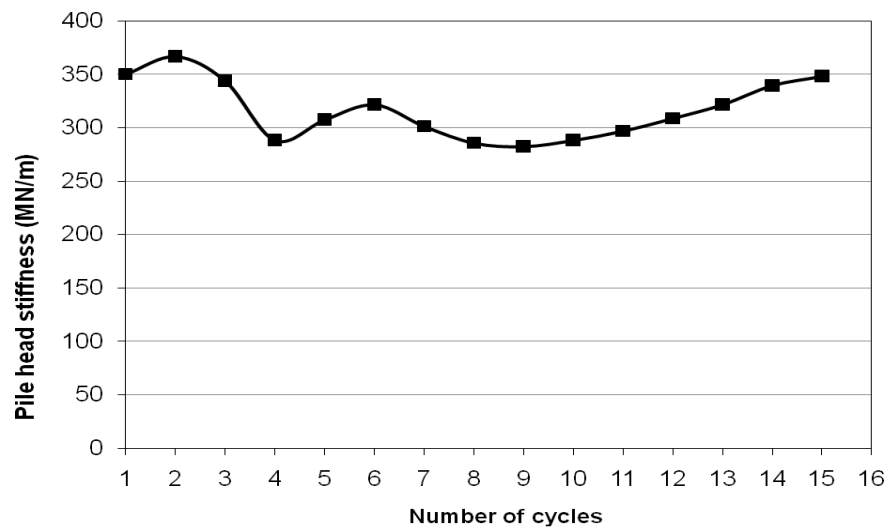


Figure 5. 17. Pile head stiffness versus number of cycles for compression cyclic tests on MP2

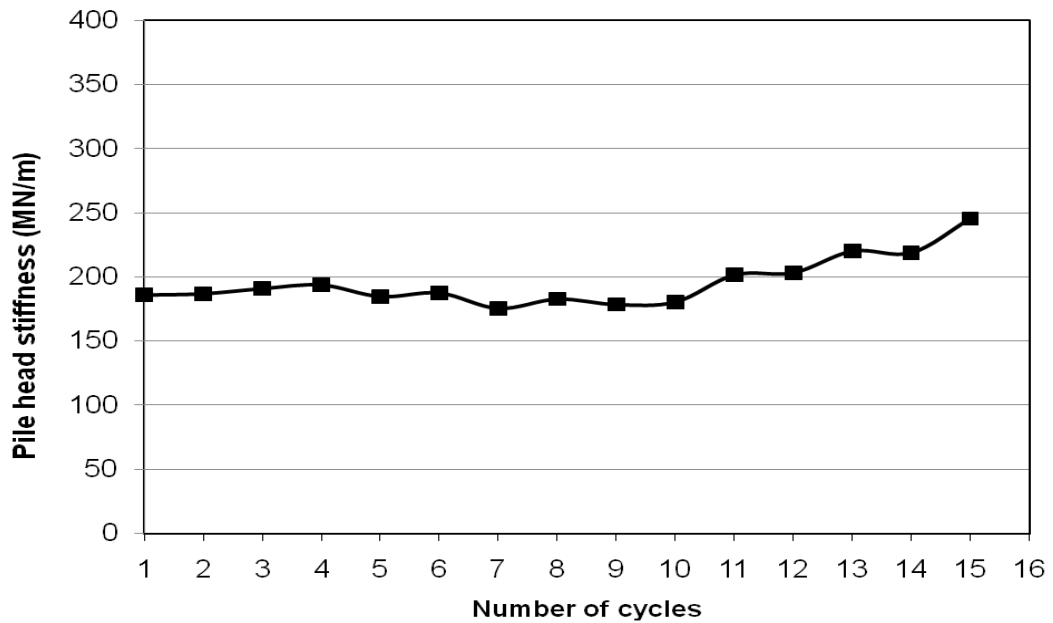


Figure 5. 18. Pile head stiffness versus number of cycles for compression cyclic tests on MP3

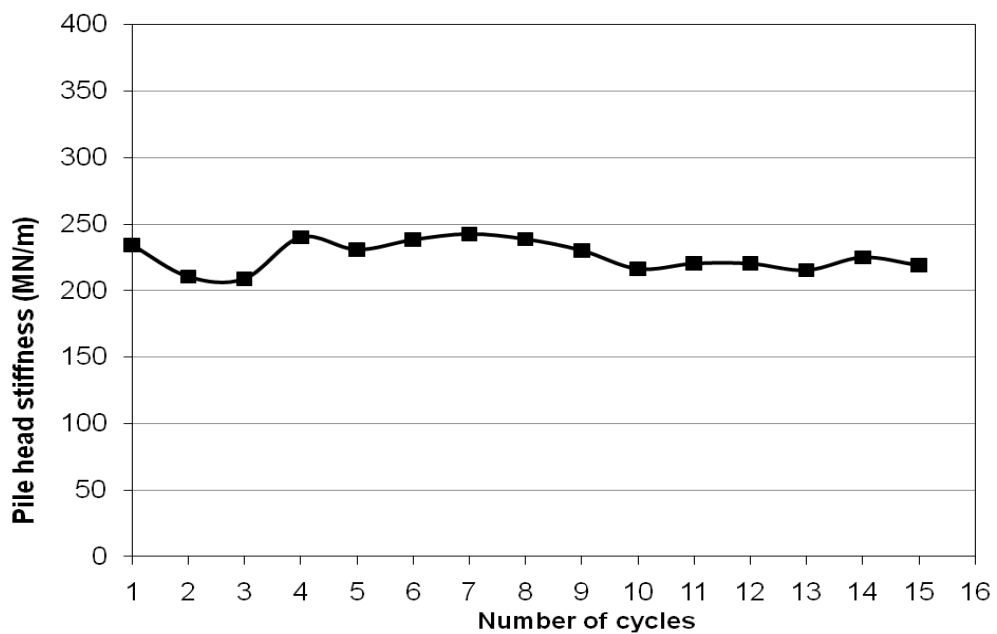


Figure 5. 19. Pile head stiffness versus number of cycles for compression cyclic tests on MP4

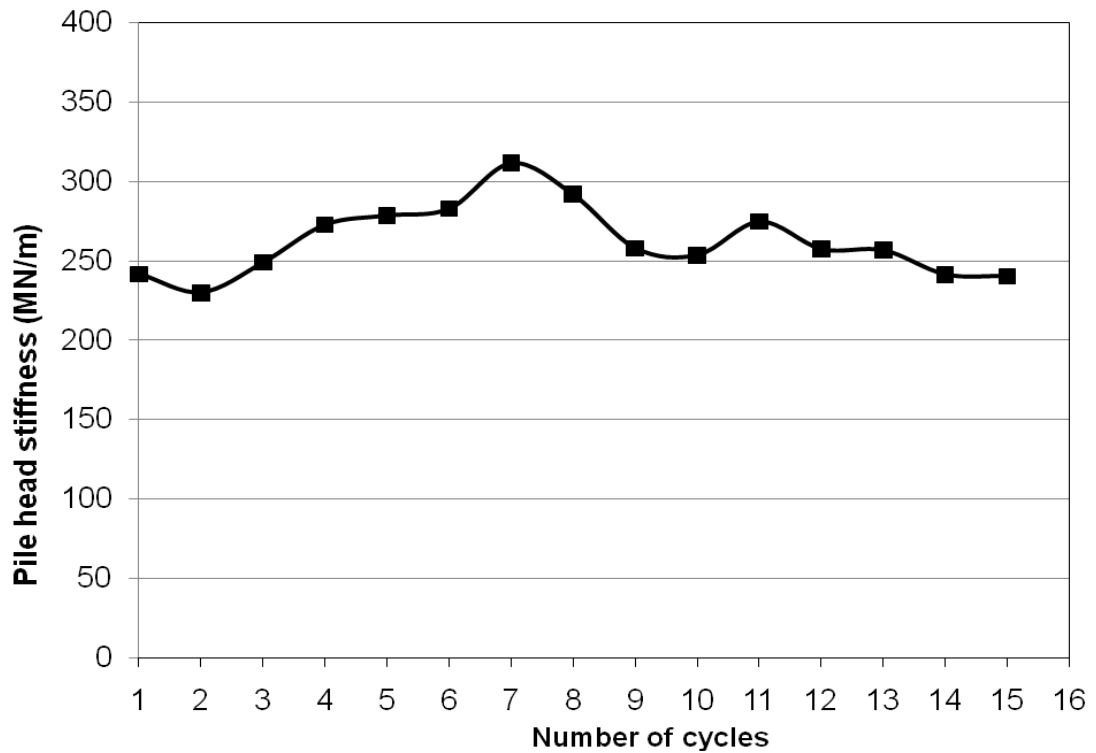


Figure 5. 20. Pile head stiffness versus number of cycles for tension cyclic tests on MP4

5.4 Numerical Analysis

The field test results provided useful information on the performance characteristics of the hollow bar micropiles. In addition, the soil investigation program provided the soil strength and stiffness properties required to characterize the behavior of different soil layers. This information can be invested in calibrating a numerical model that can provide further insights into the load transfer mechanism and performance characteristics of hollow bar micropiles. Once the numerical model with has been calibrated with the field data, it can be used to perform further analyses to identify failure criteria, establish

the load transfer mechanism and develop a design procedure for the hollow core micropiles.

The finite element method (FEM) represents a powerful tool for numerical analysis. Nowadays, numerical analysis using FEM is well accepted in the field of geotechnical engineering due to the possibility of modeling the soil employing a range of constitutive models from simple to complex with the input of few material parameters. In this study, FEM analysis is carried out utilizing the ABAQUS software package (Hibbitt et al, 2008). The program is capable of modeling the soil and the micropile geometrically and materially in a near to real fashion. The program outputs include stresses and strains as well as deformations at different locations. In this section, numerical simulations for hollow bar micropiles under monotonic and cyclic axial loads are presented, and the obtained results are discussed.

5.5 Axial Loading Numerical Models

Two sets of models were created to simulate the performance of hollow bar micropiles under axial loading: a monotonic axial loading model, and a cyclic axial loading model. Upon calibrating each model, a parametric study is conducted and some design guidelines are introduced.

5.5.1 Monotonic axial loading models

5.5.1.1 Geometric modeling

The case of a single pile can be described as a cylindrical structure with a relative uniform radial cross-section and an axisymmetric loading scheme around the center axis. In this case, the stress and deformation are assumed to be identical in any radial direction. Accordingly, a two-dimension (2D) axisymmetric model can be used to model the behavior of the hollow bar micropile under axial loading.

The axisymmetric model is generated by revolving a plane cross-section about the symmetry axis, and is readily described in cylindrical polar coordinates r , z , and θ . Figure 5.21 shows a typical reference cross-section at $\theta = 0$. The radial and axial coordinates of a point on this cross-section are denoted by r and z , respectively. Thus, the model has two coordinates: 1 (or r) is radial; and coordinate 2 (or Z) is vertical. At $\theta = 0$, the r -direction corresponds to the global x -direction and the z -direction corresponds to the global y -direction (Hibbitt et al, 2008). Hence, each node in the model has two degrees of freedom; degree of freedom 1 which is u_r , and degree of freedom 2 which is u_z .

The axisymmetric elements are used to analyze the problem by discretizing the reference cross-section at $\theta = 0$. In Fig. 5.21, an element of an axisymmetric body has the nodes i , j , k , and l are actually nodal circles. Accordingly, the volume of material associated with the element is that of a body of revolution. As a result, the value of a prescribed nodal load or reaction force is the total value on the ring, integrated around the circumference. Four nodes continuum axisymmetric elements, CAX4, were used to model both the soil

and micropile. The element CAX4 allows for only radial and axial loading. It has isotropic or orthotropic material properties, with θ being a principal direction. Figure 5.22 presents the geometry of a CAX4 element and the position of its integration points.

Randolph and Wroth (1978) recommended the vertical boundary of a model to be extended a distance not less than 25 times the pile diameter, measured from the center of the pile. They also suggest the lower horizontal boundary to be at least one and half the pile length underneath the pile tip. However, Helwany (2007) used the axisymmetric model in ABAQUS to simulate the behavior of piles under monotonic loading. He performed a mesh sensitivity analysis, which indicated that suggested the same distance for the horizontal boundary as Randolph and Wroth (1978), but there is no need to extend the model dimensions more than 0.7 the pile length for single pile analysis in the vertical direction. Hence, the vertical boundary of the FE model was located at a distance $25d$ from the axis of symmetry. In order to examine the effect of the location of the lower horizontal boundary on the results, two cases were examined: the lower horizontal boundary placed at either $0.7 L$ or at $1.0 L$ ($L =$ micropile length). The outline geometry and boundary conditions of the model are shown in Fig. 5.23.

The model has four surfaces, with the following boundary conditions: vertical surfaces adjacent and parallel to axis of symmetry are fixed in the radial direction, $u_r = 0$; horizontal surface at the bottom of the model is fixed in two directions, $u_z = u_r = 0$; and the ground surface is free in all directions. Several meshes with different refinement are created and examined. The coarser mesh has 5300 elements and the finer mesh has 45000 elements, both are shown in Fig. 5.24. The aspect ratio of all elements used in the model is between 1:1 in the vicinity of the micropile, and 1:5 at the far field.

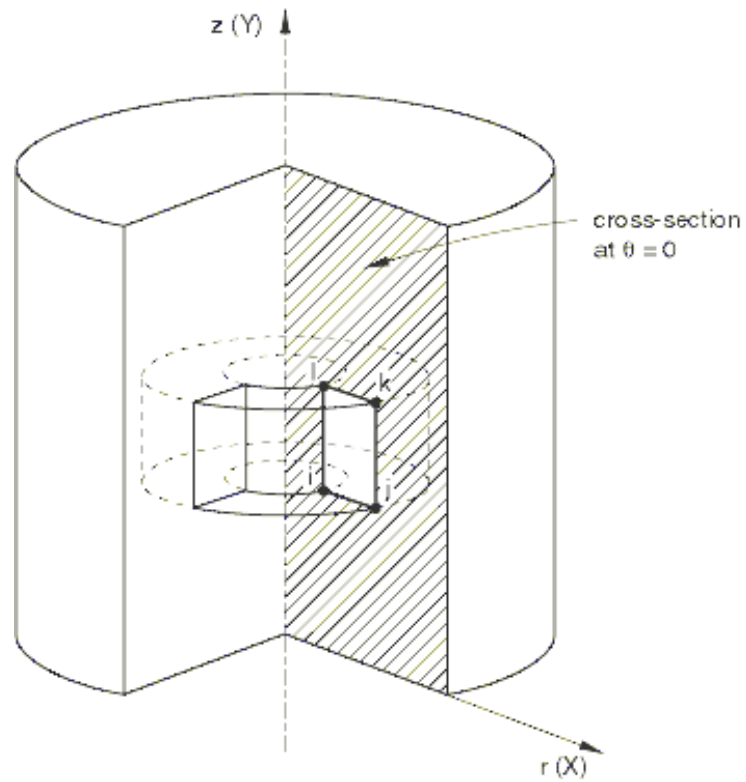


Figure 5. 21. Axisymmetric geometry model

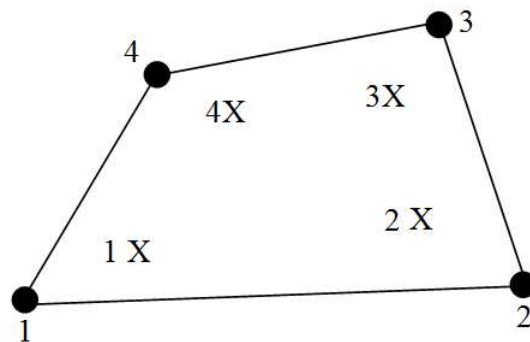


Figure 5. 22. CAX4 bilinear element with four integration points

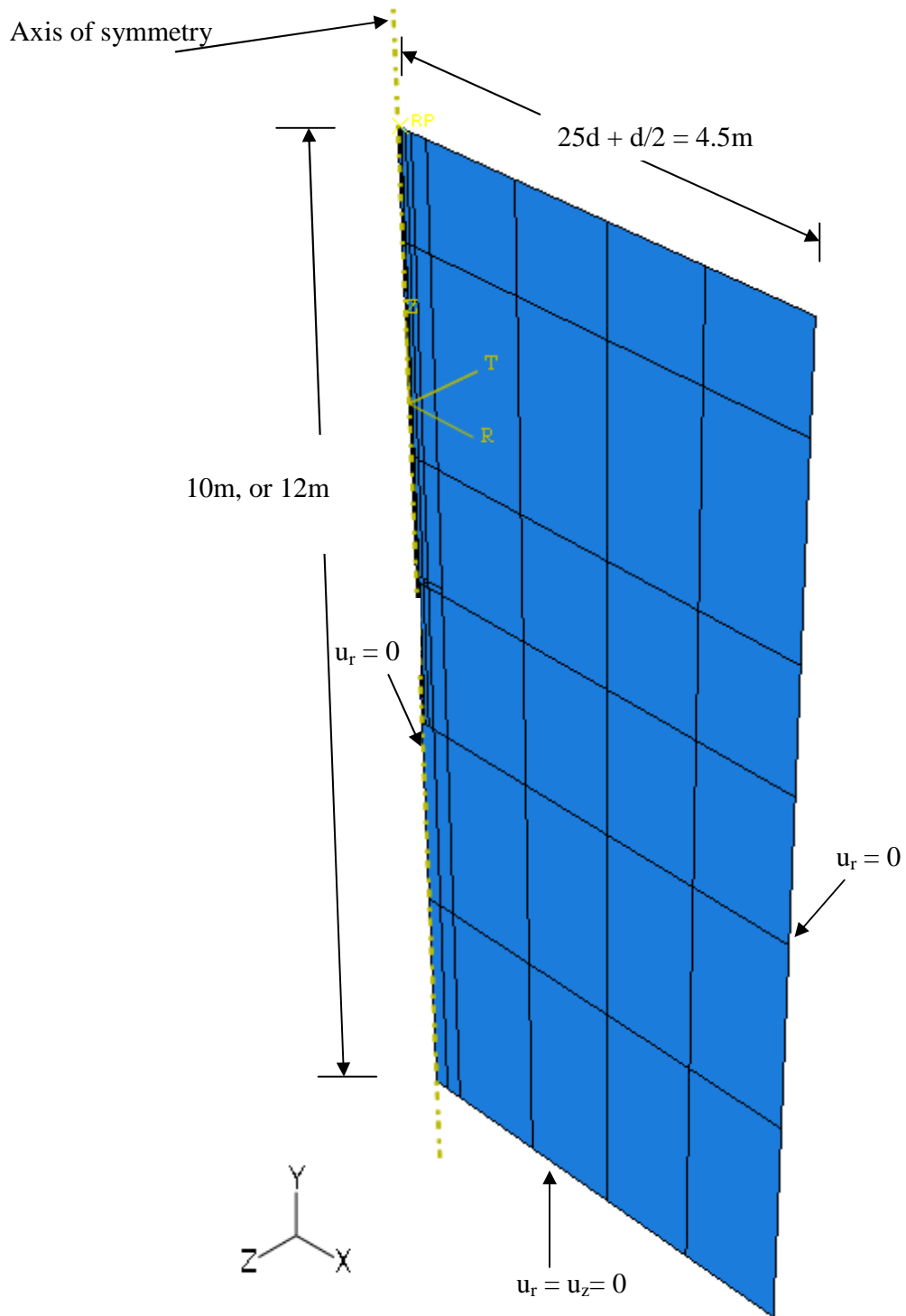
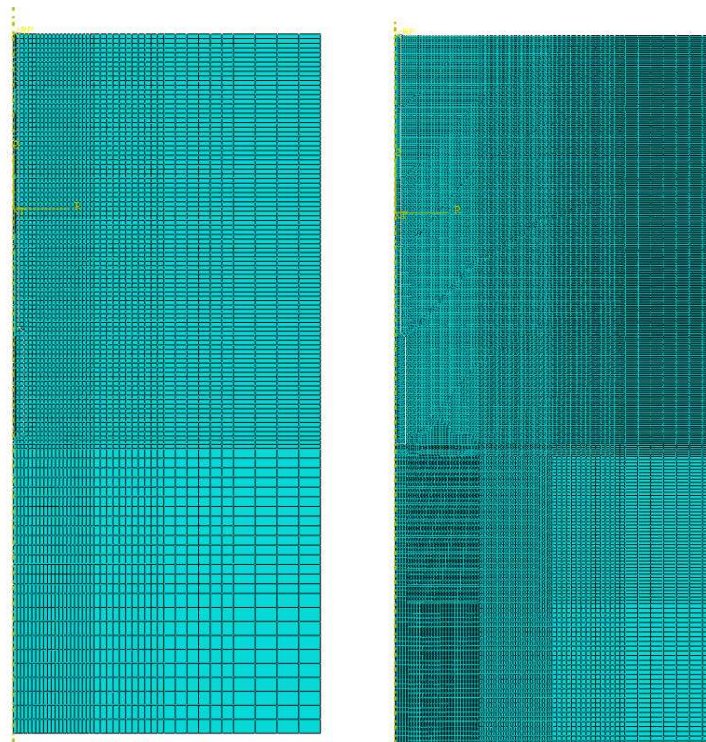


Figure 5. 23. The geometry of the axisymmetric model and the boundary conditions



(a) Coarse mesh

(b) Fine mesh

Figure 5. 24. Meshing techniques on two models

5.5.1.2 Material modeling

The micropile–soil system involves three different materials: steel, grout and soil medium. The steel hollow bar was modeled considering linear elastic behavior represented by the Young’s modulus, $E = 2E+5$ MPa, and Poisson’s ratio, $\nu = 0.3$. The grout is modeled using a nonlinear elastic-plastic model along with the grout strength parameters presented previously in Table 3.11. Figure 5.25 depicts the constitutive relation used to model the grout. The material model employed for the soil medium incorporates two segments: an elastic segment represented by E and ν ; and a plastic segment represented by the Mohr-Coulomb plasticity, characterized by a smooth flow

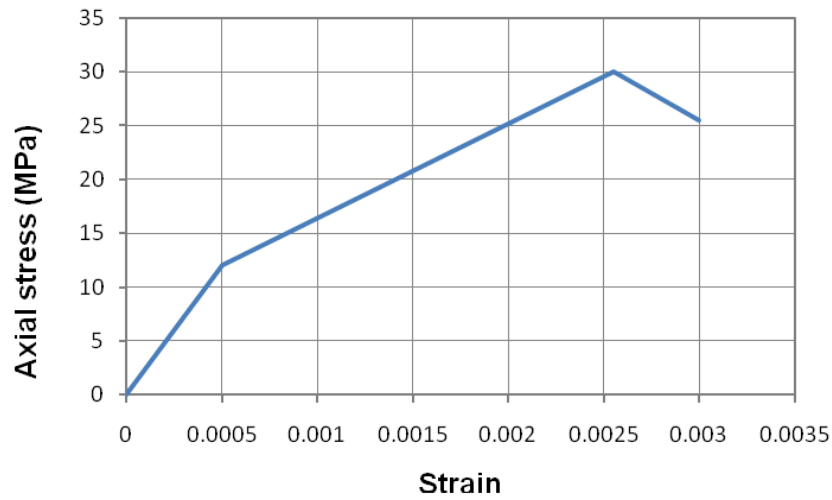


Figure 5.25. Tri-linear stress-strain relation used to model the grout material

potential that has a hyperbolic shape in the meridional stress plane and a piecewise elliptic shape in the deviatoric stress plane.(Hibbitt et al, 2008).

The Mohr-Coulomb model is defined by

$$\tau = c' + \sigma' \tan \varphi' \quad (5.4)$$

Where: σ is normal stress and is negative in compression. The shear and normal stresses can then be computed as:

$$\tau = s \cos \varphi' \quad (5.5)$$

$$\sigma' = \sigma_m + s \sin \varphi' \quad (5.6)$$

Substituting for τ and σ , multiplying both sides by $\cos \varphi'$, and reducing, the Mohr-Coulomb model can be written as:

$$s + \sigma_m \sin \varphi' - c \cos \varphi' = 0 \quad (5.7)$$

Where: s is maximum shear stress = $\frac{1}{2} (\sigma_1' - \sigma_3')$, is where σ_1 is the maximum principal stress and σ_3 is the minimum principal stress. $\sigma_m = \frac{1}{2} (\sigma_1' + \sigma_3')$, is the average of the maximum and minimum principal stresses; ϕ is the friction angle of the material; and c is the cohesion of the material.

Due to the rapid rate of loading followed during the field load tests, the soil is expected to display undrained behavior. For silty clayey soils, the undrained shear strength parameter, s_u , is used to represent the cohesion, c , in the Mohr-Coulomb model described previously.

For the sandy soil that exists at depth 5.75m, the Mohr-coulomb parameters used are the friction angle ϕ' and the dilation angle ψ . However, zero cohesion stress is not permitted in the model. Accordingly, a small value of cohesion will be given to the sandy layer to overcome any numerical error. The soil investigation program discussed in Chapter 3 provided the geotechnical parameters of the test site soils. Hence, the stiffness and strength parameters adopted in soil deposits modeling are given by the average values of those parameters as summarized in Table 5.6.

5.5.1.3 Micropile-soil interface model

The grout body and the hollow bar were assumed to be bonded and no interaction surface was assigned. On the other hand, an interaction model was assigned between the soil and grout body, which is discussed below. Generally, soil and grout surfaces transmit shear as well as normal forces across their interfaces. The normal and friction forces between the two contact surfaces are expressed by: normal behavior model to define the

developed interaction stresses in the normal direction of the surfaces; and tangential behavior model to describe shear stress transmittal via the interface.

Table 5. 6. Geotechnical parameters assigned to the Mohr-Coulomb model

Depth	Cohesion, c kPa	Friction angle, ϕ'	Dilation angle, ψ	Young's modulus, E MPa	ν
0 to 1	105	0	0	50	0.45
1 to 2	150	0	0	75	0.45
2 to 3	90	0	0	45	0.45
3 to 5.75	175	0	0	90	0.45
5.75 to 10	1	34-35	4-5	100-200	0.32

The micropile transfers the applied load to the surrounding soil through two load transfer mechanisms: shaft friction resistance and end bearing resistance. To model the shaft friction resistance, both the normal and tangential models were employed, while to simulate the end bearing resistance, only the normal model was sufficient. The normal behavior between the micropile and the soil along the shaft and at the base is modeled using penalty “hard” normal behavior model. The “hard” contact relationship minimizes the penetration of the slave surface (soil) into the master surface (grout) at the constraint locations and does not allow tensile stress transfer across the interface. The contact pressure – overclosure relationship in this model is given in Fig. 5.26.

When the linear penalty method is used, the penalty stiffness is assigned 10 times representative underlying element stiffness. This can be scaled or reassigned if needed. This approach can sometimes contribute to some degree of stress inaccuracy with displacement-controlled loading and a coarse mesh. In the current analysis, both were avoided (i.e. load-controlled and fine mesh were considered).

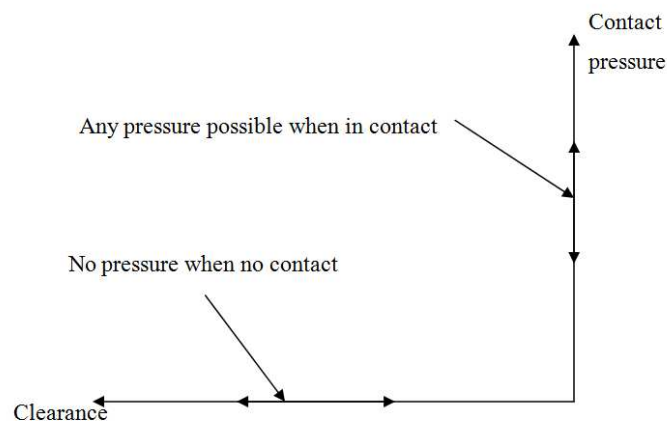


Figure 5.26. Default pressure – overclosure relationship

The tangential behaviour along the micropile – soil shaft is modeled using a penalty friction model, which is based on the Coulomb friction model. In this model, two contacting surfaces can carry shear stresses up to a certain magnitude across their interface before they start sliding relative to one another. This state is known as sticking state. When the shear stress exceeds a certain threshold, sliding of the surfaces initiates at a fraction of the contact pressure, p , between the surfaces. The Coulomb friction model defines this limit as the maximum shear stress, τ_{\max} and the fraction, is known as the coefficient of friction. The contact pressure, p , is the normal stress calculated from the normal behaviour model. Figure 5.27 shows the relation between the maximum shear stress, contact pressure, p , and coefficient of friction, μ .

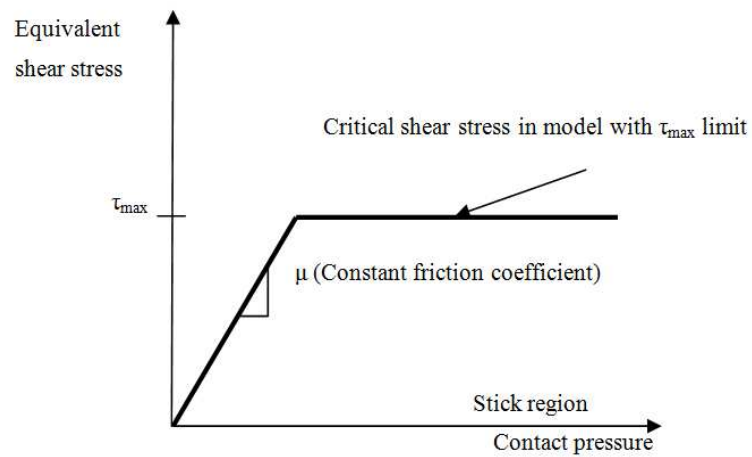


Figure 5. 27. Slip regions for the friction model with a limit on the critical shear stress.

Upon applying the initial in-situ conditions and considering the normal and tangential models along the soil – pile shaft interface, the shear stress at the beginning of analysis is:

$$\tau_{in} = \mu p \quad (5.8)$$

and:

$$p = k_o \sigma_v \quad (5.9)$$

$$\mu = \tan \delta \quad (5.10)$$

Where: δ is the friction angle between the soil and micropile surfaces = ϕ . Substituting p and μ in Eq. 5.8, the shear resistance can be inferred as:

$$\tau_{in} = (k_o \sigma_v) \tan \phi \quad (5.11)$$

Upon applying the loads at the pile head, the shear stress along the shaft is modified depending on the contact pressure developed, to be:

$$\tau_{in} = (\Delta p) \tan \varphi \leq \tau_{max} \quad (5.12)$$

Where: Δp is the change in the contact pressure due to the applied load. The maximum shear stress developed at the micropile – soil interface for micropile embedded in sand is computed from:

$$\tau_{max} = k_s \sigma_v \tan \varphi \quad (5.13a)$$

and for micropile embedded in clay is compute using:

$$\tau_{max} = \alpha s_u \quad (5.13b)$$

Depending on the outcome of Eq. 5.12, two states may occur; if $\tau_{in} \leq \tau_{max}$, the two surfaces are sticking, while if $\tau_{in} > \tau_{max}$, slipping takes place, and no more shear stresses will be transferred to this part of the soil. Equations 5.8 to 5.12 are considered a comprehensive interaction model for simulating the shaft resistance of micropiles embedded in sand. However, when applying the same equations to micropiles embedded in clay, a discrepancy will occur. The source of this discrepancy is that during undrained analysis, the shear resistance of clay is solely due to its adhesion property and not friction property. In addition, the shear resistance of clay in undrained analysis is independent of the in-situ horizontal stresses.

Since the micropiles were embedded in silty clay deposits, the Coulomb friction model needs to be modified to account for the adhesion rather than the friction at the interface

between the micropile and the clay. Recalling Equations 5.8 to 5.11 and by imposing an equivalent pressure upon applying the load in order to replace the in-situ horizontal stress by a constant stress along the interface equal to αs_u , Eq. 5.12 will take the form of:

$$\tau_{in} = (\Delta p) 1.0 \leq \alpha s_u \quad (5.14)$$

If the developed contact stress is less than αs_u , the interface will be sticking, while if the contact pressure increases than αs_u , slippage will occur.

To complete the tangential model, the stiffness of the interface is assigned through a tolerance elastic slip ratio as shown in Fig. 5.28. The relationship between the shear stress and the total slip is set analogous to the elastic-plastic material behaviour without hardening. In Fig 5.28, κ , the stiffness of the interface, corresponds to Young's modulus, and τ_{crit} corresponds to yield stress. Accordingly, sticking friction corresponds to the elastic regime, and slipping friction corresponds to the plastic regime. Defining this stiffness requires the selection of an allowable elastic slip, γ_i . The software manual recommends a value for γ_i that provides a balance between efficiency and accuracy, which is defined by:

$$\gamma_i = F_f \acute{l}_i \quad (5.15)$$

Where: F_f is the slip tolerance; its default value is 0.005; \acute{l}_i is the characteristic contact surface length

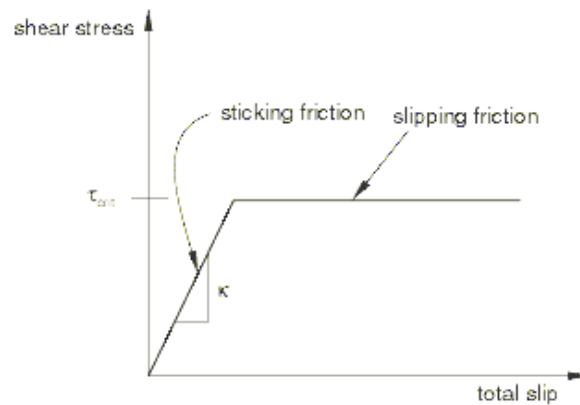


Figure 5. 28. Elastic slip versus shear traction relationship for sticking and slipping friction.

Defining an interface surface in ABAQUS requires specifying a contact formulation involving: a contact discretization; a tracking approach; and assignment of “master” and “slave” roles to the contact surfaces.

The master–slave contact formulation requires defining the slave and master surfaces. Generally, it is recommended that the master surface is selected as the surface of stiffer body or the surface with coarser mesh. Accordingly, the micropile surface was defined as the master surface and the soil was defined as the slave surface in all interaction formulations; either between the shaft surfaces or between the end bearing surfaces.

Two methods of discretization are available in ABAQUS: node-to-surface contact and surface-to-surface contact. With node-to-surface discretization, the contact conditions are established such that each “slave” node on one side of a contact interface effectively interacts with a point of projection on the “master” surface on the opposite side of the contact interface. Thus, each contact condition involves a single slave node and a group of nearby master nodes from which values are interpolated to the projection point. On

the other hand, surface-to-surface discretization considers the shape of both the slave and master surfaces in the region of contact constraints. The surface-to-surface formulation enforces contact conditions in an average sense over regions nearby slave nodes rather than only at individual slave nodes. The averaging regions are approximately centered on slave nodes, so each contact constraint will predominantly consider one slave node but will also consider adjacent slave nodes. The micropile–soil interface was modeled using surface-to-surface discretization to account for the average sense of penetration over the soil slave nodes.

In ABAQUS, there are two tracking approaches to account for the relative motion of two interacting surfaces in contact simulations: finite-sliding tracking and small-sliding tracking. Finite-sliding contact allows for arbitrary relative separation, sliding, and rotation of the contacting surfaces. In addition, the connectivity of the currently active contact constraints changes upon relative tangential motion of the contacting surfaces. Small-sliding contact assumes relatively little sliding of one surface along the other and is based on linearized approximations of the master surface per constraint. The micropile – soil interface was modeled using a finite-sliding tracking approach.

5.5.1.4 Solver analysis procedure

All FE simulations performed in this study employed the ABAQUS/Standard solver, in which the analysis are performed in steps and the Newton's method was used. Because large-displacement is expected during the analysis, geometrically nonlinear formulation is considered.

The model boundary conditions were assigned in the initial step. In order to establish the appropriate geostatic conditions, the initial step was followed by a geostatic step. Gravity loads or body forces were applied during this step to equilibrate the in-situ conditions given as initial stresses conditions. The equilibrium was checked in an iterative procedure to achieve a stress state that equilibrated the prescribed boundary conditions and loads.

Any number of static analysis steps can follow the geostatic step; the starting condition for each static general step is the ending condition from the last static general step. A total time period is assigned to the analysis as well as the time of each step “step time”. Figure 5.29 illustrates the relation of the analysis total time and the step time. Each step is divided into multiple increments. The “time” increments are fractions of the total step time. Two choices are available for controlling the incrementation scheme: automatic or user-specified. The default automatic incrementation scheme is used, in which initial, minimum, and maximum increments were specified.

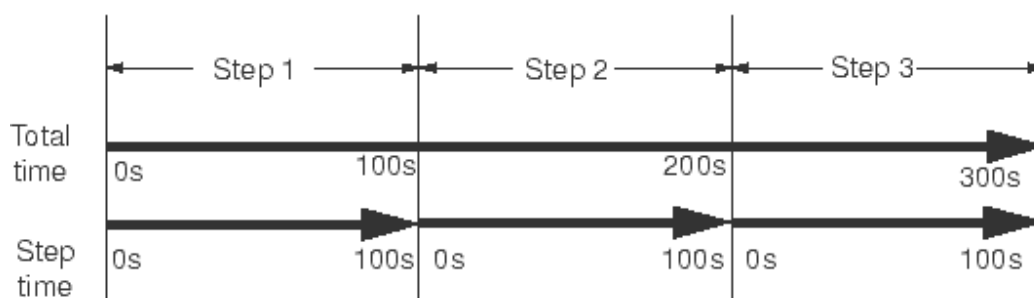


Figure 5. 29. Step and total time for a simulation

Two static analysis steps were used to calibrate the behaviour of the monotonic field tests. In the first step, “the contact step”, the contact between the micropile and the soil shaft and end bearing surfaces are established. This step simulated the change in the in-

situ stress due to the installation of the micropiles. It was followed by a static step where the load is applied at the head of the hollow core micropiles. Load control amplitude was used, similar to the load scheme used during the field load test.

5.5.2 Calibration of the monotonic field test results

The four hollow core micropiles were installed by flushing the hole using air under pressure. Upon reaching the desired depth, the grout was delivered under pressure at the pile toe and filled the annulus between the hollow bar and the sides of the hole. The hole was filled from the bottom to the top. Due to this installation process, it is anticipated that the grout column will have a bulb shape, with a variable cross section along its shaft. This cross-section variability must be considered in the numerical simulation to achieve a realistic representation of the pile behavior.

There is no clear information in the literature about the enlargement due the installation of hollow bar micropiles. Accordingly, a variable cross-section was employed to geometrically model the micropile shaft. The proposed geometry of the shaft comprises two different cross-sections: a lower segment that has an enlarged diameter, d_E , and starts from the pile toe up to a certain depth, and an upper segment up to the pile butt with diameter equal to the pile nominal (bit) diameter. The proposed geometry of the micropile is given in Fig. 5.30. The bottom segment, denoted as the enlarged segment, has a length of L_E . Hence, the length of the upper segment is $L - L_E$.

To establish the values of d_E and L_E , a trial-and-error methodology (depicted in Figure 5.31) was adopted to arrive at a representative geometric model of the hollow core micropile. The methodology is characterized by running the analysis based on the best

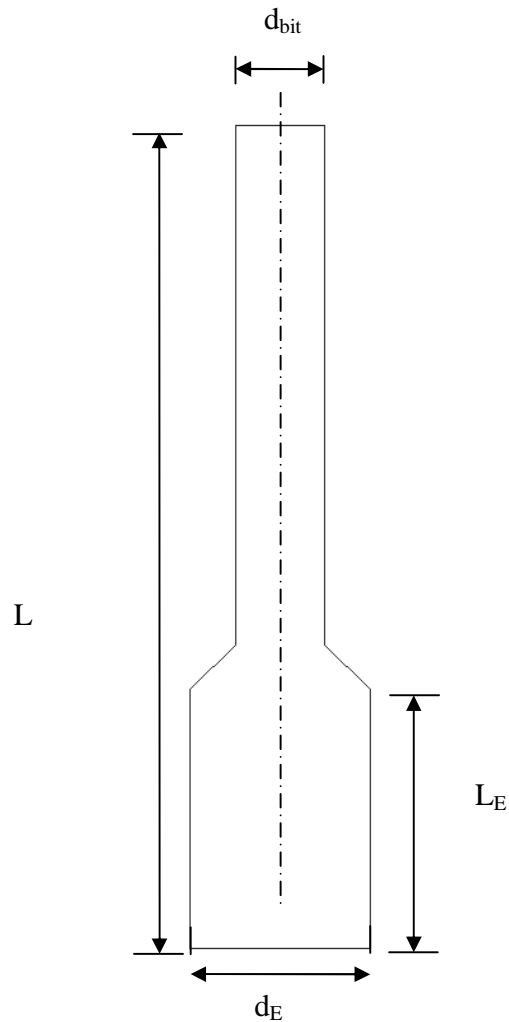


Figure 5. 30. The proposed micropile geometry

estimate soil properties evaluated from the soil investigation program presented in Chapter 3, and summarized in Table 5.6. Seventeen jobs have been tried to calibrate the monotonic field tests. The analysis stops upon reaching a calibration on both compression and tension field test results with the same geometric model. The acceptance criteria for a calibration job are:

- The adhesion factor, α , between the clayey soil along the micropile shaft and the micropile grout for compression and tension is less than or equal to 1.
- The adhesion factor between the clayey soil along the micropile shaft and the micropile in tension must be less than or equal to its corresponding value in compression for the same load amplitude.
- If two jobs could have calibration, the one with the lowest enlargement volume is considered.

The results are believed to be representative of the actual pile geometry, and hence, its behavior. This is particularly important because the calibrated geometric model will also be used to analyze the cyclic field load tests as well as the simulation of the micropile group that will be discussed in the following chapter.

Figures 5.32 to 5.34 illustrate the measured and calculated load displacement curves for compression field load tests on MP1, MP2, and MP3. The geometry of the calibrated FE model has an enlarged bottom segment with diameter of $1.75 d_{bit}$. This enlargement extends to $0.25 L$ measured from the pile toe. The adhesion factor of the clayey soil along the micropile shaft for compression and/or tension ranges between 0.9 and 1.

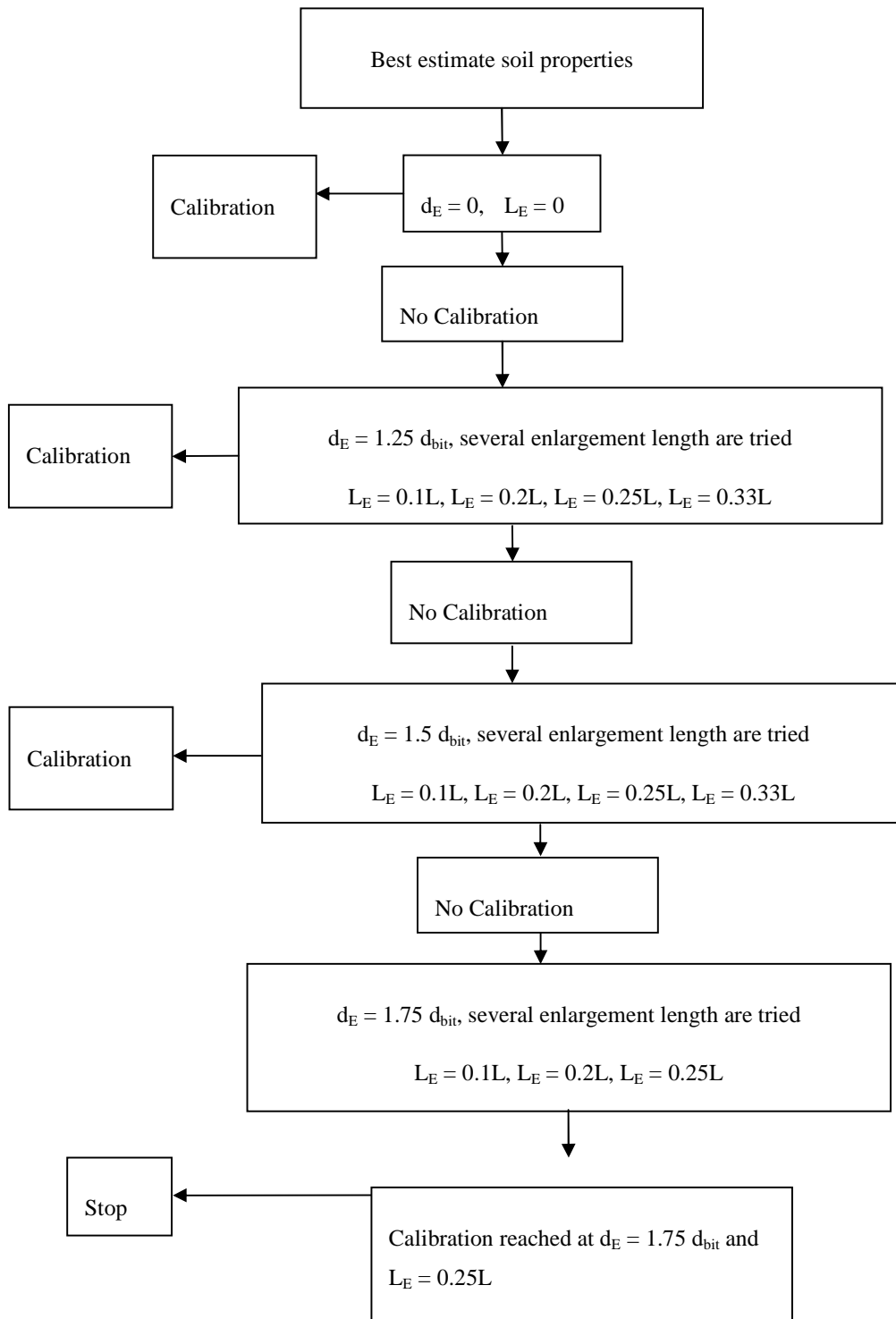


Figure 5. 31. Flow chart of the methodology used to evaluate d_E and L_E

However, because the micropiles were not loaded to failure, there is a level of uncertainty regarding the nonlinear portion of the FE model results. To resolve the aforementioned uncertainty, the experimental load test results are extended to higher load amplitudes utilizing a hyperbolic function. This methodology was introduced by Kulhawy and Mayne (1990) and Jeon (2004) to estimate the behavior of drilled shafts and micropiles at loads higher than the maximum applied load during the field test.

The hyperbolic function between the pile load and the head displacement is given by:

$$P = \Delta / (a + b \Delta) \quad (5.24)$$

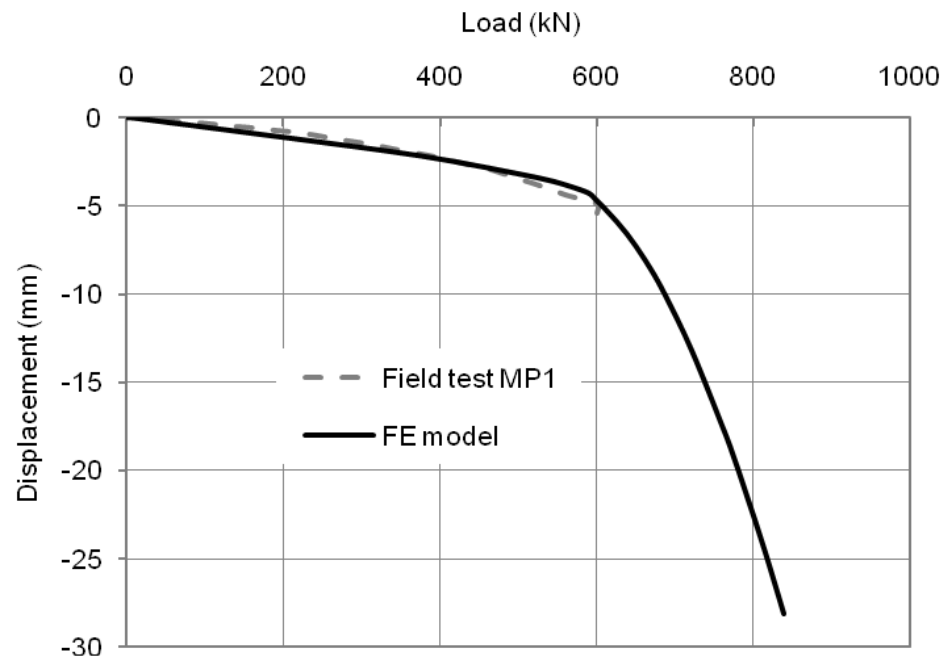


Figure 5. 32. Calibration of MP1 in compression

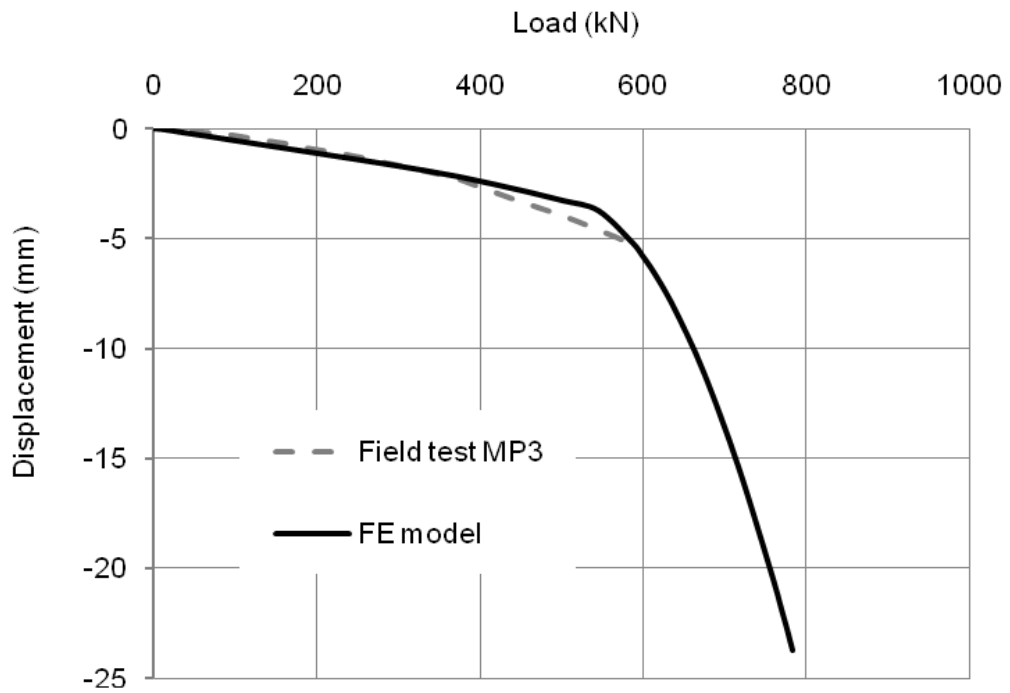


Figure 5. 33. Calibration of MP3 in compression

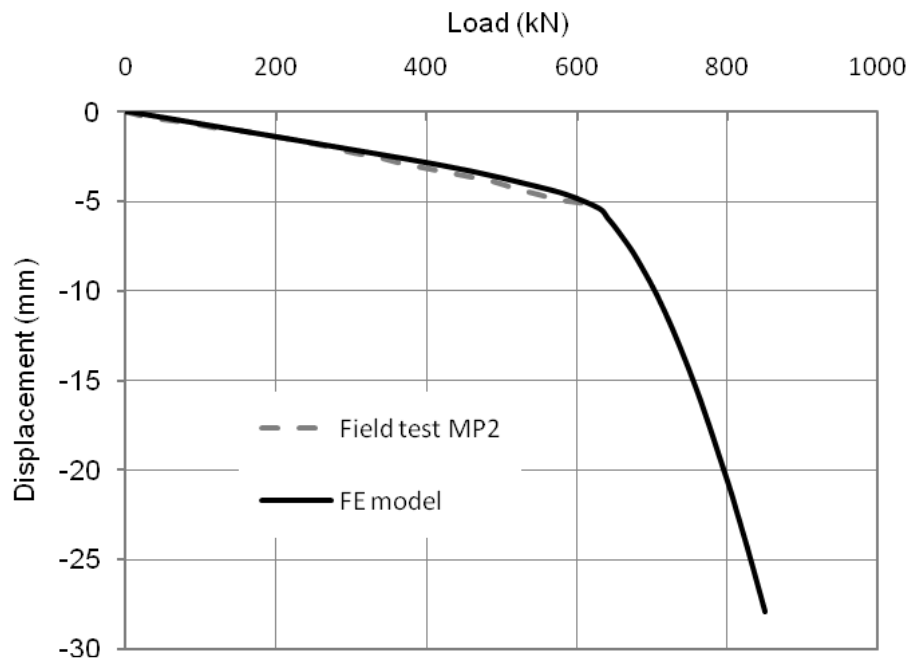


Figure 5. 34. Calibration of MP2 in compression

Where: P is the load at the pile head, Δ is the head displacement, a & b is curve fitting parameters.

The fitting parameters are obtained by plotting the relation between (P/Δ) and Δ . For micropile MP1, the parameters are found to be: $a = 0.003$ and $b = -0.012$. The field test results of MP1 are plotted in Fig. 5.35 together with the extended hyperbolic function curve utilizing the obtained fitting parameters. The hyperbolic function shows an excellent agreement with the field test results. Finally, the extended field results employing the hyperbolic function and the FE model results are plotted together in Fig. 5.36 for MP1 in compression. Similar favorable agreement is observed for the extended field test results within the non-linear portion of the curve.

Similarly, the calculated responses are in agreement with the uplift field test results displayed in Figs. 5.37 and 5.38 for MP2 and MP4, respectively. It should be noted that MP2 was loaded in tension first, then in compression and MP4 was loaded in tension only, i.e., the uplift loading was the first loading test for both piles.

The numerical models predicted brittle failure for the micropiles under tension. This brittle failure occurs as the shear stress reaches the shear strength at the grout-ground interface, and the stiffness of this region approaches zero. This phenomenon is known numerically as “snap through” where the model suddenly has no or negative stiffness, followed by partially gaining some of its stiffness with continuing loading. ABAQUS user manual recommends using implicit dynamic solver to overcome this phenomenon. However, another job was tried using the implicit dynamic solver, and the same behavior was obtained.

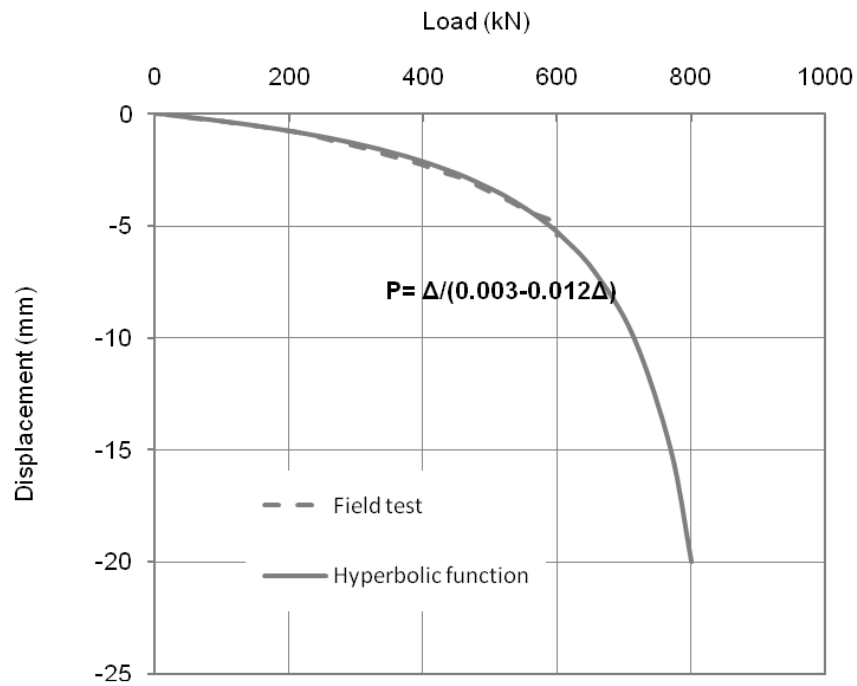


Figure 5.35. Field test results and hyperbolic function of MP1 in compression

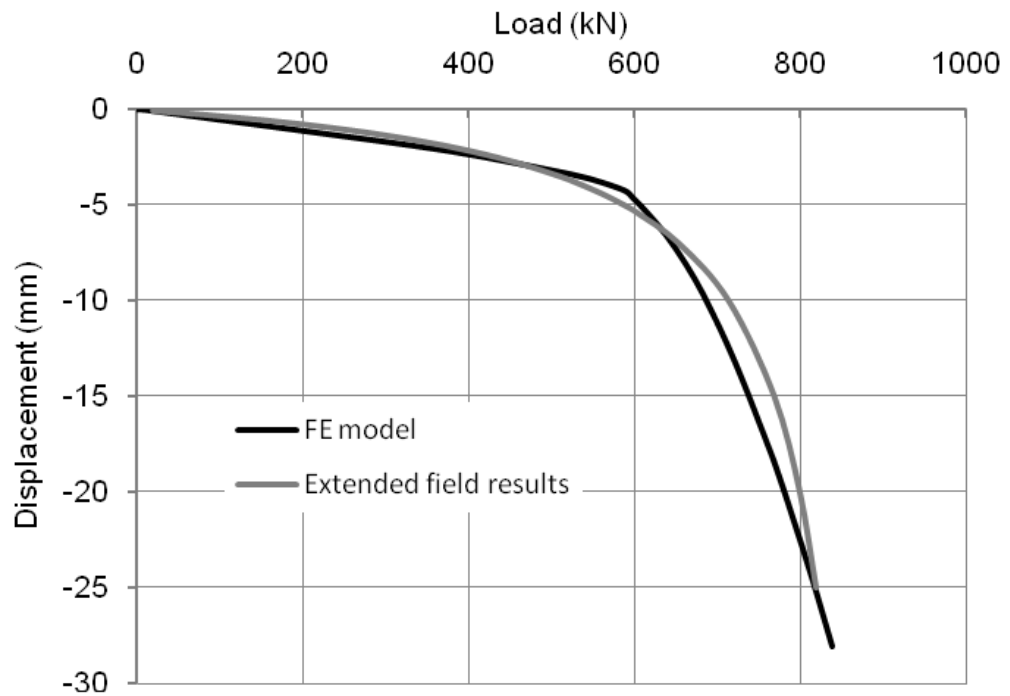


Figure 5.36. Extended field results and FE model for MP1 in compression

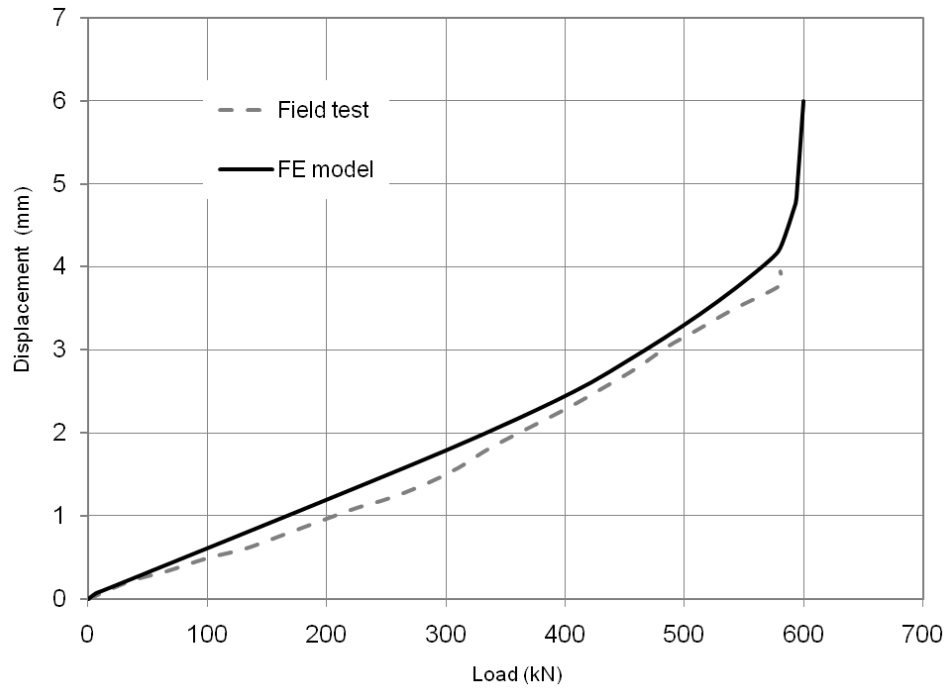


Figure 5.37. Calibration of MP2 in tension

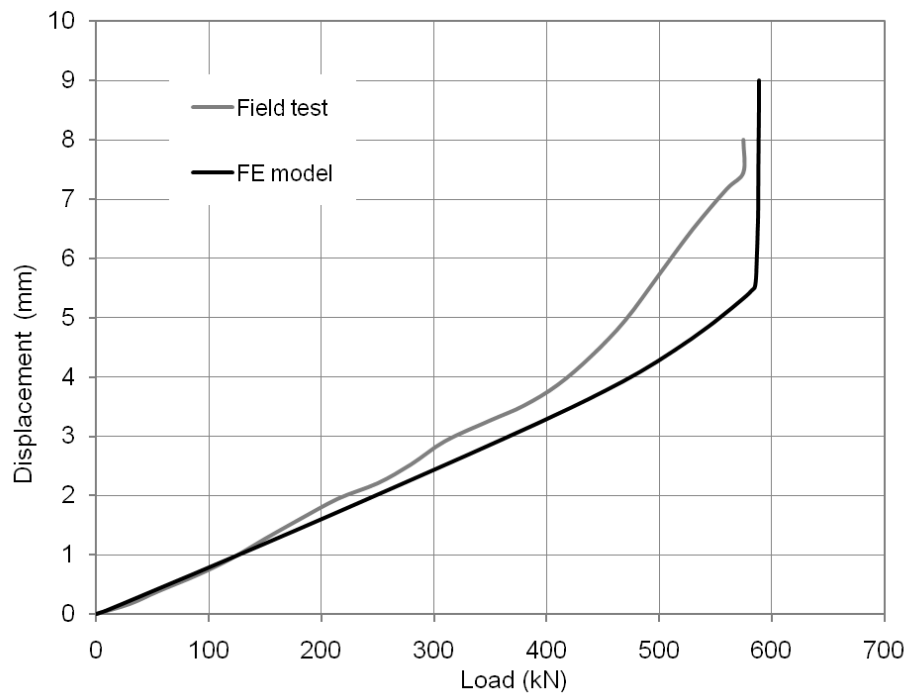


Figure 5.38. Calibration of MP4 in tension

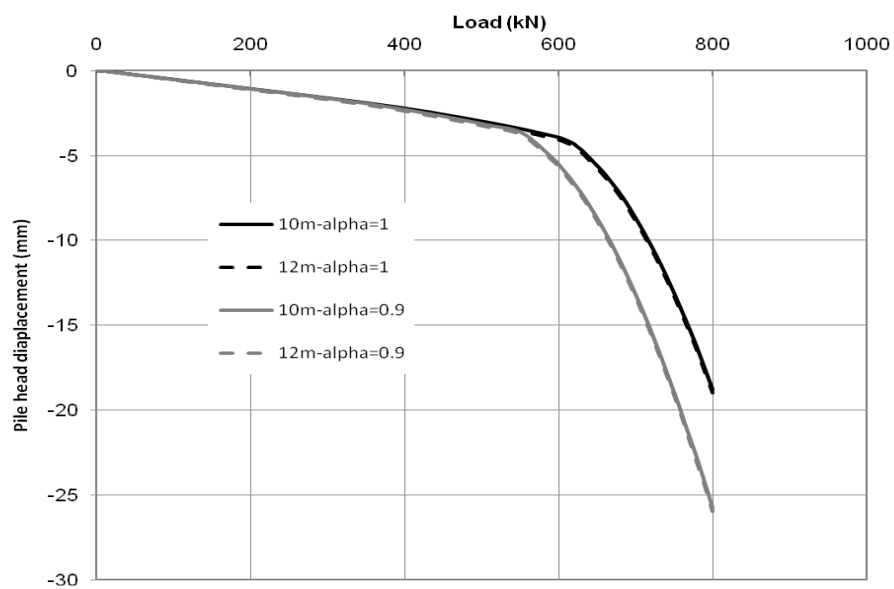
A mesh sensitivity analysis was carried out considering the verified model. Six models were created during the calibration phase incorporating the enlarged geometry of the micropile model. The aim of such analysis was to capture the effect of location of the bottom horizontal boundary and the total number of elements on the performance of the model.

Table 5.7 summarizes the two parameters assigned during the mesh sensitivity analysis. The analysis was carried out for micropiles under compression utilizing an adhesion factor within the range of the calibrated models, i.e. α is taken equal to 0.9 and 1.0. The number of elements was varied, while maintaining the aspect ratio of elements at the soil-micropile interface around 1. Figure 5.39 illustrates the effect of the horizontal boundary on the capacity of the micropile for Mesh_1. It is obvious that increasing the distance to the bottom boundary from 0.75 L to L has no effect on the micropile capacity. The same observation was recognized for different number of elements (i.e. meshes). This is consistent with the findings of Helwany (2007).

The effect of number of elements is depicted in Figs. 5.40 and 5.41, for the two horizontal boundaries assigned previously. All meshes produced the same pile response during the initial loading level. However, as the loading progressed and the pile response displayed non-linear behavior, the calculated responses started to diverge. As anticipated, the coarse mesh, Mesh_2, gives stiffer response than the other two meshes. For all levels of horizontal boundary and interaction models considered, the differences between Mesh_1 and Mesh_3 results were marginal.

Table 5. 7. Summary of the mesh sensitivity analysis parameter used

Designated mesh name	Model Depth (m)	Number of soil elements	Number of pile elements	Total number of elements
Mesh_1_12	12	18824	794	19618
Mesh_2_12	12	4967	289	5256
Mesh_3_12	12	41452	1517	42969
Mesh_1_10	10	17464	794	18258
Mesh_2_10	10	4673	289	4962
Mesh_3_10	10	37357	1517	38874

**Figure 5. 39. Effect of horizontal boundary in Mesh_1**

At the maximum applied load, the difference in pile head response for Mesh_1 and Mesh_3 is 5%, with Mesh_1 resulting in a slightly smaller response. This ratio decreases to less than 2% at 0.9 the maximum applied load, i.e. load =720 kN. On the other hand, the difference in response between Mesh_2 and Mesh_1 is 20% at load = 800 kN and about 12 % at load =720 kN. Considering the results obtained from the mesh sensitivity analysis, it was decided to consider Mesh_1 (19618 elements) with 10m length in the parametric study, which is same as that used in the calibration of the field load tests.

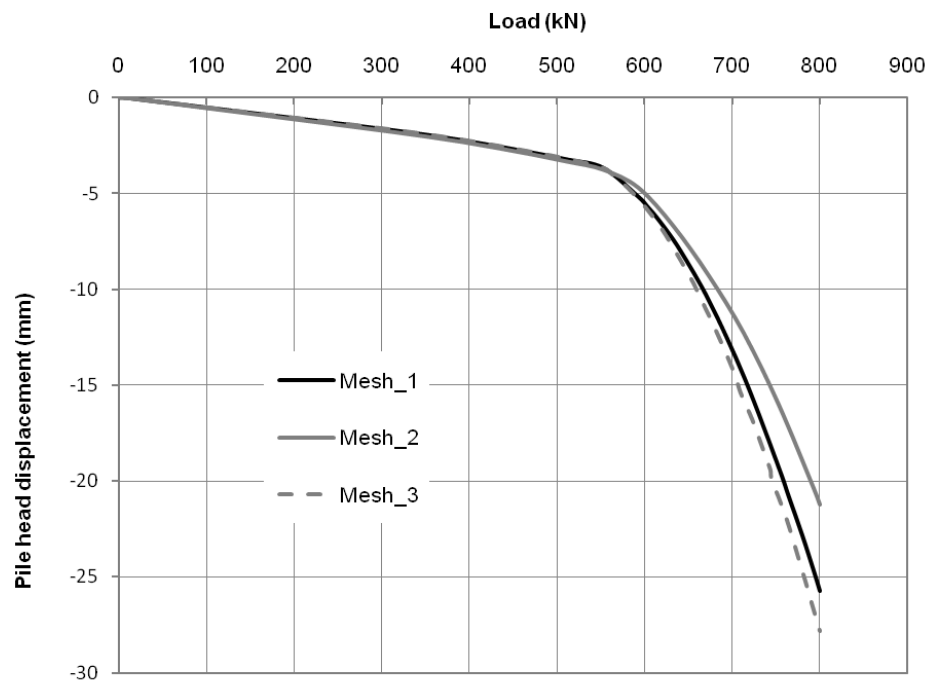


Figure 5. 40. Effect of number of elements on the micropile capacity, 10m model, $\alpha = 0.9$

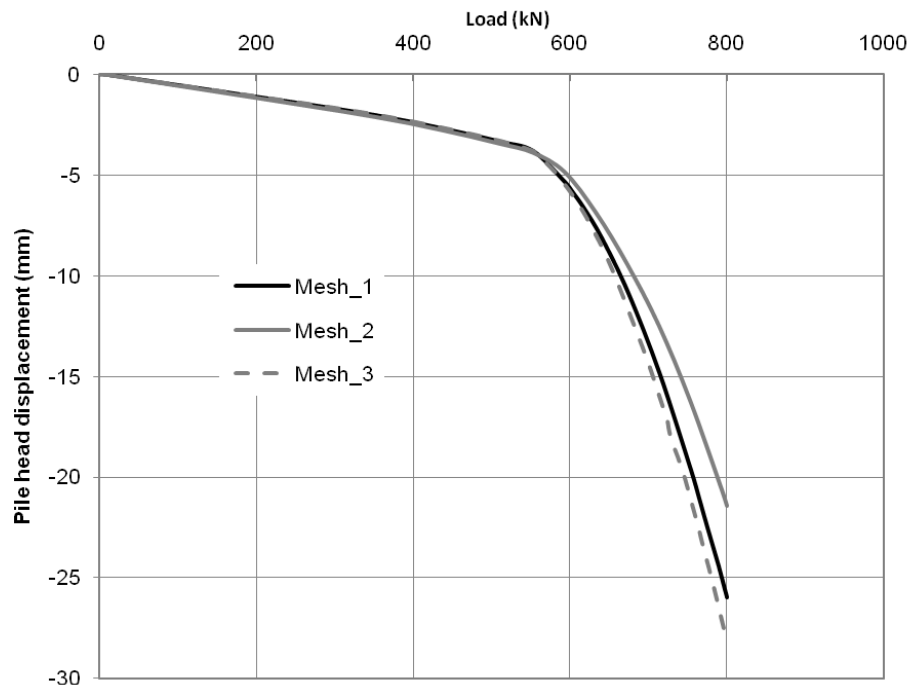


Figure 5. 41. Effect of number of elements on the micropile capacity, 12m model, $\alpha = 0.9$

5.5.3 Failure Criteria

The micropile load–displacement curve can be used to assess its performance under axial loading and to evaluate its ultimate capacity. The pile failure load may be defined as the load when the pile plunges or settlement occurs rapidly under sustained load (Prakash and Sharma, 1990). If plunging does not occur promptly, another definition for the pile ultimate load is needed, which preferably should be characterized by a mathematical rule.

The objective of a failure criterion is to consistently estimate the amount of loading and/or settlement associated with the failure condition. In other words, a failure criterion is used to characterize the pile ultimate load capacity according to a specific

mathematical condition. Hence, the term “interpreted failure load” is more appropriate to indicate that the failure load will be interpreted according to a specific criterion.

If the pile is loaded to a true failure point, the load-displacement curve would display three different regions: an initial linear region with a large slope, a strongly non-linear (transient) region, and finally, a nearly linear region with a small slope. Most of the failure criteria place the interpreted failure load within the nonlinear region of the load-displacement curve. Therefore, once a suitable factor of safety is applied, the design load of the pile will lie within the initial linear region of the curve. This will yield predictable load-displacement behavior and avoid any abrupt settlement.

The factor of safety is usually determined based on several factors that include the uncertainty related to the spatial variability of the soil properties, the effects of pile installation technique, the load transfer mechanism for the pile, the nature of loading and the pile configuration. The load transfer mechanism for micropiles is different than those for traditional piles due to the method of installation employed for micropiles. Hence, the failure criterion and safety factor should be established accordingly.

There are numerous interpreted failure criteria that are used for different pile types and in different building codes. Table 5.8 lists some of the most commonly used failure criteria for classifying the failure load for micropiles. The methods given in Table 5.8 can be divided into two main categories: failure criteria with settlement limitation, and failure criteria with graphical construction. The first two methods given in Table 5.8 are failure criteria with settlement limitation related to the pile diameter.

Those methods are difficult to apply to a micropile because of the variability in axial stiffness over the length of the micropile (due to different diameter). On the other hand, the last two methods are based on graphical construction on the load-displacement curve. Therefore, they depend on the actual performance of the micropile under the applied load without involving any pile and/or soil property. The two methods will be applied to the calibrated models. The most applicable method will be chosen for further analysis conducted on micropiles, i.e. the parametric study.

Table 5. 8. Most common failure criteria for micropiles

Failure criteria	Failure load definition	Remarks
Davisson's offset limit criterion, 1972	Load corresponding to total settlement at the pile head = $PL/AE + d/120 + 4$ (mm)	
Reese and O'Neil, 1988	Load corresponding to total displacement = 5% d	FHWA (1988) criterion
Butler and Hoy, 1977	Load at intersection of tangent sloping at 0.14mm/kN and tangent to initial straight portion of total settlement curve	NYSDOT (2008)
Fuller and Hoy, 1970	Minimum load for a rate of total settlement of 0.14mm/kN	FHWA (2005)

Figures 5.42, 5.43, and 5.44 show the failure criteria applied to the load-displacement curves for MP1, MP2, and MP3. The interpreted failure load of each micropile according to the aforementioned two failure criteria is given in Table 5.9.

The failure load obtained from Fuller and Hoy (1970) method is equal to 1.15 that obtained from Butler and Hoy (1977) intersection method for all micropiles. Interestingly, the failure load according to Butler and Hoy (1977) is matching with the 5% D criterion, if D is considered as the drilling bit diameter of the hollow bar micropile.

Using a factor of safety equal to 2, the design load obtained from Butler and Hoy (1977)'s failure load will lie within the initial linear region of the load –displacement curve. However, applying the same factor of safety to the failure load computed using Fuller and Hoy (1970) method will locate the design load at the brink of the initial linear region. It seems that Butler and Hoy (1977) failure criterion is more applicable to the hollow bar micropiles. Further discussion on the most suitable method to evaluate the failure load will be given in the next section.

Table 5. 9. Failure loads for Micropiles in compression

	Butler and Hoy 1977 (intersection) (NYSDOT 2008)	Fuller and Hoy, 1970 FHWA (2005)
MP1	665	765
MP2	695	790
MP3	645	745

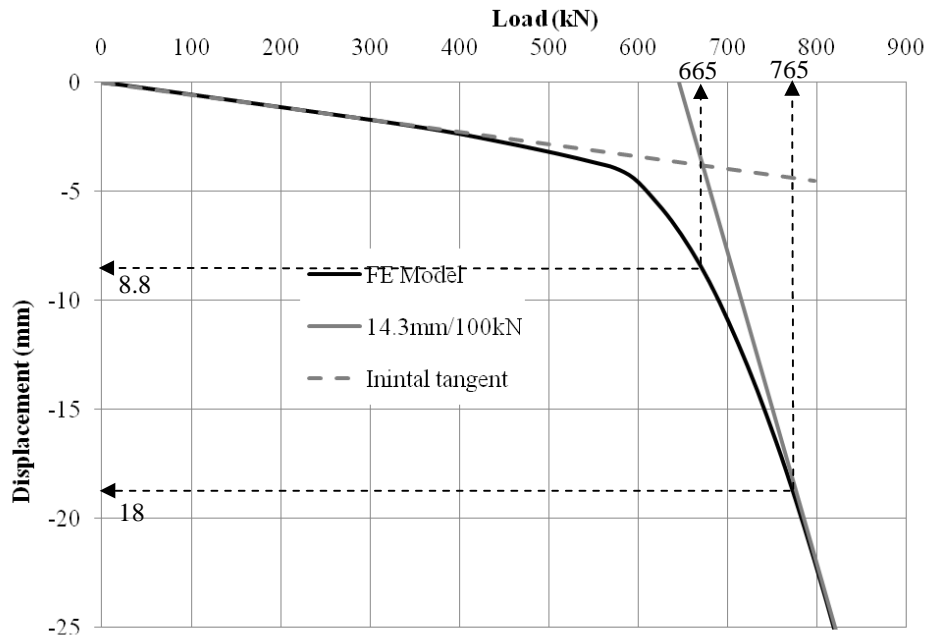


Figure 5. 42. Failure load MP1 compression

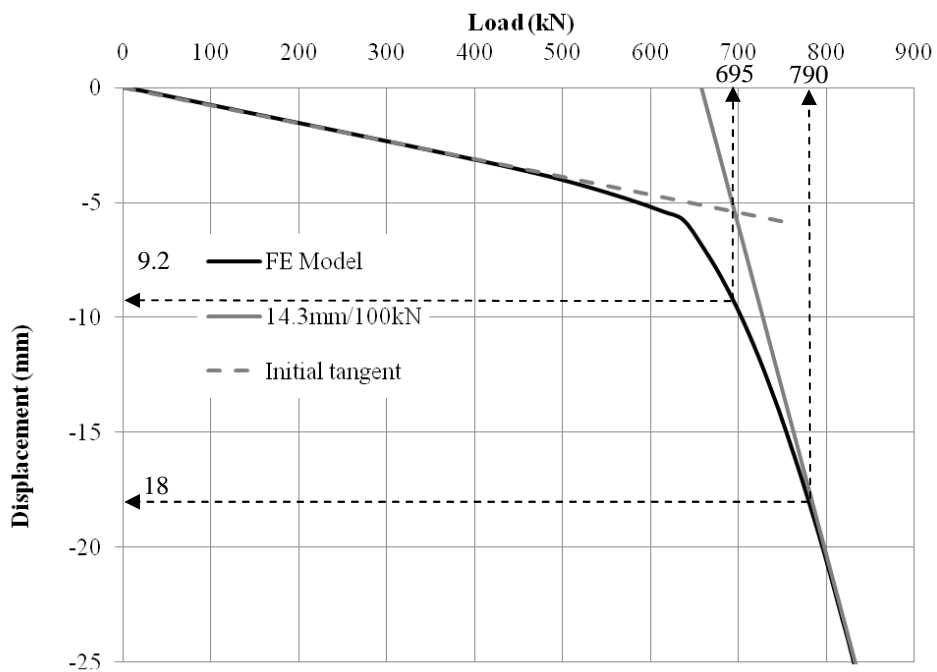


Figure 5. 43. Failure Loads MP2 in compression

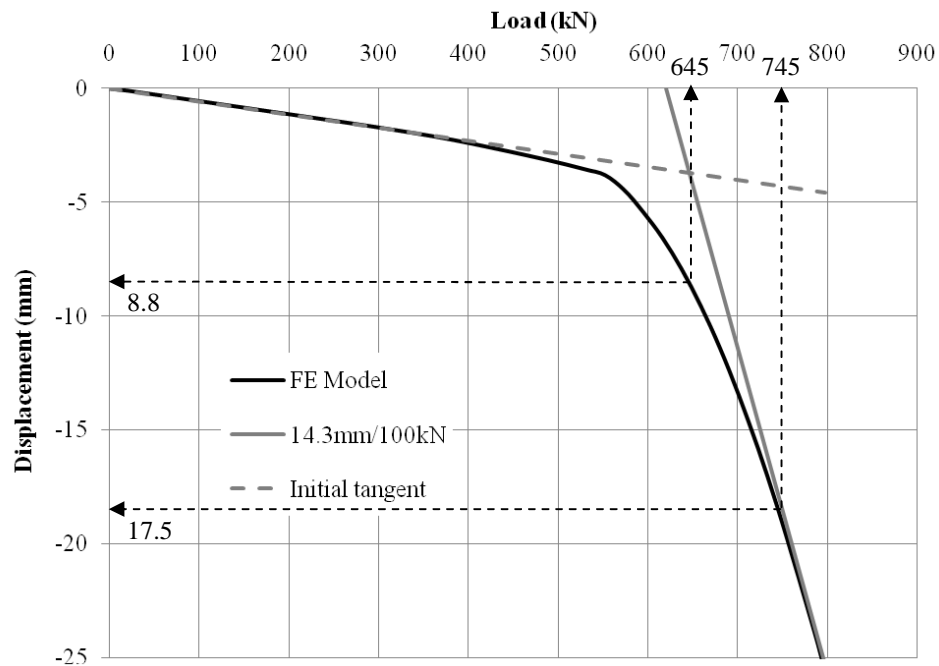


Figure 5.44. Failure load MP3 Compression

5.5.4 Load transfer mechanism

A micropile transfers all or most of its load to the soil via skin friction resistance along its shaft. Due to its small diameter, it is believed that the micropile has reached failure when the pile starts to behave in an end bearing fashion. The micropile behaves in an end bearing fashion when the entire load applied to the pile head is transferred to the soil through the pile toe. However, most of the data published about the load transfer mechanism of micropiles shows that the micropile does not show true failure upon mobilizing full resistance along its shaft. There is some end bearing resistance that is contributing to the micropile resistance upon reaching failure. In hollow bar micropiles, the same load transfer mechanism is expected as that of micropiles. For any failure

criterion, most of the pile load will be transferred through the pile shaft, with a small portion of the load transfer to the soil at the pile toe.

Hence, there is a need to understand the load transfer mechanism of the hollow bar micropile along the shaft and the amount of load transfer at the pile toe, if any, for a specific failure criterion. The load transfer mechanism of the hollow bar micropiles is evaluated employing the calibrated FE models. The amount of load transfer to the soil at any elevation at different load amplitudes is calculated from:

$$P_{ij} = (\sigma_z)_{ij} A_i \quad (5.25)$$

Where: P_{ij} is the load transfer at elevation i due to load applied j ; $(\sigma_z)_{ij}$ is the axial stress at elevation i due to load amplitude j ; A_i is the cross section of the pile at elevation i

The load transfer mechanisms for the three compression tests are given in Figs. 5.45, 5.46, and 5.47, for MP1, MP2, and MP3. The load was calculated at elevations that coincide with the beginning and ending of each subsurface layer specified previously in Table 5.6.

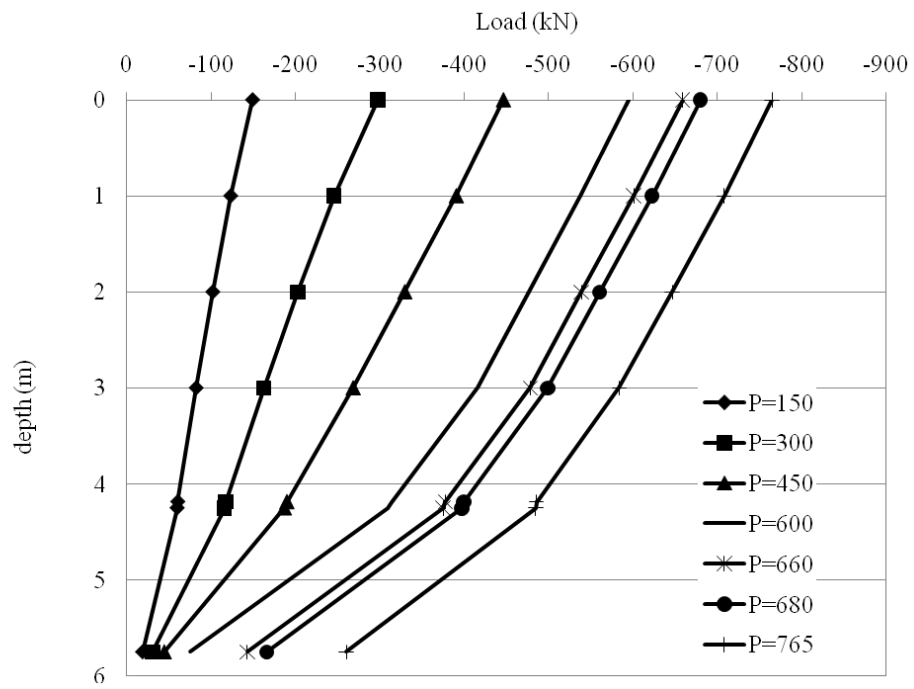


Figure 5. 45. Load transfer for MP1 Compression

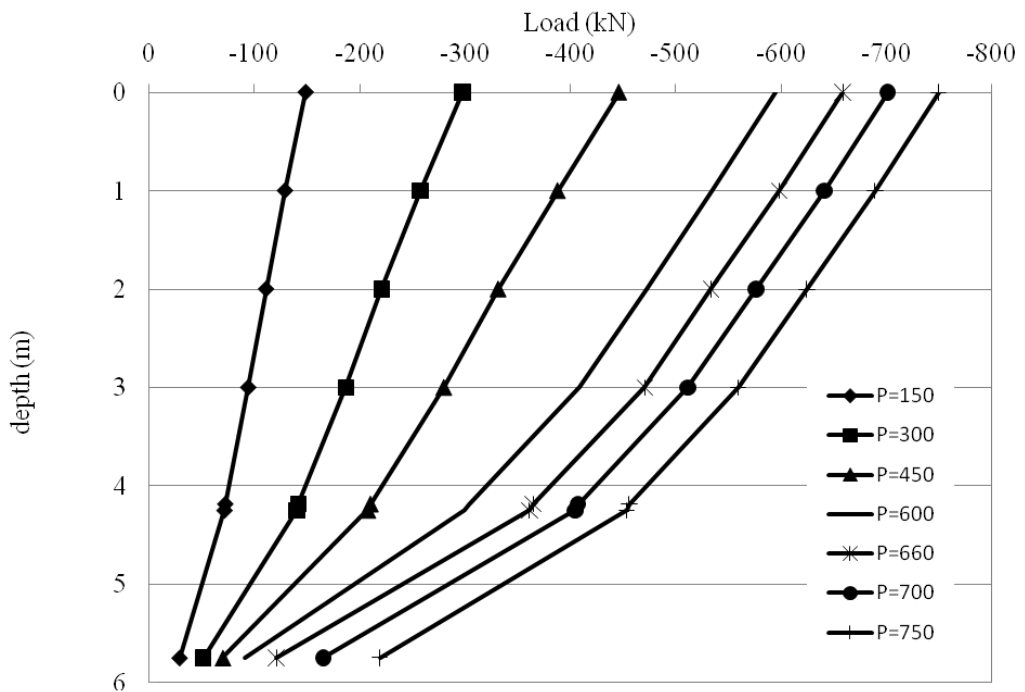


Figure 5. 46. Load transfer for MP2 Compression

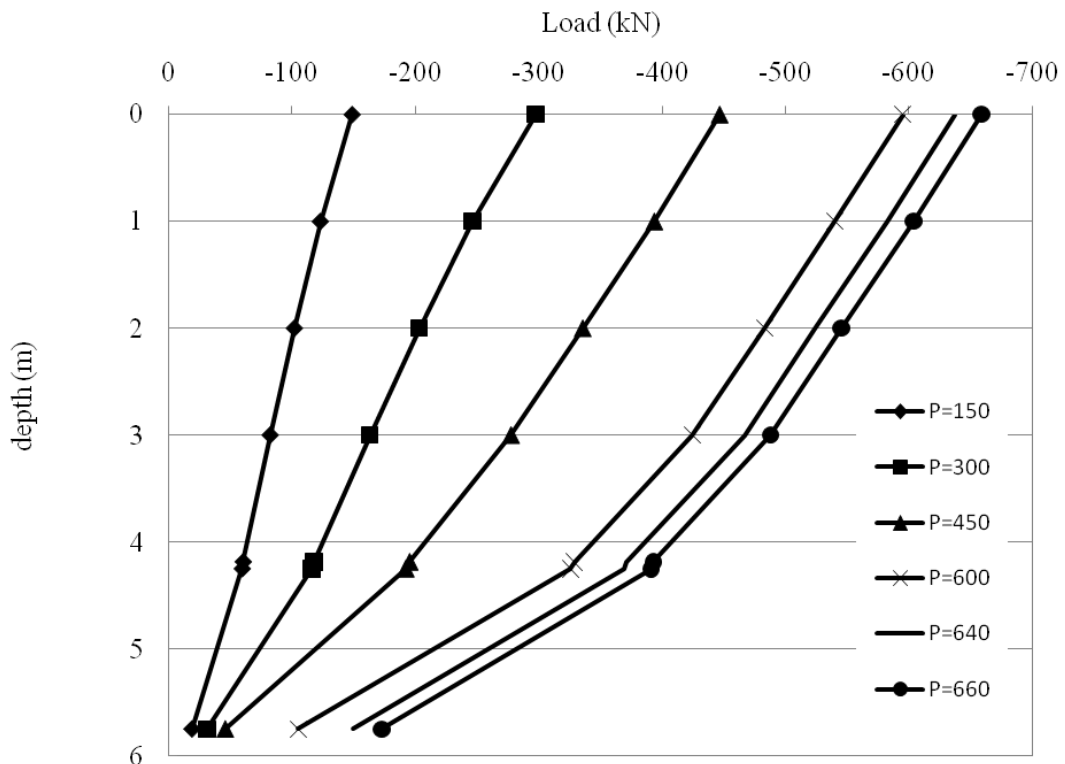


Figure 5. 47. Load transfer for MP3 in compression.

For MP1, Figure 5.45 shows the following: at load 600 kN, 88 % of the applied load is transferred to the soil via the micropile shaft, and only 12% is transferred through the pile toe. As the applied load increased from 600 to 660 kN, most of the additional load increment (55kN) is transmitted to the soil through pile toe. It seems that most of the shaft resistance is mobilized at 660 kN. When the applied load increases from 660 to 680 kN, the ratio of the load transfer to the pile toe increases to 24 %, and the amount of load transferred at the pile toe is about 20kN.

This indicates that between 660kN and 680kN, any additional loading to the micropile will be transferred to soil in a pure end bearing mechanism, after the whole shaft

resistance has been mobilized. Butler and Hoy (1977) method gives a failure load of approximately 665 kN whilst the Fuller and Hoy (1970) gives a failure load of 765 kN. Figure 5.45 shows that at a load of 765 kN, 1/3 of the load applied at the pile head is transfer to the soil through the toe.

For load transfer mechanism of MP2 given in Fig. 5.46; up to a load equal 660 kN, the amount of load transfer to the soil at the pile tip is about 17%. Then, the load is increased to 680 kN, and consequently, the ratio increases to 21%. When the load applied at the pile head increases from 680 to 700 kN, the amount of load transferred through at the pile tip is 19kN. Hence, it seems that between load of 680 kN and 700 kN the micropile starts to behave as an end bearing pile. Micropile MP2 has a failure load of 695 kN according to the intersection method pre-scribed previously. This value is between 680 and 700 kN.

The load transfer of micropile MP3 illustrated in Fig. 5.47 shows that the shaft resistance of the micropile has been totally mobilized at a load equal to 600 kN. However, when increasing the load from 600 to 640 kN, the amount of load transfer at the pile tip is less than 40 kN, which implies further resistance of the pile shaft. After 640 kN, the amount of load applied at the pile head is almost equal to the amount of load transfer at the pile tip. Interesting, the failure load according to Butler and Hoy (1977) for MP3 is 640 kN.

It can be concluded from the load transfer curves illustrated in Figs. 5.45 to 5.47 that the failure load obtained utilizing Butler and Hoy failure criterion is best describe the behavior of the hollow bar micropiles. In addition, the failure load obtained from the aforementioned failure criterion shows that this load is not only restricted to shaft

resistance of the micropile. Also, it is limited, but there is a contribution of the micropile end bearing resistance at the micropile tip.

The shear stress developed at the soil/micropile interface can be estimated from the load transfer curves. Figure 5.48 depicts the developed average shear stress along the micropile length at approximately the failure load obtained previously. The adhesion stress developed shows that the value of the adhesion factor, α , is between 0.9 and 1.0. Due to the limited field tests conducted, a variation of α with s_u is difficult to be developed. However, Fig. 5.48 suggests to use $\alpha=0.9$ as a lower bound and $\alpha = 1.0$ as an upper bound for soils characterized by s_u between 90 and 175 kPa, in calculating the hollow bar micropile shaft resistance.

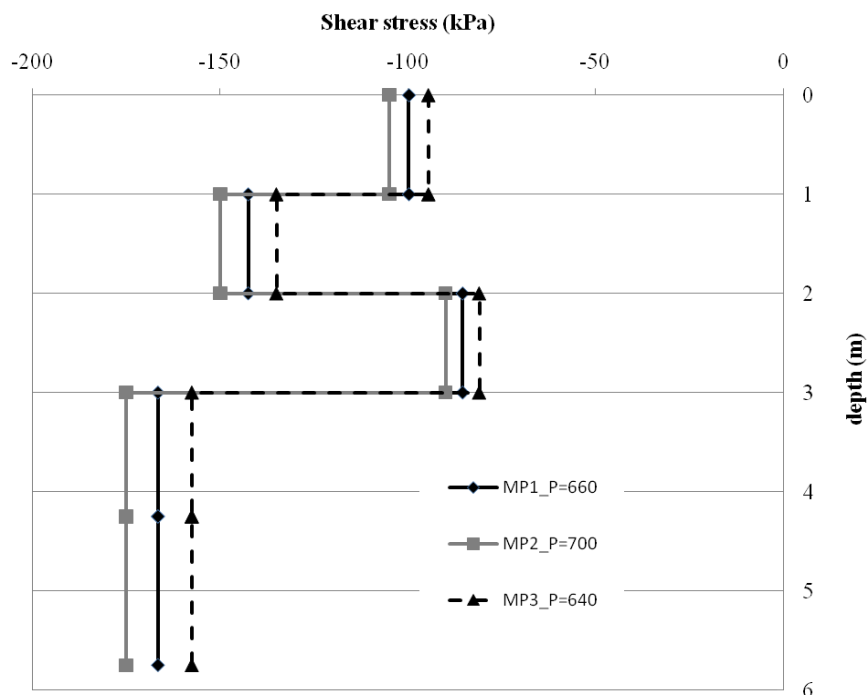


Figure 5. 48. Shear stress along the micropile at failure loads

The same procedure is followed in analyzing the FE model calibrating the uplift field test. However, in contrary to the compression loading, the failure in the uplift direction is abrupt. Thus, the uplift capacity of the hollow bar micropile can be determined readily from the load-displacement curve. Figures 5.37 and 5.38 show that MP2 started to “plunge” upwards when reaching a load of 600 kN, while MP4 plunged at 590 kN.

The calibration analysis reveals that there is a need to correlate the failure load obtained for each micropile to the shear strength of the soil surrounding the pile as well as the geometry of the micropile. Thus, a parametric study is carried in order to propose an equation that can estimate the capacity of the hollow bar micropile in clayey soils.

5.5.5 Parametric study

The calibrated FE model was used to perform a parametric study. In this study, the proposed geometry of the hollow bar micropile was subjected to soil conditions different than that used to calibrate the field test. However, the study was limited to the hollow bar micropiles embedded in clayey soils. It is anticipated that if this type of micropiles is embedded in sandy soil, its performance and behavior will be different.

The performance of hollow bar micropile is installation-dependent, thus the enlargement in its geometry in ground would change according to the installation technique employed. As shown in the previous section, the enlargement in the hollow bar micropile geometry affected the shaft resistance of the micropile profoundly. Hence, the enlargement in the hollow bar micropile geometry was investigated in this parametric study. The hollow bar micropile geometry was considered in terms of different enlargement values for diameter, d_E , and length, L_E .

The parameters used in the study are:

- Micropiles are embedded in clayey soil with s_u varying from 90 kPa to 175 kPa.
- The soil adhesion factor is considered to vary between 0.9 and 1.0.
- The slenderness ratio of the hollow bar micropiles, $d_E, L/d$, is 30 and 50.
- The enlargement in micropile diameter, d_E , varies from 25% to 100 % of the drilling bit diameter.
- The length of enlarged section varies from 0.1 to 0.33 of the micropile length.

Meanwhile, the following parameters are kept constant throughout the study:

- Unit weight of soil
- The lateral earth pressure of soil
- Poisson's ratio; for clayey soil assigned at 0.45.
- The grout and steel material properties.

For each job within the parametric study analysis, three load values are computed. These load values are: the failure load according to Butler and Hoy method, Q_F ; the amount of load transfer to the soil through skin friction, Q_{shaft} ; and the amount of load transfer through end bearing, Q_{bearing} . An example of how the three values are evaluated is illustrated in Figs.5.49 and 5.50.

Figure 5.49 shows the load – displacement curve for a job characterized by the following: the micropile is embedded in clayey soil with $s_u = 150\text{kPa}$, $\alpha = 1.0$ and $L/d = 30$. The enlarged micropile diameter is 75% of the bit diameter and the length of enlarged section is 1.5 m from the micropile tip. The load values are calculated in three steps:

Step 1: failure load is evaluated as shown in Fig. 5.49, which shows that $Q_F \approx 614\text{ kN}$.

Step 2: at failure load, the amount of load transfer to the soil at the pile tip, Q_{bearing} , is computed. Figure 5.50 depicts the distribution of the load along the micropile length at load $\approx 614\text{ kN}$.

Step 3: the shaft resistance, Q_{shaft} is $Q_F - Q_{\text{bearing}}$.

This procedure is followed in all cases. For convenience, the results of the parametric study are presented in tabular format.

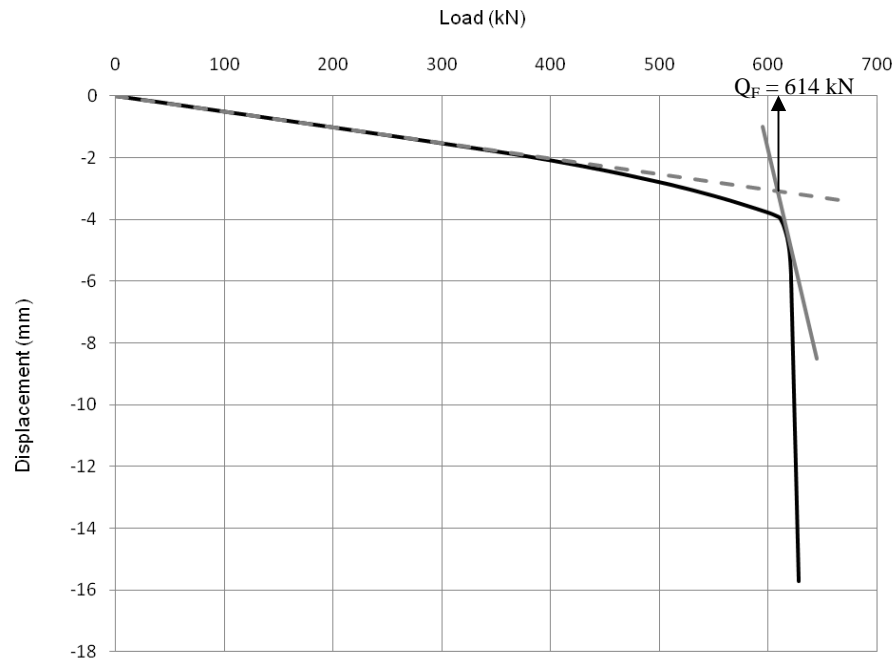


Figure 5. 49. Example of failure load obtained at $s_u = 150\text{kPa}$, $\alpha = 1.0$, $L/d = 30$

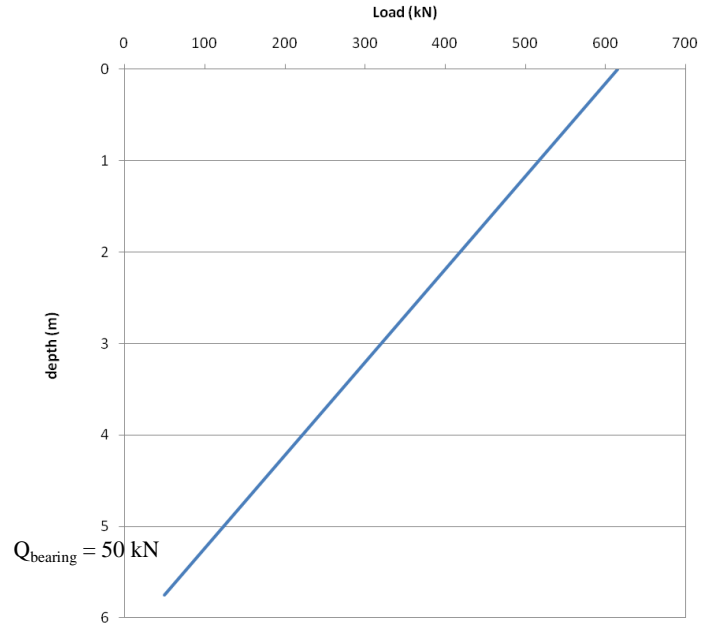


Figure 5. 50. Load distribution obtained at $Q_F = 614 \text{ kN}$, $s_u = 150\text{kPa}$, $\alpha = 1.0$, $L/d = 30$

Table 5. 10. Compression capacity of hollow bar micropile, $L = 5.75\text{m}$, $L/d = 30$, $d_E = 1.25d$

s_u kPa	$L_E = 1.5 \text{ m}, \alpha = 0.9$			$L_E = 2.0 \text{ m}, \alpha = 1.0$		
	Q_{shaft} kN	Q_{bearing} kN	Q_F kN	Q_{shaft} kN	Q_{bearing} kN	Q_F kN
90	274	18.5	293	308	18	326
100	304	20	324	342.3	19.7	362
120	364.4	22.6	387	410.7	23.3	434
140	424.8	25.5	450.3	478.8	26.5	505.3
150	455	27	482	513.3	28.2	541.5
160	485	31	516	547.5	29.5	577
175	531	34	565	599.3	32	631.3

Table 5. 11. Compression capacity of hollow bar micropile, $L = 5.75\text{m}$, $L/d = 30$, $d_E = 1.5d$

s_u kPa	$L_E = 1.5 \text{ m}, \alpha = 1.0$			$L_E = 2.0 \text{ m}, \alpha = 1.0$		
	Q_{shaft} kN	Q_{bearing} kN	Q_F kN	Q_{shaft} kN	Q_{bearing} kN	Q_F kN
90	321.22	24.78	346	332.46	24.54	357
100	356.8	26.2	383	369.3	26.5	395.8
120	428.3	30.7	459	443.04	32.46	475.5
140	499.2	34.8	534	517.7	36.3	554
150	535.2	37.8	573	554.2	39.8	594
160	571.8	38.7	610.5	591	42	633
175	624.5	45.5	670	646	45	691

Table 5. 12. Compression capacity of hollow bar micropile, $L = 5.75\text{m}$, $L/d = 30$, $d_E = 1.75d$

s_u kPa	$L_E = 1.5 \text{ m}, \alpha = 0.9$			$L_E = 1.5 \text{ m}, \alpha = 1.0$		
	Q_{shaft} kN	Q_{bearing} kN	Q_F kN	Q_{shaft} kN	Q_{bearing} kN	Q_F kN
90	306.3	30.2	336.5	339.85	30	369.85
100	340	32.5	372.5	377.5	33.5	411
120	408.5	38	446.5	452.75	40.75	493.5
140	475.98	44.52	520.5	528.2	46.4	574.6
150	510	49	559	564	50	614
160	544	54.5	598.5	603.2	51.8	655
175	595.3	60.7	656	659.7	57.8	717.5

Table 5. 13. Compression capacity of hollow bar micropile, $L = 5.75\text{m}$, $L/d = 30$, $d_E = 1.75d$

s_u kPa	$L_E = 1.0 \text{ m}, \alpha = 1.0$		
	Q_{shaft} kN	Q_{bearing} kN	Q_F kN
90	328	30	358
100	363	32	395
120	437	37	474
140	510	41	551
150	546.6	45.4	592
160	583	47.8	630.8
175	637.4	51	688.4

Table 5. 14. Compression capacity of hollow bar micropile, $L = 5.75\text{m}$, $L/d = 30$, $d_E = 2d$

s_u	$L_E = 1.0 \text{ m}, \alpha = 1.0$			$L_E = 1.5 \text{ m}, \alpha = 0.9$		
	Q_{shaft} kN	Q_{bearing} kN	Q_F kN	Q_{shaft} kN	Q_{bearing} kN	Q_F kN
90	345.77	38.03	383.8	326.5	41	367.5
100	384	41	425	362.8	42.5	405.3
120	459.7	48.3	508	435.2	50.8	486
140	535.45	54.55	590	507.7	57.5	565.2
150	574.03	58.77	632.8	543.1	65.2	608.3
160	611.2	64.8	676	579.3	67.7	647
175	667.9	72.8	740.7	632.4	78.6	711

Table 5. 15. Compression capacity of hollow bar micropile, $L = 8.8\text{m}$, $L/d = 50$, $d_E = 1.25d$

s_u	$L_E = 1.5 \text{ m}, \alpha = 1.0$			$L_E = 2.2 \text{ m}, \alpha = 0.9$		
	Q_{shaft} kN	Q_{bearing} kN	Q_F kN	Q_{shaft} kN	Q_{bearing} kN	Q_F kN
90	454.3	21.3	475.6	416.3	22	438.3
100	504.7	22.8	527.5	463	24	487
120	606	27	633	556.4	28	584.4
140	707	30	737	649	30	679
150	757.3	31	788.3	695.9	31	726.9
160	808	32.5	840.5	742	35	777
175	883.8	36.5	920.3	811.3	36	847.3

Table 5. 16. Compression capacity of hollow bar micropile, $L = 8.8\text{m}$, $L/d = 50$, $d_E = 1.5d$

s_u kPa	$L_E = 1.5 \text{ m}, \alpha = 1.0$			$L_E = 2.2 \text{ m}, \alpha = 1.0$		
	Q_{shaft} kN	Q_{bearing} kN	Q_F kN	Q_{shaft} kN	Q_{bearing} kN	Q_F kN
90	473.54	28.46	502	491	28	519
100	526.15	30.25	556.4	545.1	29.9	575
120	631.5	34	665.5	654.6	34.9	689.5
140	736.8	38	774.8	763.6	38.7	802.3
150	789.2	39.8	829	818.1	40.5	858.6
160	842	42.5	884.5	872.6	43.1	915.7
175	920.8	45.2	966	954.4	45.6	1000

Table 5. 17. Compression capacity of hollow bar micropile, $L = 8.8\text{m}$, $L/d = 50$, $d_E = 1.75d$

s_u kPa	$L_E = 2.2 \text{ m}, \alpha = 0.9$			$L_E = 1.5 \text{ m}, \alpha = 1.0$		
	Q_{shaft} kN	Q_{bearing} kN	Q_F kN	Q_{shaft} kN	Q_{bearing} kN	Q_F kN
90	468.6	33.4	502	520	34.5	554.5
100	520.5	36.5	557	577.7	36.8	614.5
120	624.7	40.3	665	693.25	41.75	735
140	728.9	47.3	776.2	808.7	47.4	856.1
150	780.9	51.2	832.1	866.5	50.5	917
160	833.4	55.6	889	924.3	54.5	978.8
175	911.9	62.1	974	1011	60	1071

Table 5. 18. Compression capacity of hollow bar micropile, $L = 8.8\text{m}$, $L/d = 50$, $d_E = 1.75d$

s_u kPa	$L_E = 1.5 \text{ m}, \alpha = 1.0$		
	Q_{shaft} kN	Q_{bearing} kN	Q_F kN
90	494.33	36.47	530.8
100	549.1	39.4	588.5
120	658.5	44.2	702.7
140	768.4	51	819.4
150	823.3	54.1	877.4
160	878.2	57.2	935.4
175	960.3	61	1021.3

Table 5. 19. Compression capacity of hollow bar micropile, $L = 8.8\text{m}$, $L/d = 50$, $d_E = 2d$

s_u kPa	$L_E = 1.5 \text{ m}, \alpha = 1.0$			$L_E = 2.2\text{m}, \alpha = 1.0$		
	Q_{shaft} kN	Q_{bearing} kN	Q_F kN	Q_{shaft} kN	Q_{bearing} kN	Q_F kN
90	517.2	47.8	565	543.5	48.5	592
100	574	51	625	603.5	52	655.5
120	686	59	745	724	59	783
140	799	71	870	845	68	913
150	855	73	928	905.2	72.8	978
160	911	77	988	964.6	80.4	1045
175	996	84	1080	1055.3	86.7	1142

Table 5. 20. Uplift capacity of hollow bar micropile, $L = 5.75\text{m}$, $L/d = 30$, $d_E = 1.25d$

s_u	$L_E = 1.5 \text{ m}, \alpha = 0.9$			$L_E = 2.0 \text{ m}, \alpha = 1.0$		
	Q_{shaft} kN	Q_{bearing} kN	Q_F kN	Q_{shaft} kN	Q_{bearing} kN	Q_F kN
90	269.32	6.68	276	304.72	6.68	311.4
100	299.1	7.4	306.5	338	7.6	345.6
120	357.2	10	367.2	405.1	9.6	414.7
140	417.77	10.63	428.4	473.2	10	483.2
150	448	11	459	506.1	11.4	517.5
160	477.5	12	489.5	539.7	11.7	551.4
175	522	13	535	590.6	12.4	603

Table 5. 21. Uplift capacity of hollow bar micropile, $L = 5.75\text{m}$, $L/d = 30$, $d_E = 1.5d$

s_u	$L_E = 1.5 \text{ m}, \alpha = 0.1.0$			$L_E = 2.0 \text{ m}, \alpha = 1.0$		
	Q_{shaft} kN	Q_{bearing} kN	Q_F kN	Q_{shaft} kN	Q_{bearing} kN	Q_F kN
90	313.7	15	328.7	325.6	14.7	340.3
100	347.8	16.2	364	362.2	15.4	377.6
120	417.35	19.65	437	434.4	17.6	452
140	486.3	22.7	509	507	20	527
150	520.5	24	544.5	543	21.5	564.5
160	554.4	27	581.4	579.8	22.8	602.6
175	605.5	30	635.5	633.4	24.6	658

Table 5. 22. Uplift capacity of hollow bar micropile, $L = 5.75\text{m}$, $L/d = 30$, $d_E = 1.75d$

s_u kPa	$L_E = 1.5 \text{ m}, \alpha = 0.9$			$L_E = 1.5 \text{ m}, \alpha = 1.0$		
	Q_{shaft} kN	Q_{bearing} kN	Q_F kN	Q_{shaft} kN	Q_{bearing} kN	Q_F kN
90	296	24	320	327	27	354
100	327.7	27.8	355.5	363	29	392
120	392.6	32	424.6	435.7	34	469.7
140	457.6	38.4	496	508.15	36.85	545
150	489.1	43.5	532.6	543.7	42.3	586
160	521.9	44.1	566	579.5	43.5	623
175	570	45	615	634	47	681

Table 5. 23. Uplift capacity of hollow bar micropile, $L = 5.75\text{m}$, $L/d = 30$, $d_E = 1.75d$

s_u kPa	$L_E = 1.0 \text{ m}, \alpha = 1.0$		
	Q_{shaft} kN	Q_{bearing} kN	Q_F kN
90	313.1	17.7	330.8
100	347	23	370
120	416	27	443
140	485	30	515
150	519.33	31.67	551
160	554.5	34	588.5
175	606	37	643

Table 5. 24. Uplift capacity of hollow bar micropile, $L = 5.75\text{m}$, $L/d = 30$, $d_E = 2d$

s_u	$L_E = 1.0 \text{ m}, \alpha = 1.0$			$L_E = 1.5 \text{ m}, \alpha = 0.9$		
	Q_{shaft} kN	Q_{bearing} kN	Q_F kN	Q_{shaft} kN	Q_{bearing} kN	Q_F kN
90	327	36	363	312	32	344
100	363	34	397	346	36	382
120	436	40	476	416	41	457
140	508	45	553	484	49	533
150	544.8	48.2	593	517	56	573
160	581	52	633	551.5	58	609.5
175	635	58	693	602	68	670

Table 5. 25. Uplift capacity of hollow bar micropile, $L = 8.8\text{m}$, $L/d = 50$, $d_E = 1.25d$

s_u	$L_E = 1.5 \text{ m}, \alpha = 1.0$			$L_E = 2.2 \text{ m}, \alpha = 0.9$		
	Q_{shaft} kN	Q_{bearing} kN	Q_F kN	Q_{shaft} kN	Q_{bearing} kN	Q_F kN
90	449.2	6.8	456	411.6	7.4	419
100	499	7.5	506.5	456.6	8.4	465
120	598.5	9	607.5	547.8	10.2	558
140	698.3	10.5	708.8	638.5	11.5	650
150	748.5	11	759.5	684.4	12.6	697
160	798.1	11.9	810	729.5	13.5	743
175	873	13	886	797.8	14.2	812

Table 5. 26. Uplift capacity of hollow bar micropile, $L = 8.8\text{m}$, $L/d = 50$, $d_E = 1.5d$

s_u	$L_E = 1.5 \text{ m}, \alpha = 1.0$			$L_E = 2.2 \text{ m}, \alpha = 1.0$		
	Q_{shaft} kN	Q_{bearing} kN	Q_F kN	Q_{shaft} kN	Q_{bearing} kN	Q_F kN
90	465	15	480	482	14.5	496.5
100	516.3	16.7	533	535	16.5	551.5
120	619	19	638	641	19	660
140	722	22	744	748.5	21.5	770
150	773	23	796	802.8	22.2	825
160	824.2	24.8	849	855.8	23.2	879
175	900	27	927	933.2	25.8	959

Table 5. 27. Uplift capacity of hollow bar micropile, $L = 8.8\text{m}$, $L/d = 50$, $d_E = 1.75d$

s_u	$L_E = 2.2 \text{ m}, \alpha = 0.9$			$L_E = 2.2 \text{ m}, \alpha = 1.0$		
	Q_{shaft} kN	Q_{bearing} kN	Q_F kN	Q_{shaft} kN	Q_{bearing} kN	Q_F kN
90	453.5	24.5	478	481	25	506
100	503.7	27.3	531	534.9	27.1	562
120	602	31	633	642	31	673
140	702.4	37.6	740	749	34.5	783.5
150	752.4	40	792.4	800.2	36.5	836.7
160	802	43	845	853	41	894
175	875.2	47	922.2	933	44	977

Table 5. 28. Uplift capacity of hollow bar micropile, L = 8.8m, L /d =50, d_E = 1.75d

s _u kPa	L _E = 1.5 m, α =1.0		
	Q _{shaft} kN	Q _{bearing} kN	Q _F kN
90	481	25	506
100	534.9	27.1	562
120	642	31	673
140	749	34.5	783.5
150	800.2	36.5	836.7
160	853	41	894
175	933	44	977

Table 5. 29. Uplift capacity of hollow bar micropile, L = 8.8m, L /d =50, d_E = 2d

s _u kPa	L _E = 1.5 m, α =1.0			L _E = 2.2m, α =0.9		
	Q _{shaft} kN	Q _{bearing} kN	Q _F kN	Q _{shaft} kN	Q _{bearing} kN	Q _F kN
90	501.5	28.5	530	527.4	34.6	562
100	555	36	591	586.8	36.2	623
120	666	39	705	704.5	41	745.5
140	776	42	818	822.4	45.6	868
150	831.5	45	876.5	880	49	929
160	887.1	48.5	935.6	937	54	991
175	968	53	1021	1025.5	56	1081.5

The parametric study showed a strong correlation between the increase in micropile volume and its shaft capacity. Thus, the percentage increase in the pile volume, V_{inc} , is plotted versus the normalized shaft resistance, Q_{shaft}/Q_s , in Figs. 5.51 and 5.52 for $L/d = 30$ and 50 , respectively. The percentage increase in pile volume, V_{inc} is calculated from:

$$V_{inc} = \frac{(V_{grout} - V_{hole})}{V_{hole}} \quad (5.26)$$

Where: V_{grout} is grout volume required for pile construction; $V_{hole} = \pi d^2 L/4$.

The normalized shaft resistance is equal to the shaft resistance obtained from the enlarged geometry, Q_{shaft} , divided by the shaft resistance, Q_s , employing the drilling bit diameter.

Q_s is computed from:

$$Q_s = \pi d \int_0^L \alpha s_u dz \quad (5.27)$$

Figure 5.53 shows that the increases in the compressive shaft resistance can be related to the increase in pile volume by:

$$Q_{shaft} = (1 + 0.35 V_{inc}) Q_s \quad (5.28)$$

For hollow bar micropile under monotonic uplift loads, the same relation between the increase in pile volume and the shaft capacity is recognized, as illustrating in Figs. 5.54 and 5.55. Considering all data points in Fig. 5.56, the increase in the shaft resistance under monotonic uplift load is related to increase in pile volume can be given by:

$$Q_{shaft} = (1 + 0.275 V_{inc}) Q_s \quad (5.29)$$

The difference between Eqs. 5.28 and 5.29 might be attributed to the effect of Poisson's ratio of the micropile material.

In all load cases, a percentage of the applied load is transferred to the soil through end bearing resistance. This amount depends on the enlarged diameter during installation; however, it is difficult to estimate the amount of increase in diameter. It is proposed to evaluate the end bearing resistance for hollow bar micropiles under compression from:

$$Q_{\text{bearing}} \approx 9 s_{\text{ub}} A_{\text{hole}} \quad (5.30)$$

And under tension (due to the enlargement in the base) from:

$$Q_{\text{bearing}} \approx 9 s_{\text{u}} 2.5A_{\text{inc}} \quad (5.31)$$

Where:

$$A_{\text{hole}} = V_{\text{grout}}/L, \text{ and}$$

$$A_{\text{inc}} = V_{\text{inc}}/L$$

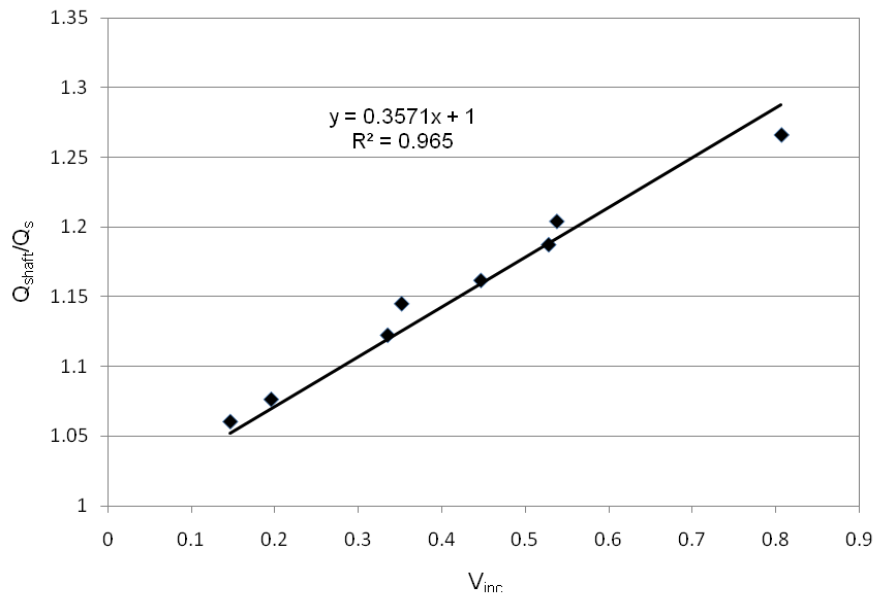


Figure 5. 51. Percentage increase in pile volume vs normalized shaft resistance under compression, $L/d=30$

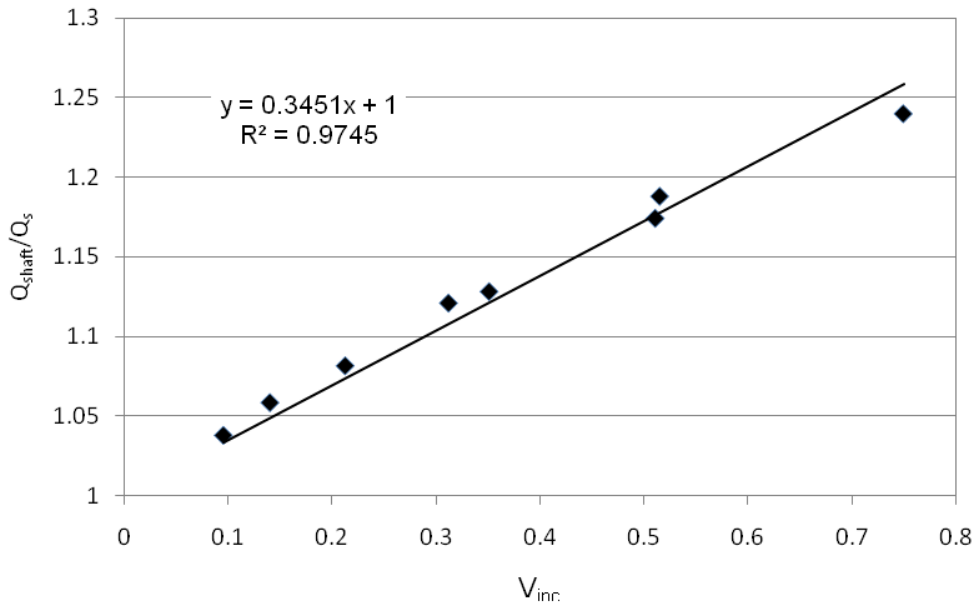


Figure 5. 52. Percentage increase in pile volume vs normalized shaft resistance under compression, $L/d=50$

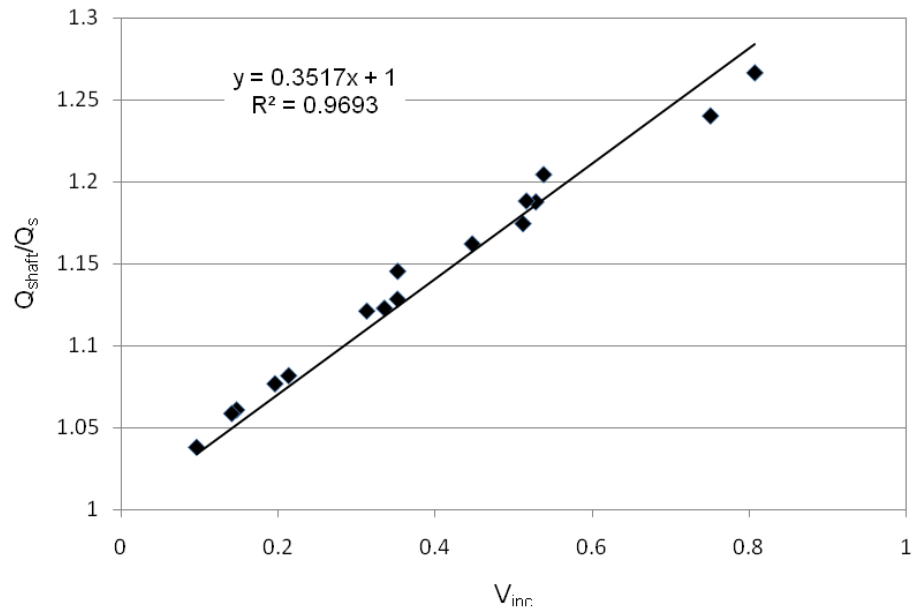


Figure 5. 53. Percentage increase in pile volume vs normalized shaft resistance under compression

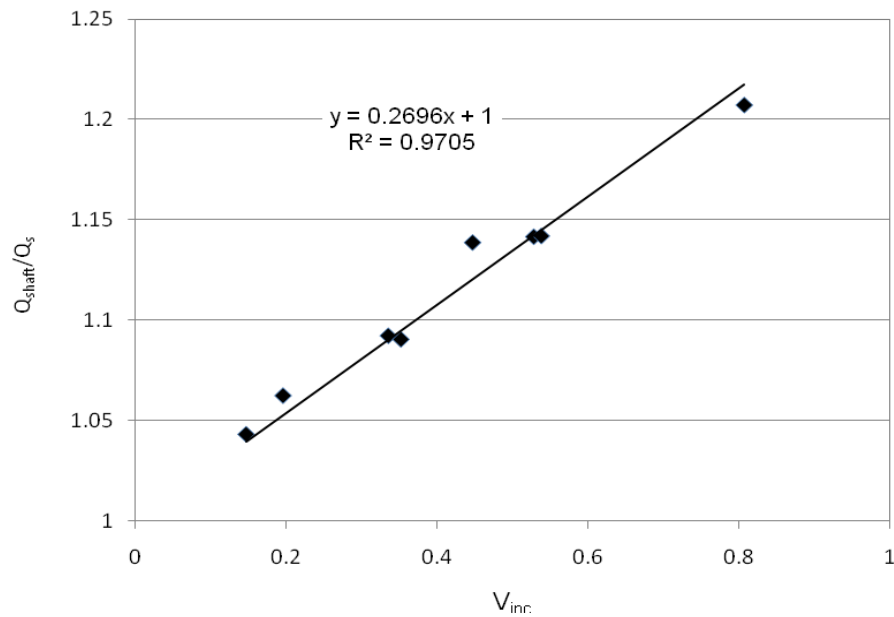


Figure 5. 54. Percentage increase in pile volume vs normalized shaft resistance under tension, $L/d=30$

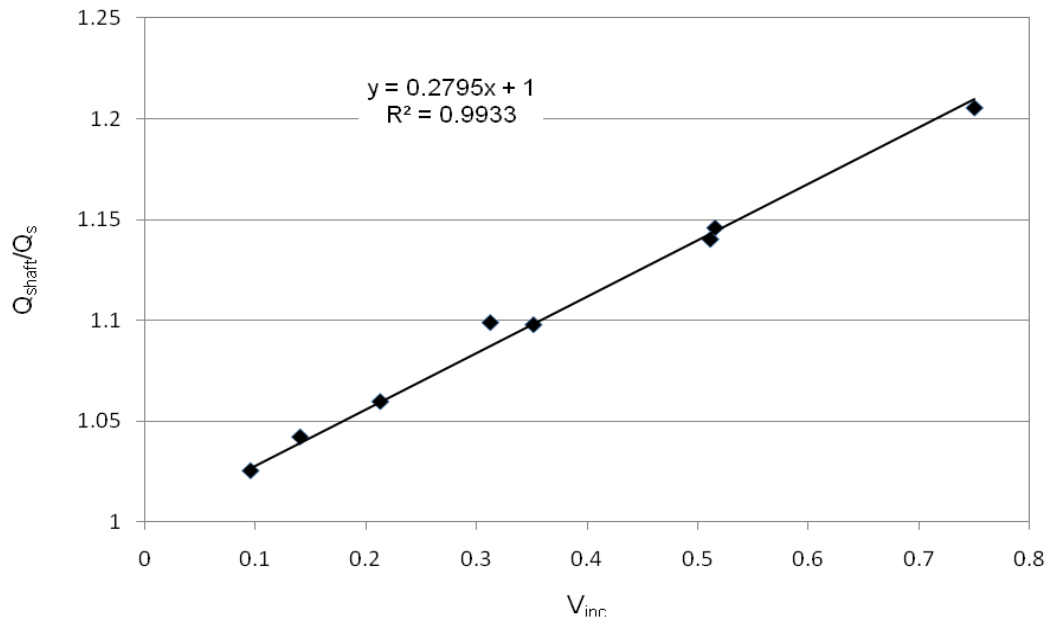


Figure 5. 55. Percentage increase in pile volume vs normalized shaft resistance under tension, $L/d=50$

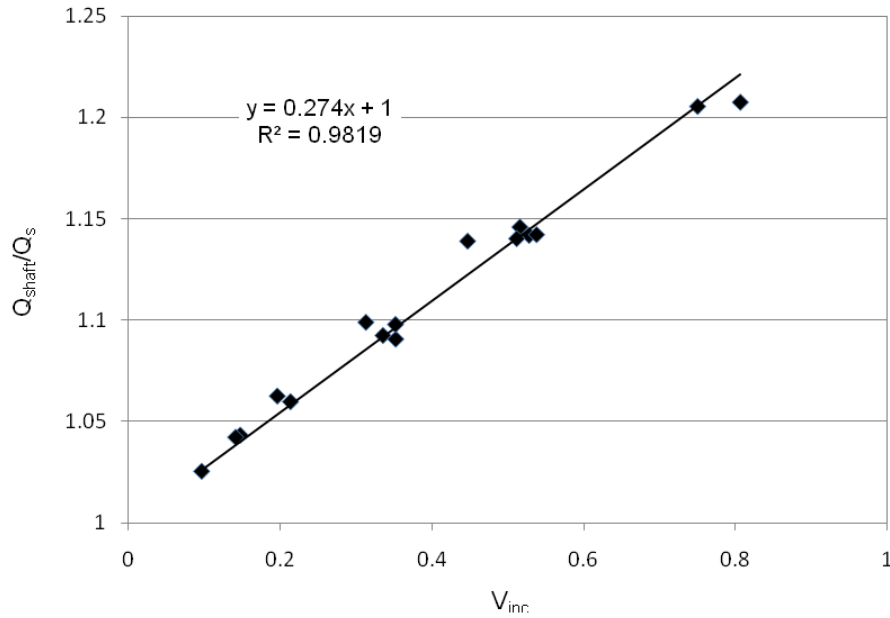


Figure 5. 56. Percentage increase in pile volume vs normalized shaft resistance under tension

5.5.6 Axial capacity of hollow bar micropiles embedded in clayey soils under monotonic loading

Based on the obtained results from the parametric study, it is possible to propose an equation to calculate the axial capacity of hollow bar micropiles. This equation calculates the geotechnical capacity of hollow bar micropiles embedded in clayey soils. The geotechnical capacity of hollow bar micropiles, P_G , recommended by FHWA (NHI, 2005) is given by:

$$P_G = \alpha_{\text{Bond}} \pi D_b L_b \quad (5.32)$$

The general practice is to use α_{bond} for Type B micropiles, and multiply the bit diameter by an enlargement factor between 1.2 and 1.3 for hollow bar micropiles embedded in clayey soils to evaluate D_b . In all cases, L_b is the bonded length of the micropile. This must be confirmed by two to three verification tests and 5% of the installed micropiles must undergo proof tests.

The calibration jobs and the parametric study presented here show that there are three modifications that can be applied to the previous equation to estimate the geotechnical capacity of such micropiles more appropriately. Those modifications are:

1- The α_{bond} factor in Eq. 5.32 is given by two parameters; α_{su} . The calibration model shows that α ranges between 0.9 and 1.0, i.e., utilize $\alpha = 0.9$ as lower bound and $\alpha = 1.0$ as upper bound for estimating the capacity.

2- The D_b is replaced by $d_{\text{bit}} f_l$; where d_{bit} is the drilling bit diameter and f_l is an enlargement factor. $f_l = (1+0.35V_{\text{inc}})$ for micropiles under compression and =

$(1+0.275V_{inc})$ for micropiles under tension. In all cases; V_{inc} is the increase in pile volume due to installation.

3- An end bearing resistance component, $Q_{bearing}$, must be added. The amount of end bearing resistance can be estimated from Eq. 5.30 under compression and 5.31 under tension.

One verification test may be required in the field to validate the calculated capacity. The proposed equation could be beneficial in monitoring the production of micropiles by tracking the amount of grout used during installation. Cavitations and necking will be easily detected and suspect micropiles should be subjected to proof tests.

5.5.7 Cyclic axial model

5.5.7.1 Geometric modeling

The same two-dimension (2D) axisymmetric model used for monotonic loading calibration was used for cyclic loading modeling and calibration (See Fig. 5.24). The model is extended vertically to 0.75 of the hollow bar micropile length, measured from the pile tip. The same enlarged micropile geometry employed in calibration the monotonic phase was used for the cyclic load test case.

5.5.7.2 Material modeling

The same material properties of the steel and the grout considered for the monotonic load test were employed for the analysis of the cyclic load tests. Due to the cyclic loading applied, it is anticipated that the soil surrounding the micropile would degrade as the

number of load cycles increases. Hence, a degradation material model is required to properly simulate the cyclic behavior of the pile.

To account for the anticipated soil stiffness degradation, a degradation index model is adopted. The model was developed by Idriss et al. (1978) to simulate the cyclic degradation of undrained clay under variable-amplitude strain controlled loading. The model was then extended to account for the behavior during transit loading. The degradation index developed by Idriss et al. (1978) is given by:

$$\delta_N = G_{sN}/G_{s1} = N^{-t} \quad (5.33)$$

Where: δ_N is the amount of degradation at the N^{th} cycle; G_{s1} is the secant shear modulus at cycle 1; G_{sN} is the secant shear modulus at cycle N ; t is the degradation parameter. The degradation parameter, t , has been found experimentally to depend on the cyclic strain, plasticity index (PI) and the overconsolidation ratio (Allotey and El Naggar, 2008).

In the FE model, the soil behavior is simulated using the Mohr-Coulomb plasticity along with the soil elastic properties (Young's modulus and Poisson's ratio). However, neither the elastic model nor Mohr-Coulomb model in ABAQUS allows the degradation of the soil properties during loading in the same job. Meanwhile, ABAQUS allows applying variability of material properties during the step time at the same job only through field variable option. The field variable option, such as temperature-dependent material properties, can be applied at the loading step only or through the whole analysis.

In such case, the material properties of the required geometry are given in a temperature-dependent data model. At the same step time, the same geometry is subjected to a

temperature field that coincides with the temperature-dependent data model. Both the temperature-dependent data and the temperature field should vary through the step time utilizing the same amplitude.

To calibrate the field cyclic tests, the aforementioned procedure is utilized in modeling the cyclic degradation of the soil. As mentioned previously (Section 5.3), the cyclic load tests involved initial monotonic loading up to the design load followed by varying the applied load with amplitude of 0.33 of the design load. In all load tests, 15 cycles of loading and unloading were applied.

Accordingly, the material model of the soil was not degraded during the monotonic loading stage then subjected to a temperature field during the cyclic phase. This field applied temperature that increased with the number of cycles achieved. Correspondingly, the soil shear modulus was modeled to degrade with this increase in temperature.

The degradation of the shear modulus was calculated utilizing Eq. 5.33 at each load cycle. The pattern of cyclic loading was used to apply the temperature field to induce the corresponding degradation of the soil. Figure 5.57 illustrates a diagrammatic chart how the degradation of the material model and the temperature field are related to the applied number of cyclic loading.

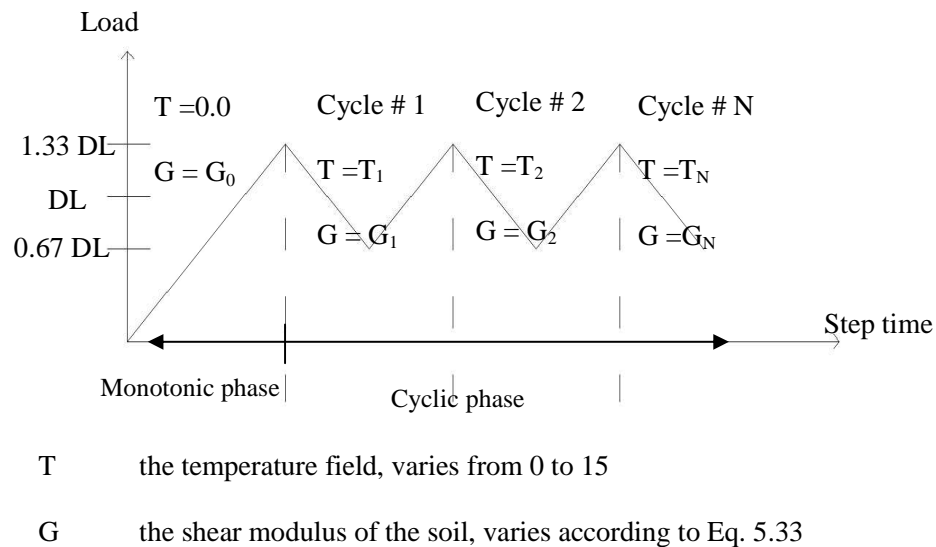


Figure 5. 57. Applying the temperature field and the degradation in soil shear modulus during calibration of cyclic field test

5.5.8 Calibration of the cyclic field test

Even though the amplitudes of the cyclic loading were nearly equal, Fig. 5.13 shows that the behavior of the four hollow bar micropiles are not the same under cyclic loading. Thus, the finite element model for each cyclic load test was calibrated separately. This was accomplished through a trial and error procedure in order to match the stiffness in each cycle. It starts by matching the secant shear modulus, G_{s1} , of the soil at the first cycle of the cyclic loading phase. Once the G_{s1} was evaluated, trial values of the degradation parameter, t , were applied utilizing Eq. 5.33 to calculate the shear modulus in progressive cycles. The target t value was achieved when the accumulating displacement at the maximum applied cyclic load of the field load test matched that of the FE model employing the pre-described t value.

Figures 5.58 to 5.61 illustrate the load-displacement curves of the cyclic field test and that of the FE model for MP1, MP2, MP3, and MP4, respectively. The results from the FE models agreed well with the field load test results at the maximum cyclic loading. Meanwhile, all the models diverge somewhat from the field test displacement at the minimum cyclic load (i.e. the unloading phase).

Gomez et al. (2003) commented that the displacement of micropiles during unloading stages in cyclic field tests should be evaluated with caution. During unloading stage, the micropile usually suffers from the locked-in stresses phenomenon. This phenomenon arises from rapidly unloading – reloading the micropile during the cyclic field tests. Loading and unloading the micropiles in this rapid fashion do not allow sufficient time for the pile to relax before re-loading it again. Accordingly, during the unloading stage, the micropile shows more flexible behavior than its actual one.

On the other hand, the locked-in phenomenon is absent in the FE model. Upon unloading, the micropile in the FE analysis, all stresses are reversed, and the slope of the load-displacement during load – unload cycle is governed only by the shear modulus assigned to each cycle. Hence, it is preferred to calibrate the cyclic field tests employing the accumulating displacement at the maximum cyclic load rather than the degradation in slope of the load-displacement curve during cyclic loading.

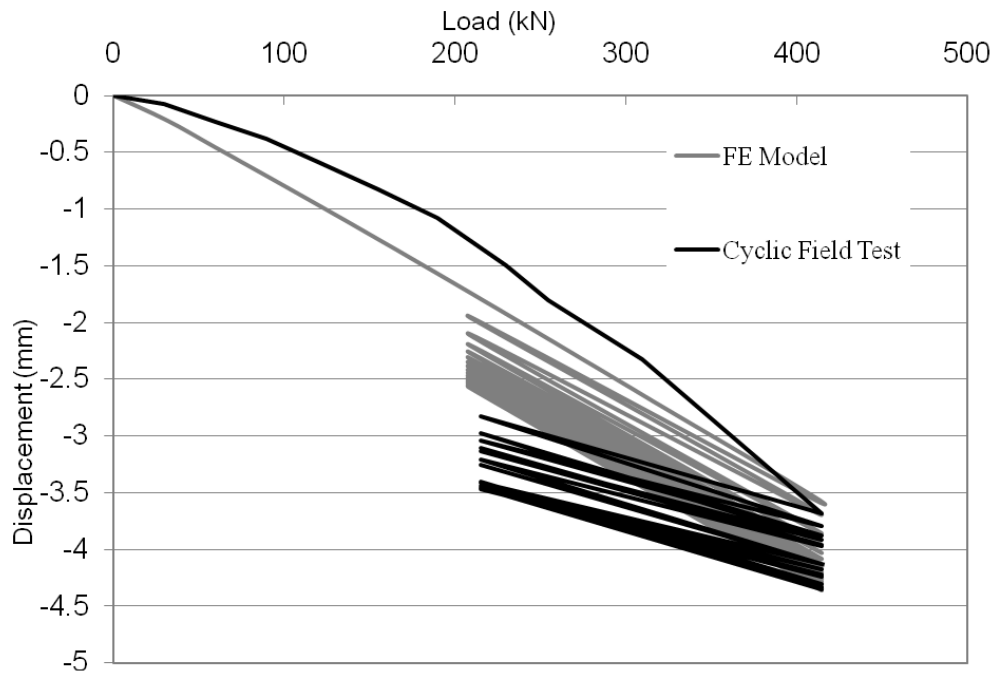


Figure 5.58. Load-displacement calibration of cyclic test on MP1

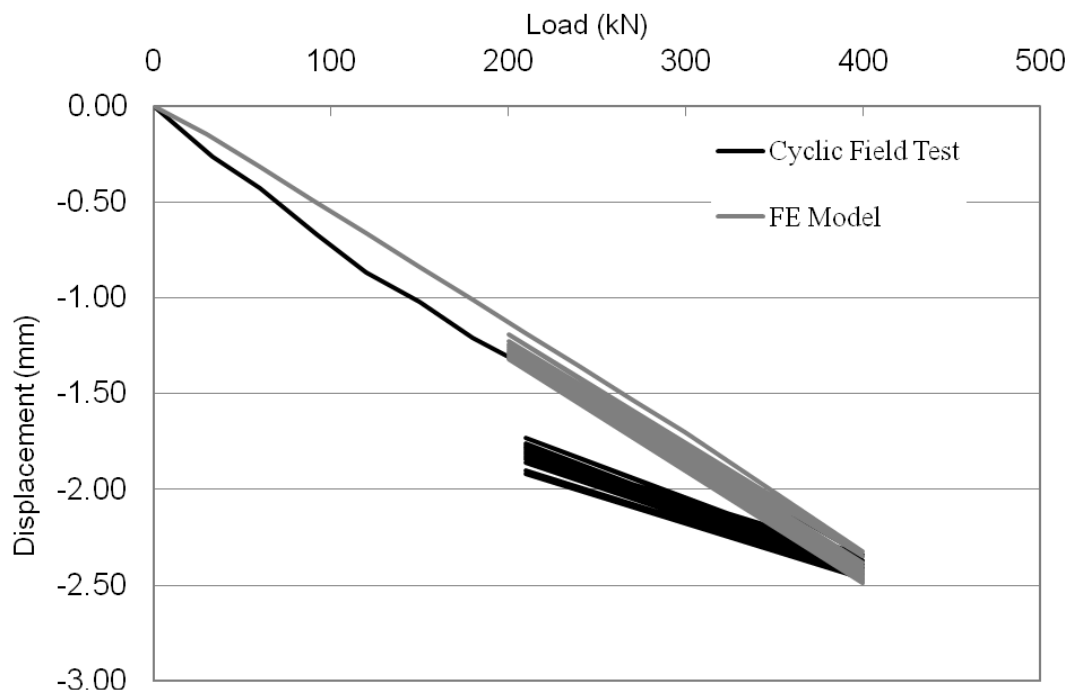


Figure 5.59. Load-displacement calibration of cyclic test on MP2

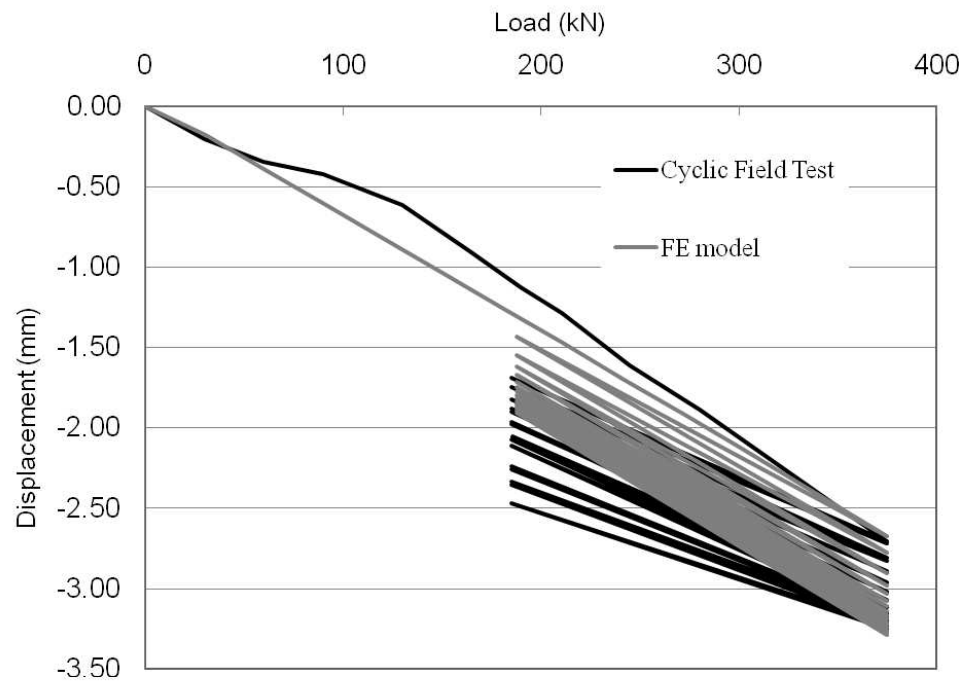


Figure 5. 60. Load-displacement calibration of cyclic test on MP3

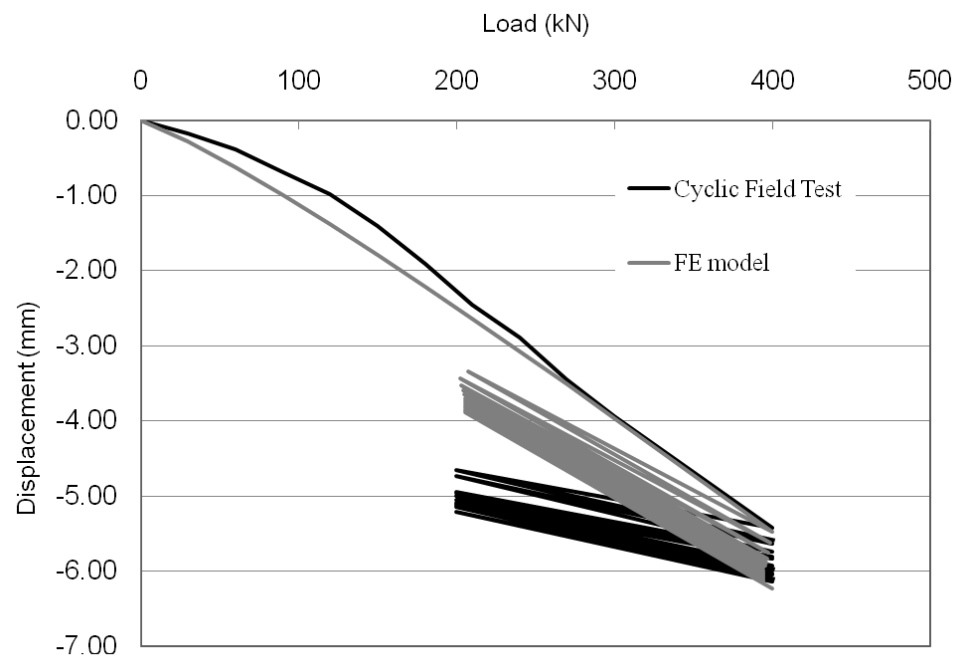


Figure 5. 61. Load-displacement calibration of cyclic test on MP4

The value of the degradation parameter, t , obtained from the calibrated FE model was found to be between 0.018 and 0.023. This value coincides with the recommendation of Pyke and Beikae (1993) for heavily over-consolidated clay with plasticity index lower than or equal to 20%. The calibrated model shows that the stiffness of the micropile at the N^{th} cycle can be estimated from:

$$K_N = K_1 (\delta_N)^3 \quad (5.34)$$

Where: K_N is the stiffness of the hollow bar micropile at the N^{th} cycle; $K_1 = P_{\text{max}}/\delta_{\text{max}}$ is the stiffness of the hollow bar micropile at the 1st cycle; P_{max} is maximum applied load during cyclic loading; δ_N is the degradation index. Figures 5.62 to 5.65 depict the stiffness degradation with number of cycles evaluated from for field tests and FE models for MP1, MP2, MP3, and MP4, respectively. The calculated and measured responses are in good agreement.

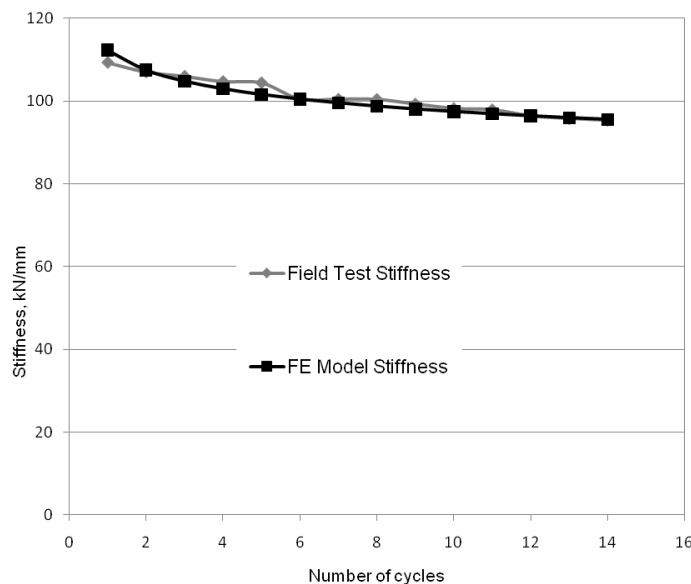


Figure 5. 62. Variation of stiffness due to cyclic loading for MP1

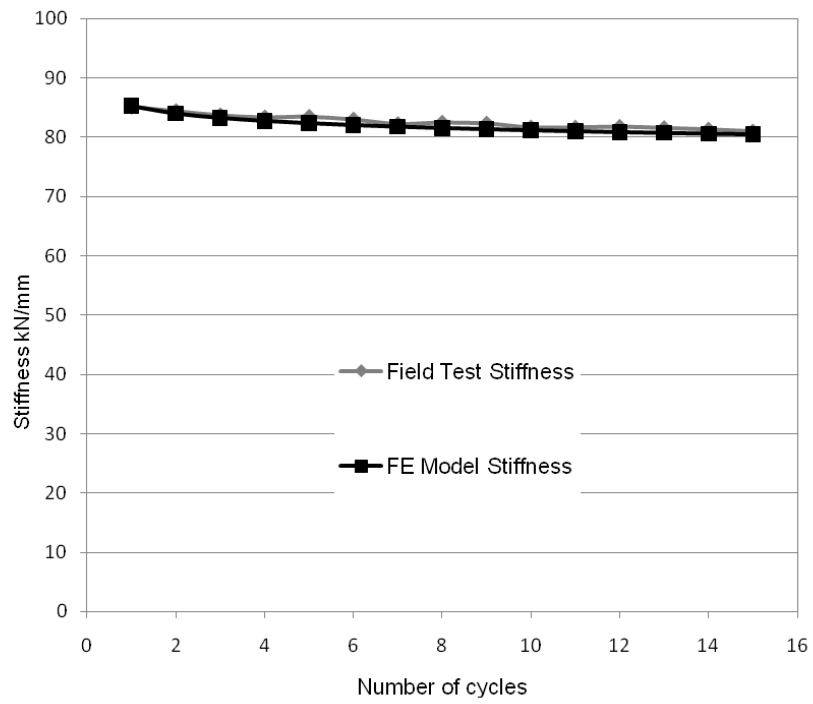


Figure 5. 63. Variation of stiffness due to cyclic loading for MP2

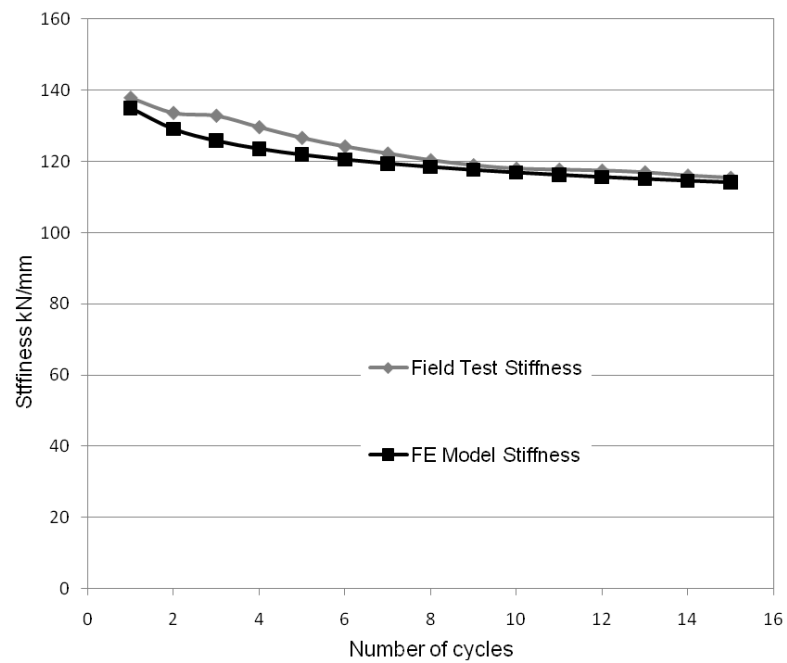


Figure 5. 64. Variation of stiffness due to cyclic loading for MP3

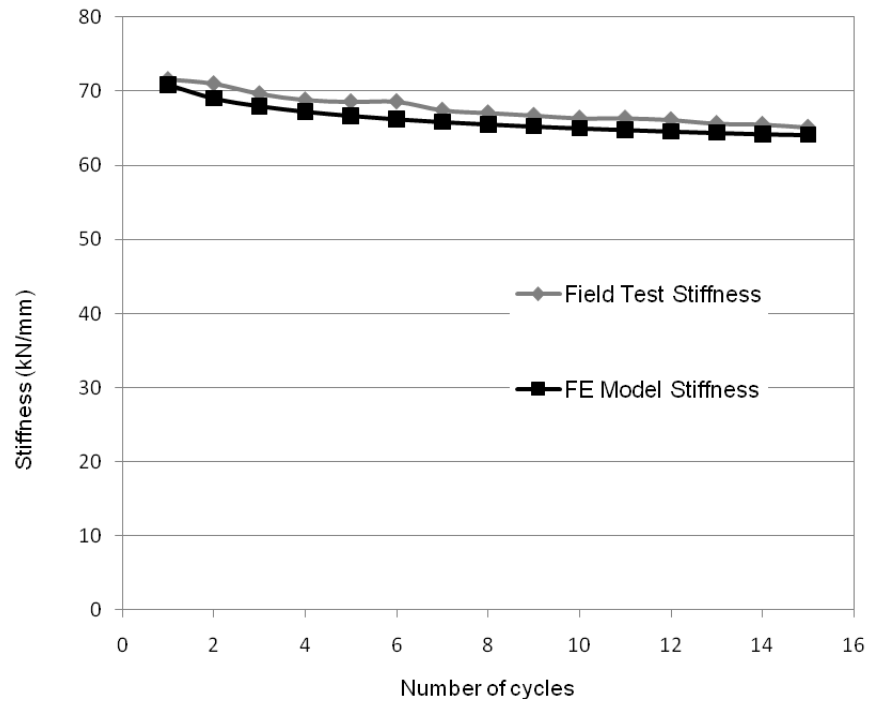


Figure 5. 65. Variation of stiffness due to cyclic loading for MP4

CHAPTER 6

HOLLOW BAR MICROPILES GROUP BEHAVIOR

6.1 Introduction

The third phase of the field load testing program involved pile group load tests. A total of four full scale group field load tests were conducted on pairs of hollow bar micropiles. This chapter documents the testing procedure followed and discusses the results obtained from the four field pile group tests performed. In addition, a 3D numerical model was established to analyze the field load tests and was calibrated using the experimental results. The calibrated model was then employed to perform a parametric study with the objective to provide data required for developing design guidelines for hollow bar micropile groups in clayey soils.

6.2 Field Pile Group Load Tests

Four monotonic axial load group tests were conducted on pairs of hollow bar micropiles. The tests were conducted in the following sequence: PG1 (MP1 and MP4), PG2 (MP2 and MP3), PG3 (MP1 and MP2), and PG4 (MP3 and MP4).

6.2.1 Testing equipment

The same reaction frame system described in Chapter 5 (see Figs. 5.1 and 5.2) was used to execute the pile group load tests. To perform the group load test, the test pair was connected together with two identical thick steel plates. The two plates served as a pile

cap during the load test. In all tests, the steel pile cap was elevated above ground (i.e. not in contact with soil).

As shown in Figure 6.1, the plates were 1278mm long, 600mm wide and 51 mm thick (i.e. total thickness of pile raft is 102 mm). During the load tests, the two plates were connected together by bearing. Combined, the two plates were designed to carry an ultimate load of 1390kN. Hence, the maximum applied (permitted) load was 1100 kN, ensuring a factor of safety of 1.25.

The plates were designed to transmit the applied load to the micropile heads by bearing. Hence, a special connection was designed to transmit the applied load safely to the micropiles' heads. The connection incorporated a square bearing plate 300x300x38 mm. A 76mm socket bar was welded to the bearing plate from the top, and a BX7-76 hex nut was welded to it from the bottom. The hex nut was threaded onto the hollow bar to increase the bearing area at the pile head from 2500mm², the hollow bar cross section, to 90000 mm², the bearing plate area. The aim of the socket bar was to constrain the steel pile cap from moving laterally during loading. Accordingly, the socket bar was designed to pass through the 78mm holes at the sides of the thick steel plates. Figure 6.2 shows the connection of the pile head before assembling the thick steel plates.

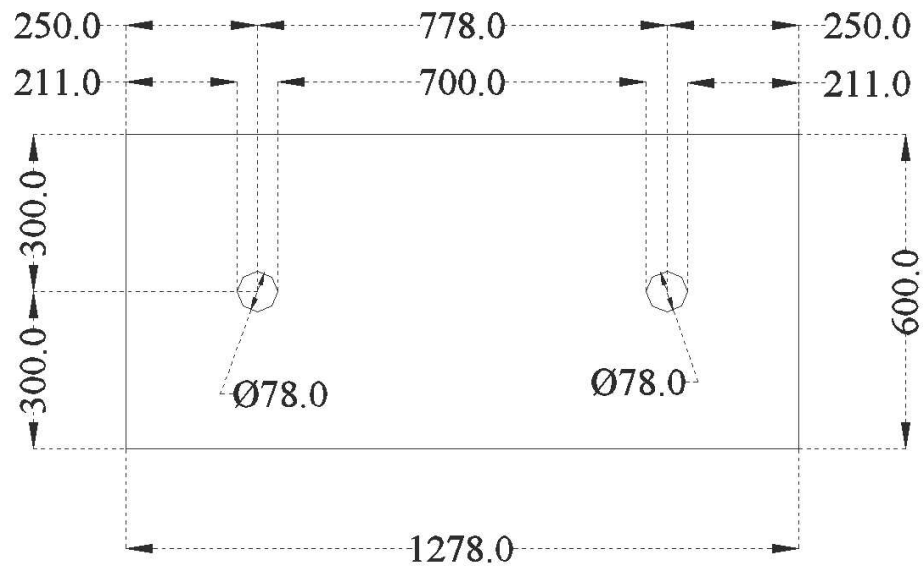


Figure 6. 1. Plane view of loading plate, all dimensions are in mm

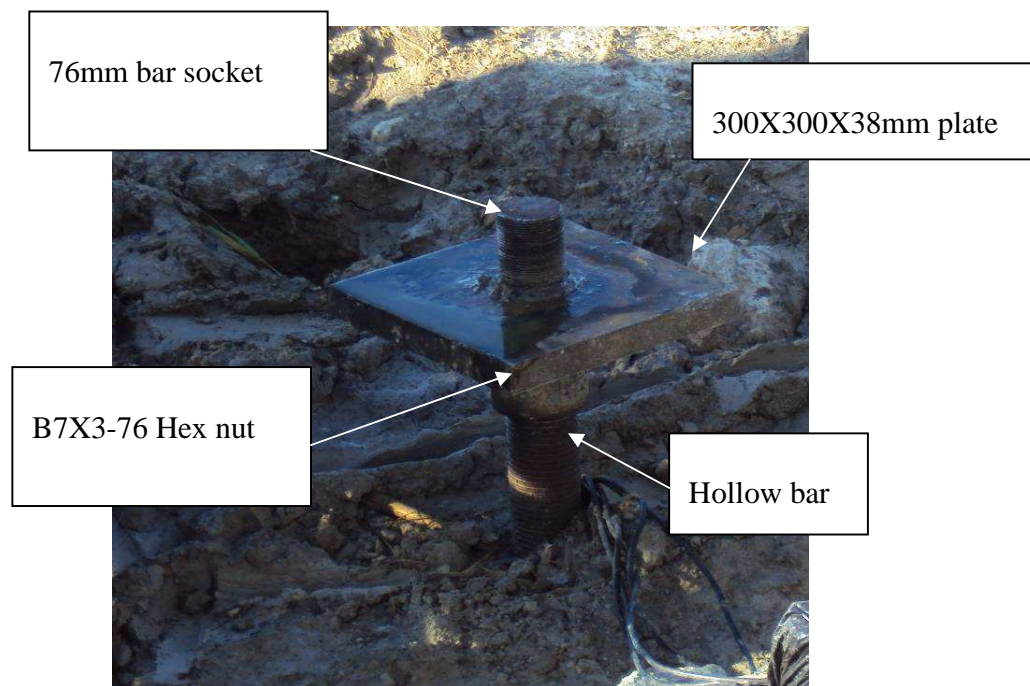


Figure 6. 2. Details of the hollow bar micropile's head connection

A shop drawing of the pile group assembly is given in Fig. 6.3. After assembling the pile cap, the loading instruments were centered at the middle of the steel cap. To avoid eccentric loading, the two cross beams used to execute the load were positioned to be centered over the loading instruments. The two beams were positioned sequentially; the two reaction piles supporting the lower beam were installed such that the lower beam was coincide with the loading instruments center, as illustrated in Fig. 6.4. The second beam was then leveled and positioned such that its center lies above the center of the lower beam, as shown in Fig. 6.5. Figure 6.6 illustrates the final setup of the group loading setup.

6.2.2 Pile head load and instrumentation

The load was exerted through a hollow cylinder hydraulic jack connected to a hydraulic pump. The jack was located at the center of the steel cap against the reaction frame. The hydraulic jack used in this phase had 2000 ton advance capacity employed by 350 mm stroke.

The pile cap was instrumented by a new load cell with larger capacity and six linear displacement transducers. The load was recorded using a strain gauge load cell SGA-1000-4-LC of 4500 kN capacity. The load cell had outer diameter of 197mm and inner diameter of 102mm. The load cell outer diameter was almost equal to the hydraulic jack stroke diameter. Thus, the load cell was situated on top of the hydraulic jack, and under the reaction frame. During testing, other loading plates were provided above the load cell to close any gap between the main reaction beam and the load cell.

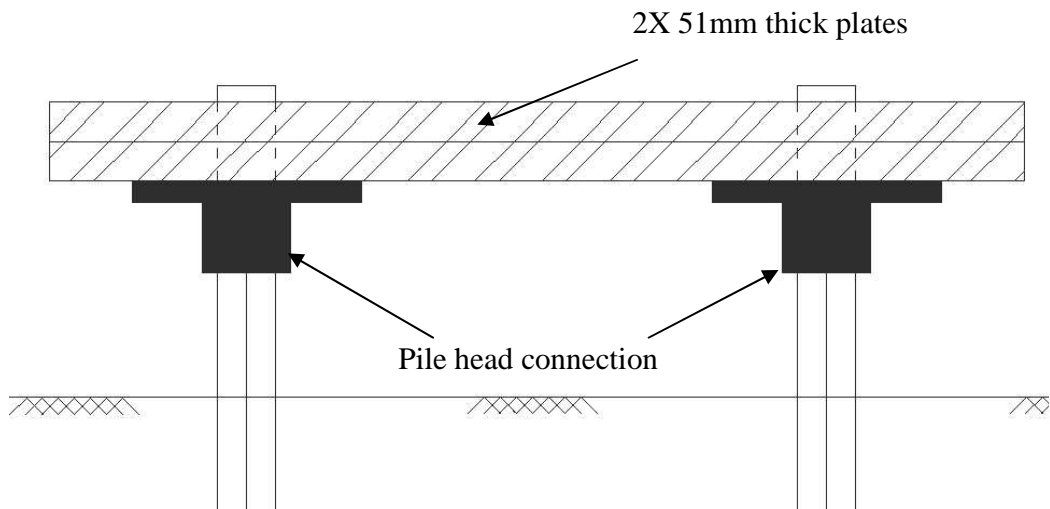


Figure 6. 3. Pile group assembly

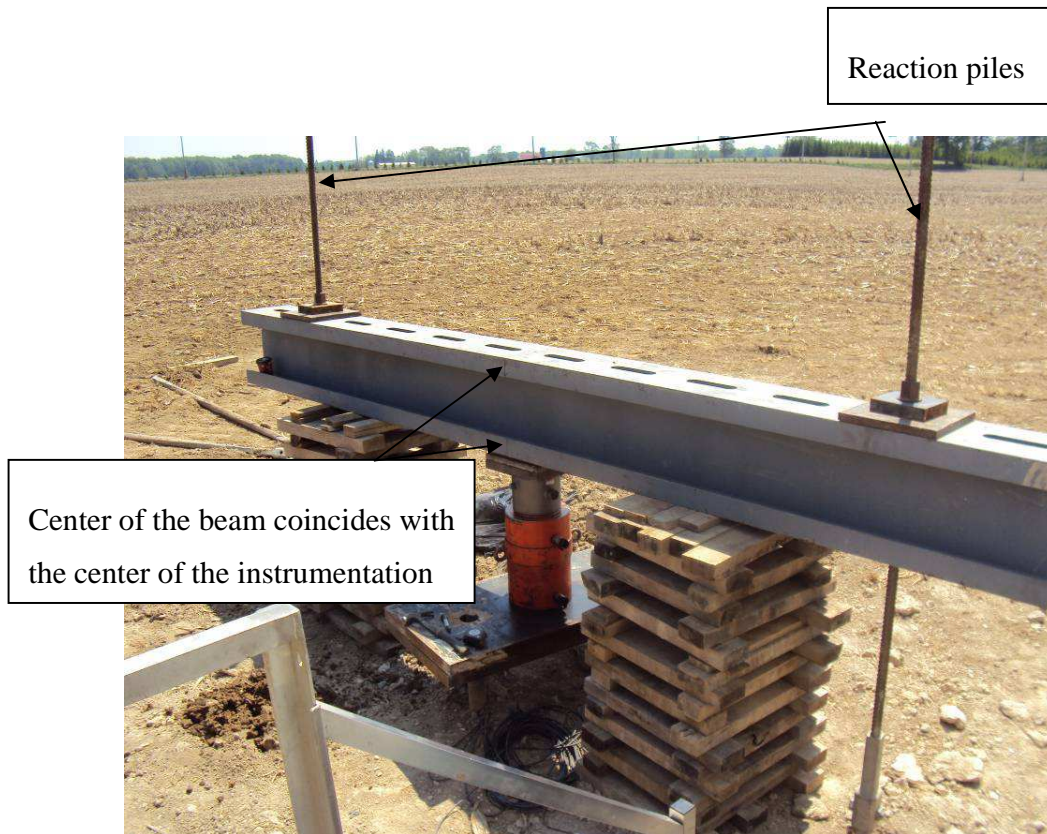


Figure 6. 4. Positioned the lower beam above the load instrumentations



Figure 6. 5. Centering and leveling the upper beam over the lower one



Figure 6. 6. Final pile group setup

The axial displacement of the pile cap was measured through six HLP 190/FS1/100/4K linear displacement transducers (LDTs), mounted on magnetic bases. The LDTs magnetic bases were mounted on two reference steel extensions supported independently from the loading system. The LDTs had 100 mm stroke with an accuracy of 0.01 mm. The LDTs were distributed in a rectangular arrangement over the steel cap plates; two near each micropile head, and two at the middle of the pile cap. The loading instruments and LDTs arrangements are given in Fig.6.7.

The load cell and the LDTs were connected to a data acquisition system to record and store the load and movement at the pile head during the load test. Once the hydraulic jack advanced in each loading increment against the reaction beam, the load was transferred to the pile and measured by the load cell. At the same time, the six LDTs measured the axial displacement of the pile head. The displacement average was considered in the data analysis in an attempt to reduce inaccuracies.

6.2.3 Pile group load test procedure

The pile groups were subjected to monotonic loading tests. The load was applied in increments until the maximum load was reached, followed by unloading in increments until zero load. The quick maintained load test procedure was employed during the monotonic group load tests. In this procedure, each load increment was maintained for at least 5 min. In this study, loads were applied in increments of 5 % of the anticipated failure load and maintained for at least 5 minutes. Generally, the micropiles were tested in compression in accordance with the ASTM D1143 (2007) quick maintained load test procedure.



Figure 6. 7. Arrangements of the instruments at the top of the steel pile raft

The schedule for the four pile group tests involved conducting four pile group tests within two weeks. Thus, the waiting period between any two consecutive tests was between three and four days. The pile group testing sequence was as follows: PG1 (MP1 and MP4), PG2 (MP2 and MP3), PG3 (MP1 and MP2) and PG4 (MP3 and MP4). It is anticipated that the short duration between subsequent load tests would affect the results of the pile group tests PG3 and PG4. When the pre-specified maximum load was reached, a 10 min creep test was conducted in accordance with the guidelines of the Post-Tensioning Institute (2004) to examine the geotechnical failure of the pile group. The pile group capacity is calculated from the following equation:

$$Q_g = \eta P_G n \quad (6.1)$$

Where: Q_g is the group capacity; P_G is the geotechnical capacity of the single pile; n is the number of piles within the group; and η is the group efficiency factor.

The group efficiency factor is affected by several parameters, including the spacing to diameter ratio, S/d , the contact condition between the pile cap and the soil, and the type of soil. As illustrated in Fig. 6.3, there is no contact between the pile cap and the ground surface. The spacing between any two tested piles considered in the group was about 778mm (Figure 6.8), which corresponded to spacing to diameter ratio of 4.5.



Figure 6. 8. Center to center spacing of the tested micropiles

Given the values of s_u obtained from the soil investigation, the soil is considered to be silty clay to clayey silt with stiff consistency. Given the spacing between the piles and stiff clayey soil, the group factor η is expected to approach 1.0. This is consistent with the suggestion of the FHWA NHI (2005) for micropiles embedded in clayey soils. Thus, the group capacity calculated from Eq. 6.1 is about 1200kN. This value exceeds the permitted resistance value for the pile cap, i.e. 1100kN. To avoid any differential settlement between the two thick steel plates, the field pile group tests were limited to 1100kN.

6.2.4 Pile group test results and analysis

It was planned to load all four groups to a maximum load of 1100kN. Because of an error in calibrating the initial load read by the data logger, the first three groups were loaded to a maximum load of only 1000kN. This error was then noted and fixed, and consequently PG4 was load tested to a maximum load of 1100 kN.

Figures 6.9 to 6.12 show the load-displacement curves for the four compression pile group tests performed in the field. For the purpose of comparison, the load-displacement curves for load tests on the single hollow bar micropiles employed in the group are plotted as well. All pile group curves show a lower initial stiffness than that of the single micropiles. This is because some stiffness degradation in the pile-soil interfaces attributed to the monotonic and cyclic load tests on the single pile during the previous test phases.

To compare the behavior of the pile group during the load tests, all curves representing pile group tests are plotted together in Fig. 6.13. Up to an applied load of 1000 kN, the behavior of all pile groups seem to be identical, except for PG3, which displayed a more

flexible behavior than other groups. That might be because pile group PG3 was conducted after pile group PG2 with micropile MP2 common between both groups. It seems that micropiles MP2 was affected by the permanent displacement from previous loading applied during PG2 test and did not have sufficient time to relax.

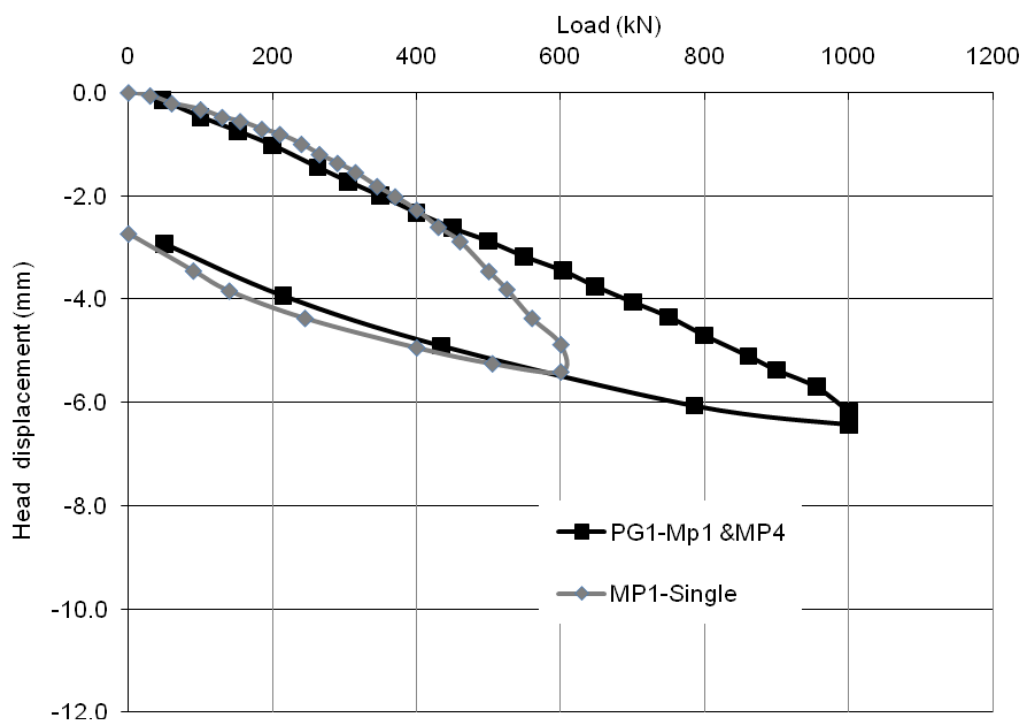


Figure 6. 9. Load-displacement curves for PG1 and MP1

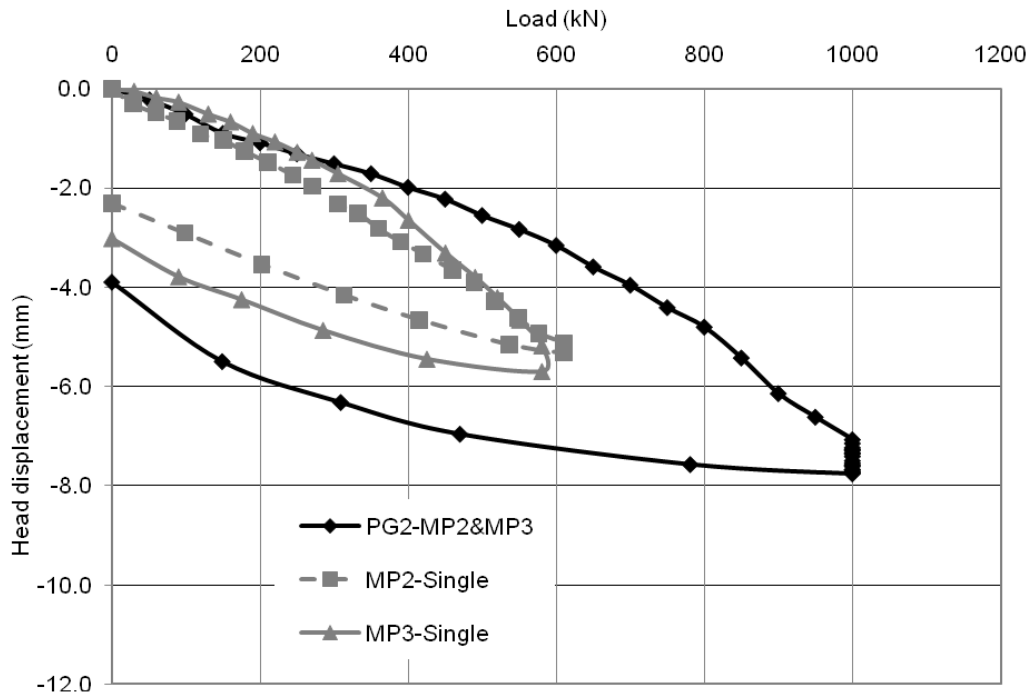


Figure 6. 10. Load-displacement curves for PG2, MP2 and MP3

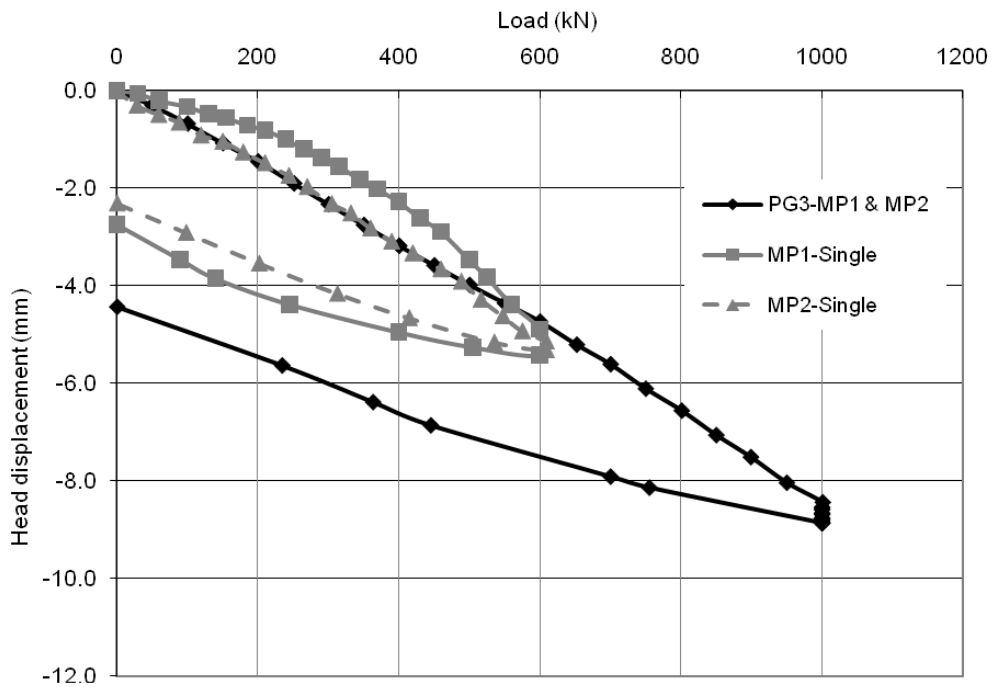


Figure 6. 11. Load-displacement curves for PG3, MP1 and MP2

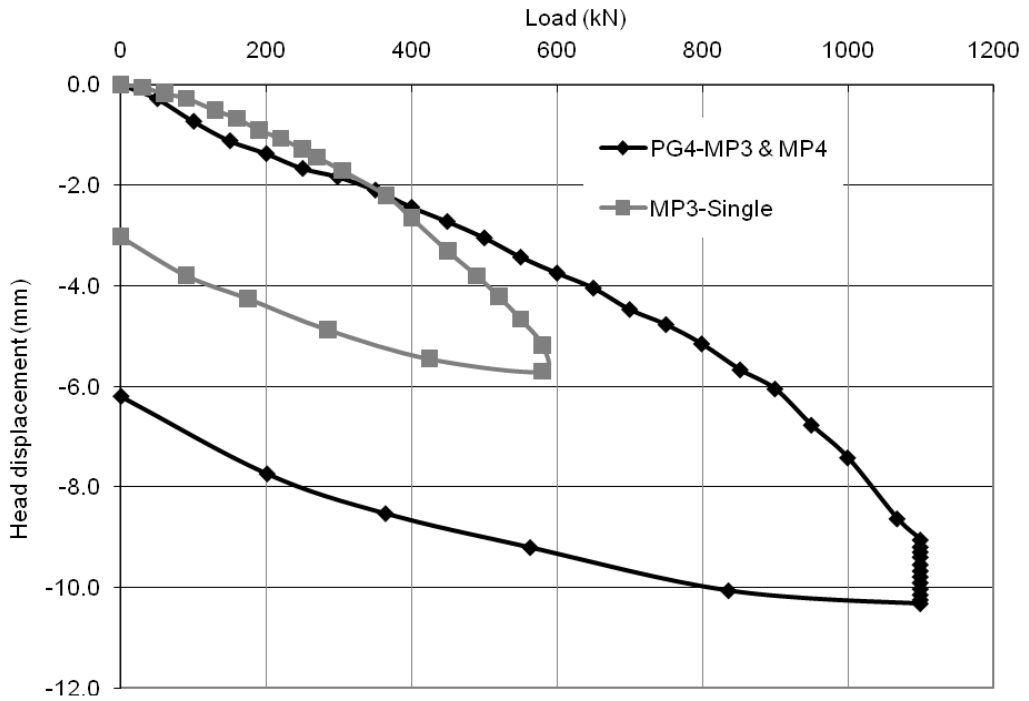


Figure 6.12. Load-displacement curves for PG4 and MP3

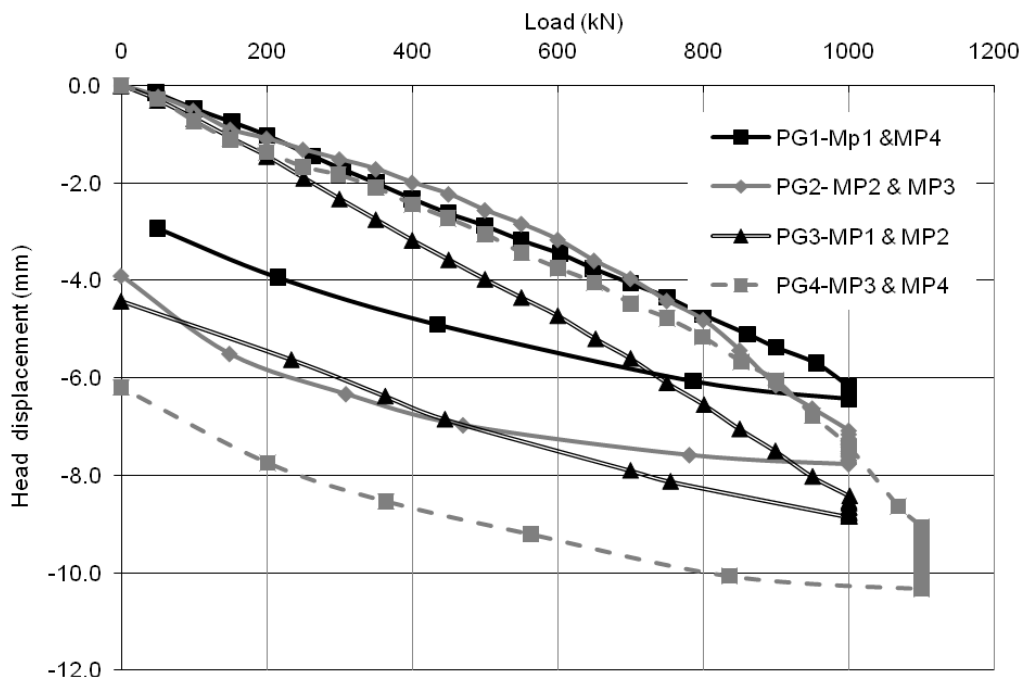


Figure 6.13. Load-displacement curves for all pile group tests

Figure 6.13 shows that none of the groups reached its geotechnical capacity, with PG4 seems to start curving at a steeper slope upon reaching 1100kN. This is further confirmed by the creep test results shown in Table 6.1. The pile group stiffness, K_g , is calculated at the group design load, i.e. 600 kN and at the maximum applied load 1000 kN from:

$$K_g = \frac{P}{\delta_g} \quad (6.2)$$

Where: P is the applied load, and δ_g is the corresponding group displacement. The group stiffness values calculated using Eq. 6.2 for all groups are presented in Table 6.2. It can be inferred from Table 6.2 that the behavior of tested groups is similar at both the design load and the maximum applied load. However, at the design load, PG3 is diverging from the other three groups due to the aforementioned load test sequence. The average pile group stiffness at the design load is around 168kN/mm and at the maximum applied load is about 140kN/mm.

Table 6. 1. Micropiles group creep test at maximum applied load

	Applied Load	Creep from 1 to 10 min
	kN	mm
PG1	1000	0.2
PG2	1000	0.7
PG3	1000	0.5
PG4	1100	1.3

Table 6. 2. Pile group stiffness

Pile group	Stiffness at the design load	Stiffness at the max. applied load
	K_{600} , kN/mm	K_{1000} , kN/mm
PG1	182	161.3
PG2	193.6	140.8
PG3	127.7	120
PG4	170	138.9

6.3 Numerical Analysis

The field test results provided the required information of the performance characteristics of the hollow bar micropiles in groups. This information is used in creating and calibrating a FE numerical model. Upon calibrating the numerical model, it was used to reveal further useful information on the behavior of hollow bar micropiles group action. The additional information gleaned from the numerical modeling exercise included the group efficiency factor and interaction factors between the micropiles at the design load (performance requirement) and at the failure load (capacity requirement). The finite element analysis was performed using the software package ABAQUS, which allowed simulating the behavior of the micropile-soil foundation system under different loading conditions and geometrical configurations.

6.3.1 Geometric modeling

Unlike the case of single micropile, the group tests were modeled using three dimensional (3D) FE models. In order to reduce the computational time, symmetry was exploited by considering only a half or a quarter of the required geometry. Figure 6.14 shows the geometry of a pair of micropiles during a field load test, which has two axes of symmetry. Accordingly, only a quarter of the soil deposit and one half of one hollow bar micropile will be modeled to calibrate the field test results.

The soil and the pile are modeled utilizing C3D8R elements. The C3D8R element is a continuum stress/displacement element with first-order (linear) interpolation. The element has a hexahedra (brick) shape with eight nodes. It is characterized by reduced integration, which saves considerable computational time, and has hourglass control. The element is recommended by ABAQUS standard library for problems involving contact or large distortions. The element has three active degrees of freedom: u_1 , u_2 , and u_3 . The degrees of freedom 1, 2, and 3 coincide with the three global Cartesian directions X, Y and Z, respectively. Figure 6.15 depicts the shape of the element and the corresponding nodes.

The dimensions of the model were selected to fulfil the recommendation of Helwany (2007) to model pile groups utilizing the ABAQUS software. The model was extended in the horizontal direction to a distance ≥ 25 the micropile bit diameter in both X and Y directions. A limited mesh sensitivity analysis was carried out to identify the computational optimum configuration of the model and the location of the horizontal bottom boundary with respect to the micropile toe. Two models configurations were

considered: a square plan and a quarter circle plan, employing two different horizontal boundaries. The two models are illustrated in Figs. 6.16 and 6.17.

The boundary conditions assigned to each model face are as follow:

- The vertical faces perpendicular to the X- axis are fixed in X direction $u_x = 0$
- The vertical faces perpendicular to the Y- axis are fixed in Y direction $u_y = 0$
- The horizontal face at the bottom of any model is fixed in all three directions, $u_x = u_y = u_z = 0$
- The ground surface is free in all directions.

For each model, two horizontal bottom boundary locations were assigned at a distance 0.75L and 1.0L (L is micropile length) measured from the micropile toe. The geometry of the model was discretized into a number of elements, maintaining an aspect ratio of the elements between 1:1 at the vicinity of the hollow bar micropile, and 1:5 at the far field. Table 6.3 gives the number of elements assigned in each model and boundary case.

In both models, the hollow bar micropile was modeled utilizing the shape shown in Fig. 6.18. As shown previously in Chapter 5 during the calibration of the single pile monotonic load phase, the hollow bar micropile had variable cross section along its shaft. Hence, the same geometry was used for the analysis of the micropile group test. In all models, the hollow bar micropile was simulated using 3528 elements.

Four analysis jobs were performed, two for each model. The jobs are denoted: Q0.75L, Q1L, C0.75L, and C1L. The first letter in the job notation indicates the model shape; square or circular while the number indicates the position of the bottom boundary. The load displacement curves obtained from all analyses are given in Fig. 6.19.

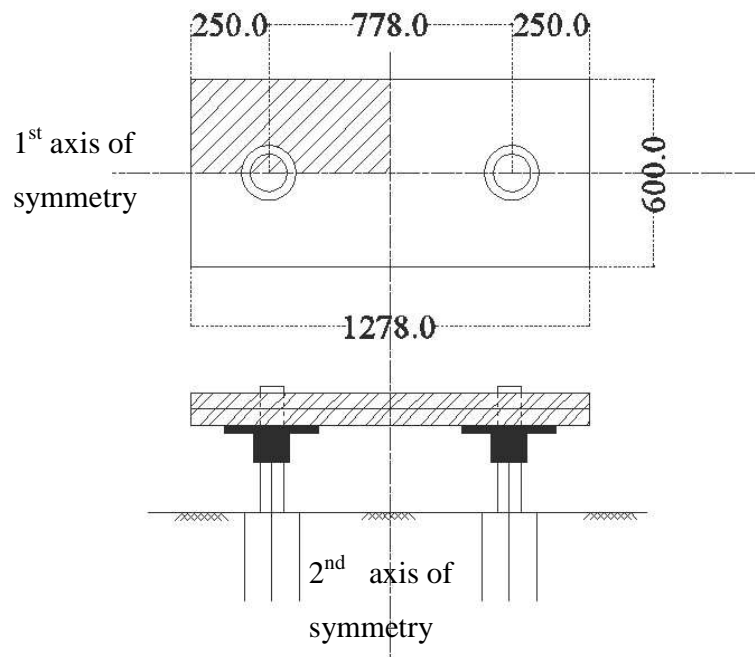


Figure 6. 14. Axes of symmetry in micropile group assembly

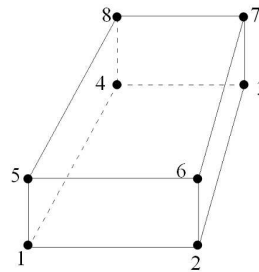


Figure 6. 15. C3D8R element geometry

Table 6. 3. Number of elements for each model

Model	Quarter shape model	Circular shape model
Boundary at 0.75 L	84896	70506
Boundary at 1.0 L	116875	91808

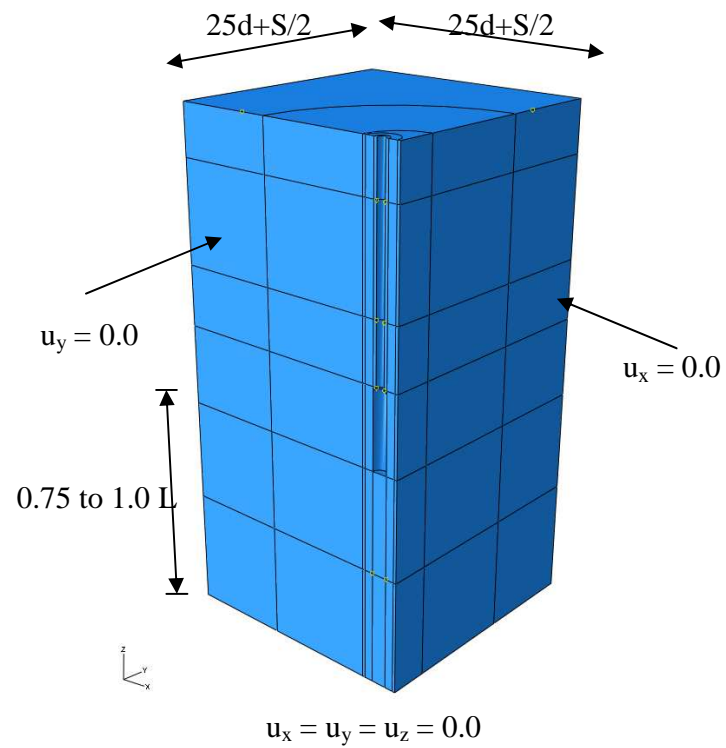


Figure 6. 16. The 3D quarter shape model of the soil

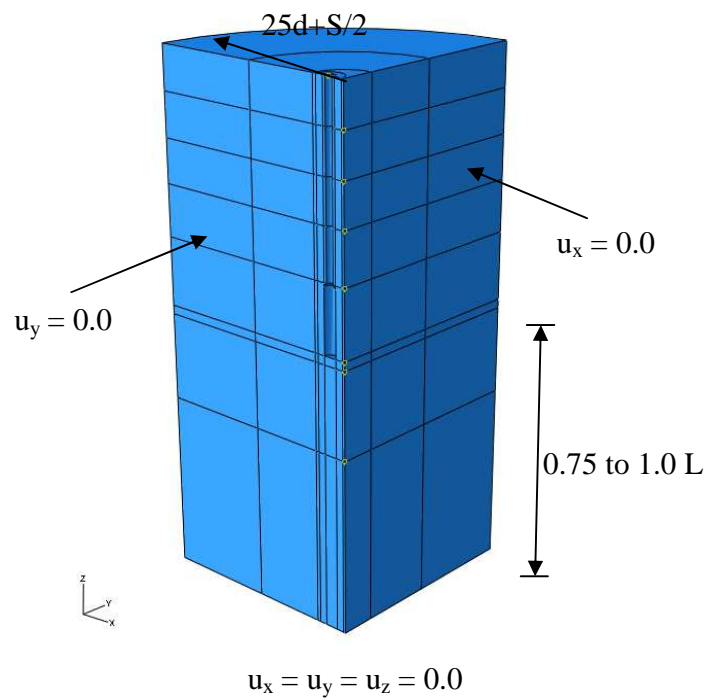


Figure 6. 17. The 3D circular shape of the soil



Figure 6. 18. The geometric model of the micropile in the group analysis

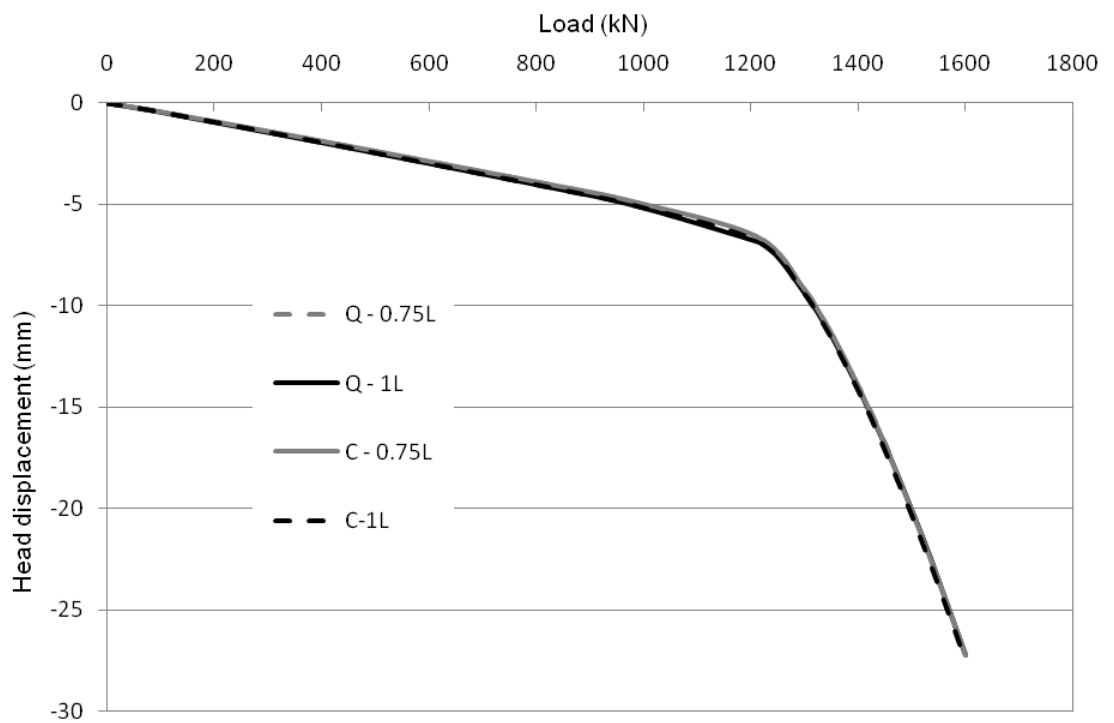


Figure 6. 19. Effect of model shape and vertical boundary on model behavior

The four analyses produced almost identical behavior up to the maximum applied load. It can be deduced from Fig.6.19 that:

- Moving the vertical boundary of the model a distance further than a circle with radius = $25d + S/2$ has no effect on the performance of the model.
- The location of the lower horizontal boundary of the model has no effect on the model performance if it is located at a distance larger than 0.75 the micropile length.

Accordingly, the circular shape model with the lower horizontal boundary located at 0.75 the micropile length was employed in calibrating the pile group numerical models.

6.3.2 Material modeling

Three different materials are involved in the hollow bar micropile – soil system, steel, grout and soil. The material models adopted in the pile group calibration followed that described in section 5.5.1.2: steel was modeled using linear elastic behavior; grout was modeled using nonlinear elastic-plastic model (Fig. 5.27) and soil was modeled utilizing the Mohr-Coulomb plasticity model accompanied by elastic properties to model the linear –elastic behavior of the soil. The soil deposit was divided into sub layers following the parameters given in Table 5.6. The grout body and the hollow bar were assumed to be bonded due to the mechanical bond arisen from the installation technique of this kind of micropiles. The micropile – soil interface was simulated employing the penalty interaction model in ABAQUS standard.

6.4 Calibration of Pile Group Field Tests

The same geometric model used to represent the geometry of the single hollow bar micropiles calibration was employed here. The geometry of the calibrated FE model has an enlarged pile diameter equal to $1.75d_{bit}$. This enlarged section extends to $0.25L$ measured from the pile toe.

Figures 6.20 (a) through (d) illustrate the load – displacement curves for the field tests and numerical calibrations for micropile groups PG1, PG2, PG3, and PG4. The figures show that the calculated response curves using the FE model are in excellent agreement with the field load test results. In all calibration analysis performed, the same geometric and material models are used, but the interaction model parameters are tuned to reach the calibration of each individual pile group. This explains the small difference in the initial slope of the load – displacement curves for the different load tests. The parameter was refined to achieve a match of the pile – soil interface surface stiffness, κ . The parameter was discussed previously in Section 5.5.1.3.

The interface stiffness was adjusted to represent the sequence of the field test followed in site. This is explained in the following. Pile group PG1 was calibrated using interaction stiffness equal to κ , κ is the default value as described previously in section 5.5.1.3. To calibrate PG2, the stiffness of the interface should be less than κ , which was achieved by assigning interface stiffness equal to 0.75κ . Similarly, pile group PG3 was calibrated using interface stiffness equal to 0.5κ , and PG4 was calibrated utilizing stiffness equal to 0.6κ .

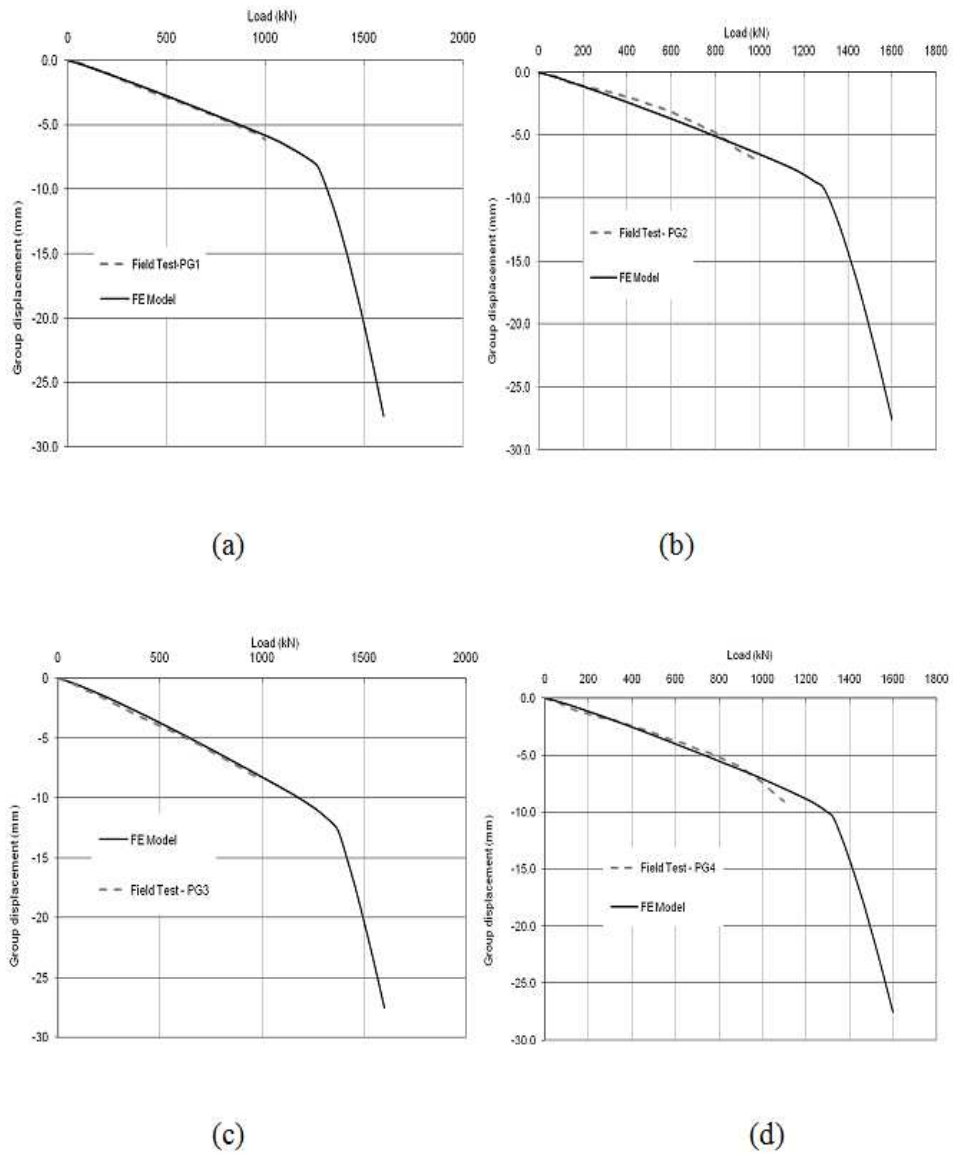


Figure 6. 20. Load – displacement of field test and its FE calibration:

(a) PG1; (b) PG2; (c) PG3; and (d) PG4

The interface stiffness of PG3 was less than that of PG2 and PG4 due to the sequence of loading and short durations between tests. The adhesion factor between the clayey soil surrounding the micropile and the grout body employed considered in all models was 0.9. This value confirms the finding of the range obtained from calibration of the monotonic field tests phase.

6.4.1 Micropile group capacity

There is no established method to obtain the failure load for a group of piles from field load tests. Usually, the failure load is obtained from field load tests on single piles. The capacity of pile group is calculated subsequently by multiplying the obtained failure load by the number of piles in the group and assigning an appropriate efficiency factor depending on the piles spacing to diameter ratio.

Whitaker (1957) suggested a group efficiency factor, η , based on the spacing between the piles for groups embedded in clay, whose value varies according to the spacing as shown in Table 6.4. Meanwhile, Terzaghi and Peck (1967) suggested an efficiency factor equal to 1 for friction piles in clay. The group capacity of piles installed in clay can also be estimated by the block failure method. In this method the group capacity is given by:

$$Q_g = s_{ub} N_c \bar{b}^{-2} + 4 s_{us} \bar{b} L \quad (6.3)$$

Where: \bar{b} is the width of the block containing piles and soil; L is the embedded length of the pile; s_{us} is the average undrained shear strength along the shaft of the pile; s_{ub} is the average undrained shear strength at the pile tip; and N_c bearing capacity factor.

The capacity of the pile group is taken as the lesser of the two values (given by Eqs. 6.1 and 6.3). A factor of safety is then applied to deduce the design capacity of the pile group. In addition, the group design capacity should be limited in consideration of ensuring a maximum settlement of the pile group within the acceptable tolerance specified by the local building codes. The same calculations are followed when using micropiles in groups. FHWA NHI (2005) suggests an efficiency factor equal to 1 for micropiles group embedded in clay for the following cases:

- The micropile cap is in firm contact with the ground.
- The micropile cap is not in firm contact with the ground and the ground is stiff (i.e., undrained shear strength of the soil is greater than 95 kPa)

For micropile groups embedded in relatively soft clay (i.e., soil undrained shear strength is less than 95 kPa) and the pile cap is not in firm contact with the ground, FHWA NHI (2005) suggests using efficiency factors similar to those given in Table 6.4. Nevertheless, the block capacity of the micropile group should be computed in all cases and the lesser value should be considered in design. No suggestions of group efficiency factor values for hollow bar micropiles are available in the literature. However, the guide values from the FHWA NHI (2005) can be used.

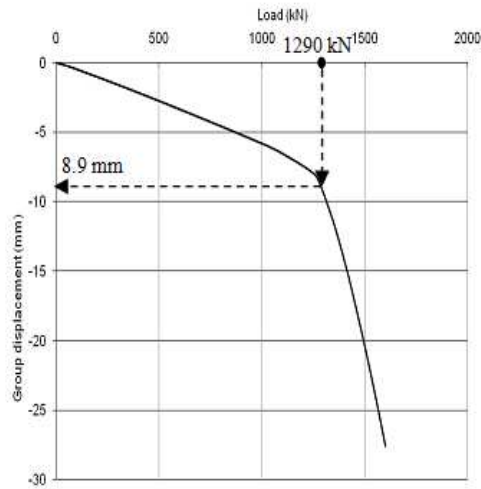
Table 6. 4. Group efficiency factor based on pile spacing

Pile spacing	3d	4d	5d	6d	7d	8d
η	0.7	0.75	0.85	0.9	0.95	1.0

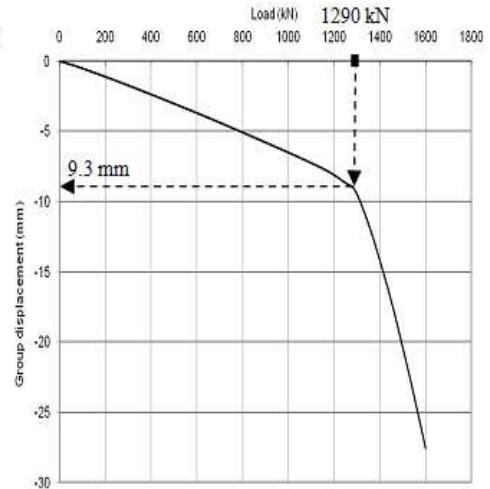
The group capacity of the hollow bar micropile conducted in this study is computed only utilizing the group efficiency approach. There is no block failure mechanism applicable for a pair of micropiles. Following the recommendation of the FHWA NHI (2005), the pair of hollow bar micropiles tested in the field should have group efficiency equal to 1.0. The calibrated models for monotonic load tests on single micropiles showed that at $\alpha = 0.9$, the failure load of this micropile was about 645 kN. Therefore, utilizing Eq. 6.1, the capacity of the pair employing a group efficiency factor equal to 1 is 1290kN. Figures 6.21(a) through 6.21(d) show the load – displacement curves of the four calibrated pile group tests with the group capacity at efficiency factor equal to 1.0 marked.

The figures show that the settlement corresponding to capacity of 1290kN varies from 9mm to 12 mm. It is observed that the group capacity utilizing efficiency factor equal to 1.0 lies within the transition portion of the load – group displacement curves, for all micropile groups. In other words, the hollow bar micropile group can experience group efficiency factor higher than one to reach a true failure point. This might be because the enlargement of the hollow bar micropile base that occurred during installation.

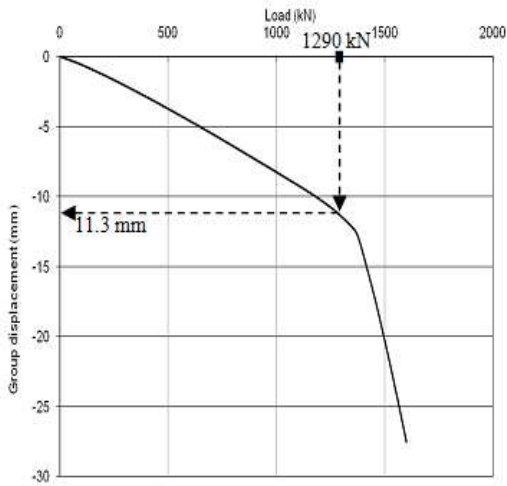
Because the performance of hollow bar micropiles is installation dependent, it has a unique feature; it is a friction pile but it has an enlarged base. However, assigning an efficiency factor bigger than one for hollow bar micropiles groups in clay will not be acceptable because it cannot be justified in all ground conditions and with different installation techniques. Meanwhile, the group capacity will be evaluated again utilizing the block failure method, and the lesser value will be considered as the group capacity.



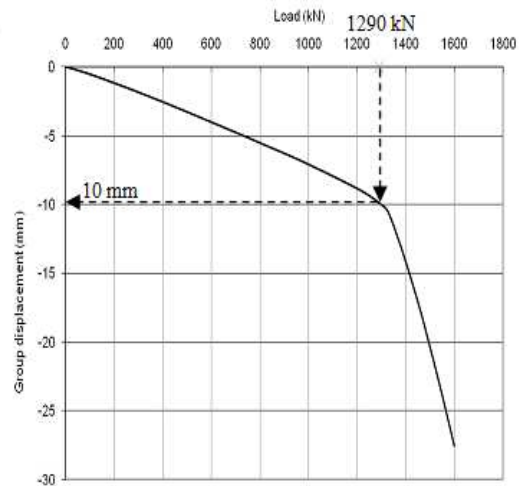
(a)



(b)



(c)



(d)

Figure 6. 21. Capacity of pile group at group efficiency equal to 1.0:

(a) PG1; (b) PG2; (c) PG3; (d) PG4

In summary, Fig. 6.21 shows that using a group efficiency factor equal to 1.0 for hollow bar micropile groups embedded in clay is neither overestimating nor underestimating the group capacity even for closely spaced hollow bar micropiles.

6.5 Parametric Study

After calibrating the models using the group field load tests, the 3D FE models were used to perform a parametric study. The proposed geometry of the hollow bar micropile is considered within different soil conditions. However, the study is limited to the hollow bar micropile groups embedded in clayey soils. The parametric study is conducted on hollow bar micropile groups incorporating two sets:

- Group capacity parametric study: this study aims to capture the group efficiency factor of hollow bar micropile embedded in homogenous clay soils using various spacing to diameter ratio.
- Group performance parametric study: the goal of this study is to develop an appropriate interaction factor approach between hollow bar micropiles in cohesive soils.

6.5.1 Parametric study for group capacity

It is required to evaluate the capacity of hollow bar micropiles group embedded in homogenous clay soils with regard to the group efficiency factor. The study was performed on pairs of hollow bar micropiles loaded until a true failure point was achieved. At that point, the group efficiency factor is back-calculated and compared to

the capacity of the group utilizing efficiency factor equal to 1. The parameters considered in this part of the study are:

- Micropiles are embedded in clayey soil with s_u that varies from 90 kPa to 175 kPa.
- The adhesion factor between the soil and the micropile is between 0.9 and 1.0.
- Slenderness ratio, $L/d = 30$ and 50 .
- The spacing to the drilled-hole diameter ratio, S/d_{hole} , varies from 2.5 to 5.

As mentioned previously in Chapter 5, the hole diameter, d_{hole} , is calculated from:

$$d_{\text{hole}} = \sqrt{\frac{4V_{\text{hole}}}{\pi L}} \quad (6.4)$$

Meanwhile, the following parameters are kept constant throughout the study:

- Unit weight of soil
- Lateral earth pressure of the clayey soil surrounding the micropile
- Poisson's ratio for clayey soil at 0.45.
- Grout and steel material modeling properties.

Since two micropiles are loaded together, therefore, the same geometric model employed during calibration of the field test is used in this set of parametric study. However, for each analysis job the spacing between the micropiles was varied within the range

considered. Figures 6.22 and 6.23 illustrate the load – group displacement plots of hollow bar micropiles embedded in clay with $L/d = 30$ and $s_u = 90$ and 175 kPa, respectively. In each figure, three load – displacement curves are plotted for $S/d_{\text{hole}} = 2.5$, 4 , and 5 . In addition, the group capacity considering a group efficiency factor equal to 1 is defined by a vertical line. The figures show that, for all S/d_{hole} and s_u values considered, the pile group capacity at failure exhibits a group efficiency factor greater than or equal 1 . Also, the results show an increase in the group efficiency factor by increasing the spacing to diameter ratio; however, this increase is marginal. As shown in Figs. 6.24 and 6.25, the same group behavior is observed for hollow bar micropile characterized by $L/d = 50$. However, for micropiles with $L/d = 50$, the group efficiency factor exceeds 1.0 .

Extra jobs are performed for hollow bar micropile embedded in softer soil. The undrained shear strength of the soil considered is equal to 50 kPa. Figure 6.26 depicts the load – group displacement curves for two values of S/d_{hole} ; 2.5 and 5 . The same behavior observed for group action in stiff clay is observed for groups in softer clay. Again, this could be due to the unique geometry of the hollow bar micropiles. The adhesion factor was assumed equal to 1 in all jobs shown in Figs. 6.22 to 6.26. Other jobs were carried for adhesion factor equal 0.9 , and the same conclusions were obtained.

Hence, it is recommended to calculate the micropile group capacity utilizing a group efficiency factor equal to 1 for hollow bar micropiles embedded in cohesive soils. The group capacity should also be calculated employing the block failure mechanism. The group capacity is then taken as the lesser value of the two.

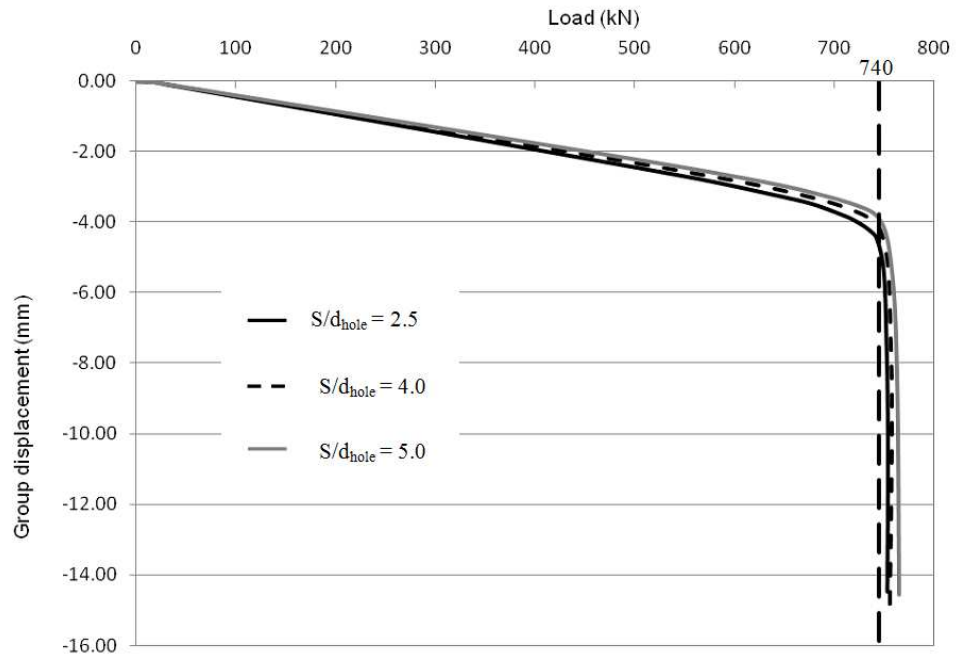


Figure 6. 22. Load – group displacement for $s_u = 90$ kPa and $L/d = 30$

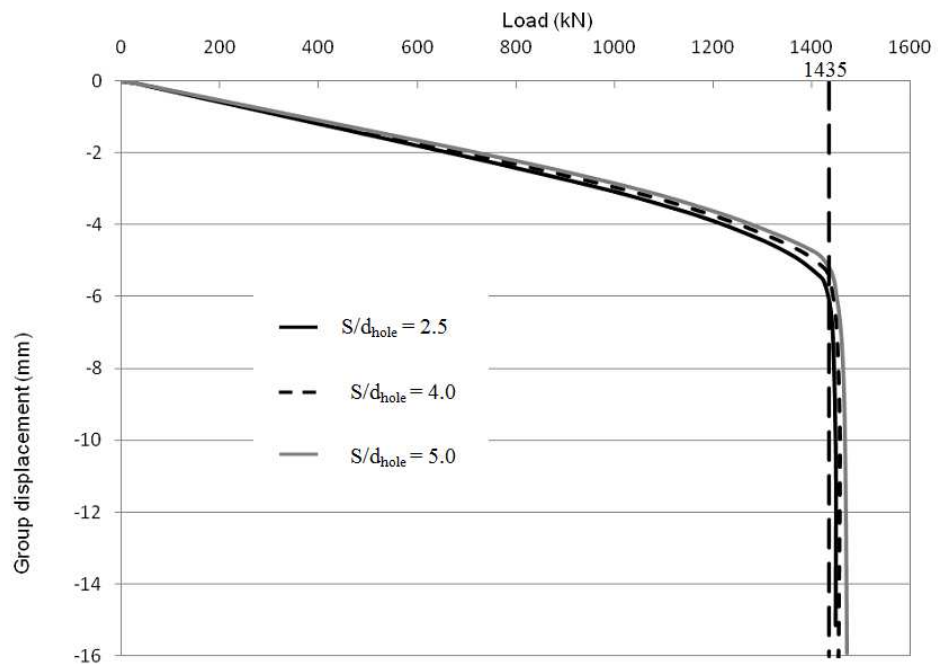


Figure 6. 23. Load – group displacement for $s_u = 175$ kPa and $L/d = 30$

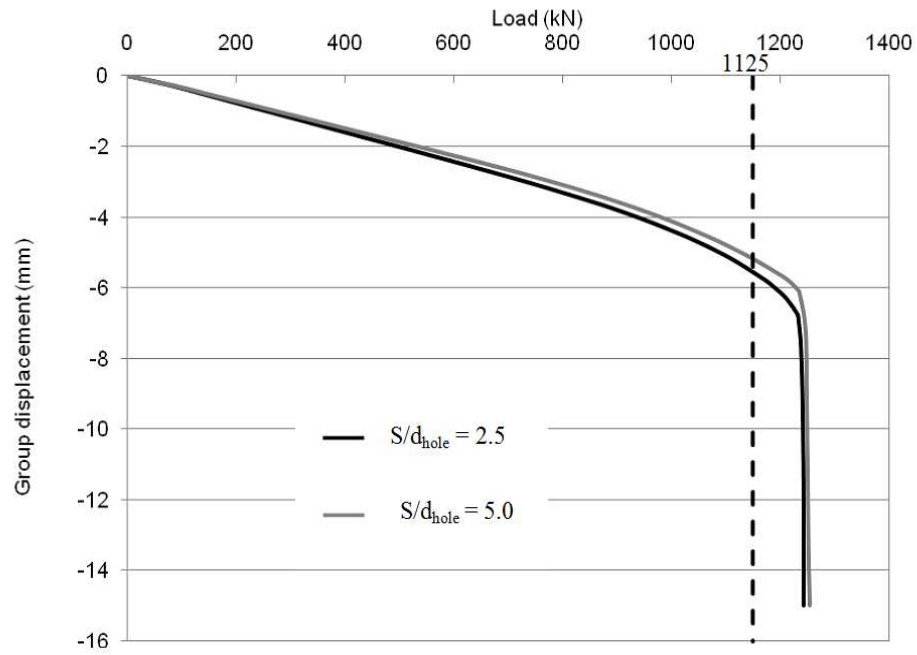


Figure 6. 24. Load-group displacement for $s_u = 100$ and $L/d = 50$

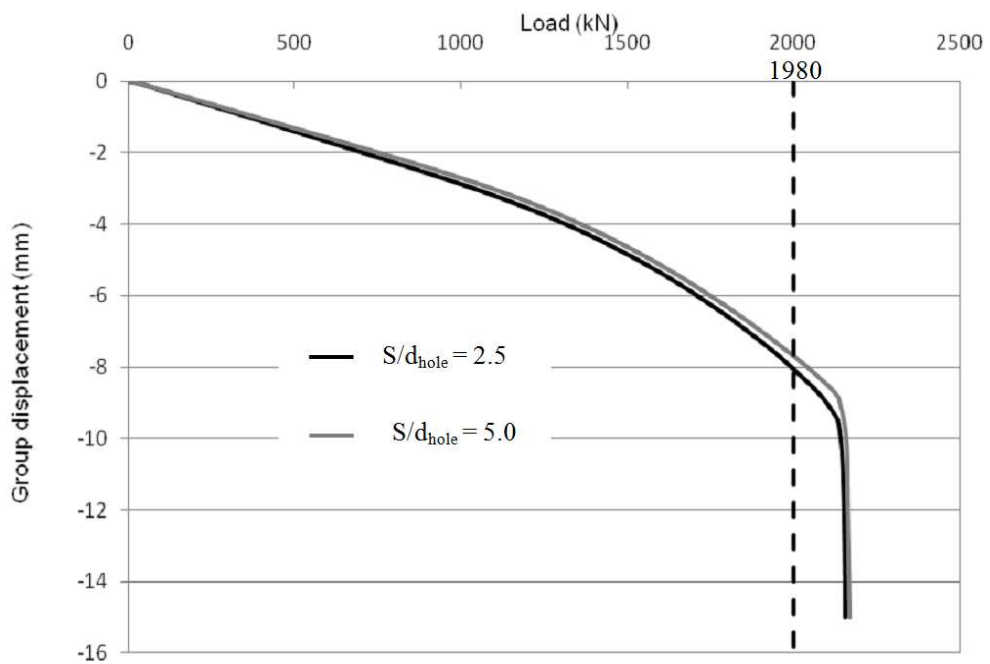


Figure 6. 25. Load-group displacement for $s_u = 175$ and $L/d = 50$

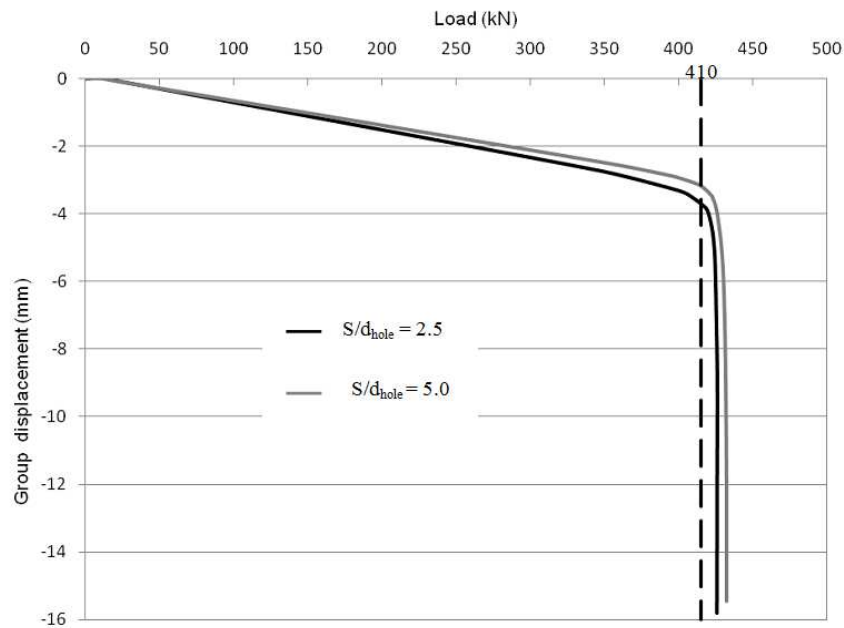


Figure 6. 26. Load – group displacement for $s_u = 50$ kPa and $L/d = 30$

6.5.2 Parametric study for group performance

When piles are installed at close spacing, the response of an individual pile within the pile group is influenced by the response of neighboring piles as the piles interact through the surrounding soil. To account for this interaction, the soil should be considered as a continuum, where the displacement of one pile will contribute to the displacement of other piles. The effect of interaction between piles can be expressed in terms of interaction factor, which is defined as the additional settlement caused by adjacent pile normalized by the pile settlement under its own load.

The interaction factors are derived from the deformations of two equally loaded piles and describe the fractional increase in deformation of a pile due to deformation of an equally loaded neighbouring pile. The flexibility is then established by the superposition of

interaction between individual pairs of piles in the group. By increasing the spacing between the piles, the interaction diminishes and the stiffness of the group is determined by summing the stiffness coefficients of the individual single piles. The accuracy of the approach appears adequate, at least for small and moderately large groups.

Pioneering research in this field had been conducted by Poulos who published his results in a number of papers (e.g. Poulos 1968, 1971, 1974, 1979), and included all results in Poulos and Davis (1980). More rigorous approaches based on computer programs considering direct analysis of pile groups under static loads have been carried out by El Sharnouby and Novak, (1985) and Lee (1993a), (1993b). These studies indicate that the main results of pile interaction are an increase in settlement of the group, the redistribution of pile stresses and, with rigid caps, redistribution of pile loads.

If a rigid cap is assumed, which implies the same displacement for all piles heads but different individual stiffness, the vertical stiffness of the group, K_g , can be evaluated approximately as:

$$K_g = \sum_{i=1}^N K_{sp} / \sum_{i=1}^N \alpha_{ri} \quad (6.4)$$

Where: K_{sp} is single pile stiffness; α_{ri} is the interaction factor between the reference pile, r , and the i^{th} pile in the group, such that; $\alpha_{ri} = \alpha_{rr} + \alpha_{r1} + \alpha_{r2} \dots + \alpha_{rN}$, where $\alpha_{rr} = 1.0$

The reference pile should not be at the periphery or at the center of the group. The assumption in this evaluation is that the reference pile rarely represents the average stiffness of the piles in the group.

For a rigid pile cap, a more rigorous formula can be derived by imposing identical displacements on all pile heads and using the interaction factors to describe group stiffness. This procedure gives the vertical stiffness (El Sharnouby and Novak, 1990):

$$K_g = K_{sp} \sum_i \sum_j \varepsilon_{ij} \quad (6.5)$$

In which, ε_{ij} are the elements of the matrix, $[\varepsilon]$, calculated from:

$$[\varepsilon] = [\alpha]^{-1} \quad (6.6)$$

The interaction matrix $[\alpha]$ lists the interaction factors between every two piles, α_{ij} , in the group. The matrix has dimensions $N \times N$, and N is the number of piles in the group. The matrix is symmetric with all the diagonal elements α_{ii} equal to unity. Meanwhile, the interaction factor approach is used to estimate the settlement of the group from:

$$S_g = S_{sp} \times \sum_{i=1}^N \alpha_{ri} \quad (6.7)$$

Where: S_g is the estimated settlement of the group; S_{sp} is the settlement of the single pile under its average load within the group

However, the interaction factors available in the literature for axially load piles are not applicable for hollow bar micropiles because of its unique geometry. Accordingly, the FE model calibrated previously is used herein to provide a set of interaction factor curves for hollow bar micropiles in clayey soil.

To compute the interaction factor between two micropiles, the geometric quarter model shown in Fig. 6.17 is extended to one half of circle, i.e. the model is mirrored horizontally along the vertical axis. This was done to accommodate inserting another

micropile, so that one micropile would be loaded and the displacement of the two adjacent hollow bar micropiles would be recorded. In all cases, only one half of the two hollow bar micropiles is modeled. Figure 6.27 illustrates the new geometric model employed in evaluating the pile-soil-pile interaction for hollow bar micropiles.

In this study, the interaction factors are evaluated for the following parameters:

- Slenderness ratio L/d is chosen to be 30, 50, and 75. This range covers the typical values used in practice for micropiles.
- Three values of the stiffness ratio K (defined as the ratio between the micropile modulus and the surrounding soil modulus = E_p/E_s) are considered; 275, 500, and 1000. The modulus of the micropile is taken approximately equal to that of the grout, which varies from 21000 MPa to 26000MPa, depending on the grout strength. The Young's modulus of the grout is considered to be constant and equal to 24000 MPa. Thus, $E_p/E_s = 275$ representing stiff soil and $E_p/E_s = 1000$ represents soft soil.
- Spacing between the micropiles to hole diameter, S/d_{hole} , ratio, is covered between 2.5 to 15.

The interaction factors are evaluated at the design load, DL. The design load, DL, here is defined as the failure load according to Butler and Hoy (1970) divided by 2, i.e. $DL = Q_F/2$. Figures 6.28, 6.29, and 6.30 give the interaction factors between two hollow bar micropiles at DL characterized by slenderness ratio, $L/d = 30, 50$, and 75, respectively.

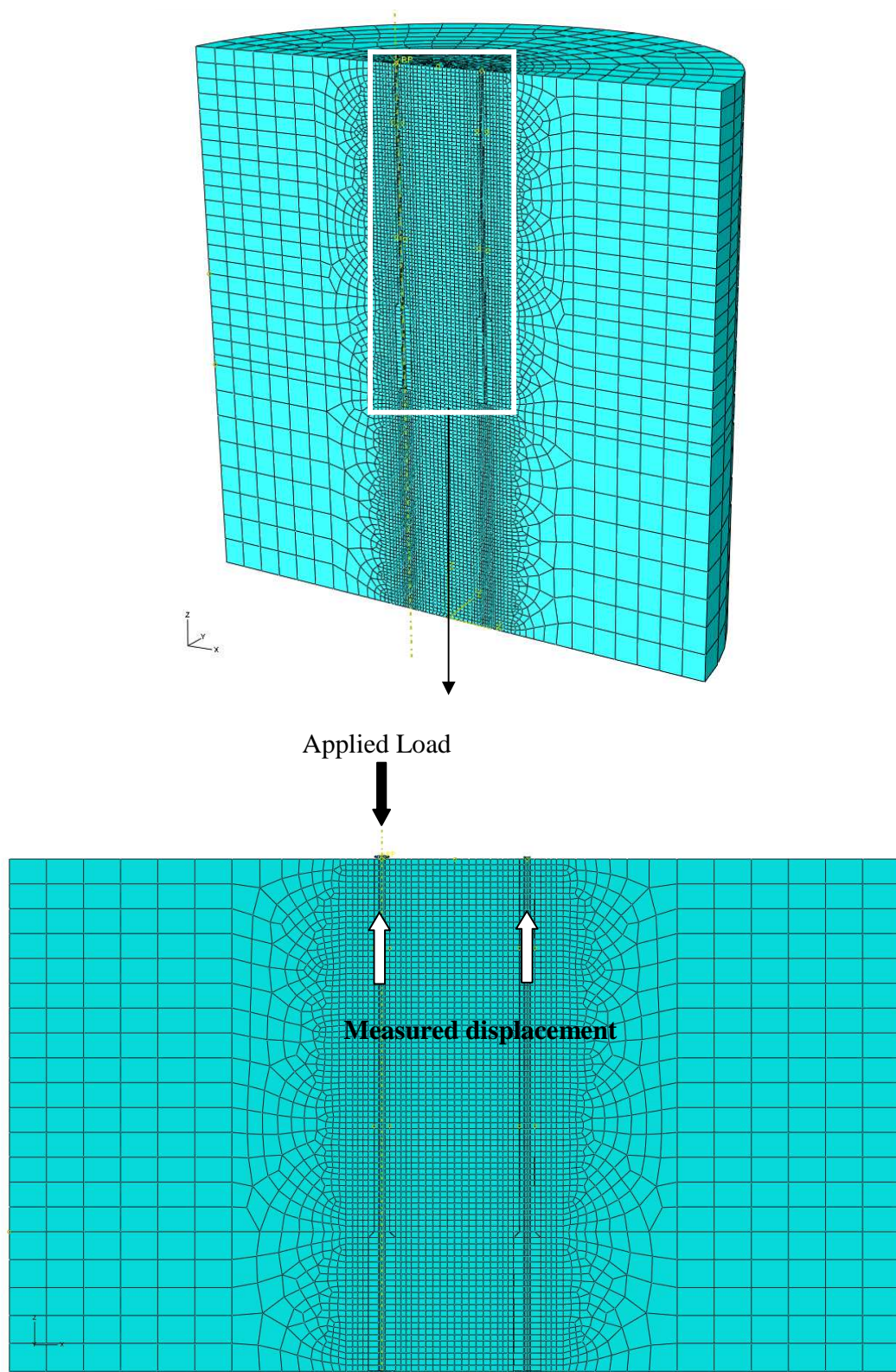


Figure 6. 27. Geometric model adopted for interaction calculations

The interaction factor graphs show that the interaction between two micropiles decreases as the stiffness ratio, \hat{K} , decreases for all values of L/d . Coinciding with the findings of Poulos and Davis (1980) for conventional piles, the interaction factor between adjacent micropiles decreases more dramatically between S/d_{hole} equal 2.5 to 5 than between S/d_{hole} equal 5 to 15. The effect of the slenderness ratio on the interaction between hollow bar micropiles is illustrated in Fig.6.31, for $E_p/E_s = 1000$ and in Fig. 6.32 for $E_p/E_s = 275$. For soft soils, $E_p/E_s = 1000$, the effect of L/d is negligible up to $S/d_{\text{hole}} \leq 5$. As the spacing between pile increases, the effect of slenderness ratio becomes more pronounced. On the contrary, the effect of the slenderness ratio on the interaction factor for stiff soils, $E_p/E_s = 275$, is more pronounced for closely spaced piles.

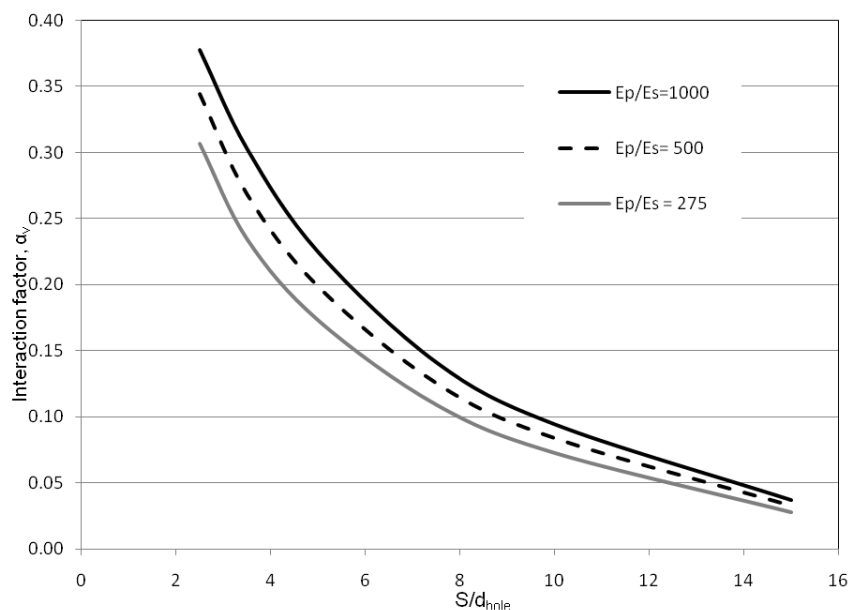


Figure 6. 28. Interaction factors at the design load for $L/d=30$

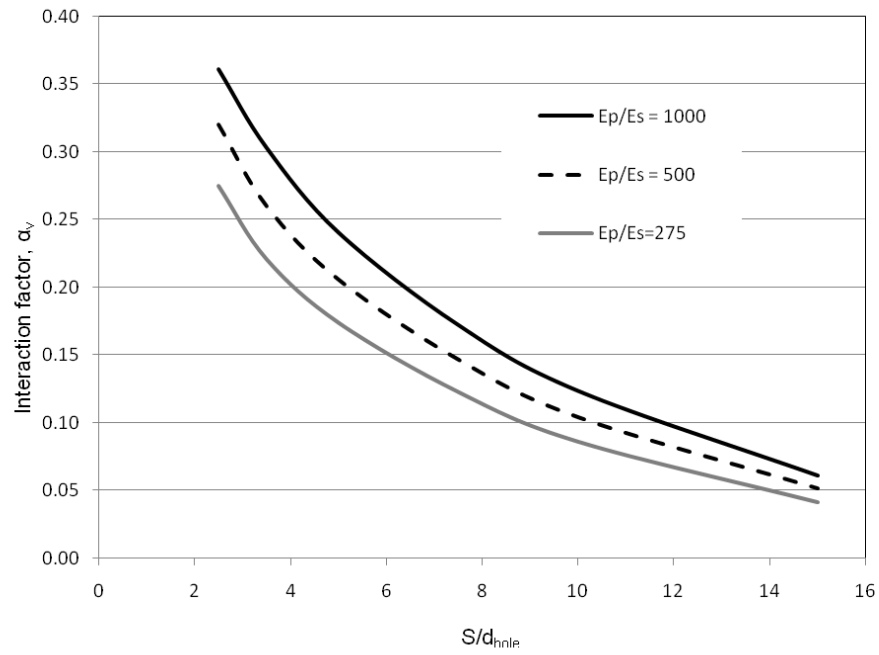


Figure 6.29. Interaction factors at the design load for $L/d = 50$

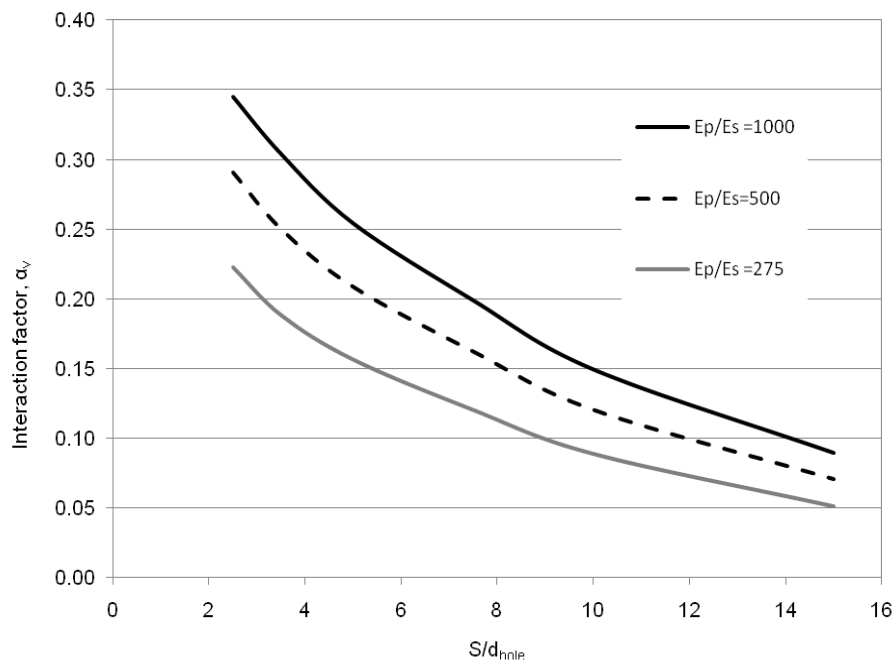


Figure 6.30. Interaction factors at the design load for $L/d = 75$

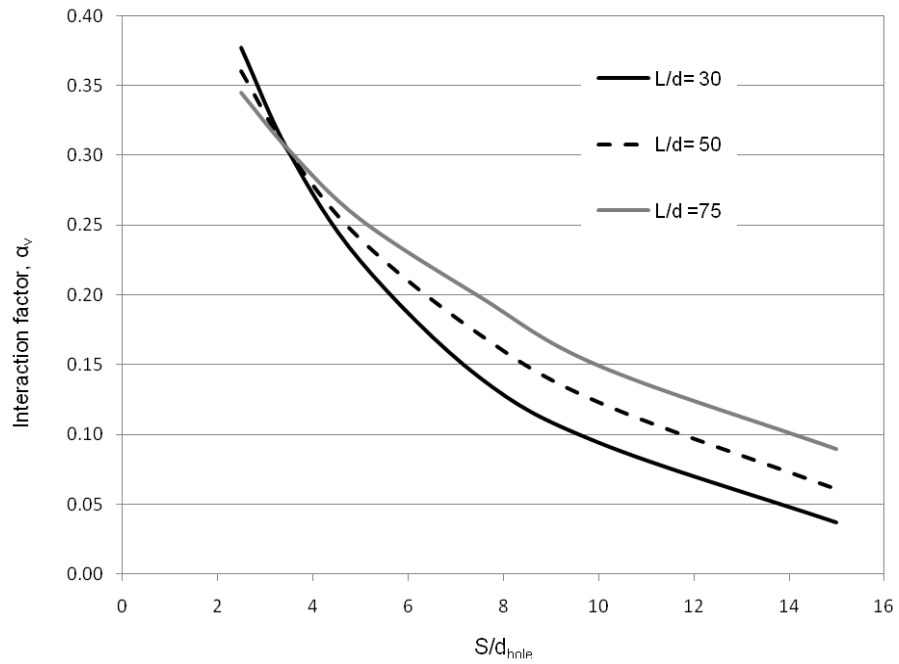


Figure 6. 31. Influence of L/d on the interaction factor between hollow bar micropiles, $E_p/E_s = 1000$

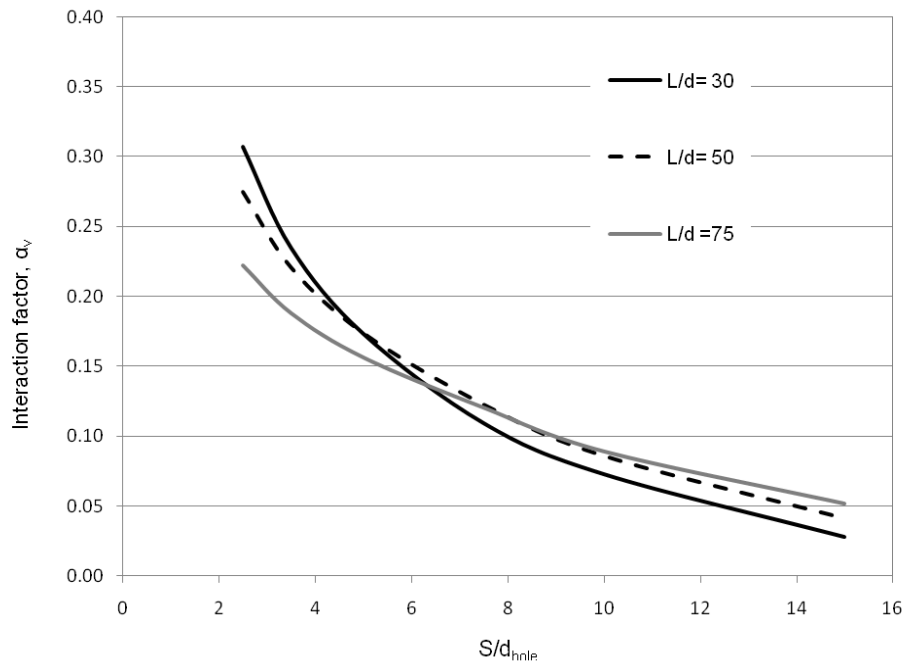


Figure 6. 32. Influence of L/d on the interaction factor between hollow bar micropiles, $E_p/E_s = 275$

Employing the given interaction charts, the settlement of a hollow bar micropile group can be estimated using Eq. 6.7. On the other hand, the interaction factor approach tends to overestimate the group settlement. This is because the interaction approach does not account for the stiffening effect of the intermediate piles when computing the interaction between any two individual piles within the group.

Accordingly, the effect of the intermediate hollow bar micropile is examined herein. This is accomplished by inserting another micropile in the geometric model shown in Fig.6.27. Hence, one micropile is loaded and the displacements of the other micropiles are calculated. The new geometric model containing the three hollow bar micropiles is depicted in Fig. 6.33. The locations of the intermediate micropile and the far micropile are highlighted in the figure.

The interaction factors are computed for three different models employing spacing to hole diameter ratio equal to 3.75, 5, and 7.5 between any two micropiles. This locates the far hollow bar micropile at a spacing ratio of 7.5, 10, and 15 times the hole diameter from the loaded one. Each model is examined for three values of stiffness ratio, \acute{K} , and for $L/d = 30$ and 50.

For each case, the interaction factor is calculated at the far micropile and compared with the interaction factor obtained previously without the intermediate micropile. The effect of intermediate micropile on the interaction factor is plotted in Figs. 6.34, 6.35, and 6.36 for micropiles characterized by $L/d = 30$ and $S/d_{\text{hole}} = 7.5, 10, \text{ and } 15$, respectively. For the same S/d_{hole} values, the effect of the intermediate micropiles is given in Figs. 6.37 to 6.39 for $L/d = 50$.

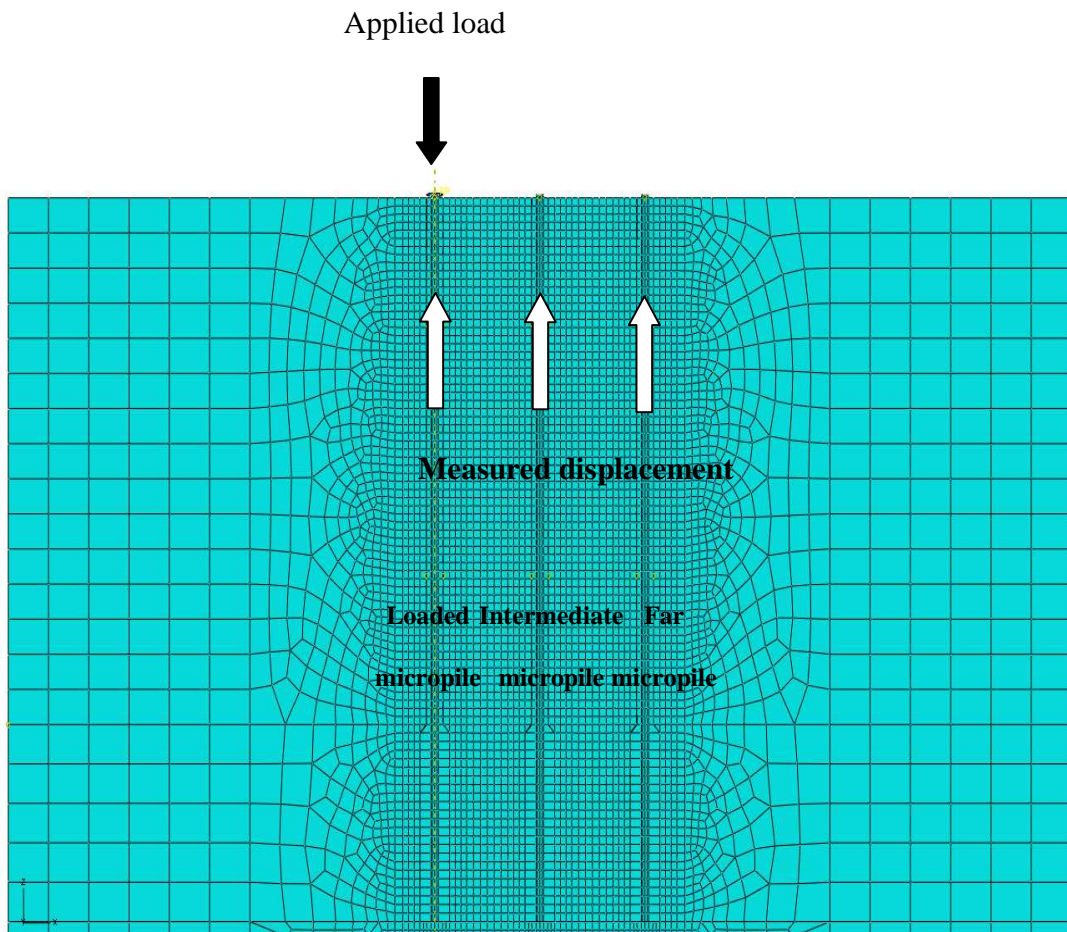
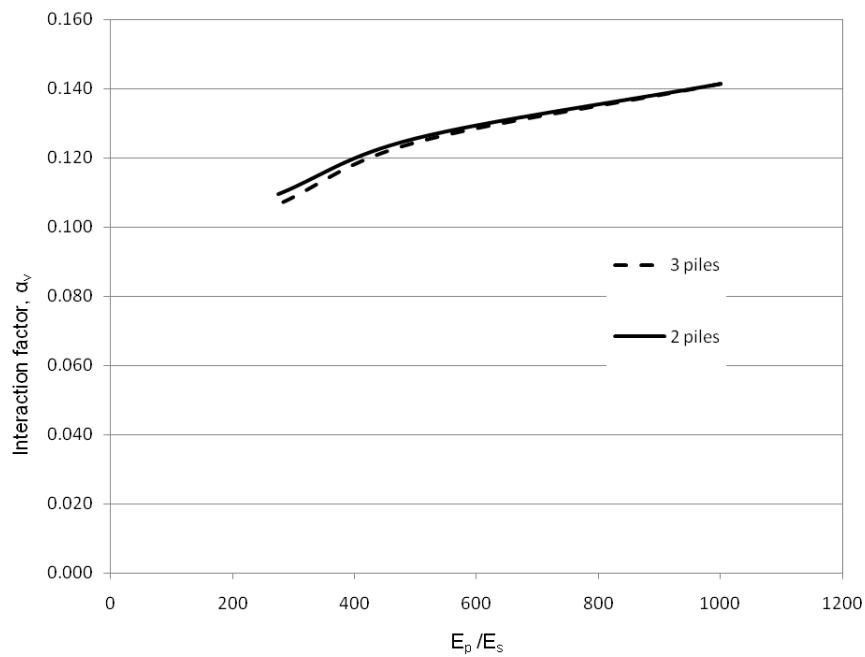


Figure 6. 33. Geometric model for three adjacent hollow bar micropiles

For all values of S/d_{hole} , L/d , and stiffness ratio examined here, the intermediate hollow bar micropile decreases the interaction factor between the loaded and far micropiles. However, the percentage of decreasing in the interaction factor due to the intermediate micropile is varying from almost 0% at $S/d_{\text{hole}} = 7.5$ to about 5% at $S/d_{\text{hole}} = 15$, for both values of L/d and all values of E_p/E_s considered the analysis.

It can be concluded from the results discussed above that the effect of considering an intermediate micropile on the interaction factor between hollow bar micropiles is limited. This may be attributed to the small diameter of the hollow bar micropiles, thus minimizing the stiffening effect of the soil between the micropiles. Therefore, Eq. 6.7 can be used to estimate the settlement of a group of hollow bar micropiles employing the interaction factors given in Figs. 6.28 to 6.30.



**Figure 6. 34. Effect of intermediate hollow bar micropile on the interaction factor,
 $S/d_{\text{hole}}=7.5, L/d=30$**

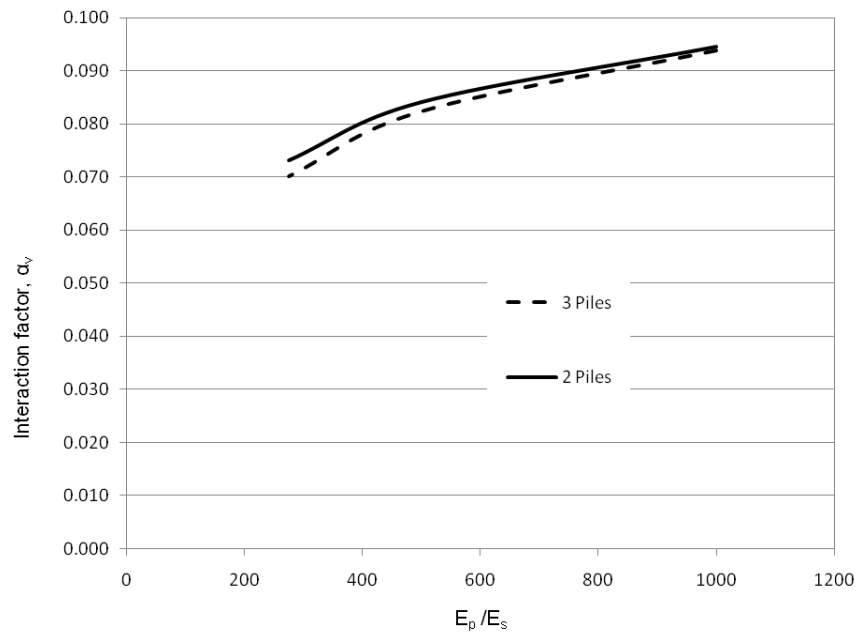


**Figure 6. 35. Effect of intermediate hollow bar micropile on the interaction factor,
 $S/d_{\text{hole}} = 10, L/d = 30$**

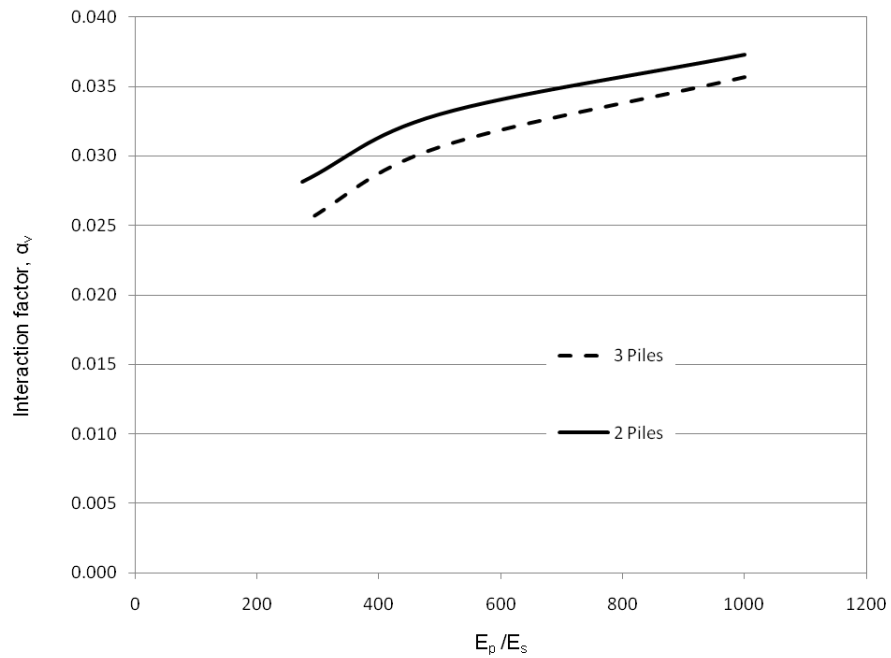


**Figure 6. 36. Effect of intermediate hollow bar micropile on the interaction factor,
 $S/d_{\text{hole}} = 15, L/d = 30$**

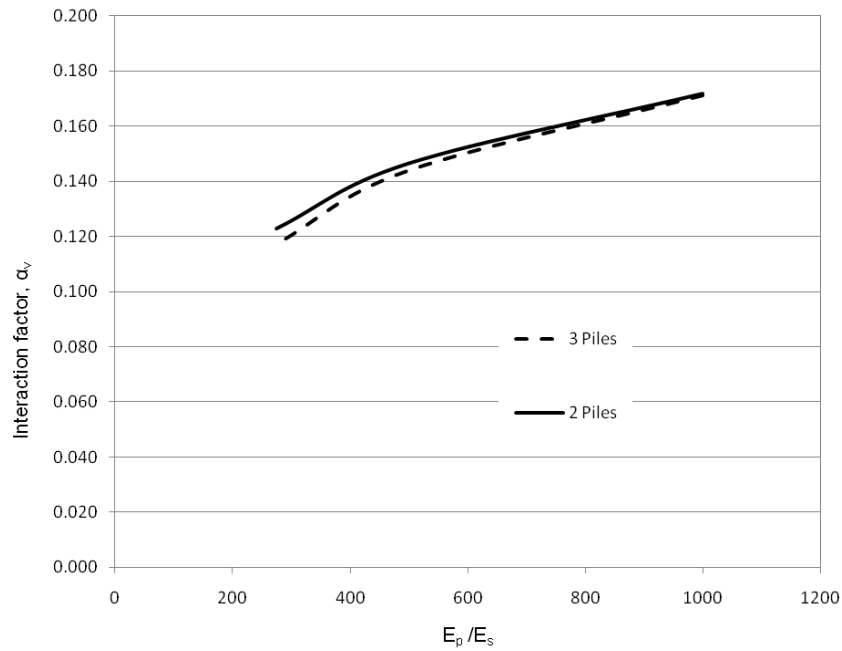


**Figure 6. 37. Effect of intermediate hollow bar micropile on the interaction factor,
 $S/d_{\text{hole}} = 7.5, L/d = 50$**

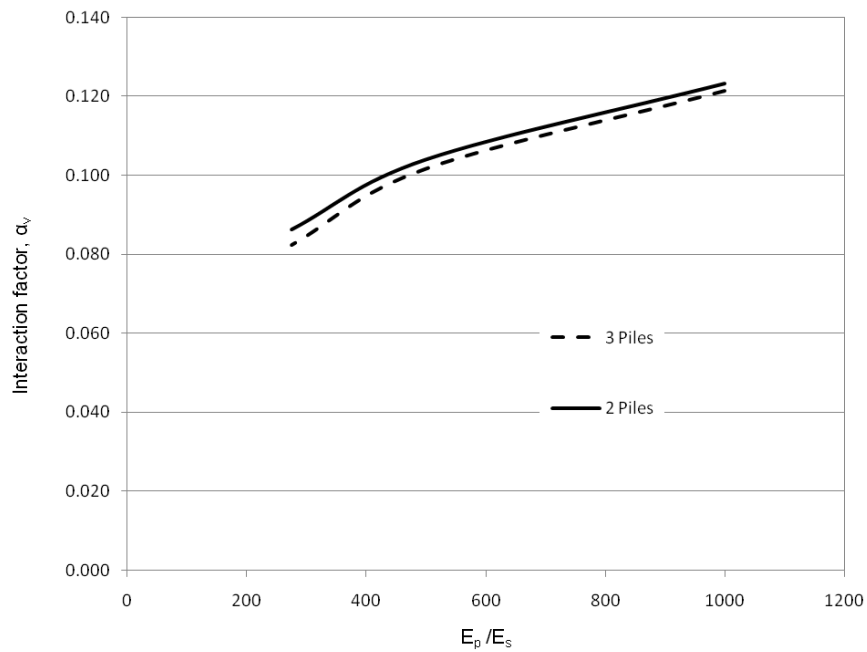


**Figure 6. 38. Effect of intermediate hollow bar micropile on the interaction factor,
 $S/d_{\text{hole}} = 10, L/d = 50$**

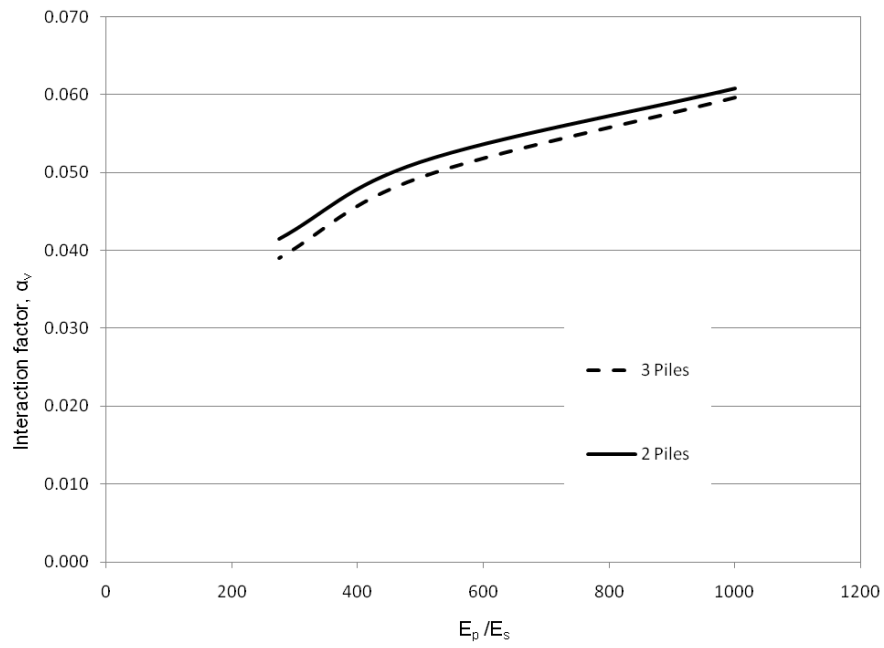


Figure 6. 39. Effect of intermediate hollow bar micropile on the interaction factor,

$$S/d_{\text{hole}} = 15$$

CHAPTER 7

LATERAL MONOTONIC AND CYCLIC PERFORMANCE OF HOLLOW BAR MICROPILES

7.1 Introduction

The four hollow bar micropiles were loaded laterally in the last phase of the field test program. Two monotonic and six cyclic lateral load tests were performed. This chapter documents the loading setup and procedures as well as the experimental results of the lateral monotonic and cyclic load tests.

The results of the monotonic load tests were employed to calibrate a numerical model established using the program L-Pile (Isenhower and Wang, 2011). A parametric study was then carried out to establish design guidelines for the hollow bar micropiles embedded in cohesive soils. Finally, the results obtained from the lateral cyclic tests are presented and discussed. An equation is proposed to estimate the degradation of the pile head stiffness under lateral cyclic loading.

7.2 Monotonic Lateral Load tests

Two monotonic lateral load tests were conducted on micropiles MP1 and MP2. The two micropiles were loaded simultaneously, i.e. each micropile was loaded and at the same time was employed as reaction pier for the other tested micropile.

7.2.1 Lateral load testing equipment and pile head instrumentations

No reaction frame system was used to execute the micropile load tests. The two micropiles being tested were connected together such that they were loaded simultaneously. This setup is known as two-in-one test, loading two piles at one test setup (Richards and Rothbauer, 2004). The idea is to benefit from the close spacing between the test micropiles to load one and use the other micropile as a reaction pier. In this setup, the two micropiles were loaded with the same load amplitude but in opposite directions.

A special setup was designed to accomplish the two-in-one test, which is illustrated in Fig. 7.1. The test setup consists of three main steel plates. As seen in Fig. 7.1, from left to right, the plates are; the load cell plate, the middle plate and the hydraulic jack plate. The load cell plate is welded to a B7X3-76 hex nut from one side and to a socket bar, 32 mm in diameter and 51 mm in length, from the other side. The middle plate contains two holes spaced at 177.8mm. It is welded from the load cell side to a socket bar similar to that welded to the load cell plate. The hydraulic jack plate is welded to another B7X3-76 hex nut from outside whilst it is welded to 400mm length threaded bar from the hydraulic jack side. The bar is 70mm in diameter. A work shop drawing for the three plates is given in Fig. 7.2.

To assemble the test setup, the load cell plate and the hydraulic jack plate were threaded onto one of the tested micropiles. An interface load cell 1240-AF-12K-B of 50 kN capacity was threaded to the socket bar of the load cell plate from one side and to the middle plate from the other side. A special steel nut was screwed into the steel rod attached to the hydraulic jack plate.

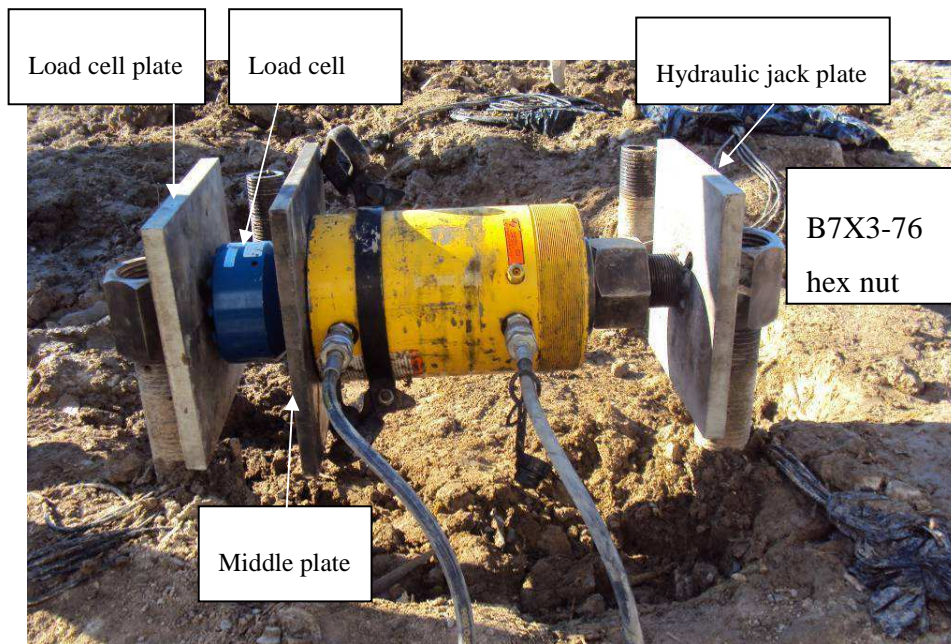


Figure 7. 1. Lateral load test setup

The steel rod was then inserted through the hole of the hydraulic jack until the top of the stroke was in contact with the special hex nut. The hydraulic jack has 100 ton advance capacity and 68 ton retract capacity employed by 150 mm stroke. The hydraulic jack was advanced until it reached the middle plate, and then bolted to the middle plates at the two holes shown in Figure 7.2.

Upon completion of the load test setup, the plates were leveled to insure horizontal applied load. The point of load application was about 250 mm above the ground surface as shown in Fig. 7.3. The lateral movement of each tested micropile was recorded by three HLP 190/FS1/100/4K linear displacement transducers (LDTs), mounted on magnetic base.

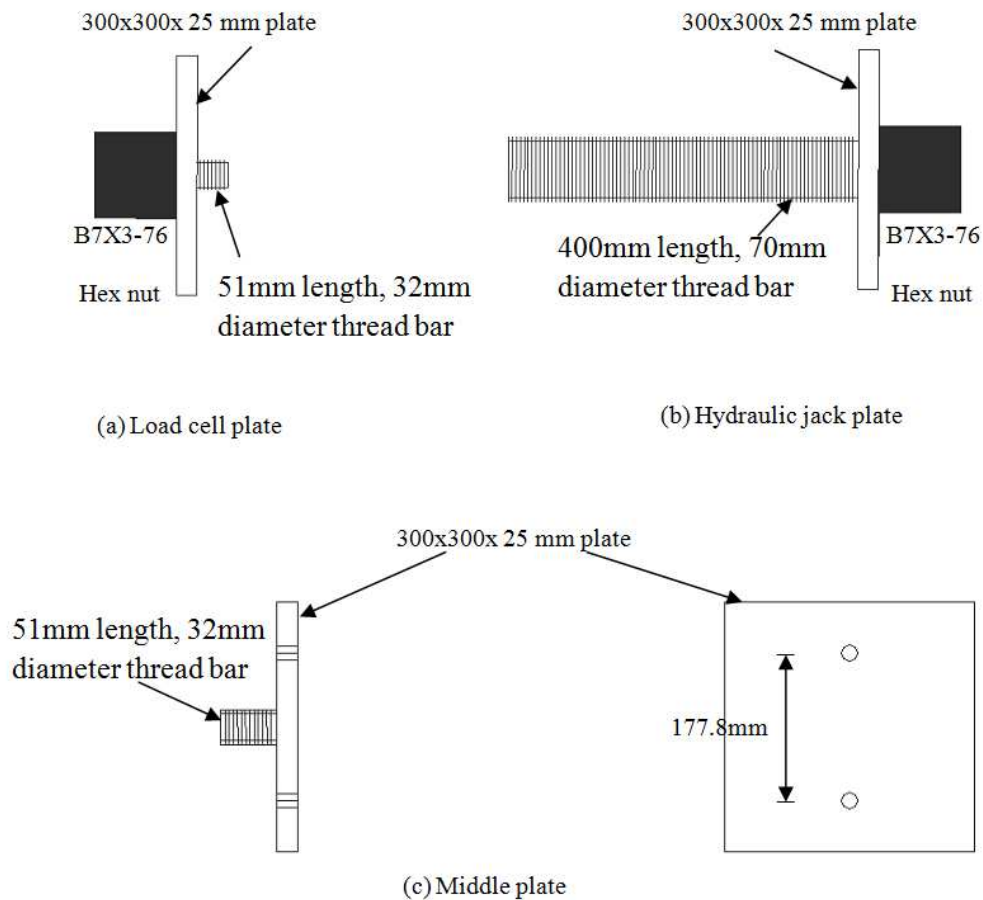


Figure 7. 2. Work shop drawing for the three main plates

The LDTs magnetic bases were mounted on reference steel extensions supported independently from the loading system. The LDTs have 100 mm stroke with an accuracy of 0.01 mm.

The LDTs were distributed in a triangle arrangement over the steel plates that were welded to the hex nuts and attached to the micropile head. One LDT was placed above the point of applied load at elevation equal 370mm above the ground surface. The other two were positioned under the point of the applied load at elevation 140mm above the

ground surface. Figure 7.4 depicts the positions of the LDTs with respect to the point of the applied load.

The aforementioned distribution of the LDTs was chosen to measure the micropile displacement at the point of applied load by interpolation between the top and bottom LDTs readings. Meanwhile, the rotation of the micropile head can be estimated from the difference in readings between the top and bottom LDTs. The load cell and the LDTs were connected to a data acquisition system to record and store the load and movement at the pile head during the load test.

7.2.2 Lateral monotonic load test procedure and results

The lateral monotonic load tests conducted in field represented free (pinned) head conditions, i.e. the micropile was free to rotate. A quick maintained load test procedure was adopted during the lateral monotonic load test. The load was applied in increments and kept for a short period of time before applying a new load increment. In this study, the load was applied in 3 kN load increments and each increment was held between 2.5 and 3 minutes. The lateral monotonic load test continued until the stroke of the hydraulic jack reached its maximum extracting value, i.e. 150 mm. when the maximum stroke length was reached, the corresponding load was held for 5 minutes.

Generally, the micropiles were tested laterally in accordance with the ASTM D3966 (2007) standard loading load test procedure. However, the ASTM D 3966 specifies that during the test, the load should be applied in increments of 25% of the design load with variable time interval increments, but smaller increments, longer time intervals, or both can be used.



Figure 7. 3. Position of the applied load during the monotonic lateral tests

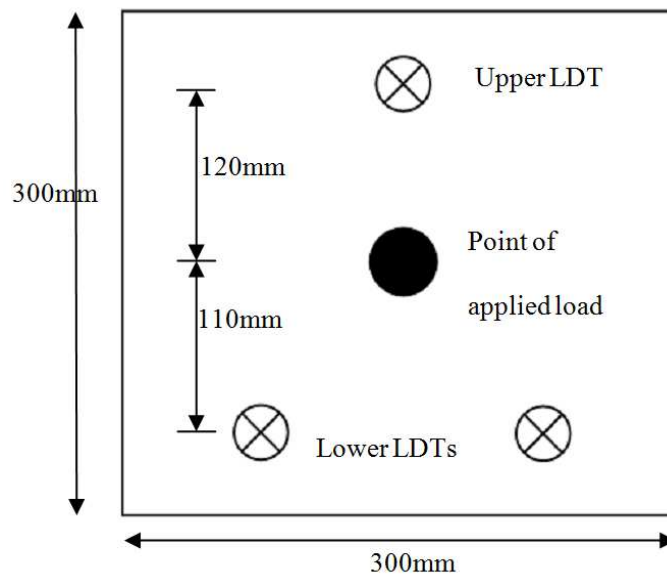


Figure 7. 4. Position of the LDTs with respect to the point of applied load

Figure 7.5 depicts the load – displacement curves for the two hollow bar micropiles loaded monotonically in the lateral direction. It can be noted from the figure that the two micropiles had almost the same response, with micropile MP2 displaying a slightly stiffer response. The increase in the micropile head rotation with the applied load is plotted in Fig. 7.6. The two tested micropiles show a steady increase in the rotation angle with the applied load.

7.2.3 Failure mechanism and ultimate capacity for micropiles under lateral loads

Pile failure under lateral loading may occur due to failure of either the soil or the pile. If the failure is due to yielding of the soil along the embedded pile length, the failure mechanism is called rigid-pile (or short pile) failure. In this case, the ultimate lateral resistance of the pile is given by the horizontal load required to cause failure of the soil mass along the pile shaft. On the other hand, if the failure is due to yielding of the pile itself at the point of maximum moment, the ultimate lateral resistance of the pile is given by the horizontal load required to produce a maximum moment equal to the yield moment of the pile section (flexible–pile failure or long pile failure).

Hence, the prediction of the ultimate lateral capacity of a single pile requires the assessment of the pile shaft rigidity. Unfortunately, no standard definition for shaft rigidity exists, but several criteria can be used to judge the rigidity of the pile shaft. Bierschwale et al (1981) defined the rigid (short) pile as the pile that is characterized by slenderness ratio less than 6 and the flexible (long) pile as pile with slenderness ratio larger than 20.

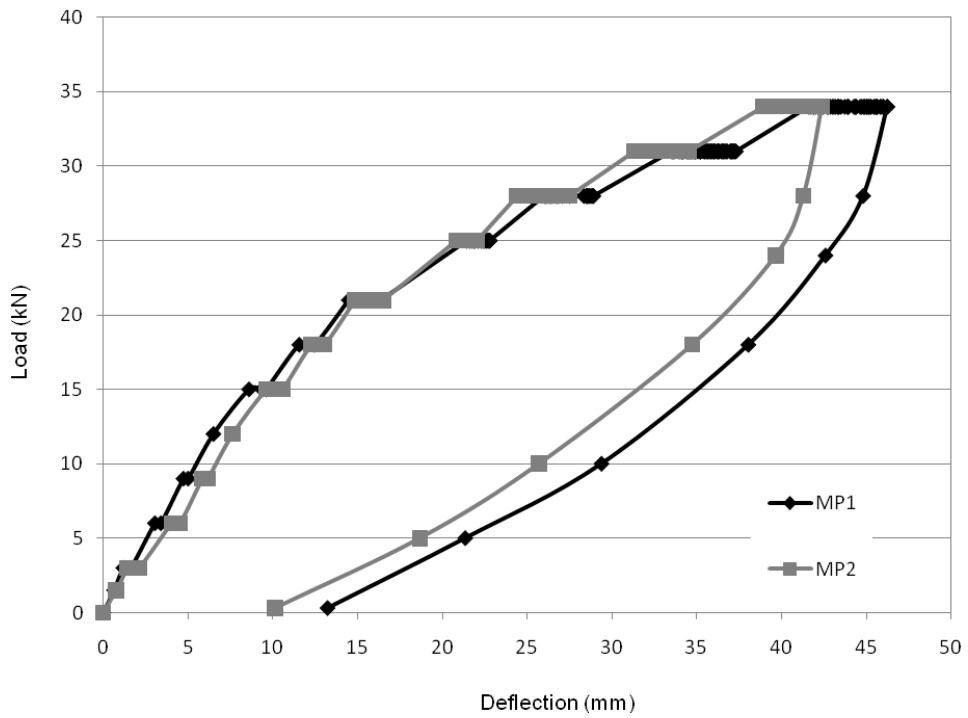


Figure 7. 5. Load-deflection for monotonic lateral tests

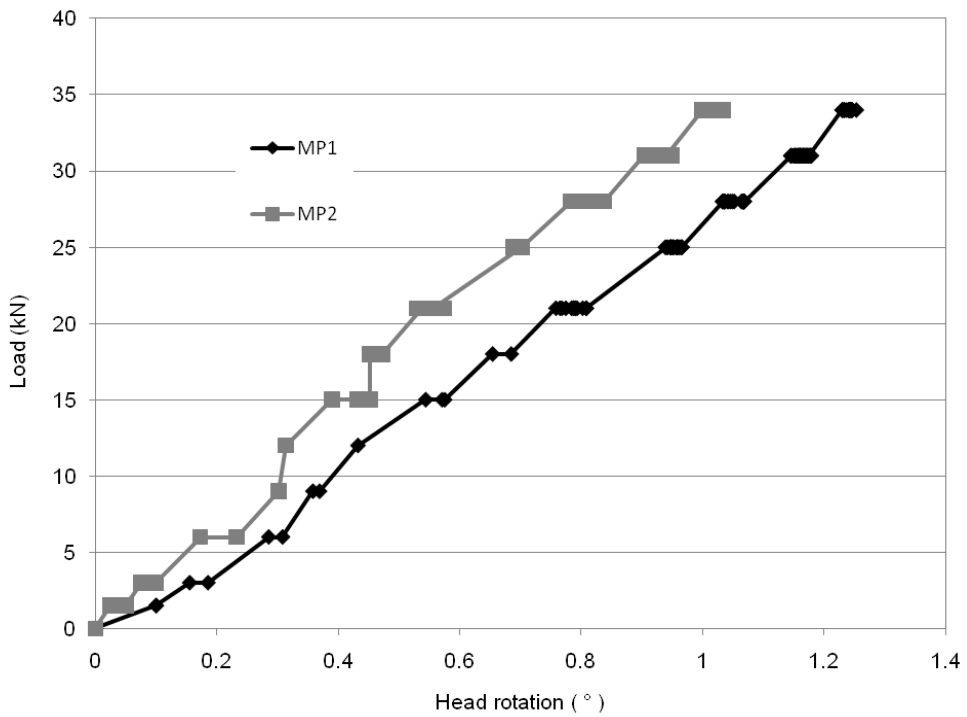


Figure 7. 6. Head rotation versus the applied load

Poulos and Davis (1980) deduced a criterion based on the elastic theory analysis in the form of flexibility factor, K_r , which is defined as:

$$K_r = (E_c I_c / E_s L^4) \quad (7.1)$$

Where: E_c is the elastic modulus of concrete, I_c is the concrete moment of inertia, E_s is the soil elastic modulus along the pile shaft, and L is the pile length. If the flexibility factor is less than 10^{-5} , flexible pile behaviour is expected, whilst if it is larger than 0.01, the pile will be definitely rigid. Employing any criteria, micropiles are considered flexible piles due to their small diameter, with slenderness ratio that is usually over 25. This categorizes the hollow bar micropile behaviour under lateral load as flexible or long pile.

The failure mechanisms that define the pile ultimate lateral capacity usually occur at large displacement or rotation levels. On the other hand, the allowable pile head displacement must be limited to the tolerable deflection for the structure it supports. Hence, the lateral capacity of most pile foundations is interpolated from load tests utilizing specific displacement criterion. This calls for the term “ultimate lateral capacity” to be replaced by the term “interpreted failure load”. Several interpolations criteria had been proposed over the years to interpolate the failure load of lateral load tests on deep foundation.

Table 7.1 lists the three most widely used interpretation criteria in piling engineering (Chen and Lee 2010). The interpreted failure load criteria given in Table 7.1 were applied to the lateral load test results shown previously in Fig. 7.5. The interpreted failure loads from different criteria are summarized in Table 7.2 for the two tested micropiles, MP1 and MP2. As discussed in Chapter 5, relating any failure load to displacement limitation

that is correlated to the pile diameter, such as Pyke (1984) method, is difficult to be applied to micropiles due to the enlargement in the diameter during installation. However, if casing is installed at the upper portion of the micropile, the diameter of the casing at that portion can be used as the diameter of the micropile and the failure criterion can be applied.

Table7. 1. Lateral interpretation criteria for piles

Method	Type	Definition of the interpreted failure load
McNulty (1956)	Displacement limitation	Load at 6.25 mm head displacement
Walker and Cox (1966)	Displacement limitation	Load at 13.0 mm head displacement
Pyke (1984)	Displacement limitation	Load at 5% the shaft diameter

Table7. 2. Interpreted failure load for MP1 and MP2

Method	MP1	MP2
Load at 6.25 mm head displacement (kN)	12	9.5
Load at 13.0 mm head displacement (kN)	19	18
Load at 5% the shaft diameter (bit diameter) (kN)	15	14

7.2.4 Numerical simulation of monotonic lateral load tests

The soil response to lateral load is nonlinear, almost from the beginning of lateral loading. As a result, the relationships among load, moment, and deflection for laterally loaded piles are nonlinear, even in the working load range. It is therefore important to base design laterally loaded piles and drilled shafts on methods of analysis that can model the nonlinear behaviour of the soil – foundation system. The widely used p - y curves approach is an effective nonlinear analysis method for designing deep foundations subjected to lateral loads (Duncan et al. 1994). Thus, the p - y curves approach incorporated in the LPILE software was utilized in this study to numerically simulate the lateral load tests conducted on the hollow bar micropiles.

The p - y curves approach is based on solution of a differential equation describing the behaviour of a beam – column with nonlinear support. The pile is treated as a beam-column and the soil is replaced with nonlinear Winkler-type springs. Hence, the reaction of the soil against the pile is related to the deflection of the pile by means of nonlinear load – transfer curves, i.e. p - y curves. Figure 7.7 illustrates the model adopted for piles subjected to lateral loading using the p - y curves approach.

The p - y method was first devised by McClelland and Focht (1958). The method was developed as a design tool for piles supporting offshore oil production platforms that were to be subjected to exceptionally large horizontal forces from waves and wind (Isenhower and Wang 2011). The use of the method has been extended to the design of onshore foundations. The method is being cited broadly by Jamiolkowski (1977), Baguelin, et al. (1978), and Poulos and Davis (1980).

The definition of the quantities p and y is necessary. The sketch in Fig. 7.8(a) shows a uniform distribution of radial stresses, normal to the wall of a cylindrical pile. If the pile is deflected a distance y (exaggerated in the sketch for clarity), the distribution of unit stresses becomes non – uniform and will be similar to that shown in Fig. 7.8 (b). The stresses decrease on the backside of the pile and increase on the front side. Integration of the unit stresses results in the quantity p which acts opposite in direction to y . The dimensions of p are load per unit length of the pile. These definitions of p and y are convenient in the solution of the differential equation and are consistent with those used in the solution of the ordinary beam equation.

The common criticism of the p - y method is that the soil is not treated as a continuum, but as a series of discrete springs (the Winkler model). However, the methods of predicting p - y curves that were derived from correlations with results of full-scale experiments have been used to make computations for the response of piles where only the pile-head movements were recorded. These comparisons show reasonable to excellent agreement between computed and experimental results (Isenhower and Wang 2011).

The method can be used to analyze conditions where the properties of the soil or the pile vary in any fashion with depth. However, the formulation of the differential equation in finite difference form and a solution by iteration mandates a computer program. LPile is an example of such computer program. LPile is used widely for analyzing the deep foundation under lateral loads employing the p - y method.

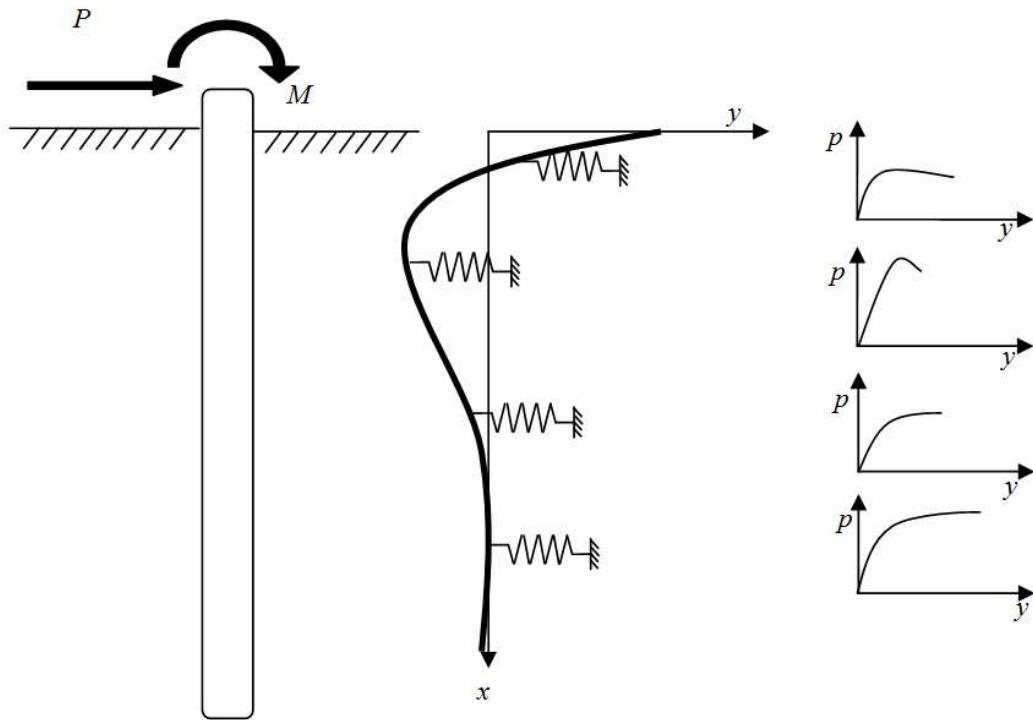


Figure 7.7. Model for pile under lateral loading with p - y curves

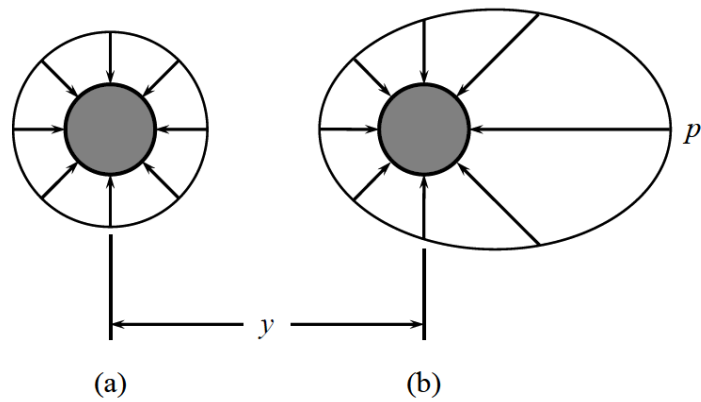


Figure 7.8. Distribution of normal stress against a pile (after Isenhowe and Wang 2011) (a) Before lateral loading, (b) After lateral deflection

In LPile, the pile and soil are defined separately. The pile is defined geometrically by its structural dimensions, shaft diameter and length. The material properties required to define the pile depend on the pile cross-section. For example, normally – reinforced concrete piles require the definition of the steel Young's modulus and yield strength as well as the number and distribution of the steel bars within the pile cross section. Meanwhile, the concrete is defined by its compressive strength only. These features are used by LPile to determine how the effective bending stiffness will vary as the concrete cracks in tension and how the reinforcing steel yields. In all cases, LPile gives the option of modeling the pile with different geometry and material properties along its shaft utilizing different cross sections.

Defining the soil in LPile depends on the soil type. In LPile, the user chooses the required type of soil and the corresponding lateral load – transfer curves (p - y) are generated automatically under default conditions. The program also allows user-specified p - y curves. Another good feature in modeling the soil in LPile is; the soil can be modeled utilizing a number of layers, each has its own generated p - y curves depending on its type. However, the number of layers is limited to 40 in LPile.

LPile version 6 offers 13 readily defined (built-in) types of soils that can be specified during lateral loading. Each soil type is defined by its effective unit weight, shear strength parameters and other parameters that depend on the soil and/or rock type selected. For example, if sandy soils are selected, the additional parameter required is the slope of the soil resistance versus lateral deflection curve. While for clay, it is the axial strain corresponding to a shear stress equal to $\frac{1}{2}$ of the shear strength of the material. In the

next section, the clay model will be presented, as the hollow bar micropiles were embedded in stiff clay.

7.2.5 Calibration of the monotonic lateral field test

A numerical simulation for the lateral field test is carried employing LPile software. The hollow bar micropile has a unique cross-section, which includes a hollow bar encapsulated in a grout body. Modeling of such cross-section is not available in LPile. However, LPile offers modeling round concrete shaft with permanent casing and core. Since, the hollow bar micropiles were installed with no casing, the round section suggested by LPile was employed and the wall thickness of the permanent casing was set equal to zero. The hollow bar micropiles cross-section utilizing the bit diameter employed in the numerical analysis is illustrated in Fig. 7.9.

The material properties of the grout and the pile employed in the analysis are summarized in Table 7.3. To ensure that the adopted cross-section correctly represented the bending stiffness of the micropile, the combined bending stiffness of the adopted section is plotted against the developed resistance bending moment of the section in Fig. 7.10. The theoretical un-cracked bending stiffness of the steel and grout, as well as the bending stiffness of the steel only are also plotted in Fig. 7.10. An excellent agreement between the adopted cross-section and the theoretical bending stiffness of the hollow bar cross section is noted from Fig. 7.10 This confirmed the suitability of using the round concrete shaft with permanent casing and core in LPile for modeling hollow bar micropiles.

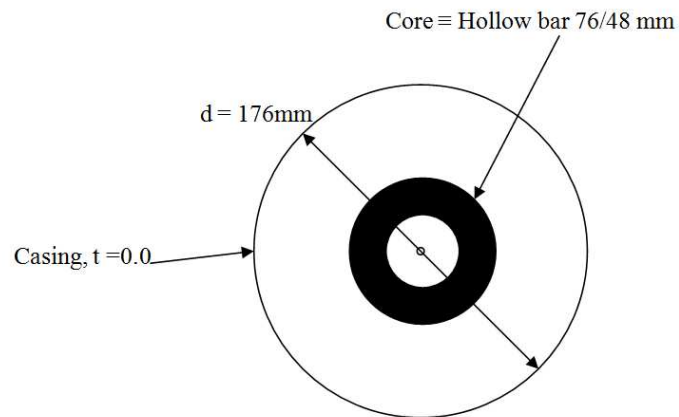


Figure 7. 9. Round concrete shaft with permanent casing and core utilizing hollow bar micropile cross section

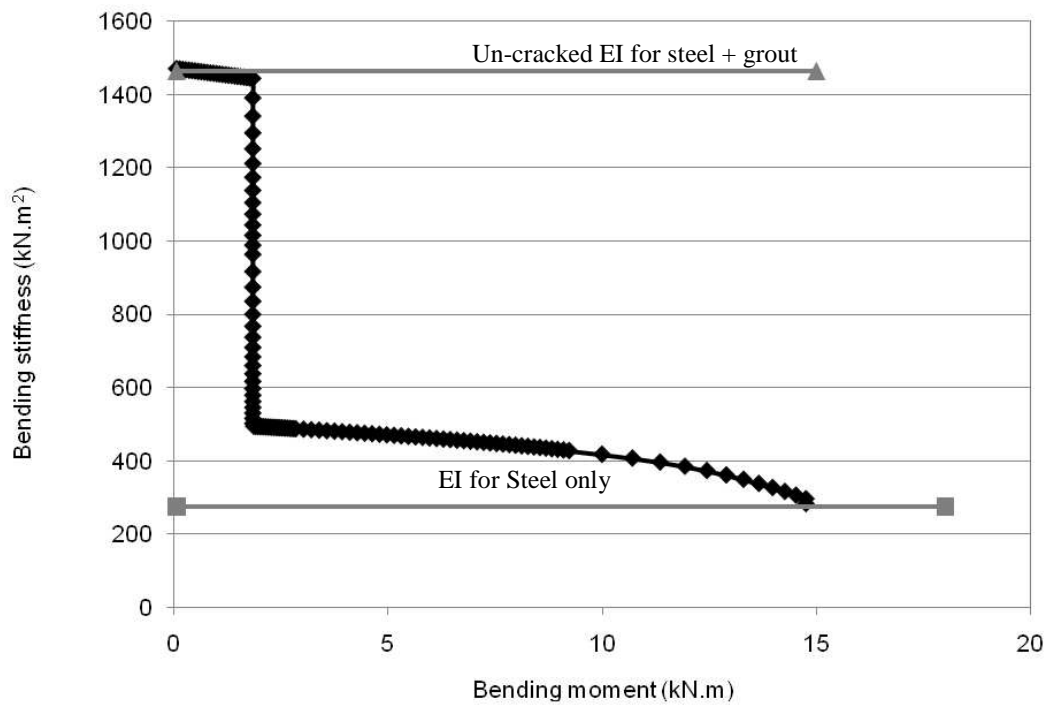


Figure 7. 10. Bending stiffness versus bending moment for the adopted cross section

Table 7. 3. Grout and steel properties adopted in material modeling

	Young's modulus (kPa)	Compressive strength (kPa)	Yield Stress, f_y (kPa)
Grout	$4730(f_c')^{0.5}$	3E+4	-
Steel	2E+8	-	5.8E+5

The hollow bar micropiles were installed in stiff to hard silty clay to clayey silt deposit as described in Chapter 3. Therefore, the soil is modeled in LPile utilizing the stiff clay model without free water. The model was developed by Reese and Welch (1975) based on full scale field load tests performed on 915mm drilled shafts. A steel pipe, 254mm in diameter, instrumented with strain gauges was inserted before placing the concrete. The average undrained shear strength of the clay in the upper 6 m was approximately 105 kPa. The p - y curves obtained for these load tests were relatively consistent in shape. The model is capable of modeling the behaviour of laterally loaded piles under static and cyclic loads.

The model is defined in LPile utilizing the following parameters: the effective unit weight of the clay, γ'_{avg} , undrained shear strength parameter for the clay, s_u , and the axial strain corresponding to a shear stress equal to one-half of the shear strength of the material, ϵ_{50} . The model has default values for ϵ_{50} depending on the soil consistency and the undrained shear strength parameter of the clay (Table 7.4). The characteristic shape of load – transfer p - y curve for stiff clay model is given in Fig.7.11.

Table 7. 4. Values of ε_{50} for stiff clay model in L-Pile (after Isenhower and Wang 2011)

Consistency of clay	Undrained shear strength (kPa)	ε_{50}
Soft	< 50	0.01
Medium	50 to 100	0.007
Stiff	100 to 200	0.005

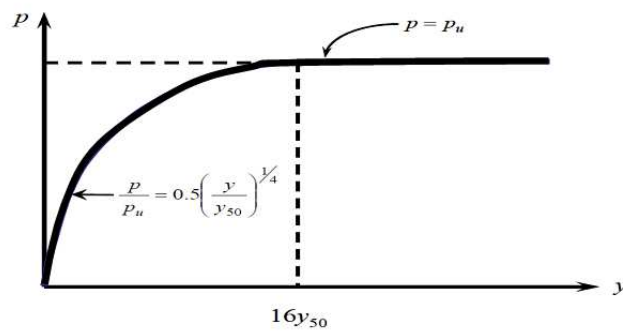


Figure 7. 11. Characteristic shape of p - y curve for static loading in stiff clay without free water (after Isenhower and Wang 2011)

The analysis starts by computing the ultimate resistance of the soil at a depth x from the ground surface, p_u , as the lesser from (Isenhower and Wang 2011):

$$p_u = [3 + (\gamma'_{\text{avg}}/s_u) x + (x/2d)] s_u d \quad (7.2a)$$

$$p_u = 9 s_u d \quad (7.2b)$$

Then, the deflection corresponding to ε_{50} is calculated as:

$$y_{50} = 2.5 \varepsilon_{50} d \quad (7.3)$$

Followed by, the points describing the p - y curve at the pre-specified depth x is computed from the relationship below:

$$p = 0.5 p_u (y/y_{50})^{0.25} \quad (7.4)$$

Finally, beyond $y = 16y_{50}$, p is equal to p_u for all values of y .

The properties of the soil employed in LPile numerical simulation is similar to that given previously in Table 5.6. The analysis was carried and repeated several times employing different values of grout diameter and ε_{50} to reach the most representative calibration model. Figure 7.12 illustrates the lateral field tests results and the numerical results obtained using LPile. The figure shows good agreement between the calculated response using the calibrated model and the lateral load test results. However, the LPile response is slightly stiffer than the field results. This might be attributed to a limited increase in the pile diameter as discussed below, which was necessary for the numerical stability of the solution.

The calibrated model involved a slight increase in the upper segment of the micropile diameter equal to 4mm plus the drilling bit diameter, i.e. 180 mm. Nevertheless, the significant enlargement of the micropile diameter took place near the pile toe showed no effect on the lateral capacity of the hollow bar micropile. In addition, the match between the calculated and measured responses was achieved when employing $\varepsilon_{50} = 0.0021$ for the upper layer. The influence of value of ε_{50} for the lower layers on the calculated response was found to be marginal.

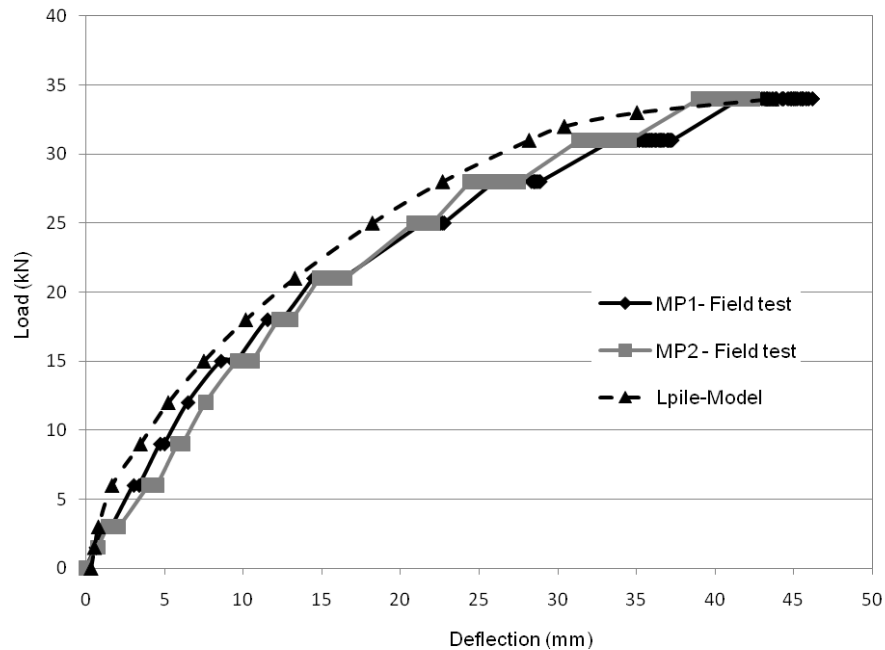


Figure 7. 12. Numerical calibration of lateral field test with LPile

Figures 7.13, 7.14, and 7.15 display the deflection, moment, and shear force profiles obtained from the LPile analysis using the calibrated model. The family of p - y curves generated by LPile to represent the load transfer mechanism at the top layer is depicted in Fig 7.16. Figure 7.13 shows that, as expected, the micropiles behave as flexible piles under lateral load. Moreover, LPile assigned the moment capacity of the micropile cross-section to be equal 14.69 kN.m. Figure 7.14 elaborates that this moment corresponding to an applied load larger than 28 kN. Hence, at the ultimate applied load, i.e. 34 kN, a plastic hinge has probably developed at the location of maximum bending moment at depth approximately equal to 0.65m below the ground surface. This is further confirmed by the bending stiffness of the employed cross-section, EI , versus bending moment plot given in Fig. 7.17.

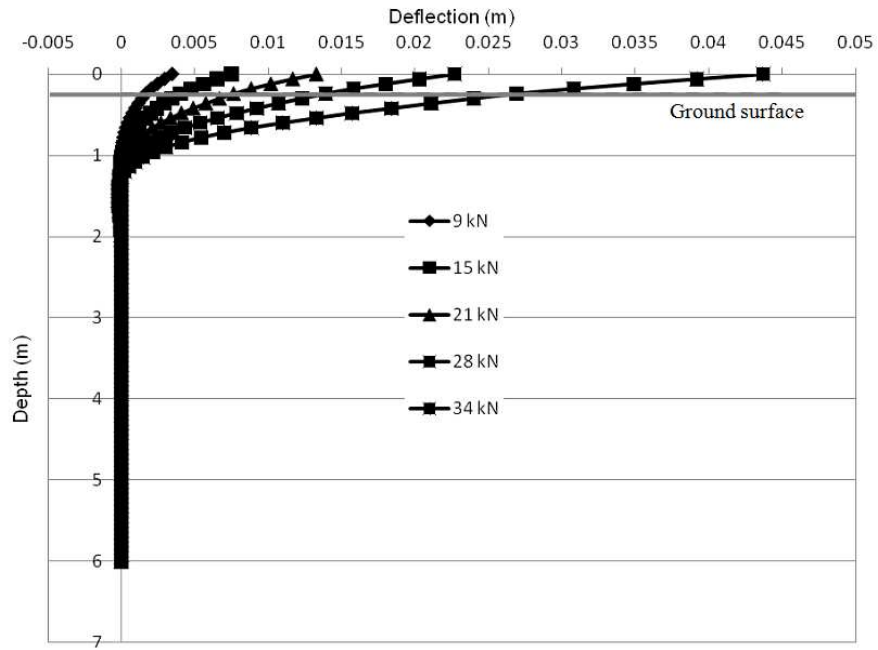


Figure 7. 13. Deflection of the micropile versus depth, LPile analysis

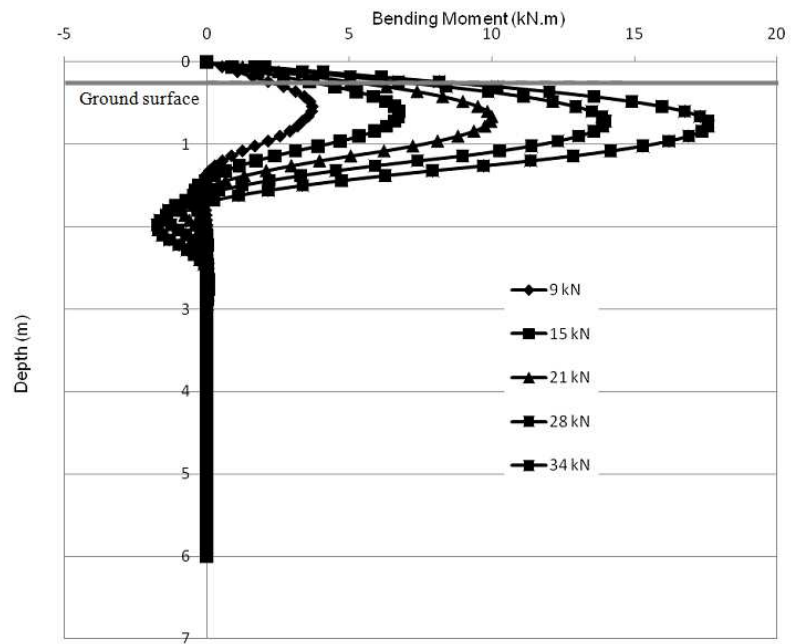


Figure 7. 14. Bending moment along the micropile shaft, LPile analysis

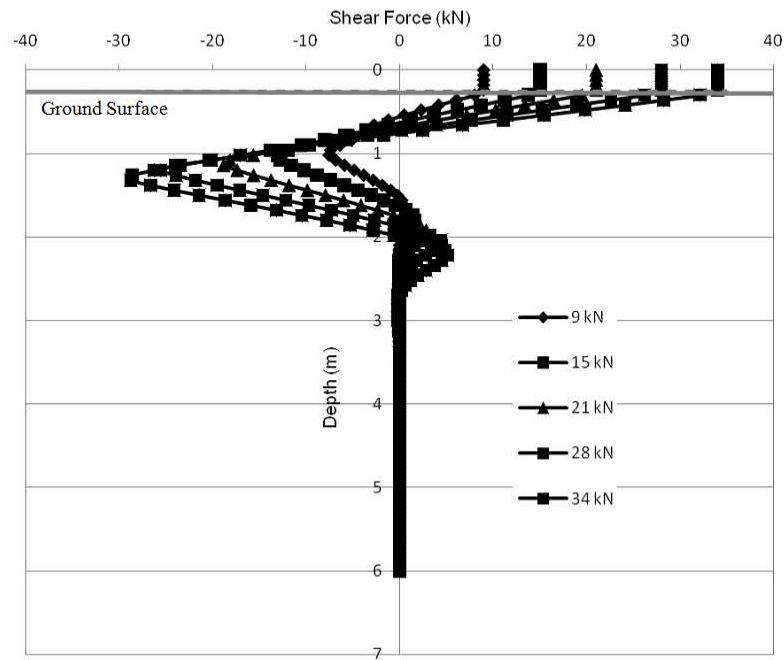


Figure 7. 15. Distribution of shear force developed along the micropile shaft, L-Pile analysis

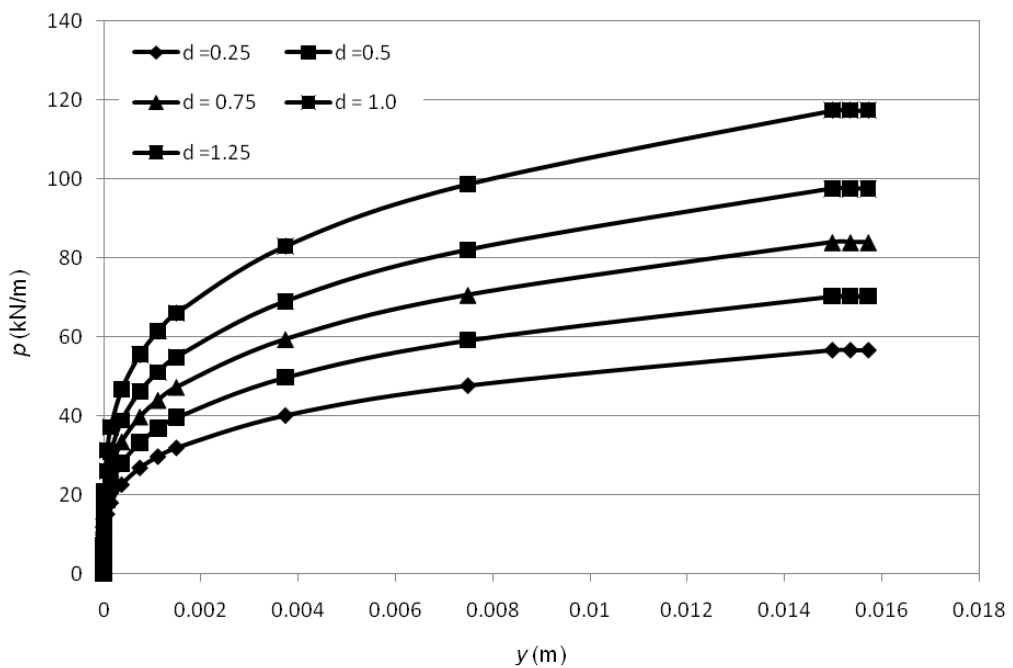


Figure 7. 16. *p-y* curves generated by L-Pile analysis

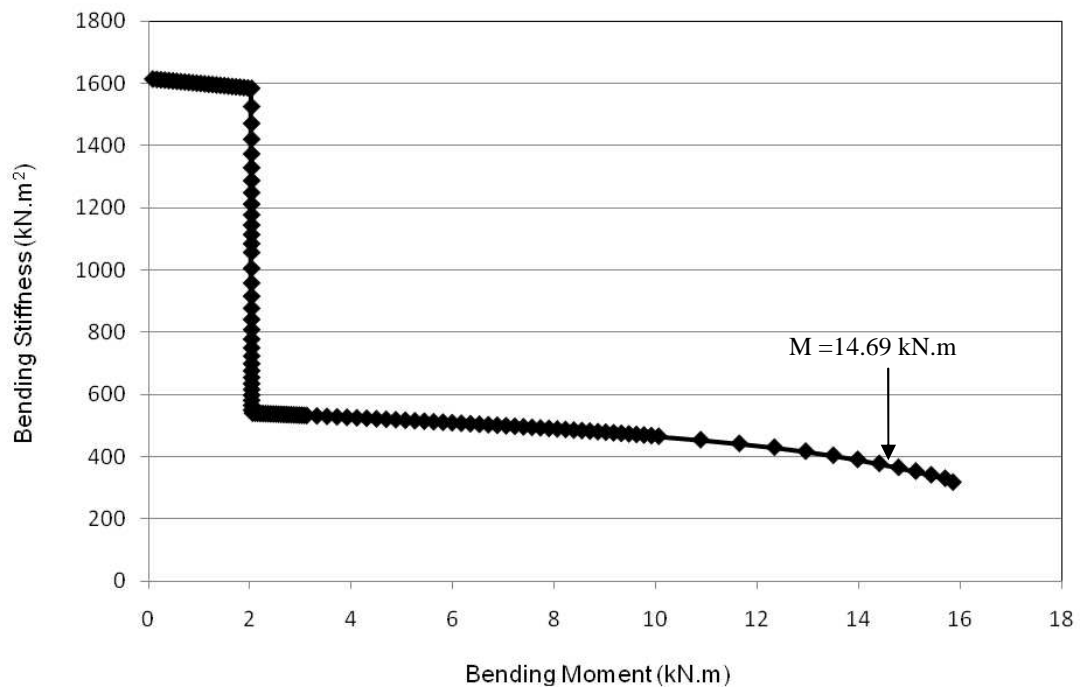


Figure 7. 17. Bending stiffness versus bending moment of the micropile cross-section

The LPile analysis also revealed that the behaviour of the hollow bar micropiles was very sensitive to the properties of soil at depth within five times the micropile diameter. Nevertheless, the behaviour of the micropiles is less sensitive to soil properties at depth from five to ten times the micropile diameter. Below depth equal to 10 times the micropile diameter, the surrounding soil has no effect on the performance of the tested micropiles.

7.2.6 Parametric study

The calibrated model was used to perform a parametric study on the behavior of hollow bar micropiles under lateral loading. The objectives of the parametric study are:

- To evaluate the effect of cased length of the hollow bar micropiles on its lateral response considering different fixity conditions.

- To examine the effect of degree of fixity on the performance of the pile.

The geometry of the micropile considered in the parametric study consists of two segments: the upper cased segment, and the lower uncased segment. Figure 7.18 demonstrates the geometry and the dimensions of the hollow bar micropile employed in the current parametric study. The hollow bar employed in the parametric analysis is 76/48 hollow bars, such bar can be used with a drilling bits of 150 to 200 mm diameter (Table 4.3). However, practically, those bars used with bits of diameter equal 176 mm and higher. In this parametric study, the uncased segment incorporates an increase in the diameter equal to double the casing thickness. In all analyses, the thickness of the casing wall was taken constant and equal to 12 mm.

The material properties of the steel and grout used are kept constant through all the study. The material properties employed are similar to that given in Table 7.3, except for the yielding strength of the casing, which is used as 550 MPa. The micropile is considered to be embedded in homogenous clay. The undrained shear strength of the soil utilized was varied from 100 kPa to 175 kPa. The value of the the axial strain corresponding to a shear stress equal to one-half of the shear strength of the clay was chosen in accordance with the default values suggested by LPile, for stiff clay model (Table 7.4).

The effect of the cased length, L_c , on the lateral ultimate resistance and the maximum bending moment for a free head micropile is illustrated in Figs. 7.19 and 7.20, respectively. In Fig. 7.19, $(p_u)_c$ is defined as the ultimate resistance of micropile with cased length, L_c , while $(p_u)_{unc}$ is the ultimate resistance results for similar un-cased micropile.

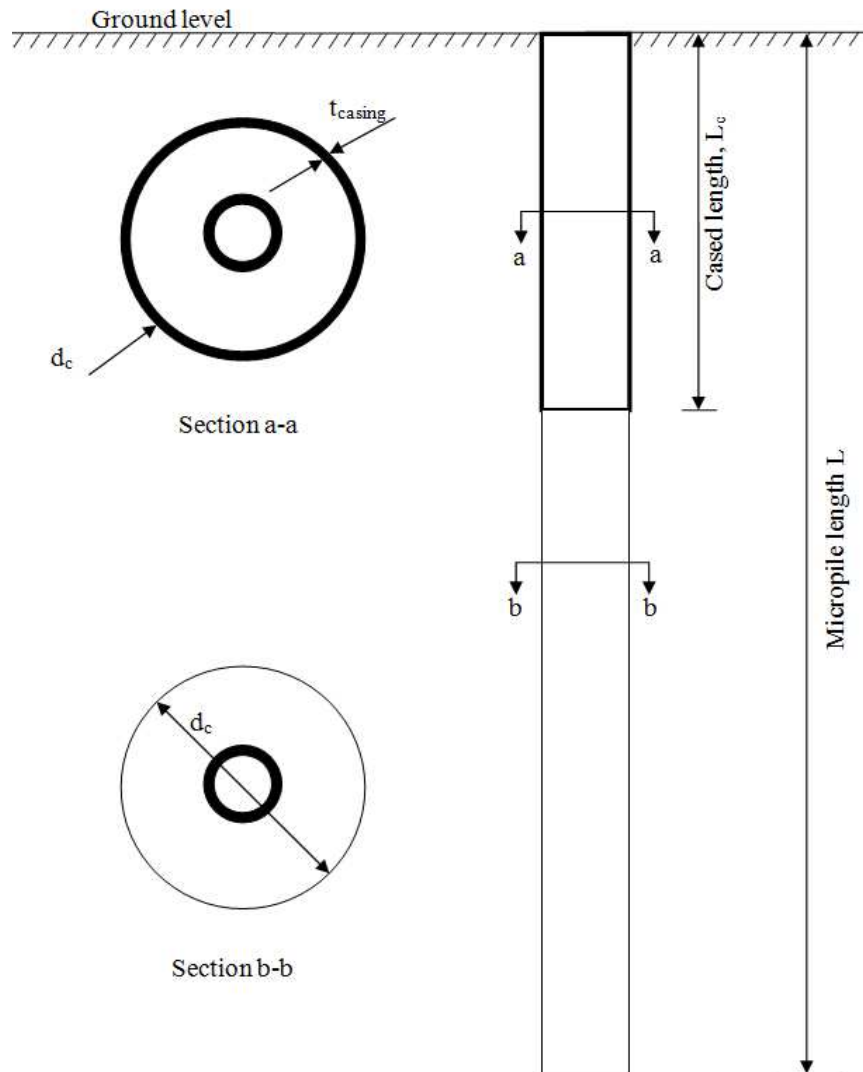


Figure 7. 18. The geometry of the hollow bar micropiles used in the parametric study

The $(p_u)_{unc}$ was calculated for hollow bar micropile diameter equal to the casing diameter, d_c , but without employing the bending stiffness of the steel case. Similarly, $(M_u)_c$ and $(M_u)_{unc}$ are the maximum bending moment for the cased and uncased micropile in Fig. 7.20. The figures show that for a free head hollow bar micropile installed in stiff clays, the length of the casing has to be larger than five times its diameter to have any impact on

the pile lateral resistance. A significant increase in the pile lateral resistance was achieved when the casing length was about 10 times its diameter.

For fixed head micropiles, Figs.7.21 and 7.22 illustrate the effect of the cased length on the ultimate resistance and its maximum bending moment. The figures demonstrate that fixed head micropiles show noticeable increase in both lateral capacity and bending moment by increasing the casing length up to 7.5 times its diameter. However, increasing the casing length more than 7.5 times its diameter would have a marginal effect on its lateral resistance. This is because the hollow bar micropile cross-section experiences yielding at that length. The same observations were noted for clays characterized by s_u between 100 and 175 kPa.

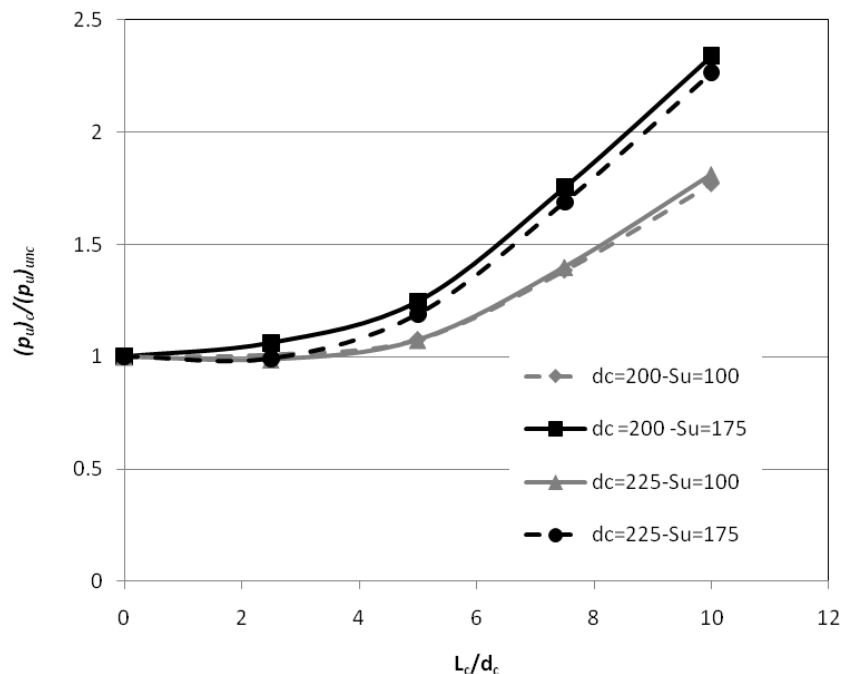


Figure 7. 19. The effect of casing length on ultimate resistance of free head pile

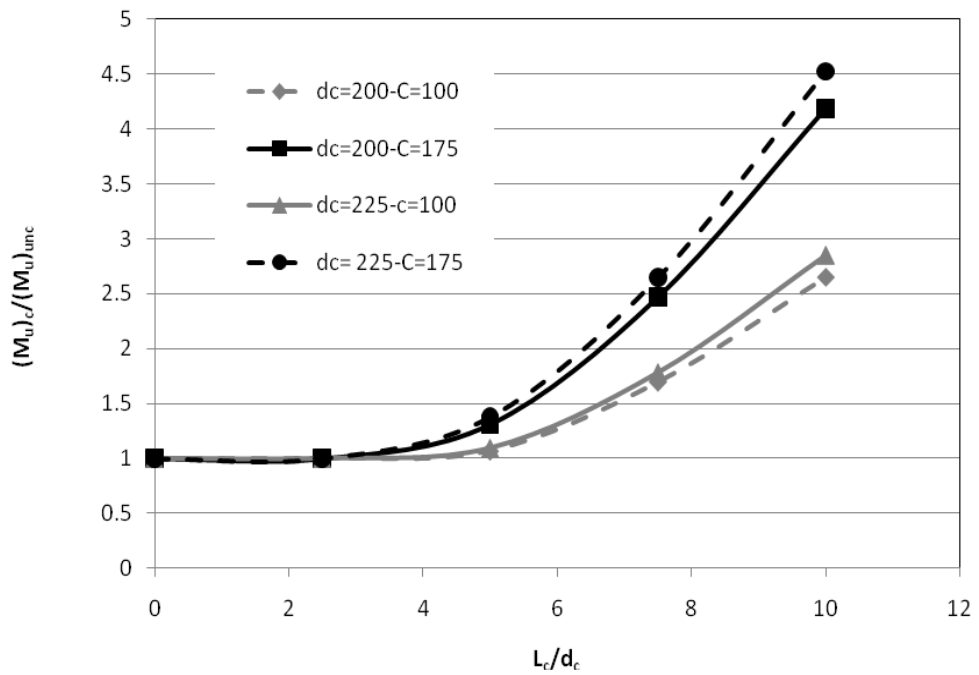


Figure 7. 20. The effect of casing length on maximum moment of free head pile

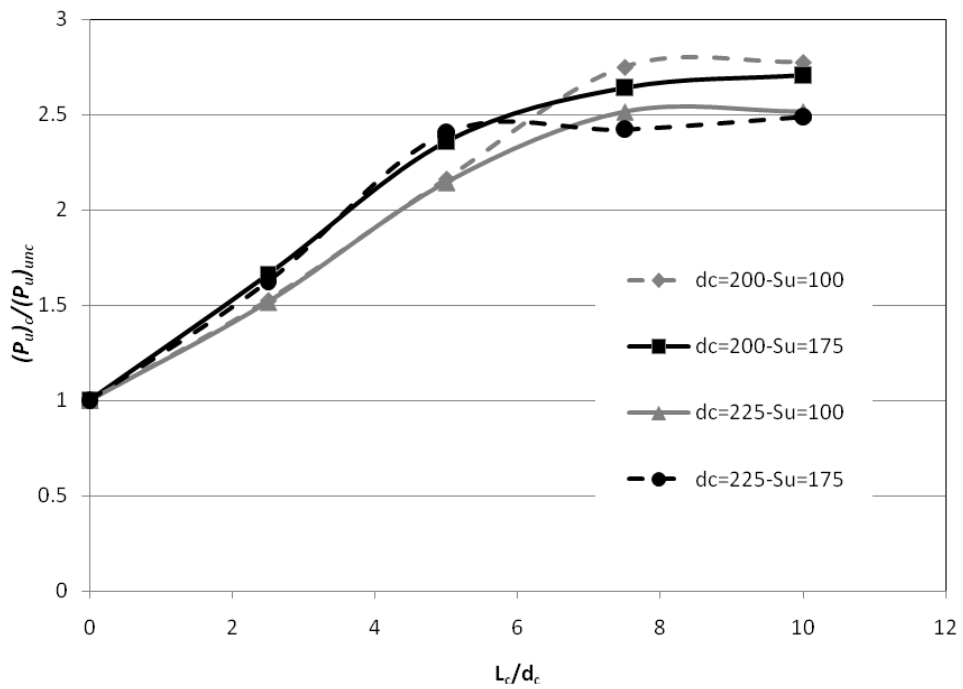


Figure 7. 21. The effect of casing length on ultimate resistance of fixed head pile

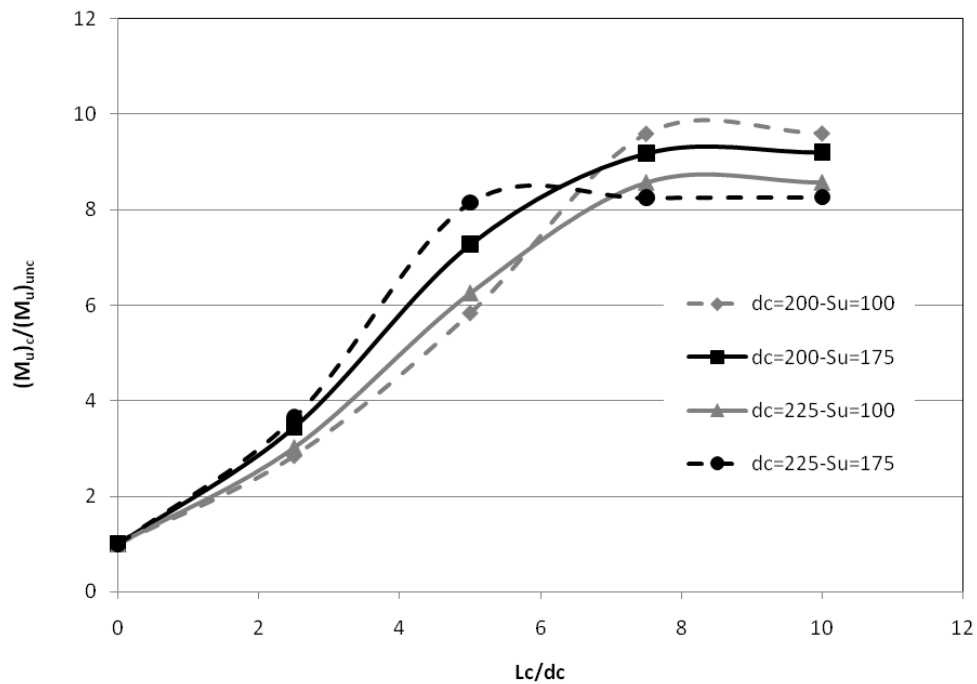


Figure 7.22. The effect of casing length on maximum moment of fixed head pile

The effect of the head fixity on the lateral resistance of the micropile was also examined. Selected cases are presented in Figs. 7.23 to 7.30. For each case, the pile head deflection and bending moment are plotted versus the applied load. It is clearly noted from the figures that decreasing the degree of micropile head fixity from 100% (fully fixed) to 50% (partially fixed) fixation will increase the ground line deflection dramatically. This means that if the pile connectivity to the pile cap does not provide full fixity (i.e. moment transfer mechanism), the lateral capacity of the pile is reduced by 50% or more.

On the other hand, the maximum bending moment of the micropile section for 50% fixity condition displays a unique behaviour. The maximum moment changes from positive moment at a point below the ground level, to negative moment at the micropile head as the applied load increases.

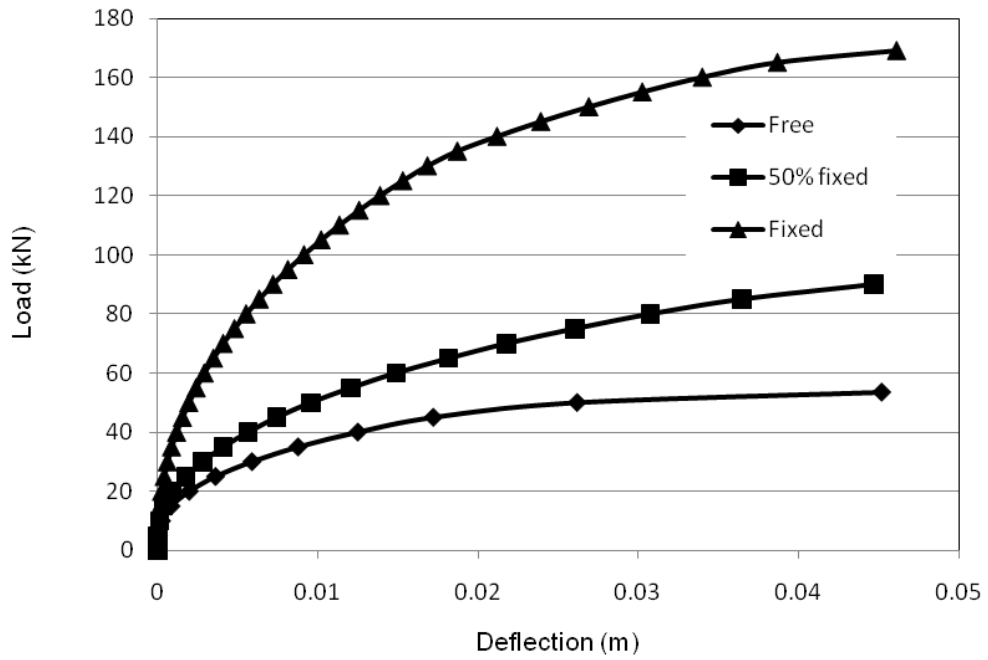


Figure 7. 23. Load-deflection for three degree of fixity, $L_c/d_c = 5$, $d_c = 200\text{mm}$, $s_u = 100$ kPa

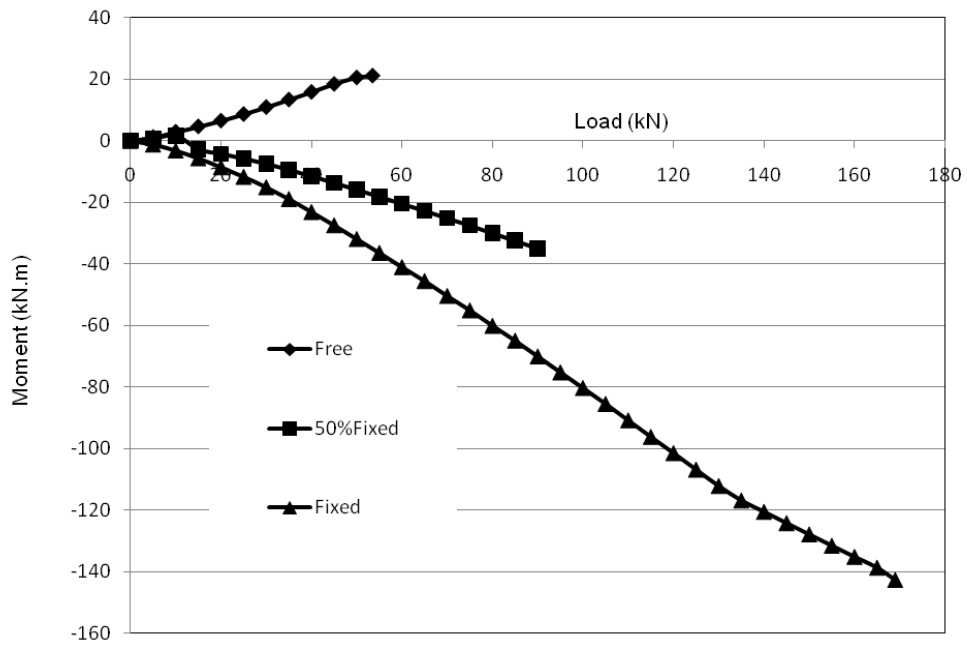


Figure 7. 24. Load-maximum moment for three degree of fixity, $L_c/d_c = 5$, $d_c = 200\text{mm}$, $s_u = 100$ kPa

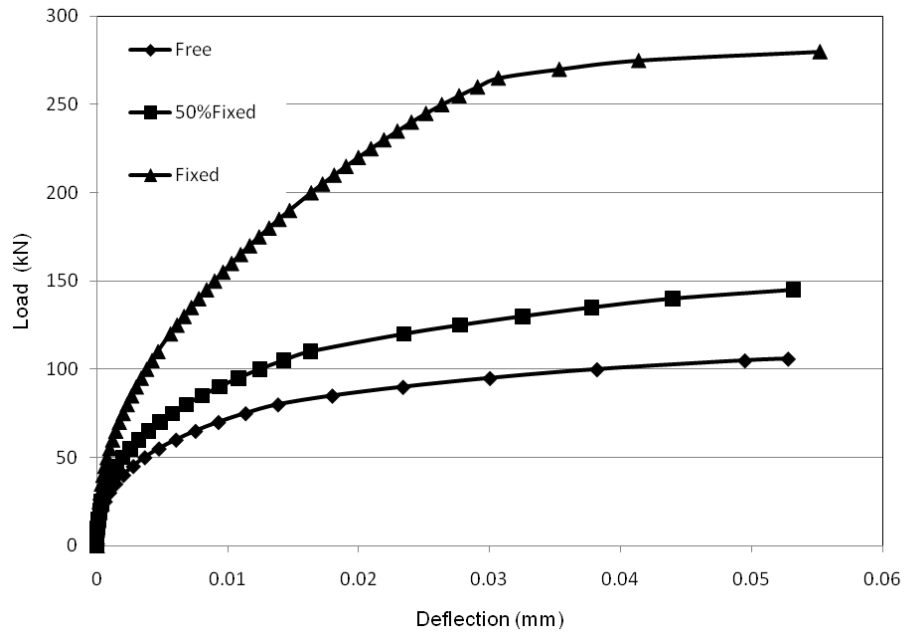


Figure 7. 25. Load-deflection for three degree of fixity, $L_c/d_c = 7.5$, $d_c = 200\text{mm}$, $s_u = 175$

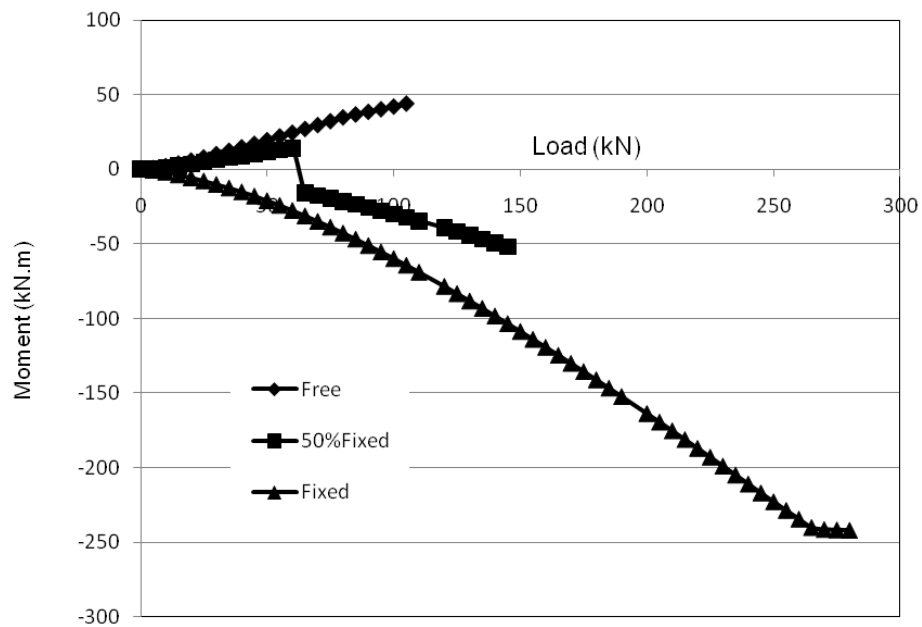


Figure 7. 26. Load-maximum moment for three degree of fixity, $L_c/d_c = 7.5$, $d_c = 200\text{mm}$, $s_u = 175 \text{ kPa}$

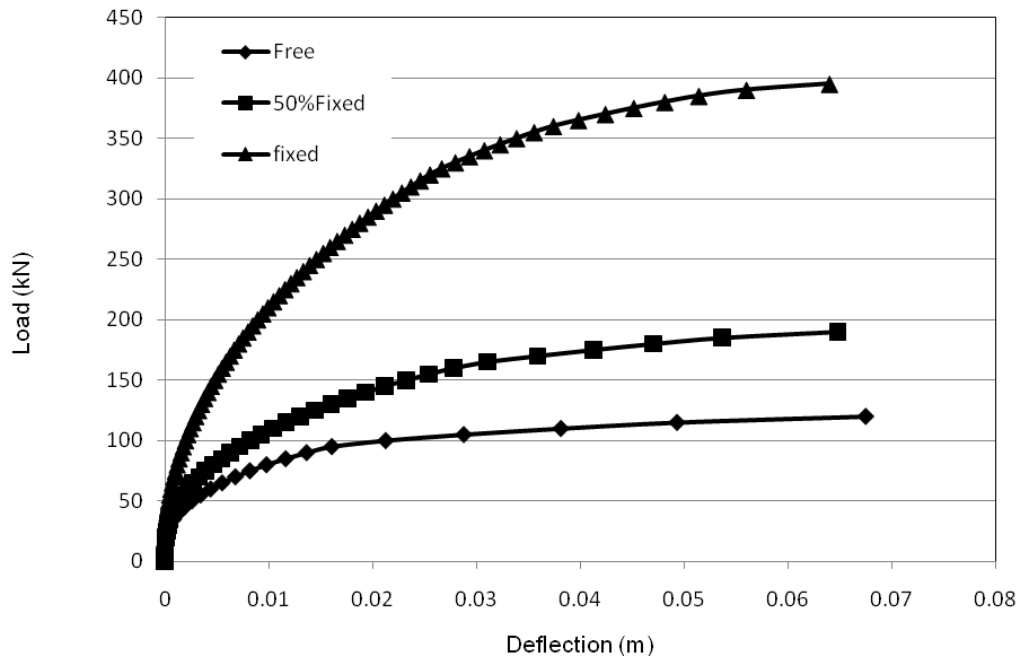


Figure 7. 27. Load-deflection for three degree of fixity, $L_c/d_c = 5$, $d_c = 225\text{mm}$, $s_u = 175$ kPa

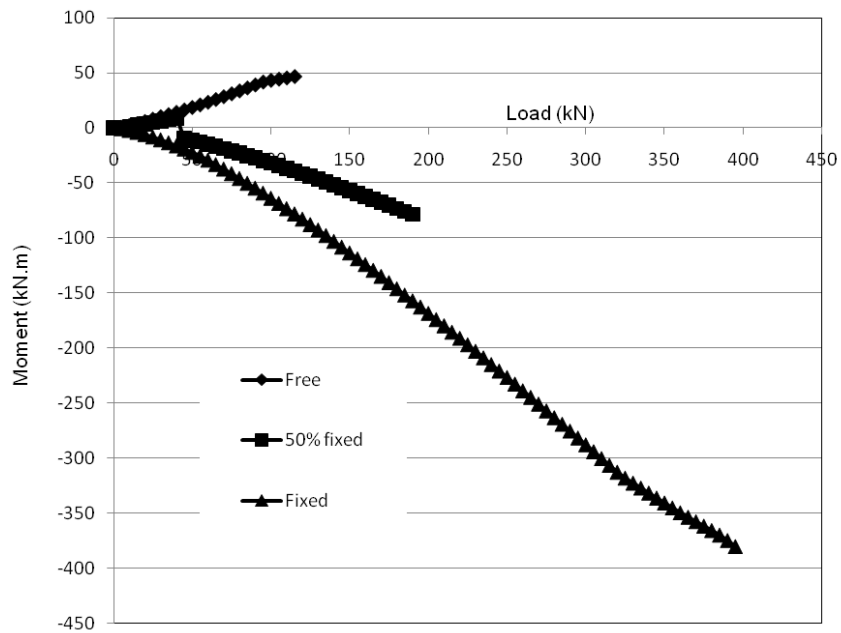


Figure 7. 28. Load-maximum moment for three degree of fixity, $L_c/d_c = 5$, $d_c = 225\text{mm}$, $s_u = 175$ kPa

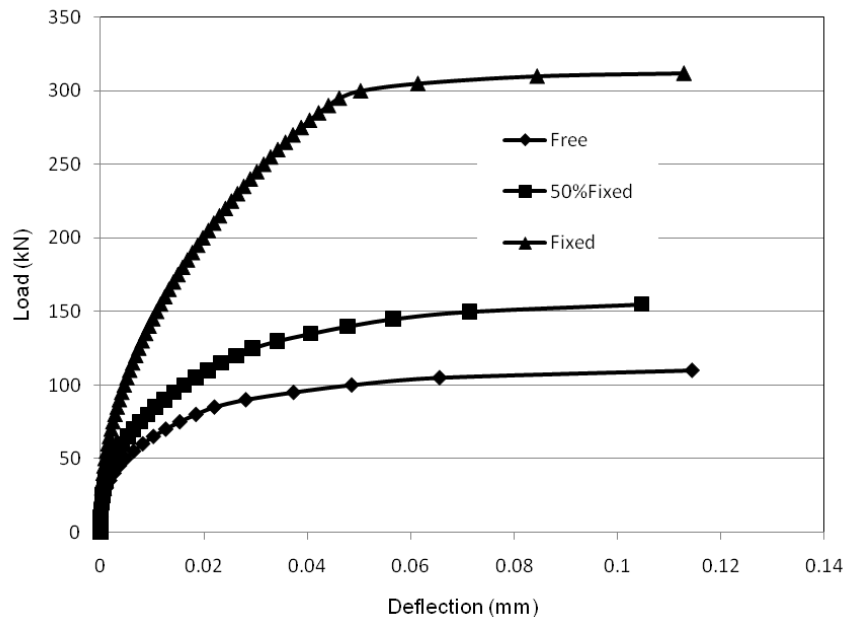


Figure 7. 29. Load-deflection for three degree of fixity, $L_c/d_c = 7.5$, $d_c = 225\text{mm}$, $s_u = 100\text{ kPa}$

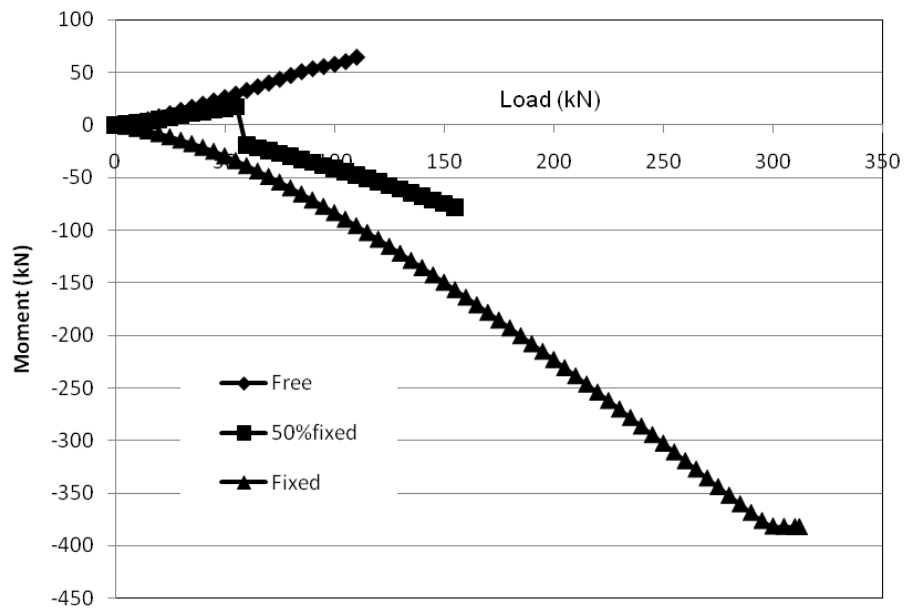


Figure 7. 30. Load-maximum moment for three degree of fixity, $L_c/d_c = 7.5$, $d_c = 225\text{mm}$, $s_u = 100\text{ kPa}$

It can be concluded from the previous analysis that the connectivity of the micropile head into the pile cap should be evaluated carefully. If full fixity is assumed, then sufficient moment transfer capacity should be provided between the pile and the pile cap. For micropiles connected to their cap by simply extending the hollow core bar 150 mm into the pile cap, the fixed head condition cannot be justified. Hence, it is recommended to assume that the pile head will have only 50% fixity condition, and evaluate the micropile performance under lateral accordingly. The types and optimum design of the connection between the hollow bar micropile and the footing is beyond of the scope of this study.

7.3 Lateral Cyclic Load Tests

Six cyclic lateral load tests were conducted on the four hollow bar micropiles. Figure 7.31 depicts the sequence and the positions of the performed cyclic load tests. The lateral cyclic load tests were conducted on each two micropiles simultaneously as shown in Fig. 7.31. Hence, the same test setup used during lateral monotonic tests (Fig. 7.1) was used in the lateral cyclic load test phase, which involved two-way cyclic loading. Therefore, the hydraulic jack used was attached to the 70mm diameter bar (see Fig. 7.2) by mean of a special collar.

Connecting the jack stroke to the 70mm bar allowed the hydraulic jack to apply the load during its advancing and retracting, which facilitated the two-way cyclic test to be conducted on the two piles simultaneously. The micropiles were instrumented by means of three LDTs distributed in a triangle arrangement, similar to that shown in Fig. 7.4. The same interface load cell was used to record the applied load.

7.3.1 Lateral cyclic load test procedure

In the two-way cyclic loading procedure adopted herein, the load was applied in a direction and reversed all the way in the other direction with the same amplitude. The load was applied in increments, each increment equal to approximately 3kN. At each increment, the two tested micropiles were subjected to five cycles of two-way loading.

The load was applied at a rate of one cycle per twenty seconds for load amplitudes 3 to 6 kN, and at rate of one cycle per forty five second at the highest load amplitude, 21 kN. The cyclic load tests were terminated when the stroke of the hydraulic jack reached its maximum value (150 mm). This procedure is different than the guidelines of ASTM D3966 (2007), which constitute one-way cyclic loading. The ASTM does not offer any guideline for two-way cyclic load tests, and no such guidelines were found in the literature for deep foundations.

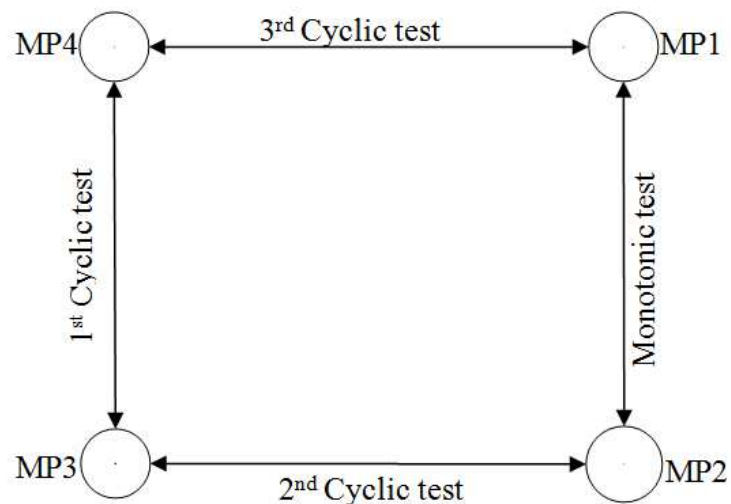


Figure 7. 31. The sequence and position of the field lateral cyclic tests

7.3.2 Cyclic load test results and analysis

Figures 7.32 to 7.37 illustrate the load – deflection curves for the six conducted cyclic lateral load tests. Each figure displays two back bone curves (BBC), along with the load – deflection curve obtained from the load tests. The two BBC are named BBC 1st cycle and BBC 5th cycle. The BBC 1st cycle is plotted by connecting the deflection of the micropile heads at the 1st cycle of loading at every load magnitude applied. While, the BBC 5th cycles is the back bone curve connecting the deflection at the 5th cycle of loading at each load amplitude applied. It is noted from the figures that the maximum load amplitude applied during the cyclic tests on MP3 and MP4 was 21kN, same as the cyclic load tests on MP2 and MP3. However, the maximum load applied during the last cyclic load test (MP1 and MP4) was only 15kN. This was governed by the maximum stroke of the hydraulic jack.

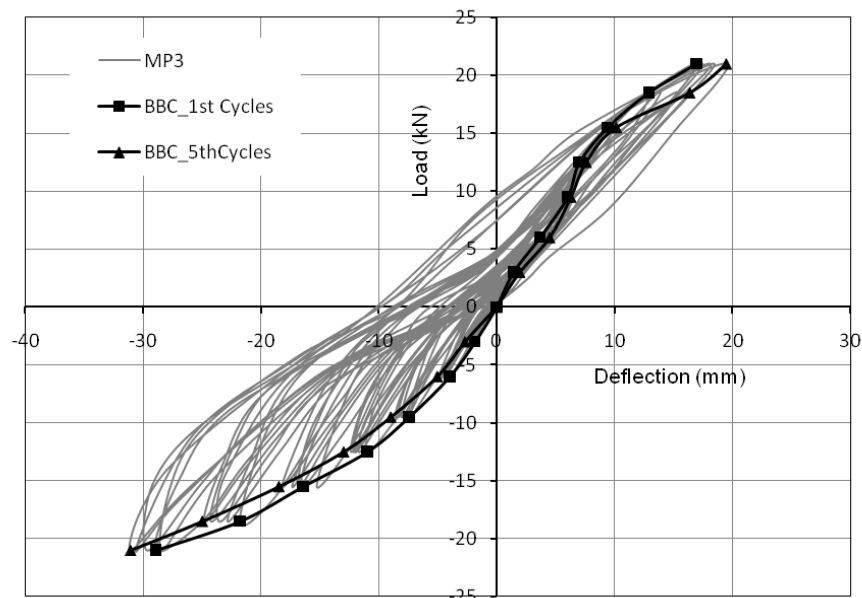


Figure 7. 32. Load-deflection curve for MP3 during cyclic test on MP3 and MP4

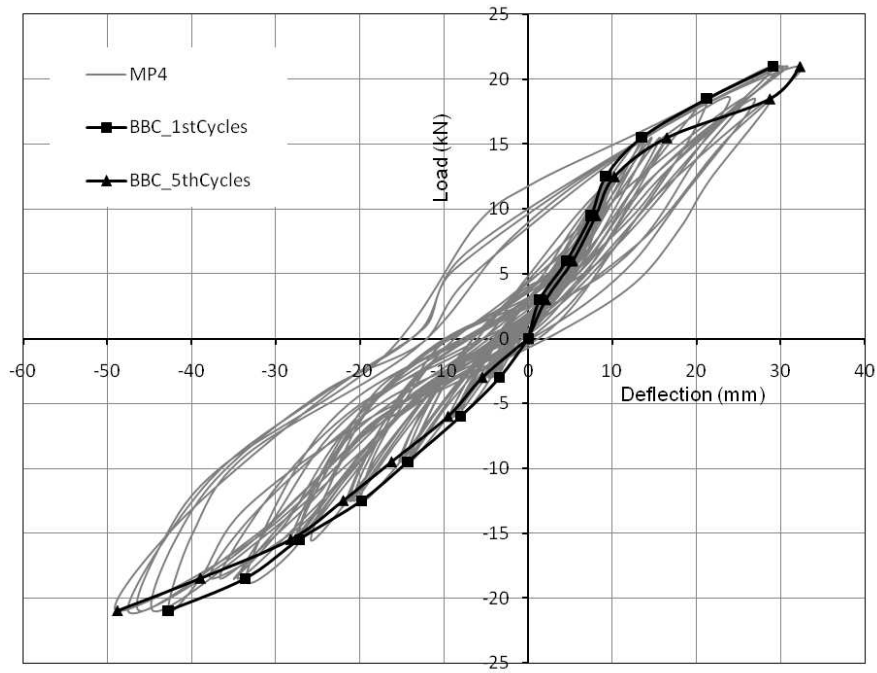


Figure 7. 33. Load-deflection curve for MP4 during cyclic test on MP3 and MP4

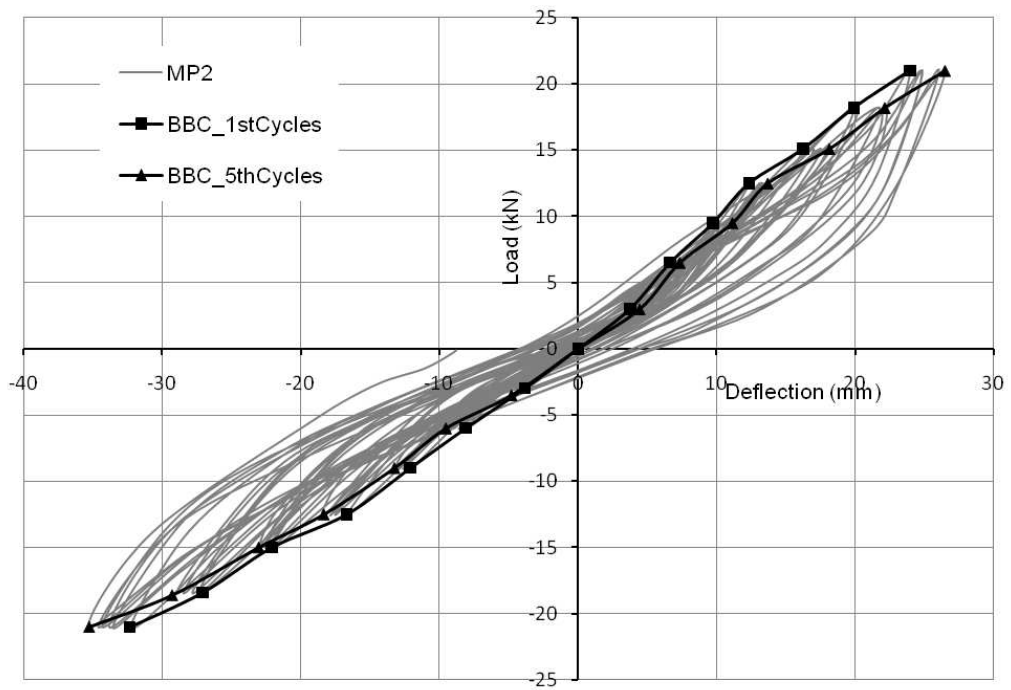


Figure 7. 34. Load-deflection curve for MP2 during cyclic test on MP2 and MP3

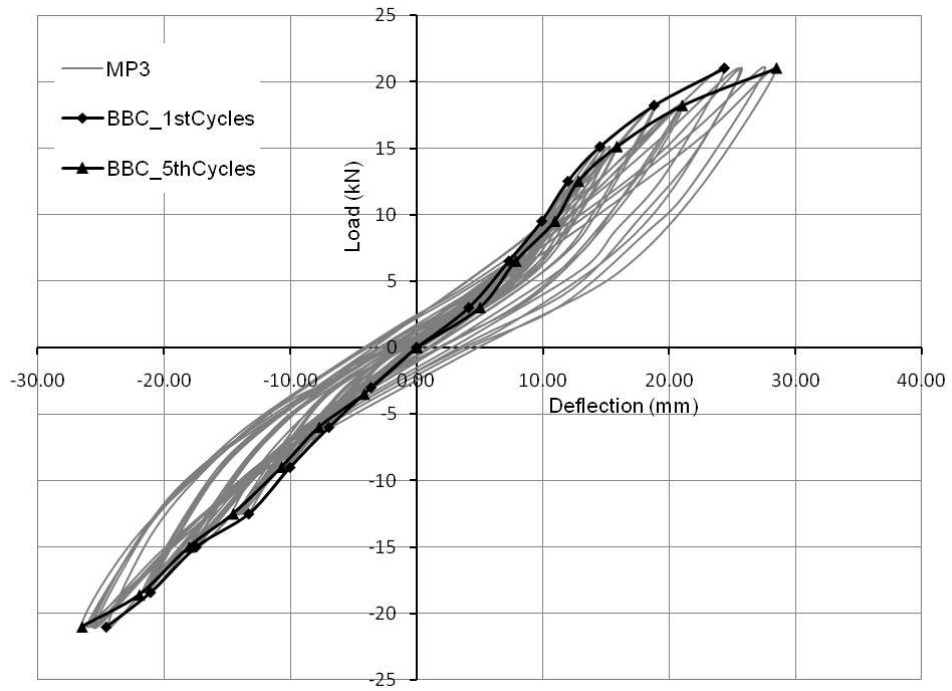


Figure 7. 35. Load-deflection curve for MP3 during cyclic test on MP2 and MP3

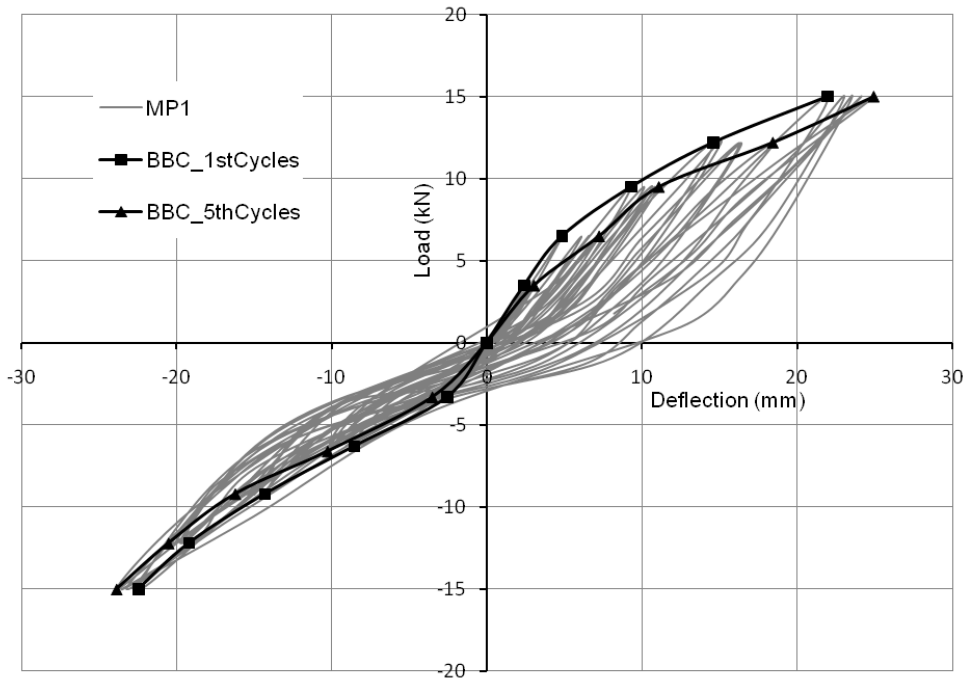


Figure 7. 36. Load-deflection curve for MP1 during cyclic test on MP1 and MP4

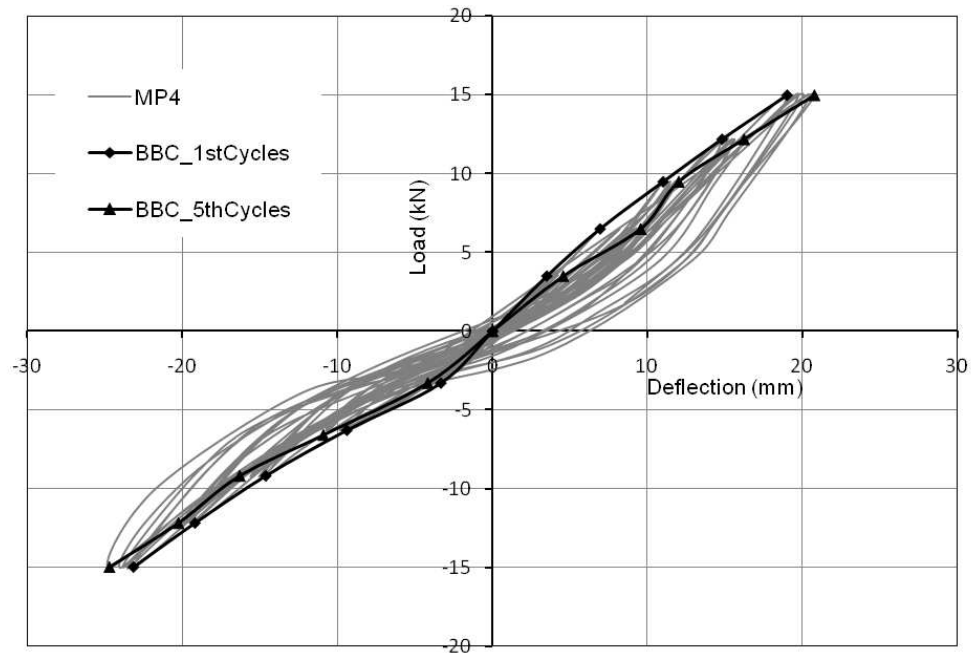


Figure 7.37. Load-deflection curve for MP4 during cyclic test on MP1 and MP4

All tests started in the negative direction of loading. Figures 7.32 to 7.37 show that the BBC curves at the 1st and 5th cycle have decreasing slope as the magnitude of the applied load increases. In addition, the pile head deflection increased as the number of load cycles increased at the same load magnitude.

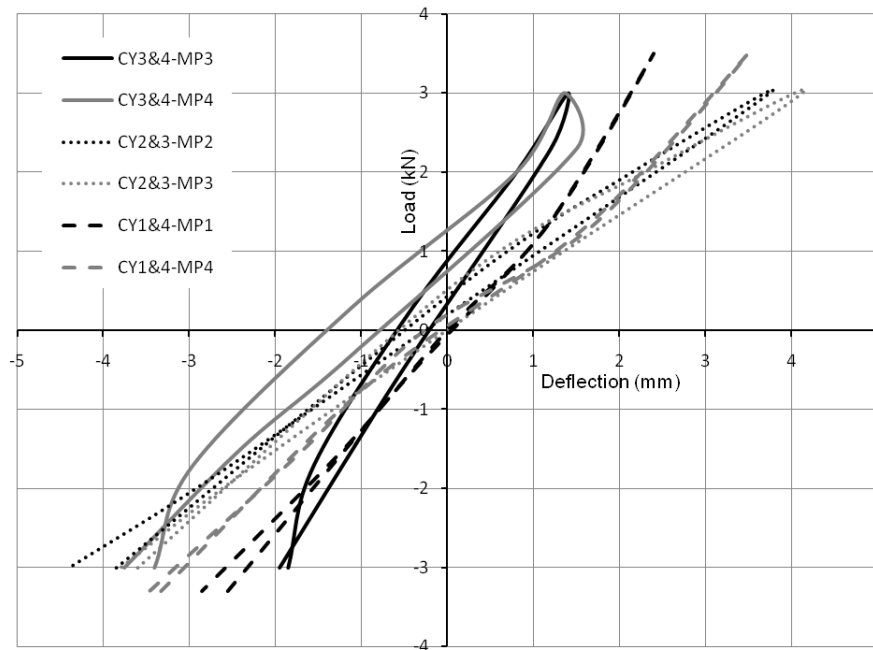
To compare the performance of the tested micropiles, their load – deflection curves are plotted in Figs. 7.38 and 7.41 for the 1st and the 5th cycles of loading at amplitudes equal to 3, 9, 15, and 18 kN. Each loading cycle started when the load magnitude was reached in the negative direction and ended when the same magnitude was reached again.

The figures show that the tested micropiles displayed different behaviour. In particular, the micropiles that were tested twice didn't show the same behaviour during consecutive cyclic load tests. For example, micropile MP4 was cyclically tested twice; firstly with

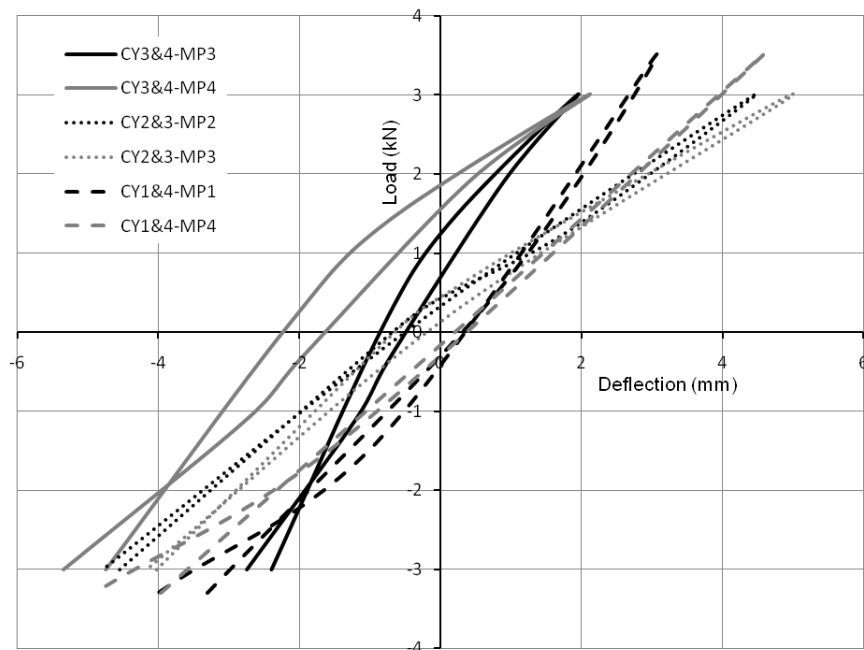
MP3 then with MP1. The behaviour of MP4 during its first cyclic load test was more flexible than its performance during the following test. That was observed for all load magnitudes presented in Figs. 7.38 and 7.41. On the contrary, micropile MP3 shows stiffer response during its first cyclic load tests, when loaded simultaneously with MP4, than its second cyclic test, when tested simultaneously with MP2. The flexible behaviour of MP3 and the stiffer response of MP4 during their second cyclic test may be attributed to the spatial variability the soil properties within the site.

On the other hand, all tested micropiles exhibited an increase in the pile head deflection from the 1st cycle to the 5th cycle at the same load magnitude. It is also observed that the negative deflections of all tested micropiles were higher than their corresponding values at the positive side at the same applied load. This might be because of gap formation between the micropiles and the soil at the opposite direction of loading during the two – ways cyclic tests. The gap effect was more obvious at the 1st cyclic test (cyclic tests on MP3 and MP4) rather than the following two tests.

To examine the degradation effect of the cyclic loading on the micropile head stiffness, the normalized stiffness of the micropile head is calculated at each cycle of loading for all load magnitudes applied. The normalized stiffness is defined as the stiffness of the micropile head at the Nth cycle divided by the stiffness of the pile head at the first cycle, both at the same load magnitude.

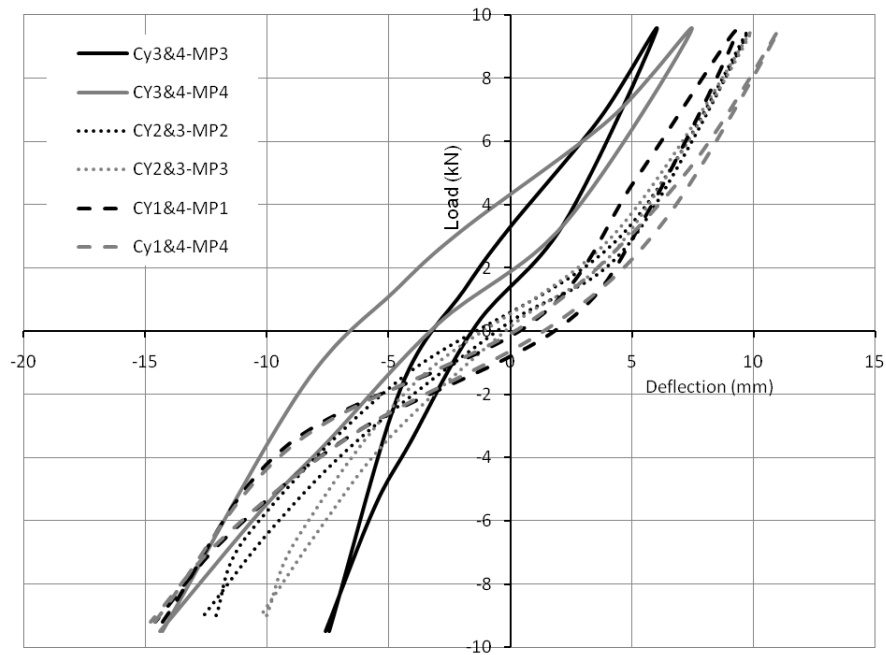


(a)

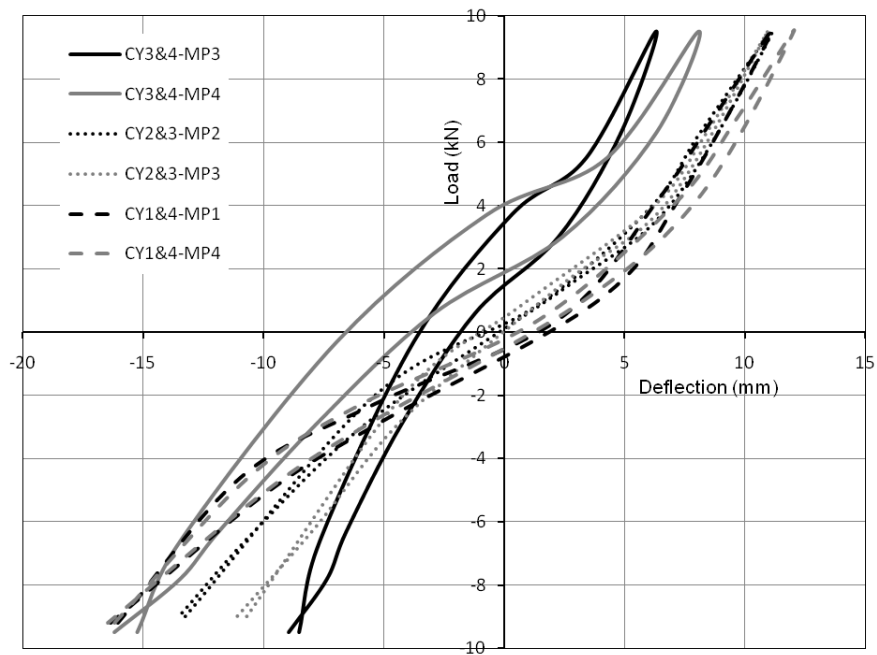


(b)

Figure 7. 38. Load – deflection for all the tested micropiles at 3kN; (a) 1st cycle of loading, (b) 5th cycle of loading

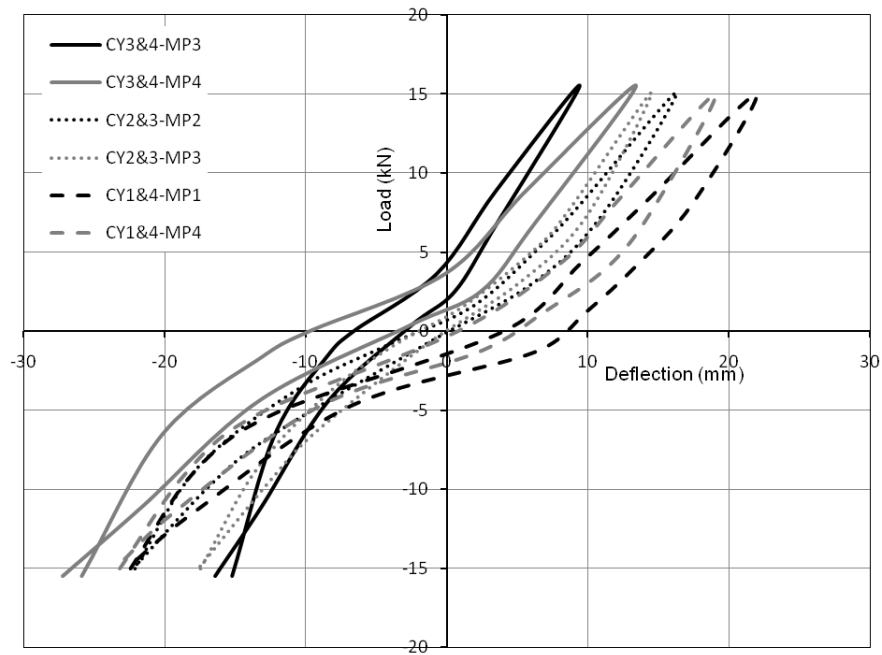


(a)

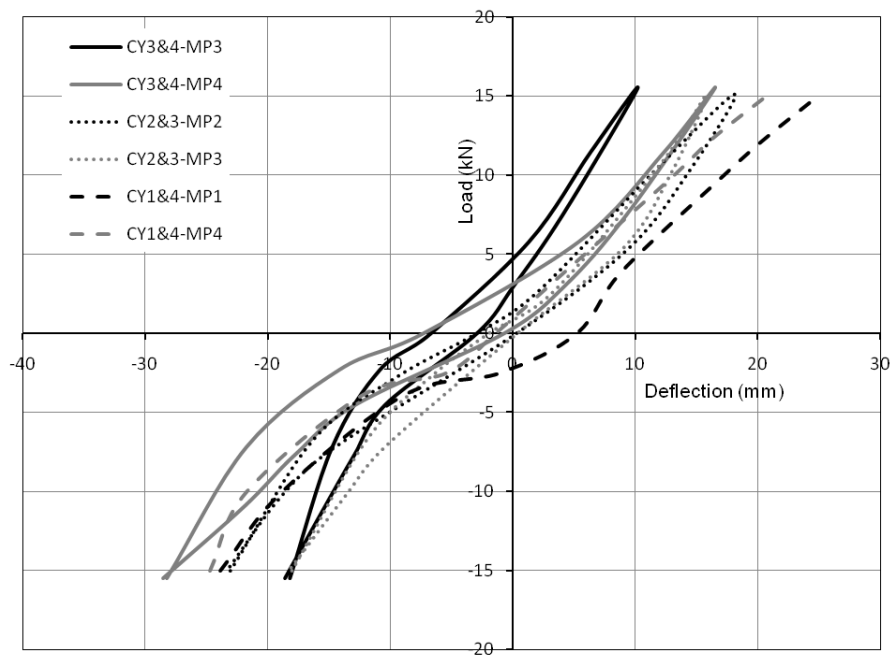


(b)

Figure 7. 39. Load – deflection for all the tested micropiles at 9kN; (a) 1st cycle of loading, (b) 5th cycle of loading

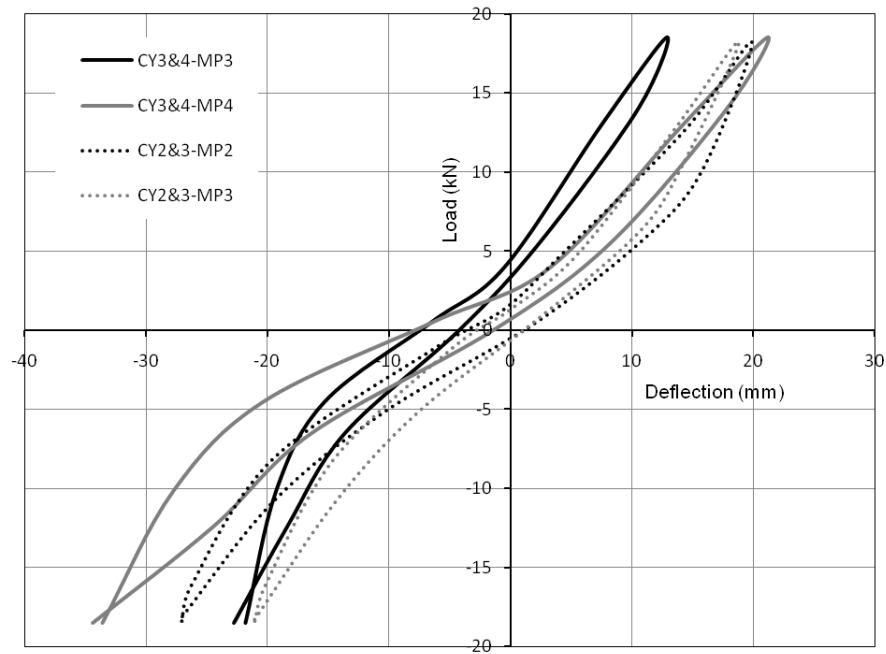


(a)

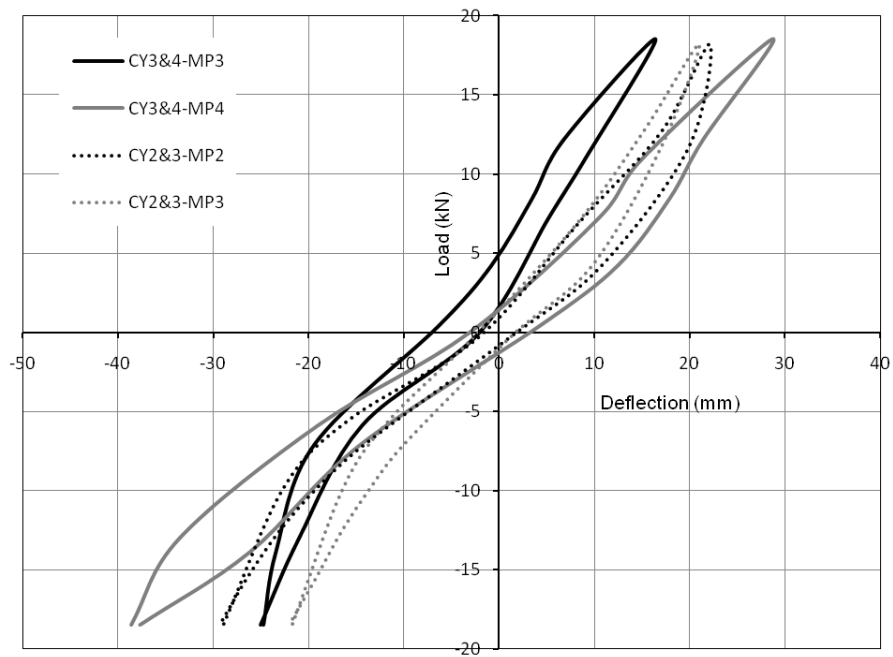


(b)

Figure 7. 40. Load – deflection for all the tested micropiles at 15kN; (a) 1st cycle of loading, (b) 5th cycle of loading



(a)



(b)

Figure 7. 41. Load – deflection for all the tested micropiles at 18kN; (a) 1st cycle of loading, (b) 5th cycle of loading

The stiffness of the micropiles at each load cycle is approximated by the slope of the load – deflection curve during each load cycle, (as given in Figs 7.38 to 7.41) i.e.:

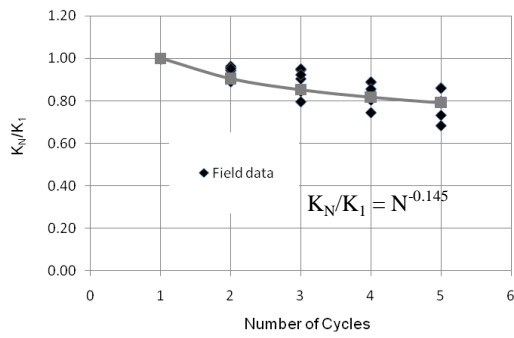
$$K_L = \frac{p_{max} - p_{min}}{y_{max} - y_{min}} \quad (7.5)$$

Where: K_L is the pile head stiffness in the lateral direction, p_{max} and p_{min} are the maximum and minimum applied loads during each load cycle (2 x the load amplitude) y_{max} and y_{min} are the corresponding pile head deflections. The calculated normalized micropiles stiffness values and the best fitting curve representing the measured data are presented in Figs. 7.42a to 7.42g. These figures demonstrate clearly that the stiffness of the piles decreases (degrades) as the number of load cycles increases. The degradation of the pile head stiffness can be related to the number of cycles utilizing a degradation parameter t , i.e.

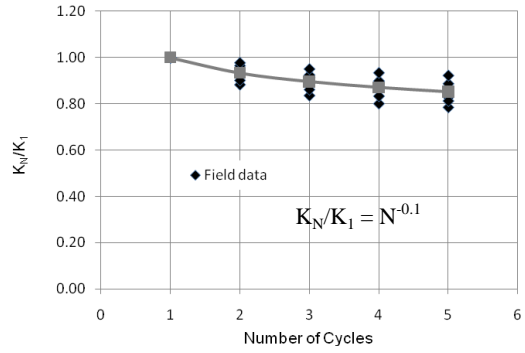
$$(K_N/K_1) = N^{-t} \quad (7.6)$$

Where: K_1 and K_N are the stiffness values in cycles 1 and N , respectively. The best fitting curve yields a degradation parameter t that varies from 0.145 to 0.055 as the load amplitude varies from 3 kN to 21 kN. It should be mentioned that for load amplitudes equal to 18 and 21 kN, the back-figured parameter depends only on 4 sets of data because the last cyclic loads tests (on MP1 and MP4) terminated at load 15kN.

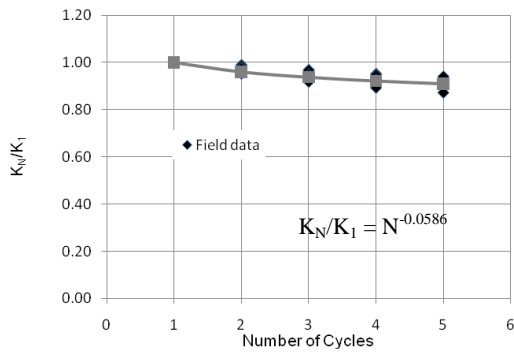
The variation of the degradation parameter t evaluated from the cyclic load tests with the stress level, p/p_u , of the cyclic amplitude applied is depicted in Fig.7.43, where p_u used in the figure is the pile ultimate resistance evaluated from the monotonic test evaluated as 34 kN.



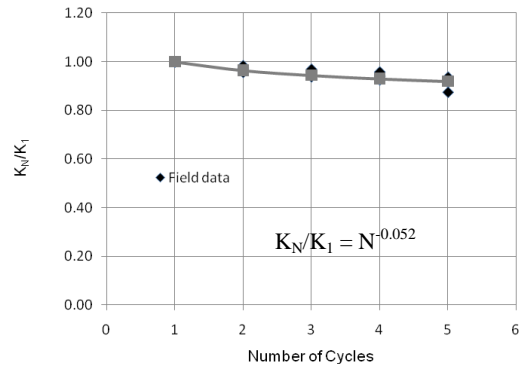
a) at load =3kN



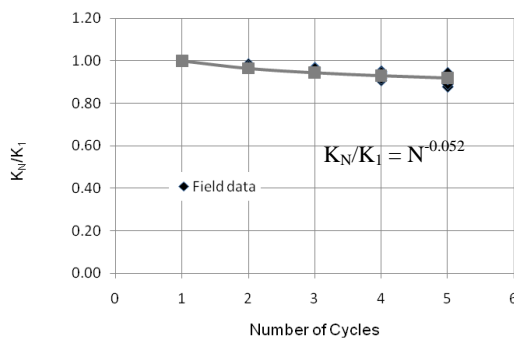
b) at load =6kN



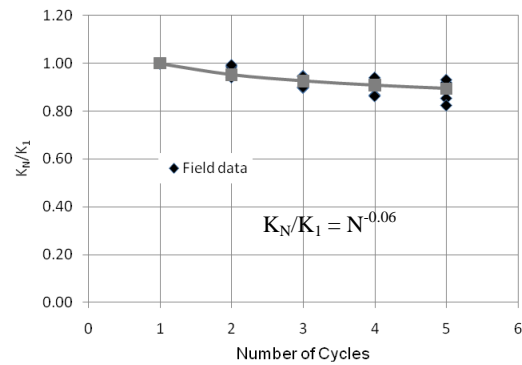
c) at load =9 kN



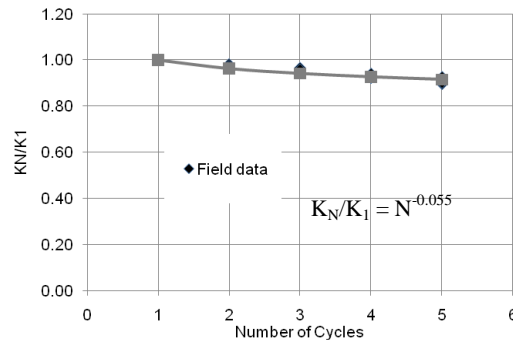
d) at load =12 kN



e) at load =15 kN



f) at load = 18 kN



g) at load =21 kN

Figure 7. 42. Normalized head stiffness versus number of cycles at all load magnitudes tested

Figure 7.43 reveals that the degradation of the pile head stiffness reaches a constant trend after specific number of cycles at the same load amplitude or at different cyclic load amplitudes. This phenomenon is similar to the shakedown condition suggested by Matlock (1970). He stated that after a large number of cycles of loading and degradation of resistance, the soil-pile system tends to stabilize and he used the term shakedown condition to define this stabilization.

The observed cyclic performance of the micropiles suggests that the stiffness degradation with number of cycles can be generally represented using Eq. 7.6 and suitably selected degradation parameter t . It should be noted that these observations are only relevant to the limited number of cyclic load tests conducted for micropiles in stiff clay. However, the observations made here can be extended to a closed form solution to estimate the degradation of the pile head stiffness during a seismic event, if the degradation parameter t can be related to the type of soil and hollow bar micropile geometry.

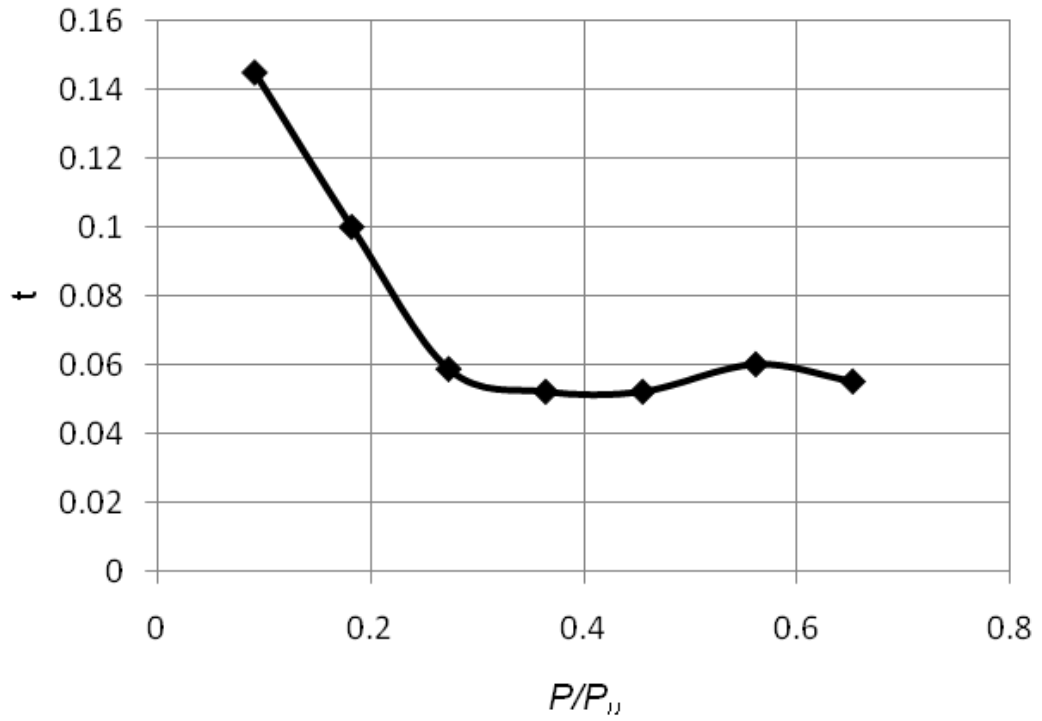


Figure 7. 43. Degradation parameter at different stress levels

CHAPTER 8

SUMMARY, CONCLUSIONS, AND RECOMMENDATIONS

This chapter summarizes the research conducted in this thesis on the hollow bar micropiles foundation system. In addition, the conclusions arisen from the research are provided. Finally, recommendations for future research are offered.

8.1 Summary

The behaviour of hollow bar micropiles was investigated through both a field study and numerical investigation, under different types of loading and configurations.

The experimental phase of this research involved a series of full scale field load tests on hollow bar micropiles. As part of this experimental phase, a soil investigation programme was conducted. The soil investigation programme incorporated two mechanical boreholes along with standard penetration tests. Disturbed and undisturbed samples were collected from the site where the micropiles were installed and load tested. Several laboratory tests were conducted to evaluate the general properties of the soil deposit as well as the shear strength and stiffness parameters. Based on the results of the soil investigation program, the site soils are classified as stiff to very stiff silty clay to clayey silt, characterized by undrained shear strength that varies from 90 kPa to 175 kPa. This cohesive layer was underlain by sandy layer with traces of silt that had an angle of internal friction between 34° and 38°.

To achieve the research goals, four hollow bar micropiles were installed using air flushing technique employing large drilling cross carbide bits. The hollow bars used for

installation and construction of micropiles were Geo-drilled injection bars with an outer diameter of 76 mm and an inner diameter of 48 mm. The all-thread bars employed had specified yield stress of approximately 580 MPa and a cross-sectional area of 2503 mm² between the threads of the bar. The large drilling carbide bits utilized had a diameter of 176 mm.

Twenty two different load tests were conducted on the four hollow bar micropiles in four consecutive phases. The first phase included three monotonic compression and two monotonic tension tests conducted on single micropiles. The second phase encompassed five axial cyclic load tests on single micropiles; four compression and one tension. The third phase involved four axial monotonic tests on pairs of hollow bar micropiles. In the last phase, eight lateral load tests were performed; two monotonic load tests and six cyclic load tests, which were conducted simultaneously on pairs of single micropiles.

The results from each set of tests were utilized to validate a numerical model for that particular loading condition and pile configuration. For axially loaded micropiles, 2D finite element axisymmetric model was developed and validated. The model was created utilizing ABAQUS software environment. The model was created employing constitutive models to simulate the micropile-soil system. Moreover, the non-linearity of the geometric deformation pattern of the micropile and the soil was considered. A 3D finite element model was established to simulate the axial behaviour of micropiles in a group. The lateral behaviour of hollow bar micropiles was simulated utilizing *p-y* method of analysis employed in the LPile software.

Upon calibration and validation of the numerical models, parametric studies were carried employing the calibrated models to further understand the performance characteristics of single and groups of hollow bar micropiles, and to develop design guidelines for their application in foundations under different loading conditions.

8.2 Results and Conclusions

The behavior of hollow bar micropiles was investigated for different loading conditions including axial and lateral, monotonic and cyclic loads. The group behavior of hollow bar micropiles was examined as well. This section presents the main observations and results of the research as well as the conclusions drawn from this study. The presentation of the findings and conclusions is divided into three parts; each part addresses the most significant findings for specific loading condition.

8.2.1 Axial capacity of hollow bar micropile

The experimental results on the axial performance and its interpretation revealed that the axial capacity of hollow bar micropiles would be underestimated when considering it as Type B, pressure grouted, micropiles, in accordance with the FHWA classification. Hence, a closed form solution was proposed to compute the axial capacity of hollow bar micropiles embedded in cohesive soils. The closed form solution was developed based on the installation method employed for the construction of the micropiles. The solution involves the following step-by-step procedure:

- Evaluate the undrained shear strength of the soil, s_u , along the micropile length.

- Inspecting the installation log, calculate the percentage increase in the hole volume, $V_{inc} = (\text{volume of grout used} - \text{nominal hole volume, based on bit diameter}) / \text{nominal hole volume, based on bit diameter}$.
- Determine the enlargement factor, f_I , which depends on the loading condition. For micropiles under compression: $f_I = (1+0.35V_{inc})$; while for micropiles tension: $f_I = (1+0.275V_{inc})$
- Calculate geotechnical capacity, $P_G = (0.9 \text{ to } 1) s_u \pi d L f_I + 9 s_{ub} A_{hole}$
- Use a factor of safety of 2 to calculate the design load.

For micropiles subjected to cyclic axial loading, an equation was proposed in order to account for the stiffness degradation. The equation incorporates a degradation parameter, t , to relate the stiffness of the micropile at the N^{th} cycle to the stiffness of the micropiles at the first cycle of loading.

8.2.2 Lateral performance of hollow bar micropiles

The experimental investigation on the lateral behaviour of hollow bar micropiles provided useful insights on their performance characteristics and the appropriate tools for their design. The observed load-displacement curve demonstrated that the strong nonlinear behaviour of the pile, reminiscent of flexible pile behaviour. Thus, the lateral pile capacity is best evaluated using a lateral displacement criterion. Additionally, the results underscored the importance of accounting for this nonlinearity when designing micropile foundations subjected to lateral loads. Furthermore, the load tests demonstrated that the lateral response of the hollow bar micropiles is very sensitive to the properties of

soil along a depth equal to 10 times the pile diameter. It was also inferred from the results that the anticipated enlargement in the diameter of the micropile near the toe has no influence on the micropile capacity.

To account for the strong nonlinear behaviour, the p - y curves method was used in the analysis of the test results. The ability of this technique to accurately represent the response of micropiles to lateral loads was demonstrated. However, the pile information introduced to program LPILE, which is widely used in industry for lateral response analysis of piles, needs to be adjusted to properly simulate the performance of micropiles. An example for the necessary adjustment was discussed.

The parametric study carried out on the hollow bar micropiles suggested that the connectivity of the micropile head into the pile cap should be evaluated carefully. If full fixity is assumed, then sufficient moment transfer capacity should be provided between the pile and the pile cap. For micropiles connected to their cap by simply extending the hollow core bar 150mm into the pile cap, the fixed head condition cannot be justified. Hence, it is recommended to assume that the pile head will have only 50% fixity condition, and evaluate the micropile performance under lateral loading accordingly. It was also found that if a free head micropile is to be assumed, the micropile should be reinforced by outer steel case that should extend to a distance at least ten times the outer casing diameter. On the other hand, if fixed head condition is to be assumed, the steel casing length can be only seven times the casing diameter. In summary, hollow bar micropiles can carry moderate lateral loads with proper reinforcement configuration and pile head fixity condition.

The degradation of the pile head stiffness evaluated from the cyclic field tests exhibited a “shake down” phenomena. The pile stiffness initially degraded as the number of load cycles increased but reached a constant value after a specific number of cycles at the same load amplitude or at different cyclic load amplitudes. The observed cyclic performance of the micropiles suggests that the stiffness degradation with the number of load cycles can be generally represented using Eq. 7.6 and suitably selected degradation parameter t . However, the observations made here can be extended to a closed form solution to estimate the degradation of the pile head stiffness during a seismic event, if the degradation parameter t can be related to the type of soil and hollow bar micropile geometry.

8.2.3 Hollow bar micropile group behaviour

The behaviour of hollow bar micropile groups was evaluated from field load as well as a parametric study conducted using 3D calibrated finite element models of the hollow bar micropiles. The results of this investigation suggested that the group capacity can be calculated utilizing a group efficiency factor equal to one for hollow bar micropile groups embedded in cohesive soils. The results obtained from the study were used to formulate a method to evaluate the settlement of a hollow bar micropile groups using the interaction approach. A family of interaction factor diagrams is developed to evaluate the interaction between two micropiles considering the spacing between the piles, the soil and pile properties, and the slenderness ratio of the micropile. It was found that the effect of considering an intermediate micropile on the interaction factor between hollow bar micropiles was limited. Therefore, Eq. 6.7 can be used to estimate the settlement of a

group of hollow bar micropiles employing the interaction factors given in Figs. 6.28 to 6.30.

8.3 Recommendations for future work

This section provides a list of recommendations for future research work to further enhance our understanding of the performance of hollow bar micropiles and improve their efficiency in foundation applications. The recommendation are organized under two heading; (a) further field tests, (b) numerical analysis

(a) Further field tests

It is recommended to carry out another series of full-scale field load tests on hollow bar micropiles embedded in both cohesive and cohesionless soils. The following should be considered during the field tests:

- Using embedded strain gauges during the field tests to measure the actual load transfer mechanism during loading of the hollow bar micropiles. The embedded strain gauges should install inside the hollow core of the steel bar.
- Employing larger drilling bits, 225mm, during installation to increase the ratio between the hollow bar diameter and the bit diameter to 1:3.
- Utilizing reinforced fibers polymer to reinforce the grout which will enhance the lateral performance and increase the capacity of the hollow bar micropile under lateral loads. Fibers polymer will control the cracking widths developed in the grout. Hence, increase its bending stiffness.

- Performing axial and lateral cyclic load tests with different loading amplitudes to verify the degradation parameter approach.
- The tested hollow bar micropiles must be installed employing different installation techniques; such as: different pressure, different applied torque (speed) during installation, and utilizing different flushing fluids
- Dynamic field test on hollow bar micropiles would be beneficial issue for design of micropiles subject to machinery loading, and/or micropiles installed in seismic areas.

(b) Numerical analysis

A calibrated model is now available to simulate the behaviour of hollow bar micropiles under different loading conditions in cohesive soils. It is anticipated that the performance of such micropiles will be different when installed in cohesionless or rock. It is therefore important to develop numerical model for the analysis of hollow bar micropiles embedded in sandy soils and in rock. The numerical model should be calibrated with field load tests results, and use the verified model to perform an extensive parametric study in order to establish comprehensive design guidelines for hollow bar micropiles system in all soil types and rock. It is also recommended to model a construction phase to simulate the effect of installing the hollow bar micropile on the surrounding soil.

REFERENCES

- Allotey, N. and Elnaggar, M.H .2008. A Consistent Soil Fatigue Framework Based on the Number of Equivalent Cycles. *Geotechnical and Geological Engineering*, Vol. 26, no.1, pp.65–77.
- Anderson, J.B., Townsend, F.C., and Grajales, B. 2003. Case history evaluation of laterally loaded piles, *Journal of Geotechnical and Geoenvironmental Engineering*, ASCE, Vol. 129, no.3, pp. 187-196.
- American Association of State Highway and Transportation Officials (AASHTO) 2002. *Standard Specifications for Highway Bridges*. American Association of State Highway and Transportation Officials Publication, Washington, D.C. p. 689
- ASTM Standard D1143-81. 2007. Standard Test Method for Deep Foundations under Static Axial Compressive Load. *Annual Book of ASTM Standards*, Vol. 04.08, ASTM International, West Conshohocken, PA.
- ASTM Standard A519-06. 2006. Standard Specification of Seamless Carbon and Alloy Steel Mechanical Tubing. *Annual Book of ASTM Standards*, Vol. 01.01, ASTM International, West Conshohocken, PA.
- ASTM Standard A615/A615M-09b. 2009. Standard Specification for Deformed and Plain Carbon-Steel Bars for Concrete Reinforcement. *Annual Book of ASTM Standards*, Vol. 01.04, ASTM International, West Conshohocken, PA.
- ASTM Standard A29/A29M-05. 2005. Standard Specification for Steel Bars, Carbon and Alloy, Hot-Wrought. *Annual Book of ASTM Standards*, Vol. 01.04, ASTM International, West Conshohocken, PA
- ASTM Standard D 2850-95. 1999. Standard Test Method for Unconsolidated-Undrained Triaxial Compression Test on Cohesive Soils. *Annual Book of ASTM Standards*, Vol. 01.04, ASTM International, West Conshohocken, PA.
- ASTM Standard D3689-07. 2007. Standard Test Methods for Deep Foundations under Static Axial Tensile Load. *Annual Book of ASTM Standards*, Vol. 04.08, ASTM International, West Conshohocken, PA, pp. 405–423.
- ASTM Standard D3966-07. 2007. Standard Test Methods for Deep Foundations under Static Lateral Load. *Annual Book of ASTM Standards*, Vol. 04.08, ASTM International, West Conshohocken, PA.

- Baguelin, F., Jezequel, J.F. and Shields, D.H. 1978. The Pressuremeter and Foundation Engineering, Transactions Technical Publications.
- Bennett, J. K. and Hothem, N. L. 2010. Hollow Bar Micropiles for Settlement Control in Soft Clay. Proceedings of the 10th International Workshop on Micropile, Washinton, D.C, USA Sept 22–25.
- Bierschwale, M.W., Coyle, H.M. and Bartoskewitz, R.E. 1981. Field Tests and New Design Procedure for Laterally Loaded Drilled Shafts in Clay. Research Report211-3F, Texas Transportation Institute, Texas A&M University, Collage Station, 116p.
- Bishop, J. A., Aschenbroich, H. K., and DeBernar, B. A. 2006. Class I and II Micro-Piles With Hollow-Bar Reinforcement Load Tests and Performance Measurements. Proceedings of the 7th International Workshop on Micropile, Schrobenhausen, Germany, May 3-7.
- Bowles, J.E. 1997. Foundation Analysis and Design. 5th Edition, McGraw-Hill Book Co. Singapore.
- Bruce, D. A., Bjorhovde, R., and Kenny, J. R. 1993. Fundamental Tests on the Performance of High Capacity Pin Piles. Proceeding of DFI Annual meeting, Pittsburgh PA.
- Bruce, J. and Gursersaud, N. 2009. Grout Flushed Micropiles Foundations for a New Rail Overpass. Proceedings of the 9th International Workshop on Micropile, London, England, May 10–13.
- Butler, H.D. and Hoy, H.E. 1977. Users Manual for the Texas Quick-Load Method for Foundation Load Testing. Report No. FHWA RD-IR 77-8, Federal Highway Administration, Washington, D.C. 59pp.
- Cadden, A.W., Gómez, J.E. 2002. Buckling of Micropiles - A Review of Historic Research and Recent Experiences. ADSC-IAF Micropile Committee.
- Cadden, A., J. Gómez, D.A. Bruce, and T. Armour. 2004. Micropiles: Recent Advances and Future Trends – Current Practices and Future Trends in Deep Foundations. Geotechnical Special Publication No. 125, ASCE Geo-Institute GSP Honoring Dr. George Goble, GeoTrans Conference, Los Angeles, CA, pp.1-27.
- Canadian Foundation Engineering Manual. CFEM. 4th Edition. 2006. Canadian Geotechnical Society, BiTech Publications Ltd. Canada, 488 p.

- Cavey, J. K., Lambert, D. V., Miller, S. M., and Krhounek, R.C. 2000. Observations of Minipile Performance under Cyclic Loading Conditions. *Ground Improve.*, Vol. 4, no.1, pp. 23–29.
- Chen, Y-J. and Lee, Y-H. 2010. Evaluation of Lateral Interpretation Criteria for Drilled Shaft Capacity. *Journal of Geotechnical and Geoenvironmental Engineering*, Vol. 136, no. 8, pp. 1124-1136
- Con-Tec system Ltd. 2011. *Micropiles Broachers*, Vancouver, BC, Canada. p.12
- Davisson, M.T. 1972. High Capacity Piles. *Proceedings of Soil Mechanics Lecture Series on Innovations in Foundation Construction*, ASCE, IL Section, Chicago, pp. 81–112.
- Duncan, J. M., Evans, Jr., L. T. and Ooi, P. S. K. 1994. Lateral Load Analysis of Single Piles and Drilled Shafts. *ASCE Journal of Geotechnical Engineering*, Vol. 120, no. 5, pp 1018-1033.
- El Naggar, M. H. and Wei, J. Q. 2000. Cyclic Response of Axially Loaded Tapered Piles. *Geotechnical Testin Journal*, Vol. 23, no. 1, pp. 100–115.
- El Sharnouby, B. and Novak, M. 1985. Static and Low Frequency Response of Pile Groups. *Canadian Geotechnical Journal*, Vol. 22, No. 1.
- El Sharnouby B. & Novak M. 1990. Stiffness Constants and Interaction Factors for Vertical Response of Pile Groups. *Canadian Geotechnical Journal*, Vol. 27, No. 6, pp. 813-822.
- Federal Highway Administration 1997. *Drilled and Grouted Micropiles, State-of-Practice Review*. Report No. FHWA-RD-96-016/019, US Department of Transportation, McLean, VA, 4 voulmes.
- Federal Highway Administration 2000. *Micropile Design and Construction Guidelines—Implementation Manual*. FHWA Publication No FHWA-SA-97-070, US Department of Transportation, McLean, VA, p. 376.
- Federal Highway Administration-National Highway Institute (FHWA NHI) 2005. *Micropile Design and Construction – Reference Manual*. Publication No. FHWA NHI-05-039. US Department of Transportation, McLean, VA, p. 436.
- Fuller, F.M. and Hoy, H. E. 1970. Pile Load Tests Including Quick Load Tests Method, Conventional Methods, and Interpretations. *Research Record 333*, Highway Research Board, Washington, pp. 74-86.

Google Earth website, <http://maps.google.ca/maps>

- Go´mez, J. E., Cadden, A. W., and Bruce, D. A. 2003. Micropiles in Rock- Development and Evolution of Bond Stresses under Repeated Loading. Proceeding of the 12th Pan-American Conference on Soil Mechanics and Geotechnical Engineering, Cambridge, MA, USA.
- Go´mez, J. E., Rodriguez, C. J., Robinson, H. D., Mikitka, J., and Keough. L. 2007. Hollow Core Bar Micropiles—Installation, Testing, and Interpolation of Design Parameter of 260 Micropiles. Proceedings of the 8th International Workshop on Micropile, Toronto, Canada, Sep 22-26
- Gronek, Paul B., Bruce, Donald A., Greenman, James H. 1993. Pin piles save silos. Civil Engineering journal, Vol. 63, no. 9, pp. 66-68
- Hibbitt, Karlsson, and Sorensen, Inc. 2008. ABAQUS/Standard User’s Manual. Hibbitt, Karlsson, and Sorensen, Inc., Pawtucket, RI.
- Han, J., Ye, S. 2006a. A field study on the behavior of micropiles in clay under compression or tension. Canadian Geotechnical Journal, Vol. 43, no 1, pp 19-29
- Han, J., Ye, S. 2006b. A field study on the behavior of a foundation underpinned by micropiles. Canadian Geotechnical Journal, Vol. 43, no 1, pp 30-42
- Helwany, S. 2007. Applied Soil Mechanics with ABAQUS Application. John Wiley and Sons, p. 385.
- Holman, T.P. and Tuozzolo, T.J. 2006. Advanced Interpretation of Instrumented Micropile Load Tests. Proceedings of the 7th International Workshop on Micropile, Schrobenshausen, Germany, May 3-7.
- Holtz, W.G. and Gibbs, H. J. 1979. Discussion of SPT and relation density in sand. Journal of Geotechnical Engineering Division, ASCE, vol. 105, NO. GT3, pp. 439-441.
- Idriss, I.M., Dobry, R., and Singh, R.D. 1978. Nonlinear behaviour of soft clays during cyclic loading. J Geotech Eng, ASCE, Vol. 104, no.GT12, pp. 1427–1447
- Isenhower, W.M. and Wang, S-T. 2011. Technical Manual for LPILE, Version 6. Ensoft, Inc. p.214
- Jamiolkowski, M. 1977. Design of Laterally Loaded Piles. International Conference on Soil Mechanics and Foundation Engineering, Tokyo.

- Jeon, S. S. 2004. Interpretation of Load Tests on Minipiles. Proceeding of Civil Engineers Geotechnical Engineering, ICE, 157(GE2), pp. 85–90.
- Juran, I., Benslimane, A., Hanna, S. 2007. Engineering Analysis of Dynamic Behaviour of Micropiles Systems. Journal of the Transportation Research Board, Vol. 1772 PP. 91-106
- Kulhawy, F.H., and Mayne, P.W., 1990. Manual on estimating soil properties for foundation design. Electric Power Research Institute, EPRI, Report No. Rp1493-6, Palo Alto, California, USA 308 P.
- Lee C.Y. 1993a. Pile Group Settlement Analysis By Hybrid Layer Approach. Journal of Geotechnical Engineering, ASEC, Vol. 119, No. 6, pp. 984-997.
- Lee C.Y. 1993b. Settlement of Piles Groups- Practical Approach. Journal of Geotechnical Engineering, ASEC, Vol. 119, No. 9, pp. 1449-1461.
- Livneh, B., 2006. The axial performance of square shaft helical piles. M.Sc. thesis, The University of Western Ontario, Canada.
- Long, J., Maniaci, M., Menezes, G. 2004. Results of lateral load tests on micropiles. Geotechnical Special Publication, no. 124, Geosupport 2004 - Drilled Shafts, Micropiling, Deep Mixing, Remedial Methods, and Specialty Foundation Systems, Proceedings of Sessions of the GeoSupport Conference, p 122-133
- MacLean, D. 2010. Typical case history of a hollow bar micropiles. DFI/ADSC micropiles seminar, Industry Trends and Developments. Mississauga, Ontario, Canada.
- Matlock, H. 1970. Correlations for Design of Laterally Loaded Piles in Soft Clay. Proceeding of 2nd Offshore Technology Conference, Vol. I, pp. 577-594
- Mayne, P.W., and Kemper, J.B. 1988. Profiling in stiff clay by CPT and SPT. Geotechnical testing Journal. ASTM, Vol. 11, no.2, pp. 139-147.
- Mayne, P.W., and Kulhawy, F.H. 1982. k_o -OCR relationships in soil. Journal of Geotechnical Engineering, Vol. 108, no.GT6, pp. 851-872.
- Mayne, P.W., Christopher, B.R., and DeJona, J. 2002. Subsurface investigation – Geotechnical site characterization. FHWA Report No. FHWA-NHL-01–031, US Department of Transportation, McLean, VA, p. 300.

- McClelland, B. and Focht, J.A. 1958. Soil Modulus for Laterally loaded Piles. Transactions, ASCE, Vol. 123, pp 1049-1086
- McNulty, J. F. 1956. Thrust loading on piles. Journal of Soil Mechanics and Foundations Division, ASCE, Vol.82, no.SM2, pp1-25
- Misra, A., Chen, C.H., Oberoi, R., Kleiber, A. 2004. Simplified analysis method for micropile pullout behavior. Journal of Geotechnical and Geoenvironmental Engineering, Vol. 130, no. 10, pp 1024-1033.
- Mitchell, C. L. B., Mathieson, W. L., and Hopkins, T.W. 2007. Micropile Load Transfer Rates and Bond Stresses in the Puget Sound Region of Washington State, U.S.A. Proceedings of the 8th International Workshop on Micropile, Toronto, Canada, Sep 23-26
- NAVFAC. 1986. Foundations & Earth Structures, Design Manual 7.02. Revalidated by Change 1 September 1986, Naval Facilities Engineering Command
- NYSDOT. State of New York Department of Transportation 2008. Standard Specifications. Albany, New York 12232.p 1068.
- Ousta, R. and Shahrour, I. 2001. Three-dimensional analysis of the seismic behaviour of micropiles used in the reinforcement of saturated soil. International Journal for Numerical and Analytical Methods in Geomechanics, Vol. 25, pp. 183-196.
- Peck, R.B., Hanson, W.E., and Thornburn, T.H., 1974. Foundation Engineering. John Wiley, New York, 2nd Edition, 514 P.
- Poulos, H.G. 1968. Analysis of Settlement of Pile Groups. Geotechnique, Vol. 18, pp. 449-471.
- Poulos, H.G. 1971. Behaviour of Laterally Loaded Piles II - Pile Groups. Journal of Soil Mechanics and Foundations Division, ASCE, Vol. 97, no. SM5, pp. 733-751.
- Poulos, H.G. 1974. Technical Note, Journal of Soil Mechanics and Foundations Division, ASCE, Vol. 100, No. GT2, pp. 185-190.
- Poulos, H.G. 1979. Group Factors for Pile-Deflection Estimation", Journal of Soil Mechanics and Foundations Division, ASCE, Vol. 105, no.GT12, pp. 1489-1509.
- Poulos, H.G. and Davis, E.H. (1980) Pile Foundations Analysis and Design", John Wiley and Sons, p. 397.

- Post Tension Institution (PTI) 2004. Recommendations for Pre-stressed Rock and Soil Anchors. Phoenix, AZ, p. 104.
- Prakash, S. and Sharma, H.D. 1990. Pile foundations in engineering practice. John Wiley and Sons, New York, N.Y.
- Pyke, R. 1984. Panel discussion, laterally loaded deep foundation (STP 835), ASTM, Philadelphia, 239–243.
- Pyke, R. and Beikae, M. 1993. TESS-A computer program for nonlinear ground response analysis: User's Manual, Taga Engineering Software Services, Berkeley, California
- Randolph, M.F., and Wroth, C.P. 1978. Analysis of deformation of vertically loaded piles. *Journal of Geotechnical Engineering*, Vol. 114, no.12, pp. 1465-1488.
- Reese, L.C., and O'Neil, M.W. 1988. Drilled shafts: construction procedures and design methods. FHWA-HI-88-042. Federal Highway Administration, McLean, Va.
- Reese, L. C., Wang, S. T., Isenhower W.M., Arrellaga, J. A., and Hendrix, J. 2000. LPILE Plus Version 4.0: A Program for the Analysis of Piles and Drilled Shafts under Lateral Loading. Ensoft, Inc, P. O. Box 180348, Austin, Texas, 78718.
- Reese, L. C., Wang, S. T., Arrellaga, J. A., and Hendrix, J. 2002. Group6.0: A Program for the Analysis of a Group of Piles Subjected to Axial and Lateral Loading. Ensoft, Inc., P. O. Box 180348, Austin, Texas, 78718.
- Reese, L.C. and Welch, R.C. 1975. Lateral Loading of Deep Foundations in Stiff Clay. *Journal of Soil Mechanics and Foundations Division, ASCE*, Vol.101, no. GT7, pp. 633-649
- Richards, T.D. and Rothbauer, M.J. 2004. Lateral Loads on Pin Piles (Micropiles). Geotechnical Special Publication "Drilled Shafts, Micropiling, Deep Mixing, Remedial Methods, and Specialty Foundation Systems", ASCE Publication, No.: 124, pp.158-174.
- Russo, G.2004. Full-scale load tests on instrumented micropiles. *Proceedings of the Institution of Civil Engineers: Geotechnical Engineering*, Vol. 157, no. 3, pp 127-135
- Sadek, M. and Shahrour, I. 2004. Three-dimensional finite element analysis of the seismic behavior of inclined micropiles. *Soil Dynamics and Earthquake Engineering*, Vol. 24, no. 6, pp 473-485.

- Sadek, M., Shahrour, I., 2006. Influence of the head and tip connection on the seismic performance of micropiles. *Soil Dynamics and Earthquake Engineering*, Vol. 26, no. 5, pp 461-468
- Sivrikaya, O., Togrol, E. 2006. Determination of undrained strength of fine-grained soils by means of SPT and its applications in Turkey”, *Eng. Geology*, Vol. 86 (1), pp. 52-69.
- Telford, W. W., Kokan, M. J., and Aschenbroich, H. K. 2009. Pile Load Tests of Titan Injection Bored Micropiles at an Industrial Plant in North Vancouver. *Proceedings of the 9th International Workshop on Micropile*, London, England, May 10–13.
- Terzaghi, K., and Peck, R.B., 1967. *Soil mechanics in engineering practice*. Second Edition, Wiley, New York, 729p.
- Terzaghi, K., Peck R.B., Mesri, G. 1996. *Soil Mechanics in Engineering Practice*, 3rd Edition, John Wiley & Sons Inc. , New York, 549 p.
- Thomson,P., Leew,B., Zakeri, A., Becker, D., Bunce, C., and Dittrich, P. 2007. Axial Compression, Axial Tension and Lateral Load Response of Pre-Production Micropiles for the CPR Mile 62.4 Nipigon Subdivision Bridge. *Proceedings of the 8th International Workshop on Micropile*, Toronto, Canada, Sep 22-26
- Traylor, R.P., A.W. Cadden, and D.A. Bruce. 2002. High Capacity Micropiles in Karst™: Challenges and Opportunities. *Deep Foundations 2002: An International Perspective on Theory, Design, Construction, and Performance*, American Society of Civil Engineers, Geotechnical Special Publication No. 116, Orlando, FL, pp. 743-759.
- Walker, J. N., and Cox, E. H. 1966. Design of pier foundations for lateral loads. *Transaction American Society for Agriculture Engineering*, Vol.9, no 3, pp. 417-420
- Whitaker, T. 1957. Experiments with model piles in groups. *Geotechnique*, Vol. 7, no. 4, pp. 147-167
- Williams Form Engineering Crop 2010. *Ground Anchored System*. No. 109, Belmont, MI, p. 76.
- Wolf, T.F. 1989. Pile capacity prediction using parameter function. Preceding and observed axial behavior of piles, *Results of a pile Prediction symposium*, Sponsored by Geotechnical Engineering Division, ASCE geotechnical special publication, No. 23 pp. 96-106.

Yacyshyn, C.J. 2007. Cyclic Quasi-Static Load Tests on Micropiles. Proceedings of the 8th International Workshop on Micropile, Toronto, Canada, Sep 10–13.

APPENDIX A: COPYRIGHT PERMISSIONS

A1. Copyright Permission from Federal Highway Administration (FHWA)

Mr. Ahmed Abd Elaziz,

Thank you for your request.

The figures to which you refer are in the public domain; therefore you are free to use them. Because you will not be making any changes to the items, you may use the following figure credit: Reprinted with permission of the U.S. Department of Transportation - Federal Highway Administration. For any proprietary commercial citation you will need to get permission from the original copyright holder.”

The reference on the reference list should carry the following reference information as an example;

Federal Highway Administration, [Micropile Design and Construction Guidelines - Implementation Manual](#) , Publication No. FHWA-SA-97-070, August 2000”

Please let me know if you have any questions.

Thanks,

Khalid

Khalid T. Mohamed, P.E., PMP

Senior Geotechnical Engineer

Office Of Bridge Technology

Washington, DC 20590

From: Ahmed Yehia

Sent: Thursday, March 29, 2012 12:52 PM

To: FHWA, Exec Secretariat (FHWA)

Subject: RE: Required Permission for Published data

Dear Sir/ Madam:

Greeting;

This is Ahmed Yehia abd Elaziz. I am at the final year of my PhD program. I am expecting to submit my thesis for defence by the next month.

My research is focused towards the performance and behaviour of hollow bar micropiles in cohesive soils. I did a series of full scale field load test on singles and pairs of hollow bar micropiles. Followed by, finite element analysis on the behaviour of hollow bar micropiles under monotonic and cyclic, axial and lateral loads.

In my thesis, I found that I will be in need to add some illustrations and information from the FHWA implementation manual 2000- Micropiles design and construction guide lines. I got a copy from this precious manual from the FHWA website.

To that end, I would like to beg your pardon to give a permission to use those illustrations in my written thesis and my presentation for thesis defence.

I would like to thank you in advance for your cooperation with me.

Please accept my best regards

Sincerely,

Ahmed Yehia Abd Elaziz

Research assistant & PhD Candidate Geotechnical Research Center
Department of Civil and Environmental Engineering
The University of Western Ontario

A2. Copyright Permission from Con-Tech

No problem Ahmed,

Good Luck

Daniel R. MacLean

Vice President Operations

Con-Tech Systems Ltd.

From: Ahmed Yehia

Sent: September-09-11 2:23 PM

To: Dan Maclean

Subject: RE: Request for Hollow Core Micropiles Figures

Dear Dan:

Greeting;

I would like to express my deep thanks and appreciation to you and to Con-Tech for giving me that permission.

The photos and illustration that I would like to use is:

- Figures at page 5 of the “A new dimension for ground Engineering”
- Figures at page 3 “ Micropiles Brochure”
- Photos at page 6 “ Micropile Brochure”

I may need one or more photos to show the wide applications of hollow core bars. I will update the list as soon I choose them.

I am expecting to defence my thesis between February and March 2012. Upon getting the degree I will send to you a copy of my works and the presentations as well.

Thank you for your help.

Best regards

Ahmed Yehia Abd Elaziz

Research assistant & PhD Candidate

Geotechnical Research Center
Department of Civil and Environmental Engineering
The University of Western Ontario

From: Dan Maclean

Sent: September-08-11 12:41 PM

To: Ahmed Yehia

Subject: RE: Request for Hollow Core Micropiles Figures

Hello Ahmed,

Thank you for your interest in using our illustrations for your thesis about micropiles.

You have our permission to use our photos, illustrations, figures etc. that are published in our brochure and technical literature.

However, we ask that you let us know which photos, illustrations, figures etc you wish to use.

Also we would be very interested in reading your thesis, if you would be so kind as to send us a copy upon completion of your work.

Daniel R. MacLean

Vice President Operations

Con-Tech Systems Ltd.

From: Ahmed Yehia

Sent: September-07-11 2:32 PM

To: ctswest

Subject: Request for Hollow Core Micropiles Figures

Dear Sir/Madam:

Greeting;

I am Ahmed Yehia Abd Elaziz; fourth year PhD student at the Civil and Environmental Department, University of Western Ontario. My research program throughout a period of four year focuses on the performance and behaviour of hollow core bars as micropiles. I

did a series of field load tests, and calibrate the data obtained by finite element analysis. I am now preparing some presentations related to my works. From all the figures and illustrations in the literature, I found that's in Con-Tech catalogues best describe the hollow core micropiles installation and components. To that end, I would like to ask your permission to use some of your illustrative figures in two presentations related to my studies; one will be presented at the 2011 Pan-Am CGS Conference, and the other will be my thesis defence presentation, at the University of Western Ontario. Upon your permission, appropriate citation will be given during the presentation to each figure used.

Thank you In advance

Best Regards

Ahmed Yehia Abd Elaziz

Research assistant & PhD Candidate Geotechnical Research Center
Department of Civil and Environmental Engineering
The University of Western Ontario

A3. Copyright Permission from Williams for hardware

Greetings:

Yes you have our permission to use images from our catalogue or web site for your project.

I would ask that you note where they are from though

Regards

Martin Hodgson

Exec. VP anchoring

Williams Form Hardware

From: "Ahmed Yehia"

Date: Tue, 17 Apr 2012 13:47:13 -0400

To: Martin Hodgson

Subject: Authorization for usage

Dear Mr. Martin:

Greeting:

I would like to beg your pardon to give me authorization and permission to use some of the data and illustrations published on "Williams Form-Ground Anchor System 2011" to use them in my Thesis and during my presentation for thesis defense.

Your cooperation is highly appreciated.

Regards

Ahmed Yehia Abd Elaziz

Research assistant & PhD Candidate

Geotechnical Research Center

Department of Civil and Environmental Engineering

The University of Western Ontario

CURRICULUM VITAE

Name	Ahmed Yehia Abd Elaziz
Post Secondary Education and Degree	<p>Faculty of Engineering, Alexandria University, Alexandria, Egypt (1995-2000), B.Sc</p> <p>Faculty of Engineering, Alexandria University, Alexandria, Egypt (2001-2005), M.Sc</p> <p>Western University, London, ON, Canada, (2007-20012), Ph.D</p>
Honors and Awards	<p>The Milos Novak Memorial Award, University of Western Ontario, 2010</p> <p>MITACS Accelerate Scholarship; internship between Williams Form Engineering Crop and the University of Western Ontario, London, Canada, 2009</p> <p>Western Graduate Thesis Research Award, 2008</p> <p>Western Graduate Research Scholarship Engineering, 2007-2011</p> <p>Egyptian Ministry of Higher Education Scholarship, 1996 – 2000</p> <p>Distinguished high school student, Alexandria University, Egypt, 1995/1996.</p>

Work Experience

Teaching assistant and Research assistant

Department of Civil and Environmental, Western University,
2007- 2012

Civil Engineer

Technical Engineering Office, Alexandria, Egypt, 2000- 2007

Assistant Lecturer

Civil Engineering Department, Faculty of Engineering,
Alexandria University, Alexandria, Egypt, 2000-2007

Relevant Publication

Abd Elaziz, A.Y. and El Naggar, M.H. 2012. Axial Behaviour of Hollow core Micropiles Under Monotonic and Cyclic Loadings. *Geotechnical Testing Journal*, ASTM, Vol. 35, no. 2, pp.249-260.

Abd Elaziz, A.Y. and El Naggar, M.H. 2010. Monotonic Axial Behaviour of Hollow Core Micropiles. *Proceeding of the 10th International Workshop on Micropiles*, IWM, Washington, D.C., USA, September 22-25.

El Sharnouby, B., El Kamhawy, H. and **Abd Elaziz, A.Y.** 2010. Vertical Response of single pile and pile groups resting on stratified soils. *Proceeding of the 7th Alexandria International Conference on Structural and Geotechnical Engineering*, Alexandria, Egypt, December 27-29.

Abd Elaziz, A.Y. and Elnaggar, M.H. 2011. Axial Behaviour of Hollow Core Micropiles under Compression and Tension Loads. *Proceeding of 14th Pan-Am and 64th Canadian Geotechnical conference (2011 Pan-Am CGS Geotechnical conference)*, Toronto, Canada, October 2-5.